A PHYSICAL MODEL OF WIND-BLOWN SAND TRANSPORT

Thesis

by

Bradley T. Werner

In Partial Fulfillment of the Requirements

for the Degree of

Doctor of Philosophy

California Institute of Technology

Pasadena, California

United States of America

1987

(Submitted 20 April, 1987)

ACKNOWLEDGMENTS

"I can fly higher than an eagle, but you are the wind beneath my wings."

-Willie Nelson

Peter Haff introduced me to the desert, and taught me to see and appreciate its myriad features. He instilled in me the confidence to follow up on my inclinations, without which the work described herein never would have been attempted. For performing the painful duty of writing the proposals to support this research and contributing many of the key ideas underlying it, for his careful critique of this manuscript, and for a rich friendship, I am truly grateful to Peter.

The minute I walked into Tom Tombrello's office five years ago, and he began to describe the multitude of possibilities for research under him with great enthusiasm, I knew that this was **the** place to be. Being a Brown Bagger, it is easy to forget how rare a find is one who will tolerate unconventional research, much less encourage it, as Tom does. Since I have known him, through thick and through thin, Tom has always been behind me 100%; I owe a debt of gratitude to Tom for this unqualified support.

Over the period encompassing this research, I have benefited from

the help and advice of many Caltech faculty members, especially Geoffrey Fox, Rogerio Livi, Ron Scott, Mark Shapiro and Bob Sharp. I appreciate the contributions to the development of my scientific skills made by Thad Vreeland and Petr Vogel early in my graduate student career.

Scientific progress requires dialogue and collaboration. For their help in this regard, I am grateful to Bob Anderson, Rob Fätland, Gary Gutt, Salman Mitha and Minh Tran.

Technical expertise was provided with patience, skill and enthusiasm by Richard Borup, Alan Rice and Steve Stryker. Michelle Vine tolerated my presence, and gave assistance at some critical junctures.

The primary tool utilized in this work was the computer. To all those who can make those damn things run, including the Caltech Concurrent Processing Group (especially Geoffrey Fox, Shirley Enguehard, Mark Johnson, Steve Otto and John Salmon), Gary Gutt and Pat Huber, I express admiration and thanks. I am grateful to the Seismological Laboratory at Caltech for the use of their digitizing system.

I thank Duncan Weathers for the loan of his desk, and all Brown Baggers, past and present, who have contributed to the success of this research.

The pleasures of non-technical friendship with Jesse, Johann, Chris and Kathy were enjoyed during my graduate years. The support and love of Mom, Carol, Jeanne, Jenny, Monte and Val are appreciated.

Caltech has been a wonderful place to work. The efforts of the staff, and all those individuals who give their time and money to maintain and advance the high quality of the research environment at Caltech are to be applauded.

Support for this research has emanated from a number of sources: first and foremost has been the contribution of the American taxpayer, who has provided grants through the Army Research Office [DAAL03-86-K-0132] and the National Science Foundation [EAR85-06817 and CEE84-12429]. A student research grant from the Geological Society of America supported the work on dynamic ripple-shape measurements. IBM provided the author with a pre-doctoral fellowship. The Caltech Concurrent Processing Group, which developed and maintained the computers for the dynamical computer simulations, was supported by the Parsons Foundation, the Systems Development Foundation and the Department of Energy [DE-AS03-83-ER13118].

Finally, I would like to thank all those who have made sacrifices

in the past, so that we of the present might be free.

ABSTRACT

Eolian saltation, the transport of sand by the wind, involves a variety of physical processes. A fundamental understanding of saltation requires an analysis starting from the level of the individual sand grain. The complexity of this nonlinear dynamical system compels us to divide the problem into more easily handled decoupled components: the saltating grain-bed impact process, the force of the wind on individual grains, the determination of the wind profile from the spatially averaged force of the moving grains on the air, and the formation of small-scale bedforms: ripples.

The impact of a moving sand grain with a bed of sand is studied with two-dimensional dynamical computer simulations and an experiment propelling single grains onto a sand bed. We find that the result of the impact may be described in terms of the rebound of the incident particle and the ejection of bed grains. The bed grain ejections originate from a localized area around the impact point, and at steps in the surface (elevation changes of one grain diameter) which are more widely distributed; these surface steps we term brinks (downstream-facing) and anti-brinks (upstream-facing).

A model for steady-state saltation is proposed which incorporates both aerodynamics and the mechanics of the grain-bed impacts, and balances the losses of saltating particles on impact with the bed by gains due to impact generated bed grain ejections. This model does not require data on blowing sand. Results are obtained which qualitatively agree with existing data. Quantitative tests will require new experiments. We argue that grain-bed impacts, not fluid stresses, are the means for entraining grains in steady-state eolian saltation.

The development of sand surface topography is viewed as a result of surface grain transport (reptation) driven by the impact of high-energy saltating grains onto the bed. The collision and merger of small collections of sand, proto-ripples, lead to the asymptotic development of uniform ripples from an initially smoothed surface. The limiting wavelength is pictured as being determined by statistical fluctuations in the saltating impact flux and/or the shortening of the saltation shadow zone below the mean reptation length during a collision between two ripples. Field observations of developing ripple cross-sectional shapes confirm these ideas qualitatively, and rough calculations of limiting wavelengths agree with existing data.

TABLE OF CONTENTS

1

THE OBSERVER

The heat shimmers off the sand warmed by the light of the westering sun. The silence is broken only by the muffled reports of rock hitting rock as a rare boulder plunges to the bottom of a distant gorge, loosened by the painfully slow processes at work in the desert. The Observer stands atop a trillion grains of sand, watching, and waiting patiently for the wind to blow. Late afternoon brings a break in the calm. As the sun sinks towards its nocturnal resting place, the firm hand of the wind exerts greater and greater stresses upon the sand surface. Finally, the dance of the sand grains commences. The first grains dislodged are impelled by the wind to accelerate, and then, experiencing the unrelenting pull of gravity, crash into the surface, propelling even more grains into the merciless clutch of the wind. This process continues in a multiplicative chorus fanning out downstream. In a few seconds resistance is abandoned, and the entire surface of the dune is filled with the motions of hopping grains, concentrated into streamers which weave their way across the surface. The power of the wind does not go unabated; it is diminished by the effort required in bending the grains to do its bidding, and a truce is established, balancing the speed of the wind and the number of indentured grains. A patch of sand smoothed by the Observer spontaneously becomes inundated with shallow topography; the small piles of sand slowly merge into a two-dimensional pattern, resembling the regular forms of ripples surrounding the patch. As the illumination begins to fail, the Observer takes one last look at the dune, and sees the grains which hop off the crest of the dune onto the steep, straight slope on its downstream side silhouetted against the amber sky. An avalanche of sand grains creeps slowly down this incline; the sound of grain scraping against grain gradually melds into an intensifying sonorous voice, quaking the air, the sand dune and its occupant, and firmly establishing the power and mystery of Nature to all of her creatures in this valley. Contented to cede her the upper hand on this day, the Observer walks off to enjoy a campfire, a can of beans, a cigar, the glory of the night sky, and the certainty of his own freedom.

CHAPTER I. INTRODUCTION

"There ain't no doubt I love this land,
God bless the U.S.A."
-Lee Greenwood

As a walk through its environs surely will reveal, the desert landscape presents an observer with an array of compelling questions, clear to see, but by no means simple or straightforward to answer. The short-term evolution of much of the land's surface can be described in terms of the movement and interaction of individual, classical particles (i.e., those particles within the realm of classical mechanics), subject to the forces of water, wind and gravity. The fluid forces are in turn affected by the character of the surface. Superimposed on this scene are the longer-term changes in the Earth's exterior, with their corresponding seismic disturbances, caused by internal impetus. An understanding of the behavior of collections of surface particles, interacting among themselves and with the fluid, gravitational, and seismic forces, would constitute a significant advance towards solving many of the problems posed on one's travels through the desert.

While the power of moving water remains dominant in the landscapes of most deserts, the wind plays a key role in shaping the

surface at select locales. The most familiar manifestation of this role is the sand dune, often well removed from the spot where water and/or gravity had deposited the sand grains. The manner in which these grains are transported, and their propensity to organize themselves into well-defined and beautiful structures, such as dunes, are subjects ripe for analysis. One mode of sand transport by the wind is called eolian saltation. The way in which steady-state saltation operates can be described best by considering the approach to the steady state. The following picture was described initially in incomplete form by Bagnold (1941), extended by Owen (1964), and reinterpreted by Ungar and Haff (1986), Mitha et al., (1986) and Werner (Chapter IV).

A gust of wind, faunal activity, a kick of a boot, or some other disturbance might cause a sand grain on an otherwise stationary bed of sand to become airborne (see Figure 1.1). This grain is accelerated downstream by the wind, but is eventually brought back to the bed by the force of gravity. If the wind velocity is sufficiently high, the sand grain will rebound off the surface with enough vertical velocity that the height it attains grows with each hop, and therefore the subsequent impact velocity rises as well. On striking the surface with sufficient velocity, it

will propel a number of bed grains into the wind stream. If this process continues, the number of grains entrained in the wind will grow exponentially. However, the act of accelerating grains extracts momentum from the wind, resulting in a decrease in wind velocity in the layer in which the sand is saltating. This in turn will lead to a lower impact velocity for the saltating grains and hence fewer sand grains ejected from the bed per impact. Steady-state saltation is attained when, on the average, one grain leaves the surface (including a possible rebound of the incident grain) for every impacting grain. With a distribution of particle trajectories in the wind, the steady-state requirement may be stated: the velocity distribution of particles leaving a representative patch of the sand surface must, after acceleration by the wind and impact on the surface, be reproduced by that same group of particles. The feature central to this picture is that the ejection of bed grains resulting from saltating grain-bed impacts is assumed to be the means of entraining particles in steady-state saltation, and that the nature of these impacts will play a major role in determining the characteristics of the steady state. The velocity distribution of grains leaving (or rebounding from) the bed as a result of the impact of one incident grain is

termed the "splash function" (Ungar and Haff, 1986).

Two additional modes of grain transport by the wind can be identified: suspension and reptation. Suspended grains are in a state where the forces of turbulent fluctuations overpower gravitational settling, and thus they are generally transported great distances by the wind. Grains so transported are smaller (< 0.01 cm) than standard sand grains, are often referred to as dust, and are not treated here (see, e.g., Gillette, 1981). Reptation (Bagnold's "creep") is the motion of surface grains driven by the impacts of saltating grains but which do not rise sufficiently high to be affected significantly by the wind. Such grains range in size from sand (e.g., Bagnold, 1941) to pebbles (e.g., Weir, 1962; Sharp, 1963; Smith, 1966) to 4 cm cinders (P.K. Haff, 1984: personal communication), depending on such factors as wind velocity, saltating sediment supply, etc. The number and velocity distribution of reptating grains will be determined both by the character of the steady-state saltation, and by the mechanics of the grain-bed impacts. Saltation and suspension are pictured in Figure 1.2.

Saltation over an initially smooth sand surface will cause that surface to evolve into a regularly-spaced sequence of undulations

oriented perpendicular to and propagating along the wind direction, which are termed eolian sand ripples. In sand, these ripples are asymmetric in cross section, with shallow slopes (up to 10 °) on the upwind, or stoss side of the ripple, and steep slopes (up to the angle of repose, ~ 35°) on the downwind, or lee side. The ripple wavelength ranges from a few centimeters to tens of centimeters, and the ratio of the wavelength to height of a ripple, termed the ripple index, varies from about 10 to 70, but is most commonly between 15 and 20. The ripples constitute coherent entities along their crests for up to on the order of one-hundred times their wavelength, although they often can be rather irregular and ragged. Figure 1.3 shows ripples at the Kelso Dunes of the Mojave Desert.

The surface grains are rearranged primarily by saltating grain impacts, and thus the question of ripple formation is intimately entangled with that of saltation. The transition from a smooth to a rippled surface is accomplished by the initial formation of bumps in the surface (Bagnold, 1941; Sharp, 1963) resulting from small scale fluctuations in the saltating (and hence reptating) flux, which are due to a stochastic wind profile and grain liftoff velocity and position nonhomogeneities; these bumps then execute a number of mergers until growing into full-sized

ripples. Larger scale bedforms, the sand dunes, result from the long-term effects of saltation. Saltating particles also are responsible for the formation of erosion features such as yardangs (e.g., McCauley, et al., 1977) and ventifacts (e.g, Sharp, 1964; 1980).

The scientific endeavor is not just the dry manipulation of mathematical expressions, computer codes, or gadgets. Its success depends to a large degree on the availability of inspiration, excitement, a sense of adventure and innovative ways of thinking. In the field of eolian sand transport, such indispensable tools often are not to be found in one's office in front of a computer terminal, but rather in the environment one seeks to study. The value of being on a sand dune during a saltation episode cannot be overstated. We feel compelled to pay tribute to this aspect of research, which so often goes unrecognized or unmentioned.

The study of natural phenomena in times gone by often entailed ventures into the unknown of a type which is difficult to locate in today's world. A trip through Death Valley, the Sahara, or the Grand Canyon does not involve the uncertainties, nor the concommitant feeling of accomplishment, of the past. Untrodden land is rarely encountered. One may recapture elements of the experiences of the great explorers by

travelling in the nearby Mojave Desert, but some aspects must remain forever elusive for adventurers of the present age.

The primary tools utilized in this dissertation include direct observation, simple experiments and computer simulation. Our ability to look beyond the fine work of previous generations, despite seeing with a less-practiced eye, depends on our access to high-speed computers. The additional physical insight afforded by the computer has allowed us to reexamine these processes from a fresh perspective; however, the importance of direct observation in combination with this insight should not be discounted. Examples of researchers who combined the careful study of eolian phenomena with adventure in the early days of this century include Dr. Vaughan Cornish and Brigadier Ralph Bagnold.

Cornish is best known for his analogies between water waves and the undulating structures which appear in sand and snow, a subject he termed kumatology: the study of surface waves of the atmosphere, hydrosphere, and lithosphere (Cornish, 1914). The similarities in the appearance of water waves and ripples on the beach at his home on the coast of Britain evoked in him a sentiment that the disparate areas of physical geography which involved wave-like forms should be brought

under the auspices of a coordinated scientific study. Cornish travelled extensively undertaking his kumatological studies, from Egypt to Winnipeg. His writings are filled with a fascination for the unusual, such as snow mushrooms and the eolian transport of leaves. His observations of cahots, large scale undulations in the snow caused by the passage of many sledges over an area, and his experiments in sand to investigate the mechanism of their production, anticipated some of the experiments and conclusions of more recent workers in the area of washboarded roads (Mather, 1963). Cornish's quantitative observations and his performance of simple, yet illuminating experiments are important to mark in an era when sophisticated equipment is often emphasized over less complex approaches. Reflecting on the difficulty of undertaking investigations along uncharted paths, Cornish (1914) wrote that in the "Land of the Unknown,"

> . . . there are no sign-posts to direct the traveller, no roads for him to follow, no maps to show him how to shape his course. Here watchfulness, patience, and docility to experience are the only passports. But it is a delightful land, and its call is like the 'the call of the wild.'

Bagnold's interest in eolian sand transport was subordinate to his love of adventure. Stationed in Cairo in the 1920s as an officer in the

Royal Engineers, Signals and Tanks, he and a few brave colleagues ventured out into the surrounding desert on ever lengthening journeys. Spurred by the desire to explore the sandy desert to the west of Cairo by automobile, Bagnold set about understanding the structure of sand dunes to lessen the pain of travelling in a sand-covered world, in particular to avoid becoming bogged down in soft sand. He found that there were areas on dunes which were navigable, and developed a mobile sun-compass to compensate for the lack of recognizable landmarks in the dune fields. He and his companions, on leave from army duty, were exploring country previously uncharted. Their travels were reported in a systematic manner to the Royal Geographical Society (e.g., Bagnold, 1931). This systematic reporting, as well as Bagnold's curiosity concerning the sand features he saw, led to his scientific study of wind-blown sand transport and its effects, both in the field, and later with a wind tunnel in the laboratory, culminating in the seminal work on the subject, The Physics of Blown Sand and Desert Dunes (Bagnold, 1941). Bagnold applied his knowledge to the cause of freedom in World War II by observing and harrassing the enemy in Northeast Africa, using his superior knowledge of the country and how to move within it.

In relating the compelling need to go beyond the present state of knowledge, to seek a discovery which we know is forever beyond our grasp, Bagnold (1935) employed the fabled lost oasis of the Libyan Desert, Zerzura:

> Zerzura is sought in many places, in the desert, at the Poles, in the still unsurveyed mountain regions of Asia. There is no fear that the quest will end, even though the blank spaces on the map get smaller and smaller. For Zerzura can never be identified. Many discoveries will be made in the course of the search which will make the seekers very happy, but none will surely be Zerzura... The answer to the riddle of the dunes may be discovered, but it will not tell us where Zerzura lies.

We may never be able to unravel all the complicated aspects of eolian sand transport, but Bagnold's accomplishments, and those of succeeding investigators, provide a plethora of inspiration for the current generation of researchers to continue the quest.

Saltation is just one small piece of a much larger puzzle. The general problem consists of describing the behavior of collections of classical, macroscopic, irregularly-shaped grains which interact through stiff-compressional and frictional forces, move under the action of external driving forces, such as gravity or fluid stresses, and remain within the realm of classical mechanics. When the motion of these systems is dominated by the grain-grain interactions, they are termed

granular materials. Examples include dry soils, rockslides, icebergs in an ice jam, planetary rings, dry snow avalanches and the transport and handling of ores, seeds, pills and dry dogfood. It is desirable to determine the general properties of these and other granular systems starting from the level of the dynamical properties of individual grains, in a fashion analogous to the derivation of the kinetic theory of gases and fluid mechanics from a consideration of the properties of the individual constituents.

Because of the great complexity of granular systems, progress has been made in understanding their behavior for only a limited number of very special cases. This suggests that a frontal attack on the grain dynamics problem would be of very little use. An alternative approach is to consider simple cases which involve properties of granular materials which have general applicability. Wind-blown sand transport is one such case. The impact of saltating grains involves accoustic propagation through the bed, as well as rearrangement, packing and sorting of the sand grains. The avalanche of grains down the slipface of a dune, although not treated here, includes gravitational transport and shearing between the grains. All of these are basic properties of granular materials, which, if

understood for one case, could significantly contribute to the elucidation of the general problem. Thus saltation is a process of general interest in the field of classical mechanics, as well as of particular importance to those interested in the evolution of desert landscapes.

There may be a tendency for some to dismiss this avenue of research as outside the purview of physics. We believe that this view is mistaken on two counts. One is that the techniques employed in this investigation, as may be readily discerned through a perusal of this document, are those of the physicist. Second, it is toward a fundamental description of the motion of a particular granular system, wind-blown sand, that this research is directed. Feynman (1965) wrote that "There is . . . a rhythm and a pattern between the phenomena of nature which is not apparent to the eye, but only to the eye of analysis; and it is these rhythms and patterns which we call Physical Laws." Granular systems tend towards order in many circumstances in which they are observed in nature or industry. Wind-blown sand grains exhibit this type of organizational tendency. They form ripples and dunes, they sort themselves by size, shape and composition, they produce loud booming sounds when sliding down a dune slipface. Underlying this strange and

beautiful conduct is a set of "rhythms and patterns"; it is certainly within the bounds of physics to explore the mechanisms producing this conduct. If not a physicist (considering the abundance of physical detail inherent in the study of granular systems), who? If not now (with the advent of high-speed computers), when? If not here (at Caltech), where?

Man has been curious about the nature of wind-blown sand features for a very long time, but systematic studies of the phenomenon were rare prior to this century. Here we present a brief outline of the history of eolian studies, with some more detailed references to specific aspects of past work given in the individual chapters of this thesis.

There is no question that Bagnold's labors in the field of eolian transport have defined the framework from which most subsequent researchers have proceeded. The foundation for careful experimental studies was laid with his observations of wind-blown sand in the wind-tunnel and the desert. He noted that sand saltation could be induced by a sufficiently high wind velocity (the fluid threshold), but that, once initiated, saltation could continue at lower wind speeds down to a critical value of the wind-shear stress (the impact threshold). The difference he attributed to the ease with which grains could be entrained

by grain-bed impacts relative to their entrainment by fluid stresses. In short, Bagnold (1941) concluded that "once saltation is started, [the grains] are jerked up into the air not by the action of the wind but by the impact of descending grains." He was able to observe some grain-bed impacts in his wind tunnel. In addition, he found that these impacts led to a population of low-energy "creeping" (reptating) grains which constituted one-fourth to one-fifth of the total sand transport. Much of the action in saltation takes place in the centimeter just above the surface. This region is generally obscured by the large numbers of reptating and lower-energy saltating grains, a problem which plagued Bagnold and all later researchers.

Bagnold devoted a great deal of effort to the measurement of wind velocities during saltation, and found that it was difficult to obtain measurements in the saltating layer. However, he was able to deduce that the wind velocities close to the surface in the saltating layer actually decreased with increasing free-stream velocity. The details of his efforts, and those of others, are described in Chapter IV.

From the perspective of sediment transport in agricultural settings, W.S. Chepil and his coworkers investigated aspects of saltation

and wind erosion, with an emphasis on practical considerations (e.g., Chepil, 1945a; 1945b; 1945c; Chepil and Woodruff, 1963). Among the observations which are of particular relevance to this work are the direct confirmation that the wind velocity does decrease in the lower portions of the saltating layer when the ambient wind velocity is increased, the importance of the nature of grain-bed impacts in transferring horizontal momentum of incident saltating grains to vertical momentum of rebounding grains, and the appearance of more widely varying saltation trajectories over rough surfaces as opposed to more uniform trajectories over smooth surfaces.

Greeley, Iversen and colleagues have concentrated on investigations of the initiation of saltation, and the extension to environments on Mars and Venus (e.g., Greeley, et al., 1974; Iversen, et al., 1976; Greeley, et al., 1984). White and Schultz (1977) and White (1982) investigated quantitatively the effect of particle rotation on trajectories as suggested by Chepil (1945a), and they obtained data on impact and liftoff velocities of high-energy grains in saltation.

Sharp's field observations (1964; 1980) provide valuable information about the importance of the constitution of rebounding

surfaces to the character of the saltation. Also, he found that larger grains rebounded to greater heights.

Owen (1964) proposed a theoretical model of saltation in the steady state. His model rested on two hypotheses: (1) The shear stress at the surface during saltation is fixed at the value corresponding to the fluid threshold. (2) The wind above the saltation layer has a logarithmic profile determined by its height, and inside the layer, the wind has a constant eddy viscosity. Owen believed that fluid stresses, rather than grain-bed impacts, were responsible for particle entrainment. Although the model put forth here follows the basic structure of Owen's calculation, we disagree with him on both of his hypotheses.

The theory of saltation was significantly advanced with the introduction of the successive saltation hypothesis (Tsuchiya, 1970; Tsuchiya and Kawata, 1972), which stated that grains in saltation, upon impact with the surface, rebound and continue in saltation. This hypothesis was expanded upon by Reitzes (1978) and Rumpel (1985). It focussed attention on the importance of the grain-bed impacts. Rumpel constructed a model of steady-state saltation within this hypothesis using a straightforward picture of the grain-bed impacts, but was unable

to fix the overall flux of particles due to the lack of feedback from the surface inherent in successive saltation.

A model of steady-state saltation, propounded by Ungar and Haff (1986), employs a delta-function splash function. The model described in Chapter IV is patterned after their approach, utilizing a more realistic splash function. The recent research of Anderson and Hallet (1986) and, in a similar vein, Jensen and Sorensen (1982) and Sorensen (1985) likewise has common elements with our saltation model. We differ in our choice of splash functions, and in that our choice of boundary conditions (both on the wind velocity and on the grain-bed interaction) requires no recourse to data on wind-blown sand. We will argue that data on wind-blown sand transport, which are difficult to obtain, at best, can be checked properly only by a model constructed independently of that data.

Learned studies of underwater saltation go back to the pioneering work of Gilbert (1914). Hydraulic transport of sediment is very different from eolian sand transport, primarily because the density of the water is comparable to that of sand, whereas the density ratio is on the order of two-thousand in the eolian case. Thus, the effect of grain-bed impacts is

diminished and the importance of fluid stresses is correspondingly increased in underwater saltation. However, the approach to the two problems may have similarities, as is illustrated by some recent work on sediment transport in water (Gordon, et al., 1972; Wiberg and Smith, 1985; Drake, et al., 1986).

Snow saltation shares many characteristics with sand saltation; in particular, if the snow is of the dry, pellet-like variety, its collisional properties will resemble those of sand, and the density remains very high relative to the density of air. Work in the field of snow saltation has been primarily experimental, with noteworthy examples being the measurement of saltation hop lengths with a segmented-box collector (Narita, 1978) and the measurement of liftoff and impact velocities in a wind tunnel using stroboscopic photography (Araoka and Maeno, 1981).

The debate over a mechanism for the origin of sand ripples has been characterized by controversy. At least three schools of thought on ripple formation may be identified. Early ideas ascribed ripple formation to the direct stress of the wind on the sand surface. This point of view was promoted by Cornish (1914; 1935), who cultivated the concept that ripples were formed by the scooping out of material from the lee of a

ripple by a reverse eddy operating there. Sharp (1963) has shown that no such eddy exists. Von Karman (1956a; 1956b) proposed a model of ripple formation which involved the growth of instabilities due to the consequences of the equation of Bernoulli. However, such a model requires that particle trajectories are significantly affected by small changes in the fluid velocity over a typical ripple wavelength, which will not occur in air.

Bagnold (1941) founded the second school of thought, by suggesting that ripples form as a result of the existence of a characteristic path length for saltating grains. According to this view, a slope tilted upwind receives more saltating grain impacts than a flat slope, and this excess is transmitted downstream *ad infinitum* in increments of the characteristic path length. In a steady-state condition in which the ripples were propagating downstream at constant velocity, this would imply that the surface slopes separated by one characteristic path would have to be identical, leading to ripples of wavelength equal to this path length. Ellwood, et al. (1975) have expanded on this picture to claim that the spectrum of ripple sizes observed is due to differences in saltation jump lengths among different size grains.

The third school of thought is attended by the author, and emphasizes that the ripples are a result of the evolution of an initially flat surface and the growth of perturbations in the bed. Sharp (1963) observed that a flat surface evolves into small bumps, which undergo successive merging until a stable pattern of ripples is formed, and noted the importance of the saltation shadow in the lee of the ripples. He concluded that grain size and the incident angle of saltating grains control the wavelength of the ripples. Stone and Summers (1972) claimed that grain size, and size sorting alone determine the ripple wavelength, and Walker (1981) found that grain size and wind velocity govern the ripple shape. Most observers from the time of Bagnold have noted that the ripple amplitude decreases as the sands become better sorted (by size).

Detailed theoretical attempts to incorporate these ideas go back to the work of Kennedy (e.g., 1964), who performed a stability analysis on a perturbed bed. This was updated (Jain and Kennedy, 1974) to include the evolution of the bedforms. However, this work is appropriate to dense fluids, such as water, only, where fluid stress is capable of deforming the bed. Anderson (1986) (also, T.A. Tombrello, 1985:

unpublished notes) has extended the stability analysis to the case where the surface grains are in reptation due to saltation impacts, with the impact rate dependent on the surface slope only. He concludes that the stable ripple wavelength is on the order of ten times the mean reptation length.

Seppala and Linde (1978) observed the time evolution of ripple shapes by mapping the contours of the sand surface. They found that ripple wavelength increased with time, except at high wind velocities, where they reported a decrease in wavelength after ten minutes for a wind velocity of 760 cm/s 10 cm above the bed, accompanied by the formation of smaller ripples on the backs of the larger ripples. Cornish (1935) also noted such structures.

This document recounts an investigation into the basic physical mechanisms underlying the transport of sand by the wind. Saltation is a complicated process, involving many disparate phenomena. Therefore, we have adopted the approach of separating the problem into distinct pieces, analyzing them individually, and then melding the component parts into a model. The purpose of this work is not to produce a detailed model to describe some particular situation, but rather to elucidate the important

physical processes, and combine them into an algorithm capable of making general predictions, free from dependence on empirical data for wind-blown sand. The model is not restricted to mere adumbrations, however; it will be amenable to detailed numerical verification when the proper experiments have been performed. Qualitatively, the model reproduces the features seen in Nature.

We begin by decoupling the transport of sand from the formation of ripples. Thus, our consideration of saltation assumes a flat sand surface. We divide the saltation process into the grain-bed impact, the acceleration of grains by the wind, and the corresponding drag on the wind. The former is studied both through computer simulations and experimental means. The technique for simulating the motion of granular materials and its implementation on a Concurrent Processing Computer is related in Chapter II. Chapter III recounts the application of the simulation algorithm to the grain-bed impact problem, as well as describing an experiment to measure the splash function for coarse sand. This experiment was adapted from the work of Mitha, et al. (1986), and complements the labor of Willetts and Rice (1985a), who measured the splash function for finer sands in a wind tunnel using high-speed

cinematography.

Chapter IV details a general algorithm for determining the steady-state features of a saltating system. A simplified picture of the fluid dynamics of the wind and the air drag on the saltating grains, which was derived from the work of Ungar and Haff (1986), is employed. This is combined with the results of Chapter III on grain-bed impacts, and Ungar and Haff's steady-state requirement, to yield a numerical representation for steady-state saltation.

The mystery of ripple formation is approached as a problem in the instability of a flat surface under random impacts. Evolution of a surface to periodic topography is seen in other circumstances, such as in the "washboarding" of dirt roads, indicating that, if the underlying mechanisms have common characteristics (e.g., dirt road surfaces impacted by vehicle tires, sand beds impacted by saltating sand grains), the phenomenon, to some degree, can not be dependent on the particulars of a given situation. We consider saltation to play a role only as the driving force for the bed grain reptation. As described in Chapter V, experimental observations and theoretical considerations combine to suggest that the statistical nature of the surface disturbances plays a

prominent role in determining the asymptotic small-scale topography.

APPENDIX I.1 A NOTE ON ORGANIZATION AND CONTENT

This monograph contains various portions of work which have been reported previously. Chapter II includes parts of (Werner, 1986a) and (Werner and Haff, 1985a; 1985b). Most of (Werner and Haff, 1986a) and (Werner and Haff, 1986b) are presented in Chapter III. (Werner, 1986b) and (Werner and Haff, 1987) materialize, in slightly altered form, in Chapter IV. The beginning section of Chapter V on ripple-cross-sectional measurements has appeared as (Werner, et al., 1986). These publications will not be referenced within the text; rather, we will refer to them by pointing out their locations in this document.

All references are collected at the end of the document. Figures, appendices, nomenclature lists, and tables may be found at the close of each chapter, as each chapter is generally independent of the others.

The ideas advanced in the following pages were developed in collaboration with P.K. Haff at the whiteboard of Room 304, under the star-speckled skies of Cima Dome, or navigating a canyon in some obscure mountain range of the Mojave Desert. Unpublished work of others cited in this dissertation include that of S. Stryker (sand gun construction, Chapter III), R.S. Anderson and P.K. Haff (saltation over hard surfaces,

Chapter IV), T.A. Tombrello (a smoothing algorithm, Chapter V), P.K. Haff (computer simulations of worms on a ring, Chapter V), and P.K. Haff, also R. Fätland (computer simulations of ripple formation, Chapter V). Unless otherwise noted, all other work described herein was performed by the author, and he assumes full responsibility for the veracity of this document's content.

FIGURE CAPTIONS: CHAPTER I.

Figure 1.1 With sufficiently high incident velocity, a single sand grain impacting a bed of grains may lead to the ejection of other grains from the surface. Downstream, a steady-state balance between the force of the wind on the saltating grains and the drag on the wind may be achieved, with the average sand grain which impacts the surface reproducing itself.

Figure 1.2 Saltation at the sand dunes of southern Owens Valley, California, with a dust cloud from the surface of Owens Lake (dry) in the backdrop.

Figure 1.3 Eolian sand-grain ripples at the Kelso Dunes, California.

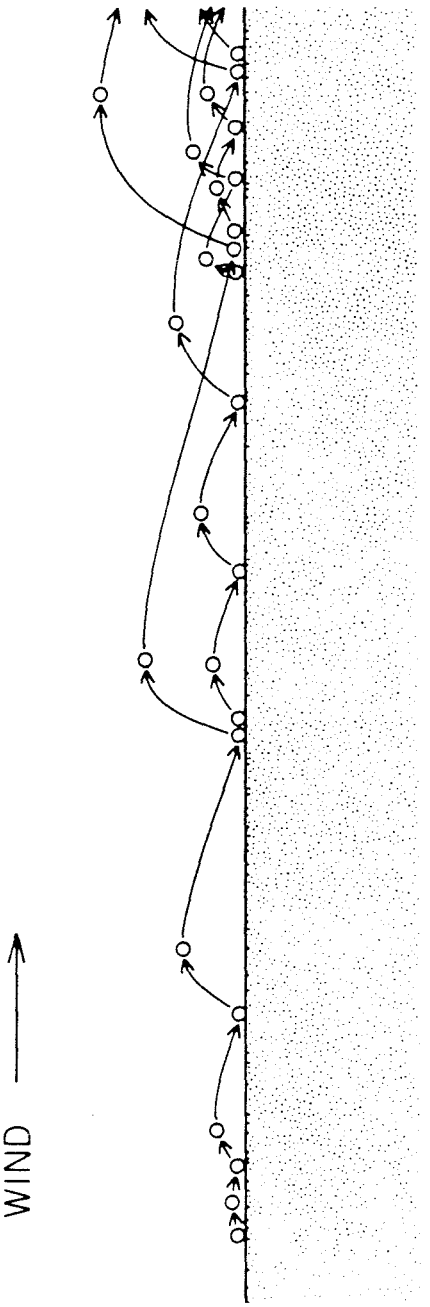

Figure 1.1

Figure 1.2

Figure 1.3

CHAPTER II. GRAIN DYNAMICS SIMULATIONS

". . . thinking remains a good deal harder than computing . . ."

-A.K. Dewdney

A granular system presents a perplexing panoply of problems not readily amenable to quantitative description. A can of mixed nuts provides a perfect illustration of the difficulties faced in attempting to describe such a system. Consider the rigor involved in solving a system of equations to describe the process of pouring a few nuts into one's hand. Additional anguish can be found in pondering the processes which led to the configuration encountered upon opening the can: the high concentration of Brazil nuts at the top and "the settling which occurred during handling," i.e., the increase in the packing density due to jostling.

Such are the frustrations confronting the present-day grain dynamicist. The situation can be likened to that encountered by a worker in the difficult field of fluid dynamics, except that no generally unsolvable equation (as the Navier-Stokes equation) has been derived yet to describe the motion of most classes of granular materials. Faced with this vicissitude and desiring a theoretical model for granular materials, one may proceed in one of two directions: either utilize empirically

derived relationships in a phenomenological model to predict the behavior of systems within the limited range of experimental applicability, or construct a detailed theoretical treatment, at a fundamental level, of a simpler problem than the one posed, in hopes that this might lead to sufficient insight to attack the full problem from first principles.

The field of soil mechanics, which is closely allied with that of grain dynamics, has been characterized primarily by the former approach, although effort has been devoted to relating microscopic properties of soils to their macroscopic behavior (see, e.g., Scott, 1963); generally, stress-strain relationships derived from experiments are used to predict the failure and flow properties of soils. A similar course has been followed in the study of glacier flow (e.g., Patterson, 1981). While both fields have enjoyed enormous success in this, they have not provided what we seek, a microscopic description of the material, so that, given the properties of the individual grains, one can predict its behavior under a variety of circumstances. Moreover, continuum approaches are largely unacceptable for problems in which individual grains are dominant, as is true for grain-bed impacts in saltation.

One means of gaining insight into the microscopic nature of

moving granular materials is through experiment. Careful experimental analyses of grain motion in gravity flow (e.g., Savage, 1979), sorting (e.g., Williams and Shields, 1967) and packing (e.g., Scott, 1960) have been performed, with the chief difficulty arising from the opaque character of granular materials, as opposed to clear fluids, a condition which prevents the observation of three-dimensional motion except at the boundaries. Drake and Shreve (1985) have avoided this issue by observing gravity flow of plastic beads in two dimensions. Saltation impacts are also amenable to experimental observation, since most of the action takes place at the surface.

Theoretical treatments of micromechanical grain dynamics thus far have been limited to systems of grains with highly specialized characteristics or behaviors. Most recent work has dealt with spherical particles interacting through non-frictional binary collisions, resembling molecules in a gas (e.g., McTigue, 1978; Ogawa, 1978; Ogawa, et al., 1980; Savage and Jeffrey, 1981; Shen and Ackermann, 1982; Ahmadi and Shahinpoor, 1983; Haff, 1983; Jenkins and Savage, 1983; Shahinpoor and Ahmadi, 1983; Hui, et al., 1984; Lun, et al., 1984; Haff, 1985; Haff, et al., 1985). Most granular systems, however, are characterized by sliding,

scraping and rolling of the grains; the grains are likely to be in continuous contact with their neighbors. Thus, the collisional descriptions, although useful for a limited set of questions, represent only an end member of possible models. Theoretical work on systems composed of grains in continuous contact has achieved limited success (e.g., Deresiewicz, 1958; Visscher and Bolsterli, 1972; Davis and Deresiewicz, 1977; Schwartz, et al., 1984).

As is the case for many modern scientific endeavors, progress in theoretical grain dynamics is facilitated by seeking the aid of the high-speed computer. Campbell and Brennen (1985) and Haff and Werner (1985) have reported on the results of computer simulations of grains interacting through binary collisions. Although these algorithms do not treat the more widely applicable continuous contact regime, they do allow for testing of the theoretical models, as well as the investigation of the effects of frictional collisions and arbitrary boundaries.

The successful use of computer simulations for the study of molecular systems in which the equations of motion of the molecules interacting through specified pair potentials are solved explicitly, termed molecular dynamics (MD) calculations (e.g., Alder and Wainwright, 1959;

1960), suggests an analogous approach for granular systems. Cundall pioneered this technique in simulating the quasi-static behavior of collections of circular and polygonal particles (Cundall and Strack, 1979). His grains interacted through stiff, inelastic-compressional and frictional forces. The basic algorithm consists of computing the forces between the particles at a particular time, and then stepping ahead a small time increment according to Newton's equations. This sequence is repeated in order to build up a time profile of the system's motion. This approach was used primarily for the study of failure modes and load-bearing characteristics of granular systems.

Walton (1983; 1984) extended Cundall's work to study systems where the grains moved large distances relative to one another, breaking and forming contacts. Computation time significantly increases with this innovation, requiring the use of careful programming techniques and a high-speed computer. Walton also made studies of the form of the contact force law, coupled these studies with detailed experimental confirmation of the simulations, and has recently extended the algorithm to spherical particles.

The One Particle Problem

In planning an attack on the knotty question of how granular materials behave, it is instructive to focus initially on a system composed of just one particle. This line of research was originally suggested to the author by the practical need to build a device for separating sand grains on the basis of their shape. One method for accomplishing this is to place the grains on an inclined ramp and use the distance a grain travels down the ramp as a measure of its degree of roundness. Glezen and Ludwick (1963) have constructed a device on a similar principle, which uses the velocity achieved by the sand grains on a ramp of fixed length to automatically classify their shape. The question arises as to what the property being measured, "roundness", actually means. An answer to this question requires an understanding of how individual particles move downslope in a gravitational field.

An informal experimental investigation was undertaken with P.K. Haff in a sandy spur to Spanish Canyon of the Mojave Desert for the purpose of suggesting ways in which to approach the single particle problem. A long, steep slope containing a hefty supply of boulders was located. We climbed to the top and began dislodging individual rocks and

sending them down the slope. A striking attribute of their journey to the bottom was that particles which went any significant distance possessed a large degree of rotational motion. In fact, the motion appeared to be a variant of rolling, where the boulders contacted the surface at only a few points on their periphery. In addition, the rotation tended to take place around an axis corresponding to the principal axis of the greatest principal moment of inertia. A boulder would occasionally hit another rock of similar or larger size squarely, and be thrown off its path; such boulders either would come to a rest quickly or the erratic motion caused by the collision soon would decay into the more regular rolling motion. A graphic illustration of this rolling motion is shown in Figure 2.1; the large rock at the right hit the sandy wash in the rolling mode, creating a series of indentations in the sand: rockprints.

Analytical calculations of one particle motion are not possible in general. Even the limitation to two dimensions does not help a great deal. The motion of a circle interacting with an inclined line through inelastic normal collisions and friction can be predicted through a straightforward calculation (P.K. Haff, 1984: unpublished notes). For instance, after a sufficiently long time, such a particle will be either

rolling or spinning with slipping, depending on the coefficient of friction, our solution being faciliated by the decoupling of the decaying normal component of motion from the tangential and rotational modes of motion.

A polygonal particle on an inclined line more closely resembles tumbling sand grains and boulders. A computer simulation program based on the ideas of Walton and Cundall, but coded without reference to their programs, was used to analyze this case. The interaction force between the polygon and the line is shown in Figure 2.2. The contacts are presumed to occur at the points defining the polygon. A real collision between two particles involves deformation at the contact, typically less than one percent of the particle radius, and described by the laws of elasticity and plasticity (e.g., Goldsmith, 1960). Within our algorithm, the polygonal particle and the inclined line remain undeformed during a contact; instead, they are allowed to overlap, with a force normal to the contact plane applied which rises rapidly with the amount of penetration Δr. Following Cundall and Walton, we chose the normal force applied to the polygon, f_n, to depend linearly on Δr, and introduced inelasticity

through a velocity dependent damping term; this is, in essence, a damped harmonic oscillator, which is turned on only when the particles overlap. Thus,

$$f_n = k_n \Delta r + \gamma_n \Delta \dot{r}: \quad \Delta r > 0$$
$$f_n = 0: \quad \Delta r \leqq 0, \tag{2.1}$$

with k_n and γ_n constants. The normal inelasticity can also be described in terms of a coefficient of restitution ϵ, the ratio of the outgoing to ingoing velocities normal to the surface of contact in a two-body collision, which can be related directly to the damping constant

$$\epsilon = e^{-\gamma_n T/4}$$
$$T = 2\pi/\sqrt{k_n/m - (\gamma_n/2)^2}\,. \tag{2.2}$$

The mass of the polygon is m, and T is the period of the spring-mass system.

When the contact point is moving, the shear force is essentially the usual friction force, i.e., the kinetic coefficient of friction times the normal force, μf_n, which is taken to oppose the motion of the contact; however, we must account for situations in which the shear force drops below this limiting value. This is accomplished by introducing a damped spring, which produces a force in the direction tangent to the inclined

line. This spring is fastened initially at the spot at which the contact between a point on the polygon and the inclined line originates. If the point (on the polygon) continues to move in a single direction relative to the line, the spot at which the spring is fastened moves along with the point so that the spring force remains equal to μf_n, until the point on the polygon shifts direction. In other words, the spot at which the spring is attached travels along the line in such a way that the shear spring drags behind the contact, never exceeding an extension which would cause the spring force to exceed the friction limit. Note that we do not distinguish between static and kinetic coefficients of friction. The mathematical form of this force for interacting circular particles is presented later in this chapter.

While this complicated shear force is necessary for mathematical stability of the algorithm, the reader may see its expression in the physical world by experimenting with a square of jello on a flat surface. The jello magnifies the elastic properties of more conventional materials. Applying an increasing force tangent to the surface on the jello, it initally begins to deform until a point is reached at which it begins to slide. As it is sliding, it remains deformed. If the driving force

is decreased, the jello will eventually come to a stop, and then acquire its former shape. Elastic materials such as rocks and sand grains will exhibit this sort of behavior on a much smaller scale. The shear spring of the computer simulation approximately reproduces this behavior.

Given the position and linear and angular velocities of the polygon at some time t, one can calculate the forces acting on it, and from these the two components of the total force on the particle and the torque about the center of mass, and use that information to predict the position and velocities at a time $t + \Delta t$. Such a numerical scheme is applied repetitively to integrate the equations of motion and to obtain a time evolution picture of the polygon's motion.

At this point, it is imperative to issue a warning to the reader, lest he be tempted to apply the results of this computer simulation algorithm directly to specific problems of practical interest. First, one characteristic of nonlinear dynamical systems is that they often display a marked sensitivity to initial conditions. Polygonal particles on inclined lines display this feature, making it impossible to predict, with finite numerical accuracy, how the motion of a polygon will evolve from given initial conditions. Second, the polygonal shape, the flat inclined line, and

the form of the contact force are gross approximations to realistic situations. However, we note that Walton (1983) has reported success in matching simulations to experiment.

The value of the computer simulation technique as used here is to identify general characteristics of the behavior of granular systems. A computer simulation experimentalist enjoys an advantage over his counterpart in the laboratory, in that all of the information concerning the particle motion is easily available to him. The laboratory experimenter must struggle to obtain the limited fraction of the data which is accessible (see Drake and Shreve, 1985). Also, the computer simulations allow one to vary system parameters at will, to isolate dependences on parameters, and to be certain of the physics characterizing the interactions between the constituents. However, the bane of the grain dynamicist dependent on simulations is the uncertainty about the relevance of his work to natural phenomena. Thus, any intelligent use of simulations must be tied to experimental and theoretical work.

Returning to the motion of a polygonal particle on an inclined line, we ran simulations of particles of various shapes, including a

square, a rectangle, and an irregular hexagon for a variety of incline angles, coefficients of friction, and contact spring parameters. The polygon was dropped with no kinetic energy, from a fixed height several times its own size, and with a random orientation, onto the line. It collided with the line in a chaotic manner for a time, but eventually achieved some sort of coherent, describable motion, which may be expressed as a combination of the three classes illustrated in Figure 2.3: bouncing, sliding and rolling. For most sets of parameters, particularly if the coefficient of restitution is not close to unity, the bouncing of the particle, which tends to be chaotic, will decay rapidly, often within the first few collisions with the line. There is some chance (again depending on the parameters) that the particle will hit the line in such a way that it loses a sizable fraction of its kinetic energy; if this occurs, it may be unable to recover, and become trapped in a sliding mode, which may bring the polygon to rest, contingent on the value of the coefficient of friction. However, if the friction coefficient is sufficiently high, the polygon may prefer to travel in a rolling mode, in which the particle approximately moves as if it were a circle of radius equal to the greatest distance from the center of mass to one of the points defining the polygon, rolling down

the incline. In this case, only the furthest points from the center of mass contact the line.

The rolling of the polygons corresponds well with the observations of tumbling rocks in Spanish Canyon; there the rough slopes provide a high effective coefficient of friction. This causes a point on the boulder which contacts the surface to remain fixed, forcing the boulder to pivot around that point and thereby inducing rotational motion. Apparently, stable transport by means of the rolling mode is favored in a high friction environment on a steep slope, both in nature and on the computer. The study of the motion of a single particle on a slope provides an example of how dynamical computer simulations can aid in producing general statements about particle systems. While a detailed predictive model is not yet available for this problem, the next section demonstrates how the computer simulations may be used to produce the simplifying assumptions necessary to construct a numerical model.

The Loaded Gambling Die

'Ανερρίφθω κύβος[1]

—Julius Caesar

Extension of the one particle problem to three dimensions is intriguing. A simple example is the interaction of a cubical particle with a flat horizontal plane. We might consider the motion of the cube to be akin to the motion of a gambling die. Altering the position of the center of mass of the die (by introducing unsymmetrically placed weights) so that it is no longer at the center of the cube, i.e., loading the die (Scarne, 1980), gives one the opportunity to attempt to predict something definite, i.e., the probability that each face of the die will land up. The number on the die facing up when it comes to rest is termed its value.

Expanding the one particle computer simulation algorithm to treat a three-dimensional particle is straightforward. A polyhedron interacts with a plane under the influence of gravity. The contacts occur at the points defining the polyhedron (e.g., eight for a cube). Because of the

---

[1]This famous phrase, translated as "Let the die be cast", is presented in the Greek because Plutarch, in his Life of Pompey, wrote that Caesar spoke this Greek proverb in that language. The Greek necessitates the use of the imperative, thus the correct translation into Latin is "iacta alea esto!" rather than "iacta alea est!" (The die is cast!); the latter variant is found in the manuscripts of Suetonius, who was writing in the early second century A.D., possibly being a corruption of the earlier text (G. Pigman III, 1986: personal communication)

limitation to one particle, we avoid the complication of edge-edge contacts. Again, the particle does not deform, but upon penetration of the plane, a stiff force normal to the plane is applied. The form of the normal and shear forces is the same as for the two-dimensional case, except that the shear force now acts to oppose the instantaneous vector velocity of the point in the plane. The orientation of the polyhedron is specified by the three Euler angles, and the angular integration is accomplished through Euler's equations (see Goldstein, 1950). Simulations of a loaded die reveal that, in terms of predicting the value of the die, the tumbling which occurs just prior to the cessation of motion can be described by a sequence of die-plane collisions (Figure 2.4). If the die is restricted to motion in two dimensions, the sequence of collisions becomes well-defined. We consider such a two-dimensional loaded die, with the center of mass lying along a diagonal. Two types of faces can be identified on the die: high-faces and low-faces, as shown in Figure 2.5.

In constructing a model to predict the value of a two-dimensional die, the die-plane collisions are taken to be characterized by a constant coefficient of restitution, and the faces of the die are the local minima

of the gravitational potential energy of the die in contact with the plane, plotted versus the die orientation, Figure 2.6. The probability that a given face will land up is given by the chance that the die becomes trapped in the energy well associated with the opposite face. By taking the initial kinetic energy to be random, following the trajectory of the die in energy space, which is determined by the decay of energy due to the coefficient of restitution ϵ, assuming that the die "rolls", so that the loss of energy due to friction is small, and enumerating the possible journeys to each of the final states (faces of the die), one arrives at an expression for the probability that the high side will land up, p_h, as a function of the fractional distance the center has been moved along the diagonal, f. This calculation is not unlike that of Housner (1963), who studied the stability of structures during an earthquake, although, for his model, it was necessary to consider the detailed dynamics. Here we are merely working on energy principles. This expression, derived in Appendix II.1, is displayed in Figure 2.7. The probability p_h decreases with the coefficient of restitution, reflecting the fact that a lower rate of energy loss allows a system to seek out the various possible final states more efficiently,

and choose the "preferred" energy state, i.e., the state of lowest energy, with higher probability. This is analogous to crystal formation under a slow rate of cooling versus the production of an amorphous material by rapid quenching from the melt. If ϵ is zero, the value of the die is that corresponding to the face which was up upon impact, and the probability of being in either state is one-half.

A generalization of this model to three dimensions would involve careful consideration of how a die transits from one face to the next, since, unlike two dimensions, this can happen in an infinite number of ways. A naive extension of the above model to three dimensions suggests that a drilled die, of the type found in a Monopoly game, where the dots are defined by gouges in the die faces, will land with a value of six on the order of 0.5% more often than expected for a fair die. This is due to the removal of mass from that face, which, being opposite the "one" side, effectively moves the center of mass away from the "six" and toward the "one." This number is arrived at by using the linear relation between probability and displacement of the center of mass, as suggested for a nearly elastic die in Figure 2.7. This result may help explain why advocates of "psychokinesis" (reviewed by Girden, 1962), in testing their

ability to force dice to do their bidding with the power of their minds, preferentially chose to wish for the value of the die to be six.

The ability to improve the chances of a loaded die finding its lowest energy state by picking the die-plane coefficient of restitution closer to unity suggests that the loaded die could be used as a paradigm of a tunable automatic stochastic decision-maker (Werner, 1987). For instance, consider a simple economics problem in which we wish to choose one of four items costing \$1, \$2, \$3 and \$4, with the only requirement being that we minimize the cost. If we load a die as in Figure 2.8, with the distance of the center of mass from each face inversely proportional to the value of that face, a roll of the die will preferentially pick the item of lowest cost. In this example, it was easy to choose the lowest cost item. However, in many decision-making problems, it is not possible to ennumerate all of the possibilities. Haff (1986) has reported a general technique for optimization and zero-finding using dynamical systems of classical particles.

Finally, we discuss some research on the motion of three-dimensional particles on slopes. Melton (1965) examined rock mobility on slopes, identified categories of downslope motion (including

our rolling mode), and related this to the slope parameters. Bozzolo and Panami (1982) have studied the tumbling of individual boulders down Alpine inclines, for the purpose of protecting highways and their occupants from this danger. Also, we have done some preliminary work on this subject, utilizing the loaded die computer simulation program. We found that simulated noncubical blocks moving on a steep inclined plane could be induced into the rolling mode, rolling preferentially around the body axis with greatest moment of inertia. In Figure 2.9, we show a side view of a sequence of images of a 5x5x1cm block moving down an incline, with $g = 981$ cm/sec^2. The fraction of total rotational energy shared in rotation around the x (perpendicular to the face of the block), and the y and z (identical moments of inertia) body axes is plotted versus distance down the plane in Figure 2.10. While occasional perturbations occur, most of the rotational energy remains in rotation around the x body axis. The free-body oscillation around the y and z axes, and the constant rotational energy around the x body axis between collisions with the plane, to be expected for an object with two degenerate moments of inertia, is evident. Future work along these lines may lead to a

quantitative description.

Simulations of Systems of Circular Particles

The effort expended in investigating the one-particle problem has enlightened us in several respects important to the study of the many-particle problem, including teaching us how to extract general features and simplifying asssumptions necessary for model building, as well as an appreciation for the difficulty of the field. This insight has prompted us to limit ourselves to simulations involving circular particles for the probing of grain-bed impact mechanics in saltation.

Circular particles may be described intrinsically by a radius r_i, a mass m_i, and parameters specifying their interaction with other particles. Here i denotes an integer identifying the particle. The extrinsic state of a circular particle is described by its horizontal and vertical positions x_i and y_i (also described by the vector $\vec{x}_i$), and velocities v_{xi} and v_{yi} respectively (or $\vec{v}_i$), as well as an orientation angle θ_i and an angular velocity ω_i. A circular particle computer simulation code which we have written allows these circles to interact among

themselves and with line segments which are either fixed in space or programmed to move in a specified manner; for example, boundary line segments may be vibrated.

The forces acting between the circular particles resemble the forces we described on the polygonal particle. When the two circles overlap, a damped spring force acts in the direction connecting their centers, and a damped spring limited by friction opposes relative motion on the surfaces of the circles. For two circles labelled i and j, the force on particle i due to particle j at time t_0, $\vec{f}_{ij}(t_0)$, is:

$$\vec{f}_{ij}(t_0) = \hat{n}\{ k_n[(r_i + r_j) - (\vec{x}_i - \vec{x}_j)\cdot\hat{n}] - \gamma_n m_{eff}(\vec{v}_i - \vec{v}_j)\cdot\hat{n} \} + \hat{s}\{ min\{ [-k_s \Delta t v_s - \gamma_s m_{eff} v_s + \Phi_{ij}(t_0 - \Delta t_0)], \mu f_n \} \}$$

$$f_n = \vec{f}_{ij}(t_0)\cdot\hat{n}$$
$$v_s = \hat{s}\cdot(\vec{v}_i - \vec{v}_j) + r_i\omega_i + r_j\omega_j$$
$$\Phi_{ij}(t_0 - \Delta t_0) = -k_s \Delta t_0 v_s + \Phi_{ij}(t_0 - 2\Delta t_0)$$
$$m_{eff} = m_i m_j/(m_i + m_j). \qquad (2.3)$$

In these expressions we have made reference to the unit vector along the direction from the center of j to the center of i, $\hat{n}$, the unit vector tangent to the circles at the contact, $\hat{s}$, chosen so that $\hat{s}\times\hat{n}$ points out of the page, the relative velocity of the surfaces along $\hat{s}$, v_s, the reduced

mass, m_{eff}, the integration time step, Δt_0, and the spring portion of the shear force remembered from the previous time step, $\Phi_{ij}(t_0 - \Delta t_0)$, which acts to constrain the spot at which the shear spring is fastened to move along with the contact.

The true nature of contact forces between real particles is more complex than the form used in our model (Bowden and Tabor, 1950; Deresiewicz, 1958; Goldsmith, 1960; Landau and Lifschitz, 1970). We have ignored two facets of real interactions. First, for all but the gentlest collisions, the energy loss occurs primarily through plastic deformation. Second, the form of the force law may be nonlinear for three-dimensional particles, as in the Hertzian contact law (force ~ $\Delta r^{3/2}$). Walton and Braun (1985) have gone to a great deal of trouble to make the contact force as realistic as possible. However, we are interested primarily in those properties of granular materials which, one hopes, do not depend on these details. We have used very simple contact and friction forces in the hopes that much of the system's behavior will be determined by geometrical effects of the packing, and by the gross nature of the forces (e.g., stiffness, inelasticity, and friction

coefficient), rather than by the detailed formulation of the interaction. This is supported by our own work, in which we have found that sorting of granular materials by size is not sensitive to the stiffness of the particles, and by the work of Walton and Braun (1985), who report that the shearing of disks is not sensitive to the value of the (nonzero) coefficient of friction.

If the general behavior of granular materials cannot be described without recourse to a detailed model for the interparticle forces, the field of computational grain dynamics will soon wither away, for we cannot hope to include all of the complexity of interactions between real particles in our models. However, there is cause for some optimism. Nature has revealed herself, on the whole, to be rather elegant. When we have appreciated some of that elegance for the grain dynamics case, if it in fact exists, it will be appropriate to refine our understanding by using more realistic interactions between the grains in the computer simulations.

The interaction between a line segment and a circle is similar to that described above for two circles. The line is assumed to have infinite mass. If the center of a circle penetrating the line passes the end point

of the line segment, the contact is then defined by that point penetrating the circle, rather than the circle penetrating the line. This approach has the advantage that no discontinuity in forces occurs when a circle drops off the edge of a line segment.

A first-order predictor-corrector method was used to integrate the equations of motion. Starting at a particular time t_0, the forces and corresponding torques on the particles are determined as above. From these forces, new values of the velocities and positions are predicted a short time later $t_1 = t_0 + \Delta t_0$. The forces and torques are then determined at the predicted velocities and positions, and are averaged with the values at time t_0. The velocities and positions are stepped forward from t_0 to t_1 again, except that the averaged forces are used. The differences between the predicted and corrected velocities for the three degrees of freedom for each particle are compared to the change in those velocities over the time step, to determine whether to accept the integration step, or reject it in favor of reducing Δt_0 by a factor of two and repeating the step. If the maximum fractional difference between predictor and corrector velocities is sufficiently small, the time step size is increased by twenty percent.

The equations for numerical integration of the x coordinate and its velocity, from the current coordinates at time t_0 to those at time $t_0 + \Delta t_0$, are given below:

$$
\begin{aligned}
v_{xp}(t_0 + \Delta t_0) &= v_{xc}(t_0 - \Delta t_{-1}) + 2[\Delta t_{-1} + \Delta t_0] f_x(t_0) \\
x_p(t_0 + \Delta t_0) &= x_c(t_0) + \Delta t_0 [v_{xc}(t_0) + v_{xp}(t_0 + \Delta t_0)]/2 \\
v_{xc}(t_0 + \Delta t_0) &= v_{xc}(t_0) + \Delta t_0 [f_x(t_0) + f_{xp}(t_0 + \Delta t_0)]/2 \\
x_p(t_0 + \Delta t_0) &= x_c(t_0) + \Delta t_0 [v_{xc}(t_0) + v_{xc}(t_0 + \Delta t_0)]/2, \qquad (2.4)
\end{aligned}
$$

with the subscript p denoting a predicted value, and the subscript c denoting a corrected value, i.e., one which will be used as the current position or velocity at the next integration step if the current one is accepted; Δt_0 is the current integration time step size; Δt_{-1} is the time step for the previous step; $f_x(t_0)$ is the force in the x direction computed at the current coordinates; and $f_{xp}(t_0 + \Delta t_0)$ is the x force computed using the predicted coordinates at time $t_0 + \Delta t_0$. The first-order predictor-corrector algorithm was found to be sufficient; the use of higher-order integration schemes (e.g., Acton, 1970) does not result in an automatic increase in time step size, because of the typically continuous making and breaking of contacts in a system composed of many particles.

These higher-order schemes carry the added burden of increased memory requirements and manipulations, without any significant benefits for many granular systems with which we have dealt.

The computer time required for simulating granular systems composed of many particles is large; therefore, we are forced to deal with the issue of computational efficiency. For each time step in the simulation, the program must check for contacts (overlaps) between the particles, calculate the forces where contacts exist, and update the positions and velocities of the particles. The computation time it takes to perform the contact checking is technically proportional to the square of the number of particles N^2, since each particle must be checked against every other particle for a potential contact. This N^2 dependence can be reduced to a nearly linear dependence on N by dividing the simulation region into rectangular boxes in which it is necessary to check each particle in the box against those others in the box and on the adjacent boundaries of neighboring boxes only; thus the computation time required for contact checking is proportional to NN_b, where N_b is the approximately constant number of particles in the each box (Cundall and

Strack, 1979). There are other means of dealing with the N^2 problem, including attaching to each particle a periodically updated list of other particles potentially in contact with it. The spatial division we have chosen fits in well with the alogorithm for running the circular particle program on Concurrent Processing Computers, described later in this chapter.

Both the calculation of forces and the integration of positions and velocities require computer time which is proportional to N. The contact checking, force determination, and integration comprise the computationally intensive portion of the grain dynamics simulations.

We have checked our grain dynamics simulation codes using simple single particle tests, such as a block sliding on a plane and a spinning circle impacting a line segment. For instance, it is possible to show that the rotational energy loss of a circle of radius r and mass m spinning at angular velocity w and impacting a fixed line at velocity v will be $2\mu v m r w$, where μ is the coefficient of friction, if $\mu v << rw$. We applied this test in a simulation using $w = 500\ sec^{-1}$, $\mu = 0.01$, $r = 0.5$ cm, $v = 99.1$ cm/sec and $m = 1.57$ g, and obtained a rotational energy loss

of 782 ergs, as compared with a calculated value of 778 ergs. We tested the energy damping by comparing the measured and calculated coefficients of restitution for the impact of two circular particles. As an example of this, we display in Table 2.1 the measured coefficients of restitution from six incident relative velocities of two grains of radius 1.0 cm and density 2.0 g/cm^2, with $k_n = 5.0 \cdot 10^6$ dynes/cm and $\gamma = 1000.\ \text{sec}^{-1}$. The calculated value, using equation 2.2 (with the mass being the reduced mass of the two grains) gives $\epsilon = 0.671$, no more than 1% different from the measured values in Table 2.1. Since the collisions last about 36 integration time steps, and the allowed maximum error on the velocities per time step was 0.5%, this difference falls within the expected variation of 3% ($\sqrt{36} \times 0.5\%$). Since these tests and others, as well as energy and momentum conservation criteria for many particle systems, agree with the predicted results within the expected margin for the error limit supplied to the predictor-corrector algorithm, we are satisfied that the simulations are performing as we have directed them to.

The use of the circular particle program to study the sorting of granular materials by size illustrates the practical difficulties involved.

Figure 2.11 shows a sequence of snapshots of a simulation of thirty-one particles, one of which is twice the radius of the others, in a shaking goldpan-shaped container. The large particle starts at the bottom but inevitably finds its way to the top. We found that interparticle friction enhances the rate at which the sorting takes place (Haff and Werner, 1986). The simulation shown took forty-five minutes of CPU time on a VAX/750. Most problems require considerably more particles and longer particle-simulation times than this. Thus, even the relatively inexpensive VAX-like microcomputers now becoming available will not support extensive simulations of granular materials. The situation is even worse in three dimensions: a cube of only ten particles on a side contains one-thousand grains.

Concurrent Processing Computers

A new technology is being developed at the California Institute of Technology, as well as at a number of other institutions, which may revolutionize the simulation of granular dynamics, as well as many other computationally intensive problems (Fox and Otto, 1984). In this technology, termed "concurrent processing", a number of relatively slow but cost-efficient processors work simultaneously on the same problem.

The processors are connected by communications channels to neighboring processors as well as to a conventional computer for data input/output and program control. This collection of processors is called a Concurrent Processing Computer (CPC). The bulk of the saltation impact simulations described in Chapter III were carried out on these machines.

The primary advantages of such a hardware configuration are that no expensive electronic miniaturization is necessary to construct a machine of supercomputer power and that there is no theoretical limit to the number of processors and hence the computing power of the CPC. A concurrent processor ten percent as powerful as a CRAY-1 but built for one percent of the cost is currently operating (J. Tuazon, et al., 1985). Construction of a concurrent processor as powerful as a CRAY-1 for a hardware cost of 500,000 dollars is underway (G.C. Fox, et al., 1985). Intel is presently marketing 32- to 128-processor CPCs based on the Caltech design. No scientific application requiring a great deal of computer time has been found which cannot be programmed onto the CPC with a high degree of efficiency (Fox, 1984).

The Concurrent Processing Computers consist of from 32 to 128 processors connected by communications channels in the "hypercube"

configuration (Fox and Otto, 1984), of which two- and three-dimensional arrays are a subset. Each of these processors runs the same code, which is written by the programmer. At the time this research was performed, it was necessary to write this code in the C programming language. Programming the processors is no different than programming a sequential (standard) computer, except for subroutine calls which communicate data to and from neighboring processors and a controlling processor termed the Intermediate Host. The interprocessor communication is normally necessary because the processors are all working on different parts of the same problem. Generally these different parts of the problem are in some way interdependent: either locally (along the "edges" of the processors, as in the simulations reported here) or globally (e.g., as for particles under the influence of gravitational forces). The Intermediate Host runs a user supplied program and is responsible for controlling the actions of the processors and for channeling their input and output to and from a disk. The user writes his programs, cross-compiles them and starts up the Intermediate Host program from a sequential computer (e.g., a VAX), with which he can also analyze the output. The major difficulty in programming the CPC at the

time was the lack of sophisticated debugging facilities. A program which runs on a VAX and simulates both the communications schemes and the operation of the CPC was available to alleviate this problem in part. The effort required to acquaint oneself with the CPC system is about the same as that to learn an unfamiliar programming language.

The performance of the Concurrent Processing Computer is evaluated using a quantity called the efficiency e (Fox and Otto, 1984):

$$e = \frac{\textit{Time program takes on a sequential processor}}{\textit{Time program takes on a CPC with M processors} \times M} .$$

The efficiency will always be less than one. Its value is depressed by two factors: interprocessor communication time and an unequal distribution of the computational load among the processors (e.g., more particles in one processor than another). It has been shown that the effect of communications is negligible if the number of operations in which those communicated data are used is large (Fox, 1984). Problems having fixed computational elements, as do finite difference methods for solving differential equations, have no difficulty maintaining an equal distribution of load among the processors. However, some scientific problems, including grain dynamics simulations, have an irregular

arrangement of computational elements, which are free to move, and thus special techniques may need to be invoked to assure a minimal amount of load imbalance. Most scientific problems have been found to have efficiencies greater than 0.80. The granular physics simulations run on the CPC with a small amount (generally less than about ten percent) of computational overhead.

Grain Dynamics Simulations on Concurrent Processing Computers

The method for decomposing the grain dynamics simulations onto the Concurrent Processing Computer must take into account the short range nature of the forces between the particles as well as the particle mobility. We have found two viable choices for a concurrent algorithm. The first involves dividing the simulation space into regions corresponding to the processors of the CPC. Each processor is responsible for calculating the forces between the particles within that region, and between its own particles and those on the edges of the adjoining processors, as well as integrating the positions of its particles forward in time. Particles which cross the boundaries between the regions are transferred to the appropriate processor. This algorithm minimizes interprocessor communication.

The second choice is designed to minimize computational load imbalance among the processors. The particles are initially assigned to processors according to their positions in space, as in the former case. However, as the system evolves, the particles are retained in their original processors, even though they might wander outside of that region of space. This leads to increased communications, since a particle may wander far from its original neighbors; however, the number of particles in each processor remains fixed. The assignment of particles to processors could be updated periodically to insure that interprocessor communications would remain a small fraction of the total computation time.

We have chosen the former algorithm, for it is more straightforward to program as well as being more adept at dealing with pathological cases, such as a single particle traveling rapidly from processor to processor (as in the case of a particle impacting a bed of particles), which could cause a considerable loss of efficiency when using the latter method. In addition, the latter method may sometimes fail to guarantee load balancing, since the load depends both on the number of particles and the number of contacts, which may change during the course

of the simulation.

The spatial assignment of the processors automatically limits the number of particles which must be checked for a contact with a particular particle within a processor to those particles within that processor and on the boundaries of neighboring processors. This is analogous to the division of space in the sequential algorithm to reduce the dependence of the computation time on the square of the number of particles. If the number of particles in each processor is large, there is an option in the concurrent program to divide the spatial regions assigned to the processors to further reduce the effort devoted to contact checking.

Figure 2.12 is a simplified illustration of the sequence of computations and communications between two adjacent processors for a single integration time step of our CPC simulation program. We focus on processors 2 and 3 in Figure 2.12(b). First, processors 2 and 3 exchange information regarding particles on their boundaries. Then they calculate the contact forces between the particles within their regions and with particles on the boundary. (Contact forces between boundary particles are calculated in only one of the processors.) The contact

forces of boundary particles are sent to the neighboring processor where necessary. Finally, the processors integrate forward in time the motions of the particles whose centers of mass lie within their region of space. In accordance with the predictor-corrector method, the sequence is repeated. At the end of the integration time step, any particles which have left the processor's region of space are passed to the appropriate adjacent processor. The communications scheme for a division of space among the processors in two directions is illustrated in Figure 2.13. Since the processors are connected to the four nearest-neighbor processors only, the sequence of communications must be chosen so that information about particles can be passed through nearest-neighbor processors to neighboring processors along the diagonals where necessary.

Although load balancing is relatively easy to achieve in a situation in which the particles are confined and tightly packed within some boundaries, special measures must be taken to accomplish it when particles move significantly, such as in flow down an inclined plane. Since the computational load is a determinable function of the number of particles and the number of contacts, it is possible to calculate the load

in each processor at any time during the simulation. We have included an option in our program to adjust periodically the spatial boundaries between the processors in such a way that the load is distributed as evenly as possible.

An evaluation of the performance of our program shows that the CPC is a cost-effective and reliable way of simulating granular materials. Comparisons of results between identical simulations run on a sequential computer and an CPC show no significant difference between particle positions or velocities after up to ten thousand integration time steps. The differences that do show up are attributable to a different order of floating point operations (and hence roundoffs) on the two machines.

Because the primary focus of this research was obtaining scientific results from the simulations, rather than the computational issues involved in programming and running on a CPC, extensive investigations of the efficiency of our concurrent processor grain dynamics algorithm were not carried out. A variety of tests indicated that the efficiency varied from 0.89 to 0.97, with the primary computational overhead due to load imbalance. Rough counting of the program operations indicate that communications overhead is low, at

most two to three percent. The low communications overhead results from the complicated nature of the interparticle forces and the dense packing of the grains, which means that information passed to a neighboring processor is used extensively. An example of an efficiency test is shown in Figure 2.14, for which the motion of fifty particles in a box was computed in a single processor, and two, four and eight processors. The ratio of computer time for one processor to computer time for M processors is plotted versus M. The efficiency varies from 98% for two processors to 90% for eight processors; the decline in efficiency being due to the magnification in load imbalance of one particle as the number of processors is increased.

Other Grain Dynamics Alogorithms

The simulation work described in the next chapter involves exclusively circular particles. Two extensions for systems composed of many grains are of interest: spherical particles and irregularly shaped particles, such as polygons.

We have authored and tested a computer simulation code for spherical particles interacting among themselves and with fixed or vibrating plane segments. The forces are much the same as those for

circles, except that the shear force acts to oppose the instantaneous relative motion in the contact plane, and the sphere-plane segment interaction includes the special cases of a sphere rolling off the edge of the plane segment, and off one of the four points defining the plane segment. The code to run the spherical particle program on the CPCs has been written, although it remains untested.

In addition, a many-particle polygonal grain dynamics code has been written, using the basic format of the single-polygonal-particle-on-an-inclined-line program. The interaction forces must take into account a number of special cases, such as when the points on two polygons in contact approach each other. This is accomplished by defining the contact "plane" as a line joining the two (or possibly four) intersection points between the polygons.

We anticipate that these programs will be useful in future investigations of saltation and other problems in the dynamics of granular materials.

The Correspondence between Simulations and Nature

A number of points concerning the relation between the results of computer simulations and the behavior we observe in Nature require emphasis. Qualitatively, the simulations mimic real granular materials. Qualitative correspondence has been found in the three problems we have attacked: downslope motion of a single particle, sorting, and grain-bed impacts in saltation (see Chapter III). Inasmuch as our interest here is in using the simulations as a tool for aiding an intuitive assessment of granular material behavior, rather than in making detailed numerical predictions, the evidence obtained from these three applications which we have studied suggests that grain dynamics simulations, as we have implemented them, are useful and valid for this purpose.

The simulations employed a stiff, damped harmonic oscillator interparticle force, turned on when the grains overlapped, and used a variable time step predictor-corrector integration scheme. The grain dynamics simulation code was evaluated using a variety of particle-fixed line and particle-particle interactions, as well as energy and momentum conservation tests for many grain systems, with the result that the program performed as intended.

The interaction force between our grains is essentially identical to that of Walton's (1983) program, and very similar to the interparticle force utilized by Cundall and Strack (1979). Walton (1983) has been able to accurately reproduce motion seen in the laboratory involving grain-grain collisions and assemblages of toppling blocks. Walton also obtained qualitative agreement between simulations and experiment for bin flow and shear of granular systems. Cundall and Strack (1979) found that they could roughly reproduce interparticle force networks generated by experiment with photoelastic disks using their circular particle program. These results have demonstrated the viability of spring-dashpot interactions in grain dynamics simulations, and they imply that such simulations might, with care, be useful for numerical work in some cases.

However, we have adopted, for the present work, a cautious approach. The reader will note that the major conclusions arising from our simulations are verified by independent physical reasoning (e.g., geometrical arguments) and/or experimental or field observations. Quantitative tests, in the spirit of the work of Walton and Cundall, would allow us to validate (or invalidate) the extension of the simulation data to numerical predictions.

A grain dynamics simulation can be likened to an experiment, a computer experiment. For the simulations described in Chapter III, the system has been specified sufficiently that others may repeat the experiment. The results are statistical in nature, and will not be reproduced exactly by another researcher, unless he should utilize the identical code. The limitation to statistical repoducibility is a typical characteristic of most experiments, and contrasts with an analytical calculation, where the result is exact.

APPENDIX II.1

Our purpose here is to derive and present an expression for the probability for a two-dimensional die to land on one of its two high faces, p_h, as a function of the fractional distance the center of mass has been moved along the diagonal, f. The dependence of p_h on f is displayed in Figure 2.7.

We view the problem as being one where the value of the die (the number showing when it has come to rest) is determined by capture in a gravitational potential energy well, and that the energy of the die, initially being a random value, is decreased according to collisions with a flat surface (characterized by a constant coefficient of restitution ϵ) as the die rotates, with one collision for each 90° of rotation. We calculate the probability of landing on each of the four sides by assuming that it is proportional to the width of the energy window from which the die can enter one of the four local energy wells associated with the die and get caught in that well.

To compute p_h, we must find the width of this energy window for each of the four sides of the die, and for each of the two possible

directions of rotation (clockwise and counterclockwise). Here, we give an example of one of these eight calculations: the energy window for getting caught in the low face wells (high face up) corresponding to an orientation of 90° in Figure 2.6 for counterclockwise rotation, i.e., approaching from the left of this Figure. We label the value of the energy barrier at orientation 45° (between the two low faces) ε_ℓ, the energy barrier at orientation 135° (and 315°) (between the low face and the high face) ε_M, and the energy barrier at orientation 225° (between the two high faces) ε_h. The values of these energy barriers, in terms of f, the die mass m_d and the acceleration of gravity g, are given below:

$$\begin{aligned} \varepsilon_\ell &= m_d g(\sqrt{2} - 1)(1 - f) \\ \varepsilon_M &= m_d g\{ \sqrt{2}\sqrt{1 + f^2} - (1 - f) \} \\ \varepsilon_h &= m_d g\{ (\sqrt{2} - 1)(1 + f) + f\}. \end{aligned} \qquad (2.A.1)$$

In order to enter the 90° energy well from the left, the die must possess an energy ε_0 greater than the barrier energy ε_ℓ: $\varepsilon_0 > \varepsilon_\ell$. To be captured in this well, after one collision with the flat surface, the energy of the die must be below that of the barrier on the right, i.e., $\epsilon^2\varepsilon_0 < \varepsilon_M$.

In addition, after failing to clear the right-hand barrier of the well, we must require that it does not rebound and escape over the left-hand barrier: $\epsilon^4\mathcal{E}_0 < \mathcal{E}_\ell$. Therefore, the limits on possible values of the energy prior to being caught in the well ($\mathcal{E}_0$) are $\mathcal{E}_\ell < \mathcal{E}_0 < min(\mathcal{E}_M/\epsilon^2, \mathcal{E}_\ell/\epsilon^4)$. Including the requirement that the energy window be positive, we arrive at the following expression for the width of this energy window at the 90° energy well, $\Delta\mathcal{E}_{left}(90)$:

$$\Delta\mathcal{E}_{left}(90) = max\{0, min(\mathcal{E}_M/\epsilon^2, \mathcal{E}_\ell/\epsilon^4) - \mathcal{E}_\ell\}. \qquad (2.A.2)$$

Note that we have defined the zero of potential energy at the minima of the two low-face-down wells. The calculation of the three other energy windows for entry into the well from the left proceeds in an analogous manner, with the results:

$$\begin{aligned}
\Delta\mathcal{E}_{left}(0) &= max\{0, \mathcal{E}_\ell/\epsilon^2 - \mathcal{E}_M\} \\
\Delta\mathcal{E}_{left}(180) &= max\{0, min([\mathcal{E}_h - fm_dg]/\epsilon^2 + fm_dg, \\
&\qquad [\mathcal{E}_M - fm_dg]/\epsilon^4 + fm_dg) - \mathcal{E}_M\} \\
\Delta\mathcal{E}_{left}(270) &= max\{0, [\mathcal{E}_M - fm_dg]/\epsilon^2 + fm_dg - \mathcal{E}_h\}. \qquad (2.A.3)
\end{aligned}$$

If the die was initially rolled in the counter-clockwise direction, the probability for the final state of the die to be low face down (high

face up) is proportional to $\Delta\varepsilon_{left}(0) + \Delta\varepsilon_{left}(90)$, and the probability for the high face down final state is proportional to $\Delta\varepsilon_{left}(180) + \Delta\varepsilon_{left}(270)$. Using the fact that the sum of these two probabilities is unity, we may calculate the probability p_h:

$$p_h = \{\Delta\varepsilon_{left}(0) + \Delta\varepsilon_{left}(90)\}/$$
$$\{\Delta\varepsilon_{left}(0) + \Delta\varepsilon_{left}(90) + \Delta\varepsilon_{left}(180) + \Delta\varepsilon_{left}(270)\}. \quad (2.A.4)$$

This expression also applies to a clockwise roll, since this merely exchanges the roles of the two low faces, and of the two high faces.

SYMBOL DEFINITIONS: CHAPTER II.

Δr	interacting particle overlap distance
f_n, f_s	forces normal and tangential to the contact plane
k_n, k_s	normal and shear spring constants
γ_n, γ_s	normal and shear damping constants
μ	coefficient of friction
ϵ	two-body collisional coefficient of restitution
T	period of spring
$t, \Delta t$	time and integration time step
p_h	probability for a high face on a two-dimensional loaded die to land face up
f	fractional distance along die diameter which center of mass has been moved
m_d	mass of die
g	acceleration of gravity
$\vec{x}_i, \vec{v}_i, \omega_i$	position, velocity and angular velocity of ith circle
r_i, m_i	radius and mass of ith circle
m_{eff}	effective mass of two circles in collision
$\hat{n}, \hat{s}$	unit vectors normal and tangential to contact
v_s	relative tangential velocity of circles at contact
N	number of particles in a simulation
e	efficiency of concurrent processor code
M	number of processors on a CPC
$max(a,b)$	maximum of a and b
$min(a,b)$	minimum of a and b

TABLE: CHAPTER II.

Table 2.1 Coefficient of Restitution Measurement from Circular Particle Simulation

Initial Relative Velocity (cm/sec)	Final Relative Velocity (cm/sec)	Coefficient of Restitution
10.00	6.748	0.675
50.00	33.74	0.675
100.0	67.48	0.675
500.0	337.4	0.675
1000.	663.8	0.664
3000.	2022.	0.674

FIGURE CAPTIONS: CHAPTER II

Figure 2.1 Rockprints from a rolling boulder in Spanish Canyon, the Mojave Desert, California.

Figure 2.2 Illustration of contact forces between a polygon and an inclined line. A damped spring acts in the normal direction, and a damped spring bounded by the friction limit gives the shear force.

Figure 2.3 Three classes of downslope motion: (a) Bouncing; (b) Sliding; (c) Rolling.

Figure 2.4 Simulations of a gambling die in motion, moving left to right: (a) Loaded die in three dimensions (projected onto a vertical plane); (b) Loaded die in two dimensions; (c) Fair die in two dimensions.

Figure 2.5 A two-dimensional die loaded along a diagonal has two types of faces: low faces and high faces.

Figure 2.6 Schematic plot of the gravitational potential energy of a loaded die in contact with the plane as a function of the orientation of the die.

Figure 2.7 The probability for a high face to land up, p_h, is plotted

against the fractional distance along the diagonal that the center of mass has been moved by the loading f.

Figure 2.8 A loaded die designed to make a decision between four items costing \$1, \$2, \$3, \$4, with the desire to minimize the cost.

Figure 2.9 Successive images, projected onto a vertical plane, of a 5x5x1cm block on a 40° incline.

Figure 2.10 The fraction of the total rotational energy which is to be found in rotation about the three body axes of the block in Figure 2.9 (labelled x, y, z) versus the distance down the plane. The x axis is perpendicular to the face of the block.

Figure 2.11 Sorting of a large particle in a matrix of 30 smaller particles inside a shaking container. Radius of the smaller particles is 0.5 cm and that of the larger particle is 1.0 cm. The amplitude of oscillation is 0.15 cm in the vertical direction and 0.6 cm in the horizontal direction. The shaking frequency is about 12 Hz. The larger particle rises to the top in approximately 5 cycles.

Figure 2.12 Simplified sequence of communications between processors for the circular particle program. (a) Sample time snapshot

of a simulation. Processors and particles are numbered, and the dotted vertical lines represent divisions between the processors. (b) Communication between processors 2 and 3 for a single integration time step. (1) Processors exchange information concerning particles lying along their mutual boundary. Processor 3 sends information about the positions and velocities of particles 7, 8 and 9 to processor 2 and then processor 2 sends similar information about particles 5 and 6 to processor 3. (2) Forces calculated for the contacts between particles on the boundary are sent to the processor in which they were not calculated. The convention is that contact forces are calculated in the processor which has the particle with lower particle number. Hence, the contacts between particles 5 and 7, and 6 and 9, are both calculated in processor 2, which passes them to processor 3. These two communication steps are first executed in the predictor part of the integration procedure, and then are repeated for the corrector step. (3) At the end of the integration step, processors test whether the centers of mass of any particles

moved across the processor boundaries. If so, all information concerning these particles is transferred to the appropriate processor. Particle migration did not occur in this simple example.

Figure 2.13 The communications scheme for the concurrent algorithm on a 32-processor Concurrent Processing Computer (each square represents one processor). Each processor has communications channels to the four nearest-neighbor processors, but not to the diagonal neighboring processors. Therefore, information about particles near to the corners of the processors must be channeled through one of the nearest-neighbor processors. Each processor follows the sequence: read and write (shown by the arrows) to the right, the left, the top and the bottom. The overall sequence of communications starts from the upper right-hand processor and propagates towards the lower left-hand processor. In this example, we show the communications steps at five distinct times, numbered 1-5 and circled. This scheme allows information about the particle in the lower-left hand corner

of processor A to reach processor C through processor B, and the information about the particle in the upper right-hand corner of processor C to reach processor A through processor D.

Figure 2.14 The ratio of run time for one processor to the run time for M processors versus M for a simulation of 50 particles. The slope of the line connecting the point at M to the point at M = 1 is the efficiency.

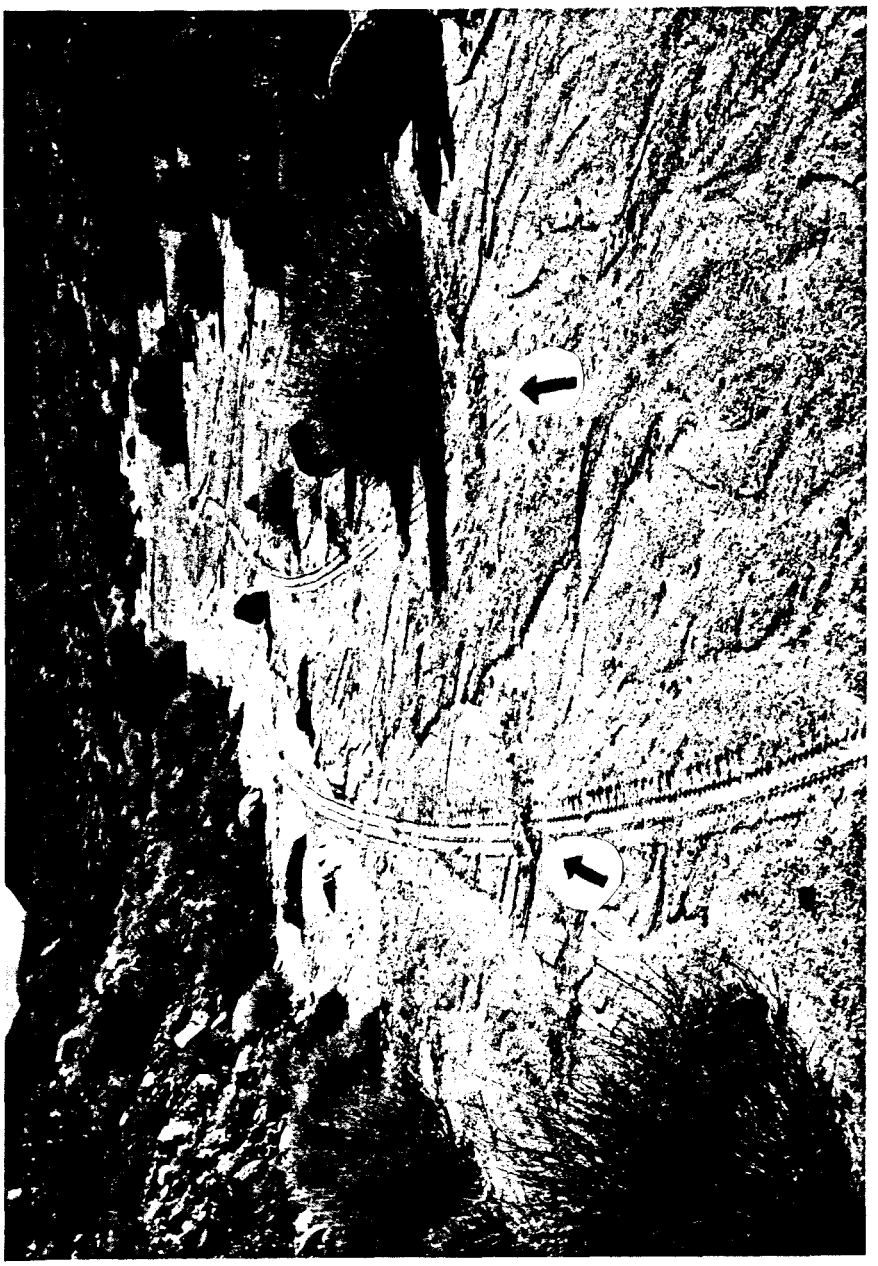

Figure 2.1

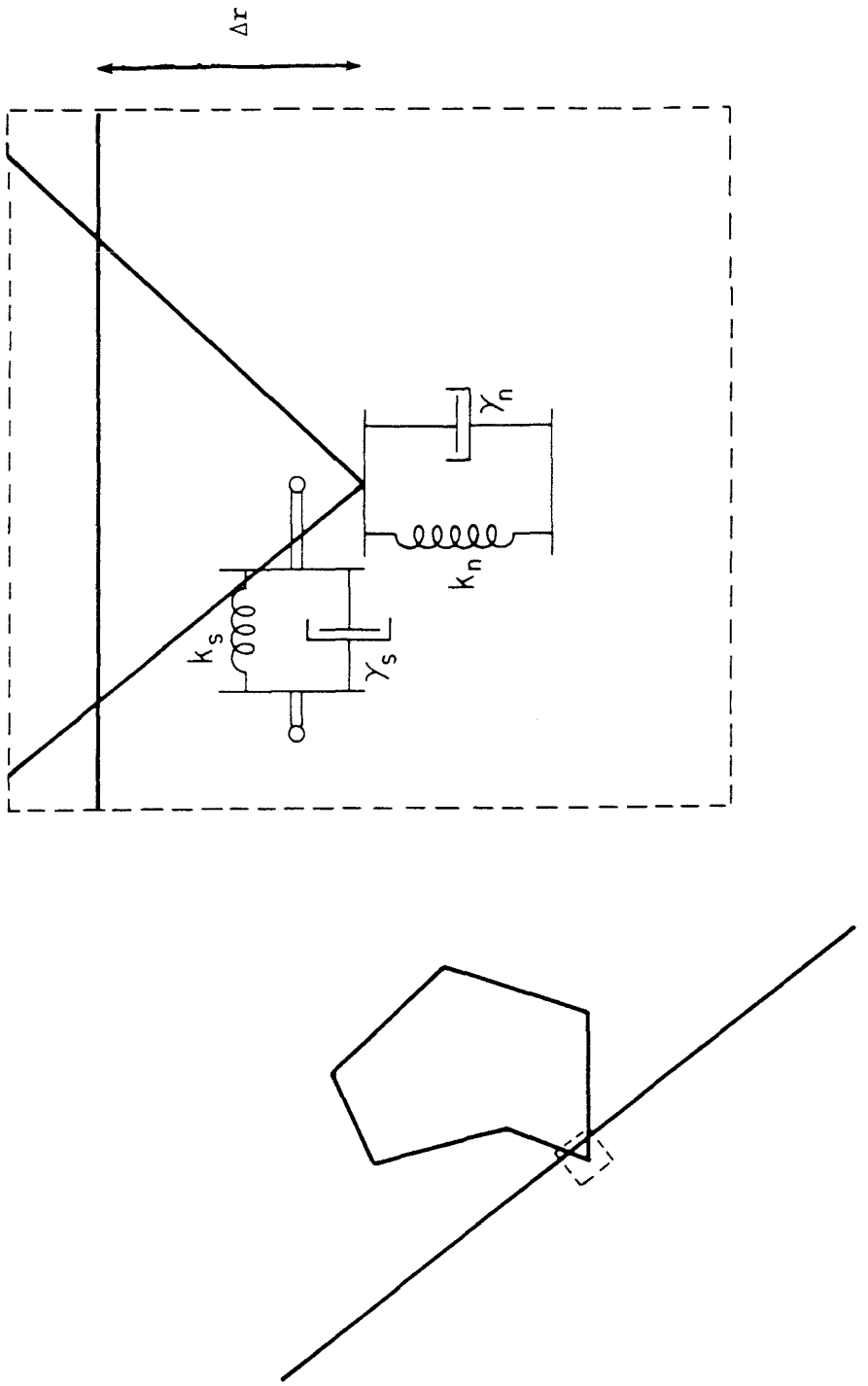

Figure 2.2

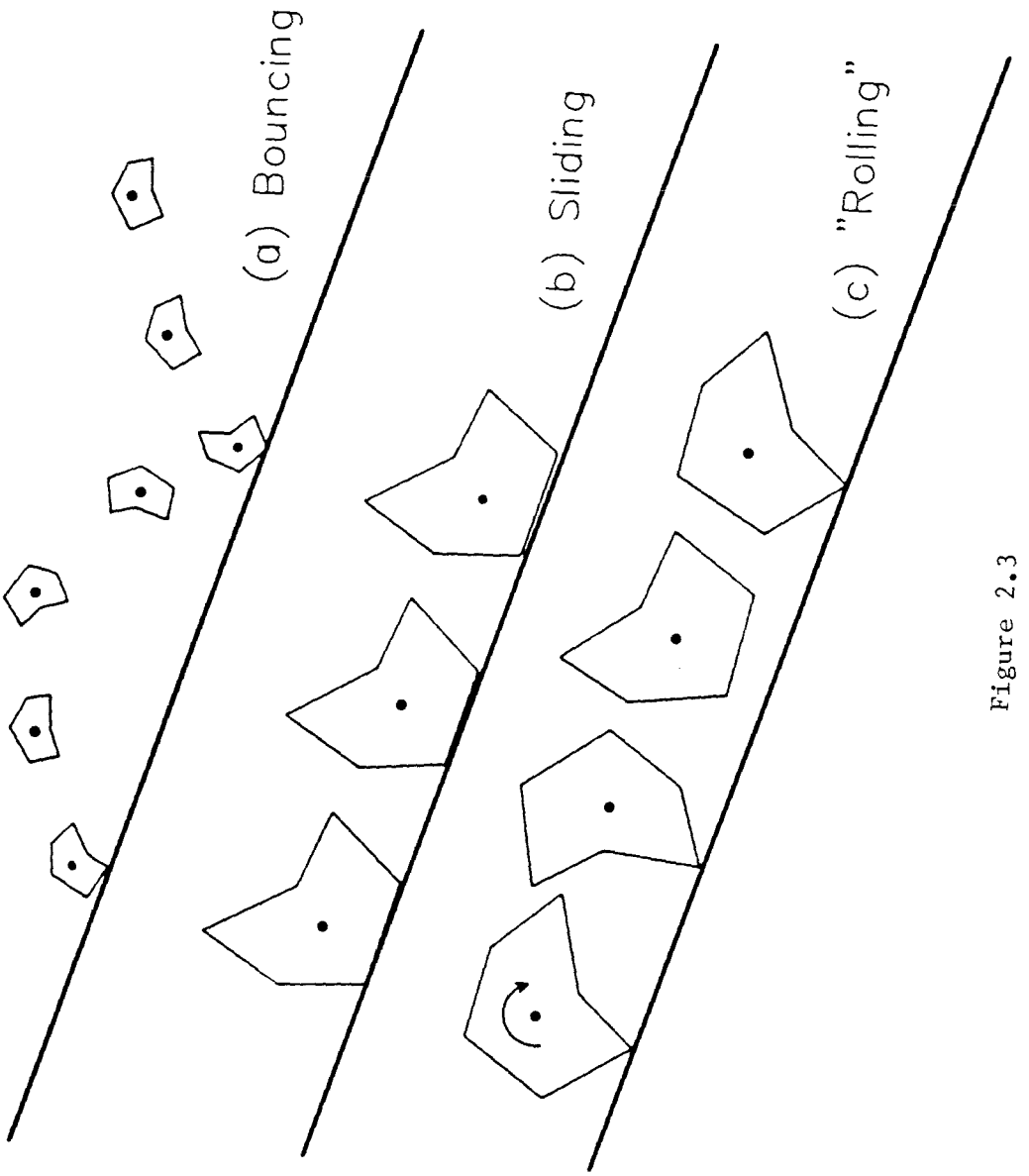

Figure 2.3

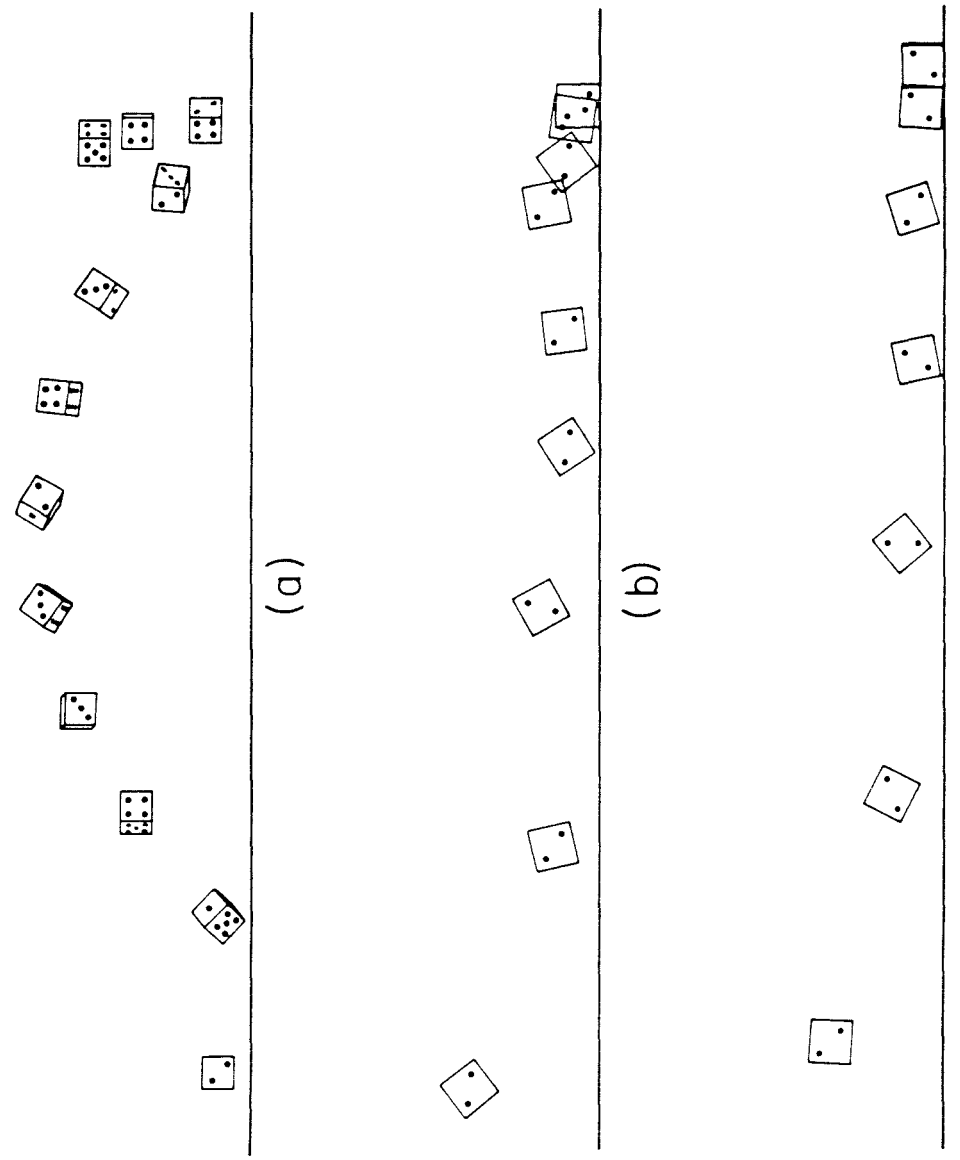

Figure 2.4

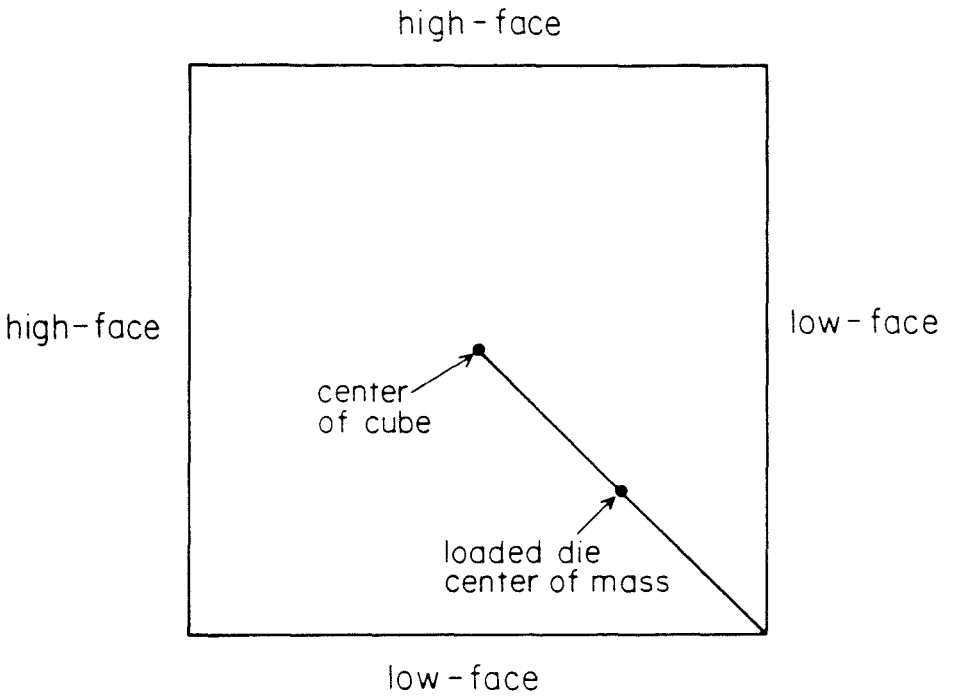
high - face
high - face
low - face
center
of cube
loaded die
center of mass
low - face

Figure 2.5

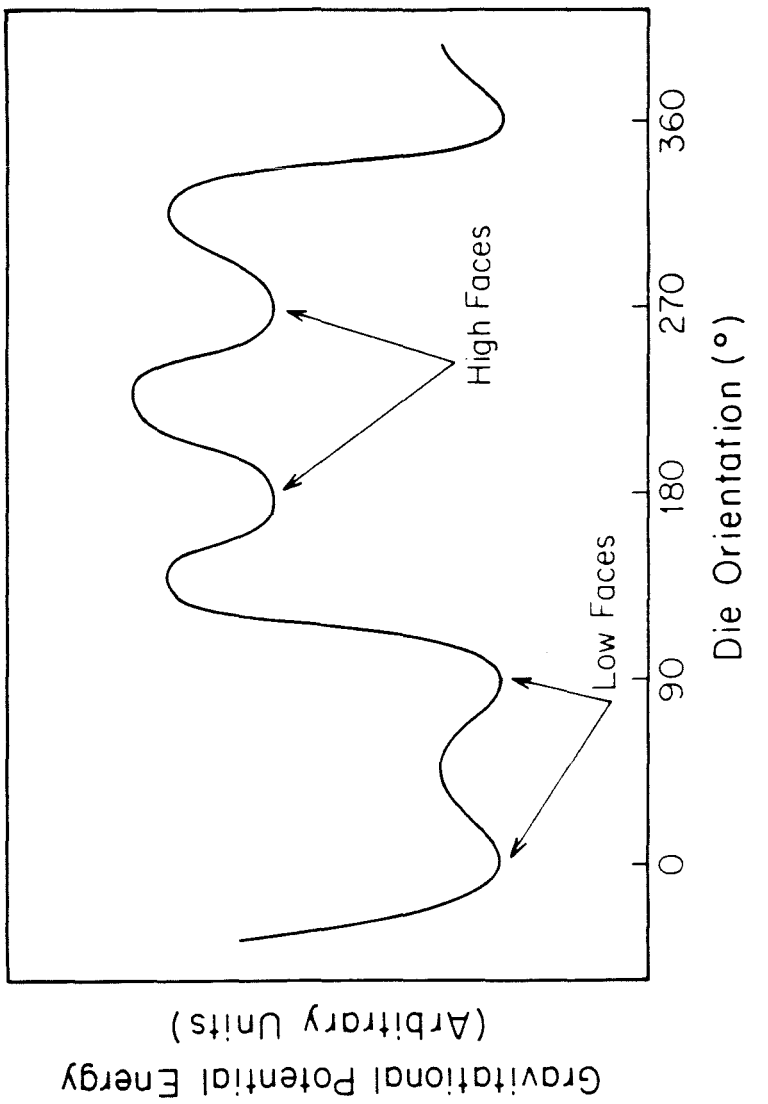
Gravitational Potential Energy
(Arbitrary Units)
0
90
180
270
360
Die Orientation (°)
High Faces
Low Faces

Figure 2.6

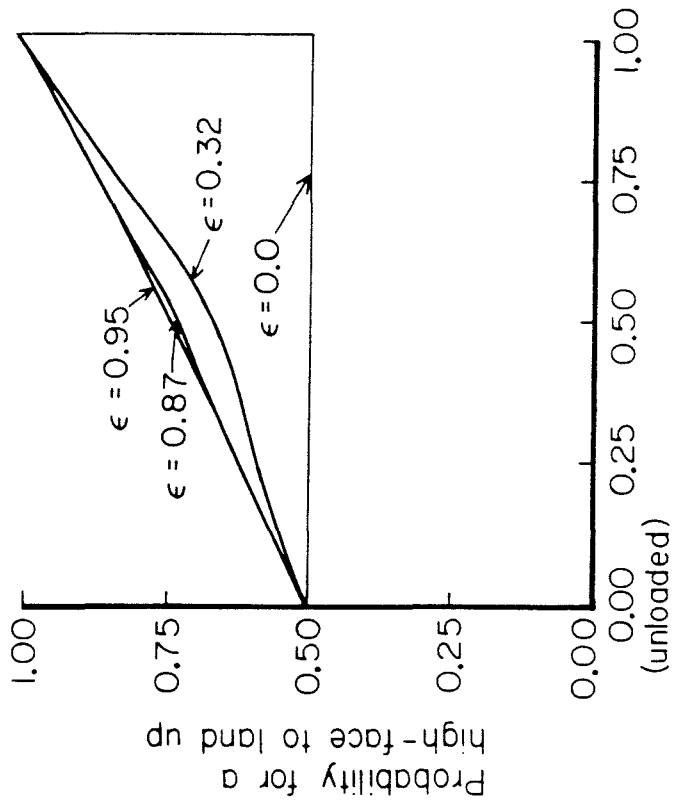
Probability for a high-face to land up
1.00
0.75
0.50
0.25
0.00
0.00 (unloaded)
0.25
0.50
0.75
1.00
Fractional distance along face diagonal of the center of mass
ϵ = 0.95
ϵ = 0.87
ϵ = 0.32
ϵ = 0.0

Figure 2.7

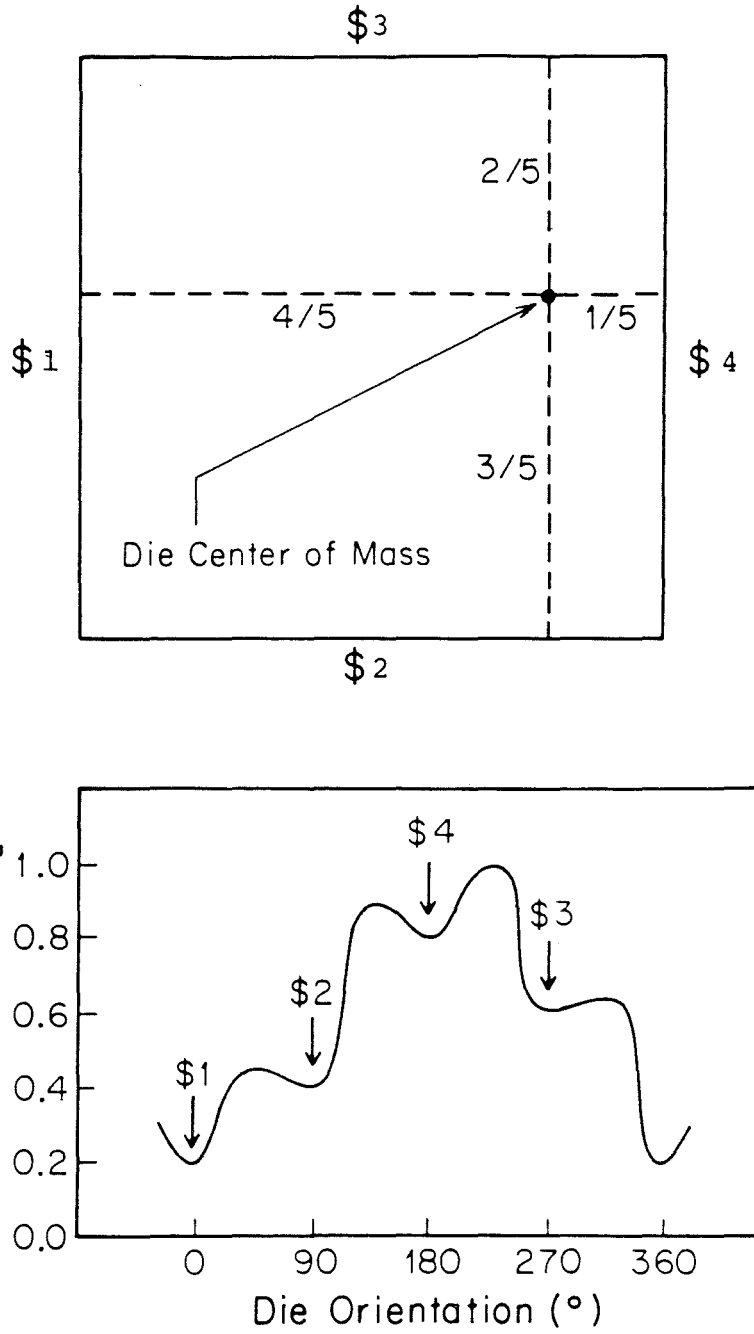
$3
2/5
4/5
1/5
$1
$4
3/5
Die Center of Mass
$2
Potential Energy / $M_d g$
1.0
0.8
0.6
0.4
0.2
0.0
$4
$3
$2
$1
0
90
180
270
360
Die Orientation (°)

Figure 2.8

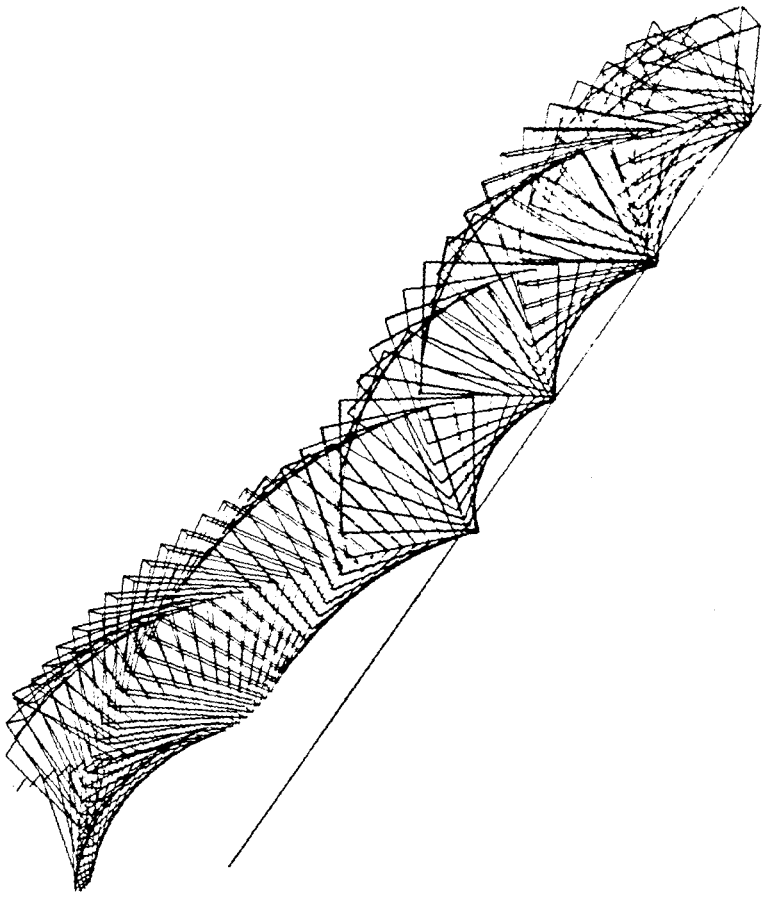

Figure 2.9

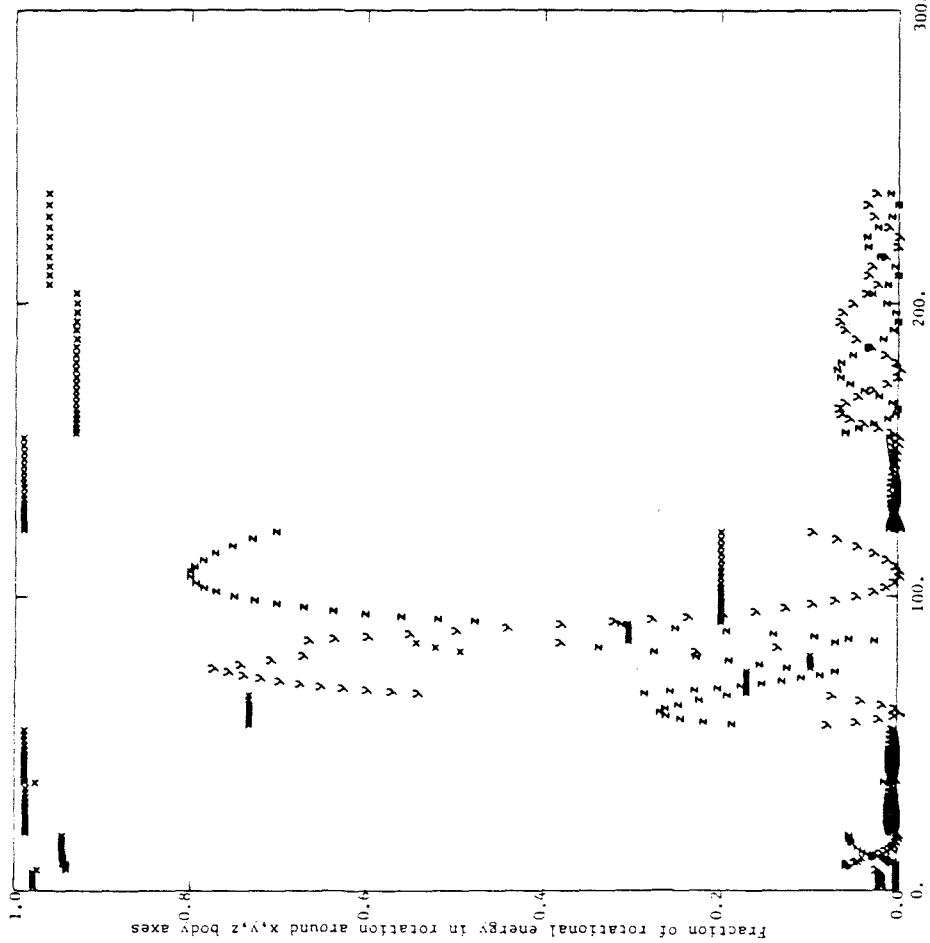
Fraction of rotational energy in rotation around x,y,z body axes
1.0
0.8
0.6
0.4
0.2
0.0
0.
100.
200.
300.
Distance down slope (cm)

Figure 2.10

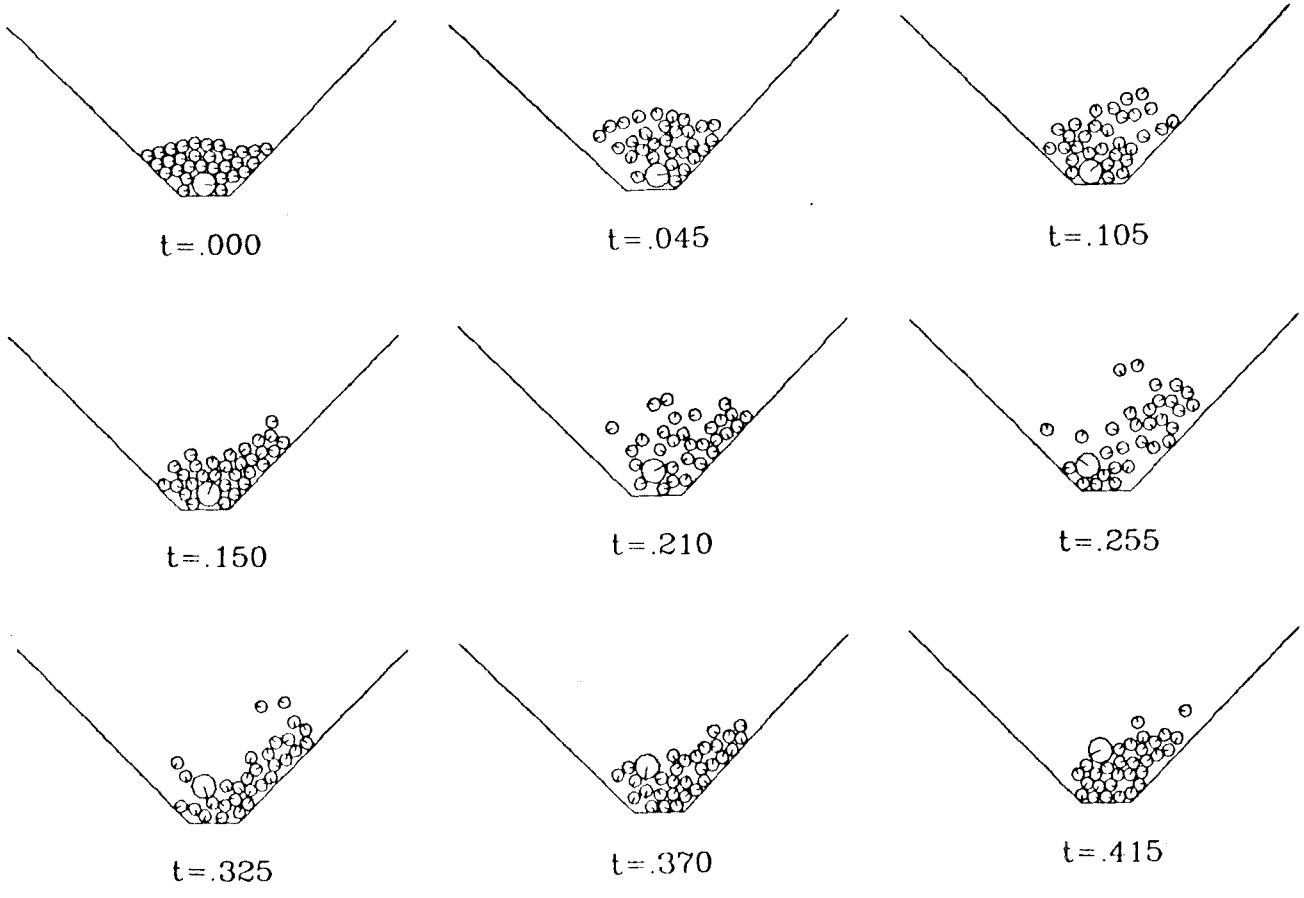

Figure 2.11

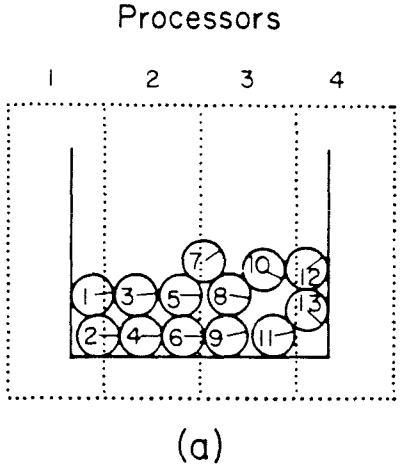

(a)

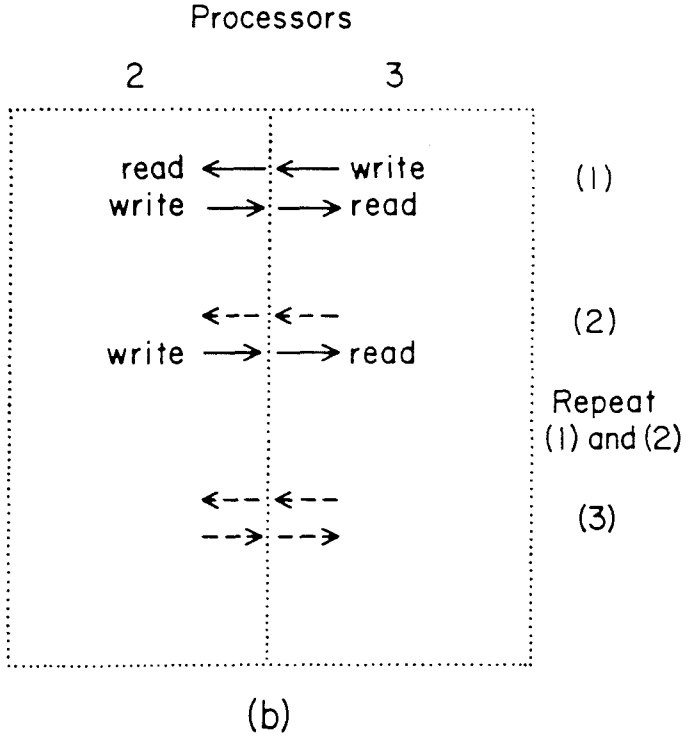

(b)

Figure 2.12

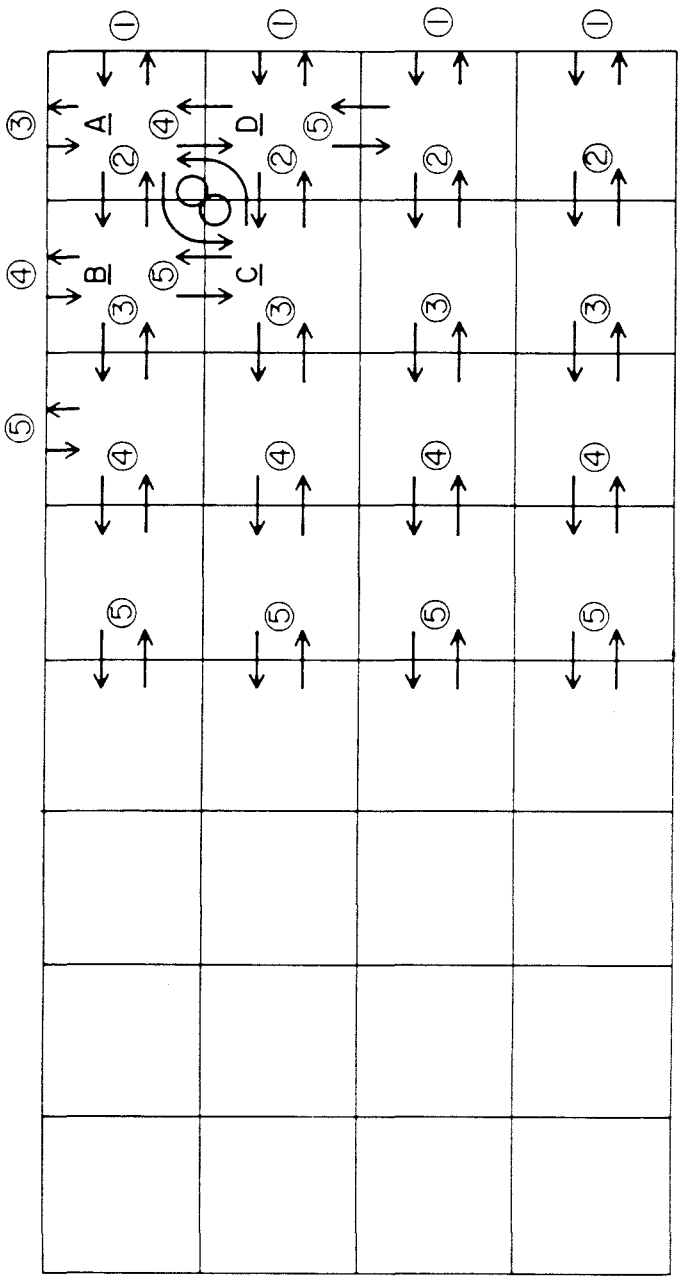

Figure 2.13

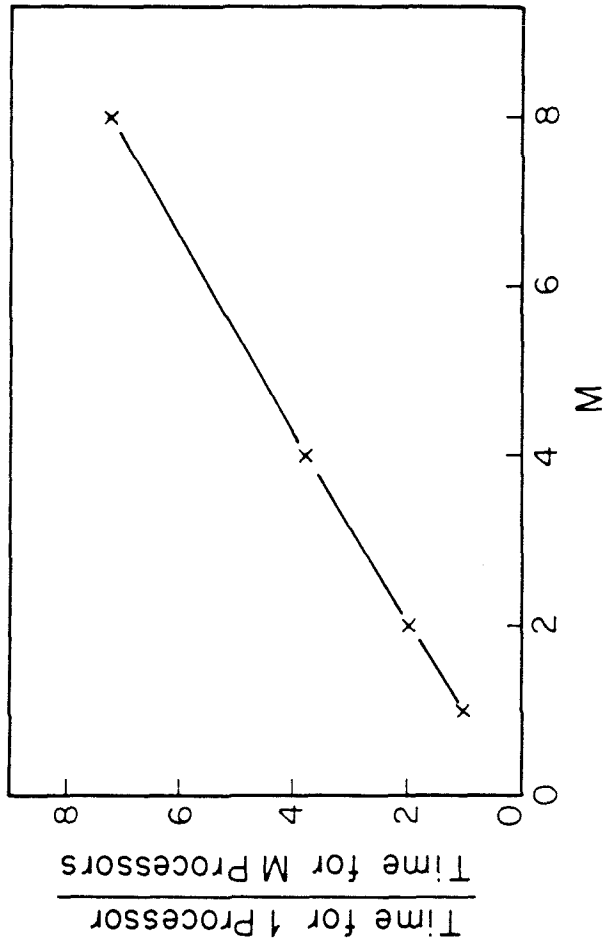

Figure 2.14

CHAPTER III. THE IMPACT PROCESS IN EOLIAN SALTATION

"To see a world in a grain of sand. . ."
-William Blake

The impact between a single sand grain and the sand surface is an important component of saltation. Each grain lofted into the airstream (excluding those in suspension) eventually returns to strike the surface, carrying with it the momentum acquired from the wind. Whether these grains rebound to return to the saltating stream and what the chances are of a particle on the bed joining the saltating population due to the impact depend on the detailed mechanics of a single incident grain hitting a loose (non-cohering) bed of grains. This in turn will determine the characteristics of the saltation, as described in Chapter IV. Moreover, the nature and evolution of the surface, its roughness on the grain-sized scale, the larger scale of sand-grain ripples, and ultimately at the level of sand dunes, can be traced back to the question of how single grains collide with grain beds. We seek the ability to predict the velocity distribution of grains coming off the surface (including the incident grain) following the impact of a grain of specified incident velocity and angle.

While the field of eolian sediment transport has benefited from the work of many talented researchers, the problem of grain-bed impact mechanics has received scant attention until lately, primarily because of its complexity. Only recently have the techniques described in Chapter II allowed us to delve more deeply into the basic mechanisms underlying grain-bed impacts. We present the first theoretical treatment of saltation impacts considered as a many-body problem. This treatment is restricted to two-dimensional particles, although we discuss the probable effects of extension to three dimensions. A controlled experiment involving single sand grains impacting a container of sand is described, with the preliminary results therefrom to be utilized in the saltation model of Chapter IV.

Grains in saltation approach the bed at low angles relative to the horizontal, generally between 10 ° and 20°. Their velocities are typically several hundred centimeters per second, depending on the wind velocity, and the size, sorting, and composition of the sand.

The problem of grain-bed impacts can be separated, from an organizational standpoint, into a consideration of the fate of the incident grain and the reaction of the bed particles. Assuming that the velocities

are sufficiently low that the grains do not lose their coherence, identity, and basic shape (as they might in meteoroid cratering, missile impacts or other hypervelocity problems), the incident grain may either rebound from the surface, may remain on the surface, or may bury itself in the bed. Depending on the energy and momentum imparted to the bed by the incident grain, the bed particles in the vicinity of the impact point may be ejected from the surface, merely may rearrange themselves without actually leaving the surface, or may do nothing detectable.

Prior to examining the detailed mechanics of saltation impacts, we first perform a dimensional analysis of the problem. Ungar and Haff (1986) introduced a dimensionless parameter $N = (v_i)^2/gd$, with v_i the velocity of the incident grain, g the gravitational acceleration, and d the diameter of the incident and bed grains, presumed to be equal. This parameter (N) is the ratio of the incident energy to the potential energy gained in lifting a bed grain its own diameter. They pictured the incident grain evacuating a crater in the bed, with N being roughly the number of grains tossed onto the surface.

Let us suppose we wished to determine the velocities of grains v_e

ejected from the bed as a function of the distance from the impact point ℓ (following Housen, et al., 1983). To simplify matters we ignore the issue of particle spin. The dimensional parameters upon which v_e might depend include v_i, the incident and bed particle radii, r_i and r_b, respectively, the incident and bed particle masses, m_i and m_b, respectively, the spring constant characterizing the normal force between interacting grains k, with the assumption that this force is linear in compression (we also take the normal and shear springs to have roughly the same stiffness), and the acceleration of gravity g. In addition, there are four dimensionless quantities governing the event: the interparticle coefficient of friction μ, the coefficient of restitution ϵ (which, with reference to the spring constant and the particle masses can be related to the damping constant of the interparticle spring force), the incident angle α_i, and a surface roughness parameter δ_b; the magnitude of the roughness is presumed to be characterized by the quantity $\delta_b r_b$. For simplicity, we have combined the amplitude of the roughness and its lateral extent into one parameter, although, in practice, one can find situations in which these two are of

different orders of magnitude (e.g., eolian sand ripples). We have not included an additional dimensionless quantity which specifies where on the bed particle the incident particle strikes (i.e., the angle of the line connecting the bed particle center to the contact point relative to the vertical - this is defined as β below), since, averaged over a large number of impacts, this will be dependent on bed and incident particle size, and bed roughness. Thus, v_e may be written as a function of eight dimensional quantities and four dimensionless quantities

$$v_e = v_e(v_i, r_i, r_b, m_i, m_b, k, g, \ell, \mu, \epsilon, \delta_b, \alpha_i). \qquad (3.1)$$

Using the π theorem (Bridgman, 1922), and assuming that the incident and bed particles have the same density, we may rewrite this as an expression involving nine dimensionless parameters (and three basic dimensions: mass, length and time), e.g.,

$$(v_e/v_i) = (v_e/v_i)(r_i/r_b, m_b g/k r_b, r_i^3 v_i^2/g r_b^4, \ell/r_b, \mu, \epsilon, \delta_b, \alpha_i). \qquad (3.2)$$

Here we are specifying that the ratio (v_e/v_i) is a function of the eight dimensionless parameters listed on the right. We withhold a further discussion of the dimensional analysis until undertaking a consideration

of the physical details of grain-bed impacts.

The circular particle computer simulations described in this chapter were performed on the Caltech Concurrent Processing Computers, as described in Chapter II. They consumed roughly one VAX/780-equivalent year of CPU time.

Grain-bed impacts were simulated by propelling a two-dimensional single particle into a bed of 384 circular particles contained within an open-topped box of dimensions 67.3 by 24.1 cm. A gravitational field in which the acceleration of gravity was g = 981. cm/sec^2 was imposed. Two types of beds were employed: a "loose" bed, in which the particles were in contact with one another but had not completely settled within the box, and a "dense" bed, which was close to two-dimensional close-packing. For calculational convenience, the radius of the bed particles (r_b) was chosen to be 1.0 cm, approximately a factor of forty larger than that of a typical sand grain. The incident velocities were then scaled according to the dimensionless parameter v_i^2/gr_b (see above dimensional analysis). The density of the particles was 2.0 g/cm^3 and the interparticle spring constant was 6.0 x 10^9

dynes/cm. With this spring constant, the maximum overlap of two grains colliding head-on at 1000 cm/sec relative velocity would be about two percent of the grain radius. The damping constant was chosen so that the two-body collisional coefficient of restitution ϵ was 0.85. The interparticle friction coefficient μ, the radius of the incident particle r_i, the magnitude of the incident velocity and its angle relative to the horizontal α_i were varied. For most combinations of parameters, ten impacts were simulated at random locations close to the middle of the bed. Each simulation followed the rebound and reaction of the bed for up to 0.07 seconds after the impact. Particles which rose to more than a particle diameter above the top of the bed were removed from the simulation and their characteristics noted.

The purpose of the simulations was to gain some insight into how one might describe simply the grain-bed interactions without ignoring essential physical features of the process. In the following section we discuss the information culled from these simulations concerning the rebound and the ejection of bed particles.

Simulation Results

The prototypical simulated impact event proceeds as follows. See Figure 3.1 for an example. The incident particle rebounds from the bed, often with a larger vertical velocity than before impact (depending on the incident angle and the various collision parameters). While the incident particle is in contact with the bed, the bed particle it strikes (the target particle) and several other bed grains in the vicinity begin to accelerate. Generally, after the incident particle has left the region, a number of bed grains continue to move significantly, having acquired roughly one to twenty percent of the incident particle's velocity. These grains originate close to the impact point and their final outgoing velocities lie predominantly in the vertical direction. In some cases, a grain several diameters away from the target particle will be ejected with a large forward or backward angle relative to the vertical. A large number of the bed grains eventually acquire a small amount of kinetic energy. For many of these particles, this is due to reflection of momentum from the artificial container (the walls of the box) and may not occur in a system of sufficiently large size. However, almost all grains described as "ejected particles" in our data lost contact with the

bed prior to the reflection of momentum from the walls. Occasionally the incident grain will strike two bed particles. This happened in only a few of our simulated events. The general picture emerging from these simulations, as described above, agrees with the experimental results communicated by Willetts and Rice (1985a) and Mitha, et al. (1986), and with experimental results reported later in this chapter.

We present the simulation results for the mean values of various quantities related to the rebound and bed-grain ejecta in tabular form. The number of simulated impacts was limited by computational power, with a consequent limitation of the statistical accuracy of the results. However, our goal is not accurate numbers, but rather to gain physical insight into the impact process, for which these data are adequate. Table 3.1 lists the characteristics of each group of ten impacts. Table 3.2 contains information about the incident particle rebound and Table 3.3 provides data related to the transfer of momentum to the bed. Tables 3.4-3.9 relate data describing the characteristics of the particles ejected from the bed. Note that the velocities and angles of ejected grains were recorded one grain diameter above the surface. We will discuss selected features of these tables.

Figure 3.2 defines some of the parameters related to the impacts. The point on the bed particle which the incident particle contacts (the target particle) is defined by the angle β: the angle between the vertical and a line connecting the center of the target particle and the contact point. The ratios of outgoing to incoming velocities of the incident particle for the horizontal component (x), vertical component (y) and total velocity are ϵ_{ix}, ϵ_{iy} and ϵ_i, respectively. (These are not to be confused with the two-particle coefficient of restitution, ϵ, which may, however, influence the values of these ratios.) ϵ_{iy} is termed the vertical velocity amplification. Note that we are using the term amplification to denote values which may be less than 1, contrary to orthodox usage. Correspondingly, the ratio of the x and y components of the momentum transferred to the bed to the x and y incident particle momenta are ϵ_{bx} and ϵ_{by}, respectively.

The following convention is observed for representation of angles: incident angles are measured relative to the horizontal, and outgoing angles are measured relative to the vertical. The incident angle

is α_i, the angle of the outgoing velocity of the incident particle is θ_i, and the angle of ejected bed grains is denoted by θ_e. The angle of the momentum transmitted to the bed relative to the horizontal is θ_b. The ratio of the outgoing angular velocity, times the radius of the incident particle, to its outgoing horizontal velocity is ξ_i.

A significant result of these simulations is that a grain-bed impact may be approximated as a two-body collision, with the bed particle struck by the incident grain, the target particle, behaving as though it possessed a mass, m_{beff}, which is greater than its true mass m_b. Using the formulas describing two-body impacts listed in Appendix III.1, we calculated the ratio of m_{beff} to the incident particle mass m_i, with the results given in Table 3.3 For most of the CASES, this ratio is close to 2., with a ten to twenty percent spread in values. Note that for CASES A-G, $m_i = m_b$.

The physical reason for the effective mass of the bed particle being greater than its true mass is that during the collision between the

incident particle and the bed, several bed particles are accelerated to a significant velocity. This is illustrated in Figure 3.3(a-d), which shows the velocities of the particles close in time to an impact. Figure 3.4(a-d) shows the corresponding interparticle forces. A simple calculation of a block hitting an array of masses connected by springs suggests that the signal will propagate on the order of a few spring lengths whilst the block is in contact with the array, corresponding to having to accelerate several of the masses in the two-dimensional array. If the interparticle force rises with penetration distance more rapidly than the linear spring law (e.g., the Hertzian three-halves-power-force law), the momentum tends to be transferred in a short pulse, more closely mimicking a true two-body collision (see Chapman, 1960). In that case, the effective bed grain mass is closer to its true mass. Walton and Braun (1985) assert that the contact force resulting from elastic-plastic interactions between particles is roughly linear, up to a limiting yield stress, with interparticle penetration distance.

In our simulations, when the incident particle first contacts the target particle, it is required to accelerate only that one particle. As the target particle moves, however, it presses against it neighbors, and

compels them to move as well. That it has the time to do this while the incident particle is still in contact is a consequence of the linear force law. When the contact is broken, several bed particles are moving. The effective number of particles which the incident particle is required to accelerate during the collision, averaged over that time, is roughly two; this number is relatively constant for frictional beds, independent of the incident velocity and angle. The effective mass for a bed with no interparticle friction (CASE D) is somewhat smaller than that for frictional beds, since the bed particles are more free to slide out of the way towards the surface.

The ratio of effective mass to bed particle mass was not given for CASES H and I (r_i = 0.5), because, with the parameters we used, the value of β changed by as much as about ten degrees during the contact. The effective mass is sensitive to β, and thus we obtained nonsensical results for m_{beff} from many of the runs. The effect of this change in β on the other derived quantities listed in the tables is to make the surface look less rough than it actually is.

As Chepil and Woodruff (1963) and Rumpel (1985) have pointed

out, in order for sand grains to saltate successively (rebound from the bed and continue in saltation), the impact with the bed must increase the magnitude of their vertical (positive y direction) velocity; there must be amplification of the vertical velocity component by the collision with the bed, so that the particles can attain the height achieved on their previous trajectory, taking into account vertical air drag, thereby reaching a sufficiently high wind velocity to accelerate them to their previous impact velocity. On a flat planar bed with circular or spherical incident particles, this is not possible. On rough beds, however, even with inelastic collisions, oblique impacts can result in an amplification of the vertical velocity component. At low incident angles, the mean value of the vertical velocity amplification $\overline{\epsilon_{iy}}$ may be greater than one.

In our simulations, the value of the vertical velocity amplification $\overline{\epsilon_{iy}}$ decreases with increasing incident angle (as measured from the horizontal) and its distribution is broad. To the incident particles with half the bed particle radius (CASES H and I), the bed looks rougher than for CASE A, and the ratio of bed particle effective mass to incident particle mass is greater, leading to a larger vertical velocity

amplification. The rebound characteristics do not appear to depend strongly on incident velocity at constant incident angle (compare CASES A, E and F). The anomalously low value of $\overline{\epsilon_{iy}}$ for the dense bed (CASE G) probably resulted from the unrelated low mean β. The horizontal positions of impact were chosen at random on the simulated bed; with only ten impacts, this sometimes resulted in a mean value of β different from that which would have resulted from a large number of such random impacts. The mean values of β calculated for a perfect close-packed bed of equal-sized circles for the three values of the incident angle for CASES A (and D-G), B and C are $\overline{\beta}(\alpha_i=15.°) = 12.9°$, $\overline{\beta}(\alpha_i=25.°) = 10.9°$ and $\overline{\beta}(\alpha_i=70.°) = 3.9°$. Thus, for the dense particle bed simulations, with $\overline{\beta} = 7.°$ (Table 3.3), there is less opportunity for the incident particle to convert its horizontal momentum to vertical momentum of the rebounding particle than there would be were additional statistics obtained, in which case the value of $\overline{\beta}$ would approach its ideal value.

The fraction of horizontal momentum retained by the incident particle, ϵ_{ix}, depends, to a large extent, on the existence of friction,

which allows strong coupling of the horizontal velocity component to the bed and to the spin of the incident particle. For real grain-bed impacts, this coupling might be affected by non-spherical shapes, as well as by friction.

The angle relative to the vertical at which the incident particle rebounds is primarily related to the incident angle. Note that at low incident angles, the rebounding particle comes off at high angles relative to the vertical, in contradiction to the usual assumption that the saltating particles come off the surface nearly vertically (e.g., Bagnold, 1941). In nature, this angle might be lessened by the upstream tilt of the ripple surfaces, surface roughness, and bed particles whose true mass is larger than that of the incident particles (see CASES H and I). In three dimensions, particles which leave the surface with a large fraction of their velocity in the direction transverse to the wind may appear to be ejected vertically when viewed from the side. Also, those grains that are ejected vertically are most likely to be seen by an experimenter above the dense layer of moving sand close to the surface, perhaps leading to a (now dubious) impression that most grains are ejected vertically.

The parameter ξ_i measures the ratio of the peripheral velocity of

the rebound particle to its horizontal velocity. Thus, if a particle bounces off a flat plane in the rolling condition, $\xi_i = 1$. Most of the rebounds with $\mu = 0.5$ come off approximately in the rolling condition.

The reaction of the bed to the impact depends on two factors: the transmission of momentum and energy to the bed, and the ability of particles to escape from the bed once they have acquired the aforementioned momentum and energy. Table 3.3 summarizes some aspects of the former. Of particular importance is the fact that the angle relative to the horizontal of the momentum transmitted to the bed, $\overline{\theta_b}$, is large even for small incident angles.

Table 3.4 shows some general characteristics of the ejected particles (i.e., those which attain heights greater than one grain diameter above the surface). The mean number of particles ejected per event is relatively independent of the input parameters, except when the incident energy is low (cases E and H). The mean angle of ejection (relative to the surface normal) is small because most surface particles are surrounded on both sides by other particles; therefore, the easiest direction in which to move is vertically. The slightly positive angle of ejection reflects the

direction of the incident momentum; moreover, the mean is also influenced by particles at the upstream end of a "step" or depression in the bed surface These particles tend to be ejected with much larger angles. The distribution of vertical velocities of grains leaving the bed (including the rebound) is given for CASE A in Figure 3.5. The curve rapidly increases at low velocity and has a small peak at high velocity corresponding to the rebound. The very low velocity dropoff in the distribution reflects the requirement that particles rise to one particle diameter above the surface before they are recorded as ejecta, and that we did not continue the simulations sufficiently long for the slowest moving potentially "ejected" particles to rise above this height.

The reptation distance per event, defined as the sum of the horizontal distances (positive for particles moving forward, negative for particles moving backward) that the ejected particles would travel from their ejection points were they to follow ballistic trajectories, decreases with increasing incident angle. The effect of friction on the trajectories of ejected particles is small; in particular, not much energy is tied up in ejected grain spin. For vanishing friction, no torques applied to the grains are possible. However, even with higher intergrain friction

coefficients, strong contacts with surrounding neighbors probably discourage rotation of many of the ejected particles, although some particles do leave the surface with rotational energies comparable to their linear kinetic energies.

The momenta and energies of ejected grains are displayed in Tables 3.5 and 3.6. We note that the total horizontal (vertical) ejected momenta per event decrease (increase) with increasing incident angle, that the ejected kinetic energy increases with increasing incident angle and that the ejected momentum and energy depend strongly on the incident velocity (compare CASES A, E and F).

The distance between the impact point and the original bed position of the ejected particles reveals which bed particles both receive enough energy and have sufficient access to the free surface to escape. We display the distributions for CASE A. Figure 3.6 shows that most particles which are ejected were hit directly by the incident grain or originated within one and one-half grain diameters of the impact point. A plot of the vertical coordinate relative to the impact point (Figure 3.7) shows that the ejected particles come almost exclusively from the first and second layers of bed particles. The ejected particles originate

preferentially downstream of the impact point (Figure 3.8). Several particles were ejected from positions many particle diameters from the contact point. Most of these were ejections of particles on the upstream edge of a depression in the surface.

For an ejected grain, the geometrical constraints at the surface tend to make it difficult to move in any direction but the vertical. Thus, the motion of the ejecta do not necessarily reflect the incident particle momentum. However, a surface defect, such as a step or brink, which we define as a change in the surface level (facing downstream) by an amount on the order of a particle diameter (see Figure 3.4), does afford an opportunity for the bed to eject preferentially particles in the forward direction. Brinks existed on the surfaces of both the loose and dense particle beds used in our simulations.

In Table 3.7 we list the mean outgoing angle, $\overline{\theta_e}$, and the ratio of the mean emerging horizontal momentum per event to the incident horizontal momentum, $\overline{p_{ex}}$ for three classes of ejecta: the bed particle which was struck by the incident particle (the target), the two particles just upstream of the brink (the brink particles), and the remaining bed

ejecta (all other particles). The escaping brink particles are responsible for carrying away the overwhelming majority of horizontal momentum from the bed, and thus may supply much of the reptation flux. Furthermore, it is the flight of the brink particles which sometimes allows other particles to escape later from the surface with forward momentum. Simulation events in which there is a large amount of forward momentum carried by the ejecta are often roughly characterized by a cascade of particles rising from the bed in sequence from the brink, as well as a kind of buckling of the bed centered around the target particle (Figure 3.9). The mechanics of brink ejection is discussed further two sections hence.

The role of the ejecta from the bed is either to act as feedback for the saltating population of sand grains (Chapter IV) or to constitute the creeping or reptating grain population (Bagnold, 1941; Chapter V). The reptating grains are believed to play some part in the formation of wind-blown sand ripples (Bagnold, 1941; Sharp, 1963; Anderson, 1986; Chapter V). Table 3.8 gives the total distance per event traveled by the ejected grains if they were to continue on ballistic trajectories. The brink particles account for most of the reptation within this calculation;

however, some of the ejected particles and many of the brink ejecta attain sufficient heights that they might be accelerated significantly by the wind, possibly causing them to become members of the saltating population. A proper distinction between saltating and reptating populations of grains can only be made within the context of a calculation which considers the grain-bed interaction and the wind-grain interaction simultaneously.

In summary, the following general information has been gleaned from the simulations:

(1) The rebound and the reaction of the bed may be decoupled.

(2) The rebound characteristics may be calculated from a two-body collision involving the incident grain and a target grain possessing an effective mass greater than its true mass. The value of this effective mass is roughly characterized by the bed properties and particle interaction parameters, and is approximately independent of the incident velocity and angle, and the contact point on the bed.

(3) Bed grains at a brink or at an anti-brink may be ejected with high velocities, and high horizontal velocity components. They may constitute the major source of reptation.

(4) Target and surrounding particles are ejected nearly vertically, due to geometrical constraints, unless they happen to be on a brink or on an anti-brink.

Model for the Rebound

The simulations have demonstrated that incident particles approaching the bed at high velocities and low angles rebound from the bed, reminiscent of the successive saltation picture. Whether they continue in saltation is dependent on the rebound characteristics. The collisions may be treated as occurring between two bodies, with the bed particles behaving as if they possessed an effective mass larger than their true mass. The simulations have also pointed out the role of surface roughness. We incorporate these features into a model for the incident particle rebound. Our intent here is to give a generalized picture of how the rebound depends on the various incident and bed particle parameters.

The model considers an incident circular particle of radius r_i, mass m_i and moment of inertia $I_i = \kappa_i m_i r_i^2$, (κ_i is a constant equal to 0.5 for circles) which approaches the bed at velocity v_i, angle relative to the

horizontal α_i and angular velocity w_i. The bed particles, with radius r_b, effective mass m_{beff}, and moment of inertia $I_b = \kappa_{beff} m_b r_b^2$, are evenly spaced with gaps of length Δ_b in a single layer, as illustrated in Figure 3.2. The frictional interaction is included through a parameter σ, the friction restitution coefficient, which varies from -1 to 1. When σ = 0, the particles disengage in the rolling condition. $\sigma = 1$ corresponds to the frictionless case and $\sigma = -1$ results in no loss of energy via frictional dissipation. Our parameter σ corresponds to $-\beta$ of Lun and Savage (1986) (see also Walton and Braun, 1985). The equations governing the impacts are listed in Appendix III.1. They reduce to those of Rumpel (1985) for $m_i = m_{beff}$, $r_i = r_b$, $\Delta_b = 0$, $\sigma = 1$ and $w_i = 0$. We follow impacts of single incident particles on the bed for up to two collisions with the bed particles. Incident particles which either continue to strike bed particles or escape down through the gaps in the bed thereafter are said to be nabbed by the bed and are assigned no emergent momentum. For each set of parameters considered, we numerically perform a weighted average over the angle β to obtain the

mean values of numerical quantities related to the rebound characteristics and their distributions. For many of our reported results, the parameters chosen will be those in CASE 1 of Table 3.10 (no spin), with one or two of the parameters altered.

The quantity of primary interest here is the mean vertical velocity amplification $\overline{\epsilon_{iy}}$ since this will determine how far up into the windstream the rebounding grain will rise, and hence, to a great extent, its velocity at its next impact with the surface. We first summarize its dependence on the various parameters, and then examine some details of the rebound.

The mean vertical velocity amplification is strongly affected by

(1) incident angle

(2) ratio of incident particle mass to bed particle mass,

moderately affected by

(1) friction restitution coefficient

(2) incident particle angular velocity,

and only weakly affected by

(1) ratio of incident particle to bed particle radius at constant mass

(2) bed particle spacing (surface roughness).

With the CASE 1 parameters, we first varied only the incident angle α_i. The mean vertical velocity amplification $\overline{\epsilon_{iy}}$ and the mean outgoing rebound angle $\overline{\theta_i}$ decrease as a function of α_i as shown in Figure 3.10. The vertical amplification varies rapidly in the region α_i = 10. ° to 20.°, which most natural saltating particles inhabit, crossing unity at about 15. °. This sensitivity of $\overline{\epsilon_{iy}}$ to incident angle suggests that its distribution will be important in developing a model of saltation. In other words, the velocity distribution of particles coming off the bed per incident grain, the splash function, is necessary for developing a model of saltation. It is not sufficient to calculate the mean incident velocity and angle at which a grain reproduces itself. The outgoing angle is relatively insensitive to α_i in this interval.

In Figures 3.11 to 3.13, we present the vertical velocity amplification as a function of the incident to bed particle radius ratio, mass ratio, and the spacing between the bed particles for the CASE 1 parameters (α_i = 15. °), respectively. Varying the geometrical variables (r_i/r_b and Δ_b/r_b) alone has little effect, because the incident particle has

little opportunity to probe the details of the bed when approaching it at low angle. However, varying the mass ratio or the radius ratio at constant density (effectively varying the mass ratio) results in a rather larger change in the vertical velocity amplification. We note that the constant density curve of Figure 3.11 was calculated for disks; in three dimensions, with spherical particles, the consequences of varying the radius ratio will be even more striking. Where sands consist of a distribution of sizes, one finds that the smaller size populations tend to be entrained in saltation, with the larger size fractions remaining on the surface (Bagnold, 1941). Our results may have some bearing on the relative character of saltation in uniform-versus multimodal-sized sands.

In our model, spin-coupling is introduced through the parameter σ, the ratio of the relative surface velocity after the collision to that before the collision. In Figure 3.14, we plot $\overline{\epsilon}_{iy}$ as a function of σ for CASE 1. The introduction of any frictional or elastic interaction ($\sigma < 1$) parallel to the surface of contact results in a lowering of the vertical velocity amplification.

With $\sigma = 0$ (colliding particles departing in the rolling condition), the dependence on the incoming angular velocity of the incident particle was studied (see Figure 3.15). We found that for incident particles spinning in the rolling sense ($w_i < 0$), the vertical velocity amplification was increased over the zero incident spin case, while the rotation of incident particles in the opposite sense had a deleterious effect on $\overline{\epsilon}_{iy}$. This result can be seen to agree with physical intuition by noting that the friction force points upwards (downwards) in the former (latter) case, when the impacts occur on the upstream side of the bed grain, as they do almost exclusively at low incident angles. Frictional rebounding particles generally depart the surface spinning in the rolling sense, and one might expect them to retain some of this spin until their next meeting with the bed. In fact, some saltating particles have been observed to be spinning rapidly in this sense (White, 1982). The effect of spin in the collision, through an increase of the mean vertical amplification, may augment the saltating particle trajectory apices an amount of the same order of magnitude as the increase in height attained by saltating grains caused by the aerodynamical Robins effect (Barkla and Auchterlonie,

1971; White and Schultz, 1977), depending primarily on ω_i, σ and α_i.

To compare this model to the simulations, we looked at the dependence of $\overline{\epsilon_{iy}}$ on α_i for the parameters of CASE 2 in Table 3.10. We chose $\sigma = 0$ to correspond to our observation that most rebounds left the bed in the rolling condition and $\kappa_{beff} = 1$ (twice its proper value in two dimensions) to reflect the fact that the bed particles encounter some resistance to rotation because of frictional contacts with their neighbors. In the absence of a detailed calculation to extract the value of κ_{beff} from the data, and due to the fact that the results are not sensitive to its value, we feel that doubling κ_{beff} was a reasonable course of action. Figure 3.16 shows acceptable agreement between the theoretical curve calculated from the rebound model and the computer-experimental points for CASES A-C.

A Framework for a Bed-ejecta Model

The ejection of particles from the bed resides in that nebulous boundary region between continuous and discrete mechanics; continuous in the sense that many particles are directly involved and discrete

because individual particles, such as target or brink particles, play an important role. The difficulties associated with dealing with problems in this regime have prevented the development of a general theory for the reaction of the bed to the impact. However, enough information about the process has been assimilated from the simulations to propose a framework for constructing such a model.

As we have demonstrated, the behavior of the rebounding particle can be characterized in terms of a two-body collision. The momentum transferred to the bed can be determined from this model. Immediately after the incident particle loses contact with the bed, this momentum is carried primarily by the the target particle and, to a lesser extent, the particles immediately surrounding it. The bed momentum is directed at a large angle relative to the horizontal, 60^{o} being a typical value. A description of how this momentum leads to the ejection of particles from the bed is sought.

The bed momentum is transferred outward from the target particle in a radiating pattern, but concentrated toward the forward direction. The near-surface particles begin to move downwards, but soon encounter resistance and reflect upwards toward the surface, as seen in

Figure 3.3. A compressional wave propagates from the target particle into the underlying granular material (see Figure 3.4). In the compressional wave, the particles are in continuous contact with their neighbors, and may be thought of as exhibiting elastic solid-like behavior. Behind the compressional wave is a rarefaction wave, in which the particles lose contact with their neighbors. Here the particle interactions are dominated by true two-body collisions, with a grain-gas description being appropriate (Haff, 1983). A model melding the behavior of the two phases (solid-and gas-like) might be able to accurately predict the ejection of particles from the target region.

The principal obstacle to the ejection of a bed particle is the interfering presence of its neighbors. Grains at a close-packed two-dimensional surface can either escape individually into the infinitesimal solid angle centered around the vertical direction, or through a cooperative effort with adjoining grains. The existence of surface defects such as steps at the surface simplify the escape problem by providing greater phase space into which the particle can move and thus, by Occam's razor, are preferential sites for the ejection of particles. We have seen the influence of surface brinks in the

simulations. The downstream brink on the loose bed led to preferential ejection of particles in the forward direction. In the region of incident particle impact, the dense bed has a step facing in the upstream direction as well (Figure 3.4), which we have dubbed an anti-brink.

Construction of a model for brink particle ejection could probably take advantage of the fact that momentum propagates parallel to the surface towards the brink particle. A simple billiard ball calculation is prevented by the fact that surficial grains also interact with the layer underneath them. Calculation of the ejecta characteristics for anti-brink ejections is yet more complex because the origin of the surficial momentum upstream of the target particle is reflection off deeper particle layers.

In Figure 3.17(a-c), we show the velocities of the grains leaving the dense bed for an impact (a) equally spaced between brink and anti-brink, (b) close to the brink, and (c) close to the anti-brink. The ejected particle velocity distribution is roughly symmetrical for the latter two cases, but skewed toward the forward direction for the former case, suggesting that a net forward reptation will result from oblique impacts on a surface composed of an equal number of brinks and

anti-brinks. We note, however, the likelihood that an ascending surface might be dominated by anti-brinks, perhaps leading to a reduction or elimination of forward reptation. This possibility could be related to the limitation of ripple stoss surfaces to roughly a ten degree inclination with respect to the mean surface (Bagnold, 1941; Sharp, 1963). Evidence for surface irregularities with amplitudes up to several particle diameters on the backs of ripples exists (Chapter V).

Even an understanding of the mechanics of brink/anti-brink ejection would not obviate the necessity of acquiring insight into the nature of the surface and its time evolution under saltation impacts, in order that the spectrum of ejecta might be properly specified. The mechanism for creation of brink-anti-brink pairs on a surface is the ejection of the target and/or surrounding particles following a saltation impact. A brink and an anti-brink may disappear by annihilation or by the filling of a depression with reptating particles. Brinks or anti-brinks could be created preferentially on an inclined surface. Additional simulations may provide further insight into the processes governing the evolution of a surface undergoing saltation impacts.

Finally, let us return to a consideration of dimensional analysis

to specify the nature of the bed ejecta. We begin by making several simplifications to equation 3.2. First, we will assume that the interaction between the bed and the incident particle can be characterized by a single parameter, for instance, the energy transferred to the bed $\mathcal{E}$. One could also make an argument that the momentum transferred to the bed should be considered, or perhaps both. In any case, the results will be similar. We are ignoring angular dependences. The reduction of the incident characteristics to a single parameter is very similar to the "coupling parameter" of Housen, et al., (1983) in their analysis of meteoroid and explosion crater ejecta, and corresponds to our separation of the grain-bed impact into the rebound and the reaction of the bed.

Second, we note that the dimensionless parameter, $m_b g/kr_b$, is orders of magnitude smaller than any of the other parameters, and thus is unlikely to enter into the expression for v_e. This suggests that the bed geometry might be more important than the detailed nature of the interparticle forces. This conclusion would not be altered if the form of the interparticle force law was nonlinear in penetration. However, the problem does depend on the spring constant indirectly through the

damping constant, which we have combined with the spring constant in specifying the coefficient of restitution ϵ. A more appropriate parameter to specify energy loss in the bed is the distance d over which the power in a grain-accoustical wave decays to 1/e of its value.

Third, we ignore interparticle friction and impose a continuum approximation, so that the density of the grains ρ replaces their mass and radius in the expression for the ejection velocity v_e

Finally, the bed is assumed to be smooth (thereby ignoring brink/anti-brink ejection) and the kinetic energies of the ejected particles are taken to be significantly larger than the energy needed to lift a sand grain its own height $2m_b g r_b$. The incident grain will evacuate a crater in the bed of radius R ($\gg r_b$ so that the continuum approximation remains valid). Only near the periphery of the crater will gravity become important in determining the ejection velocities. These approximations roughly correspond to the separation of the cratering problem into the "gravity regime" and the "strength regime" by Housen, et al., (1983).

We are left with the following expressions for v_e and R:

$$v_e = v_e(\mathcal{E}, \ell, \rho, d)$$
$$R = R(\mathcal{E}, \rho, d, g), \tag{3.3}$$

which, on dimensional grounds, can be rewritten as

$$\mathcal{E} = h_1 \rho \ell^{3-a} d^a (v_e)^2$$
$$\mathcal{E} = h_2 \rho g R^{4-b} d^b, \tag{3.4}$$

with a, b, h_1 and h_2 dimensionless constants. Note also that a and b could depend on the ratio (d/r_b). Eliminating $\mathcal{E}$ we arrive at

$$v_e \sim R^{(4-b)/2} \ell^{(a-3)/2} d^{(b-a)/2} g^{1/2}. \tag{3.5}$$

The ejection velocities must decrease with distance from the impact point and increase with d. Therefore, $a < 3$ and $b > a$. Equation (3.5) suggests that an inverse power law distribution for ejected grain velocities is appropriate down to ejected velocities which enter the gravity regime.

The above analysis is probably applicable to saltation grain-bed impacts in special cases only. A large number of grains with large energy must be removed from the bed. This will occur mainly at high wind velocities, where some grains which get far up into the windstream will impact at sufficiently high velocities.

This simplistic dimensional analysis has ignored ejection of

grains due to bed roughness. If the velocity of ejection is to have a local maximum at some distance away from the impact point, physical considerations require that this distance be a function of the distance chartacterizing the roughness of the surface, $\delta_b r_b$ (i.e., it will not depend on the other distances in the problem). It seems likely that the distribution of ejection velocities will have two components: one which rises at low velocities and is centered around the impact point, and one which peaks at higher velocities, due to ejection of particles removed from the impact point, at brinks and anti-brinks. Consideration of the impact angle will skew these distributions toward downstream ejection.

Discussion

A knowledge of the characteristics of the rebound and the reaction of the bed, i.e., the splash function, is needed for a steady-state calculation of eolian saltation (Ungar and Haff, 1986; Mitha, et al., 1986; Chapter IV). Combining this information with certain assumptions about the aerodynamics involved, it is then possible to calculate, from a fundamental viewpoint, particle fluxes, momentum transfer to the bed, etc. Rumpel (1985) executed a steady-state calculation of eolian saltation in the successive saltation approximation, i.e., all incident

particles rebound from the bed and no bed particles are entrained in saltation. Without a mechanism for achieving a balance between the number of saltating particles being nabbed by the bed and the number of bed particles ejected into saltation, there is no possibility of determining the particle flux; hence, in Rumpel's model it is arbitrary.

The two-dimensional simulations show that it is possible to eject bed particles into saltation. The inverse process, capture of saltating particles by the bed, can be accomplished in two ways. The first occurs when a saltating particle buries itself in the bed. Simulations have suggested that this is possible only for a particle significantly heavier than the bed particles (B.T. Werner, 1985: unpublished data). This may be understood by considering that only by possessing a mass larger than the effective mass of the target grain can the incident grain continue to move, after the collision, in the direction given by the line segment going from incident to target particle during the collision (i.e., into the bed). If it does so, the incident grain must then continue to collide with the target grain or other bed particles. In this case, the effective mass of the bed, averaged over the entire interaction, will be much higher than a factor of two over the mass of individual bed grains. The second may be

illustrated by presenting a plot of the distribution of ϵ_{iy} for CASE 1 of Table 3.10 (Figure 3.18). Although the mean value $\overline{\epsilon}_{iy}$ is one in this plot, there is on the order of a fifty percent chance that the particle will emerge with less outgoing than incoming vertical velocity, an event which, under the action of the wind, will generally lead to a larger incident angle on the particle's next impact, and an even smaller chance of amplifying its vertical velocity. (We are ignoring the vertical wind drag, an assumption which does not modify our conclusions.) Although the particle does have a chance to recover, there is some probability that it will be nabbed. Thus, birth and death processes are an integral part of a saltation model.

Rumpel (1985) has suggested that the decrease in vertical amplification with increasing impact angle might play some role in the limitation of ripple stoss slopes to small inclinations. We investigated this quantitatively by computing, using the rebound model, the mean vertical amplification for a particle impacting (at 15 ° to the horizontal) a bed inclined upstream at angle φ to the horizontal. The results are plotted in Figure 3.19. They show that $\overline{\epsilon}_{iy}$ actually increases for larger

upstream inclinations, except for φ well above the angle of repose for loose granular materials. The increase is a consequence of the angle of rebound being large; increasing the inclination merely brings the vertical and the outgoing velocity vector closer in orientation, resulting in a larger value of $\overline{\epsilon}_{iy}$ and offsetting the lesser decrease in the overall effective coefficient of restitution. Therefore, the limitation of ripple stoss inclinations is likely related to some property of the bed ejecta, and not to the nature of the direct rebound.

One possibility is that as the slope angle is increased, the horizontal flux of reptating particles decreases. We investigated this by comparing the reptation distance per impact for a grain with incident angle 15° (CASE A) to the (horizontal) reptation distance per impact resulting from a particle incident at 15° to the horizontal by impacting a slope inclined 10° upstream. The latter data were obtained by recalculating the ejected particle trajectories for a 25° incident angle (CASE B). CASE A gave a mean reptation distance of 120 cm, while it was -35 cm for the recalculation of the ranges on a 10° slope of the ejecta of CASE B. While this result is encouraging, we must note that some

fraction of the ejected particles attain great enough heights that ballistic trajectories are not valid.

A consideration of the effect of various parameters on the magnitude of reptation requires that a distinction be made between those ejected bed particles which reptate, and those which saltate. Heretofore we have been assuming that the reptating particles are those which experience "insignificant" acceleration by the wind. This vague definition can be quantified in the context of a steady-state model for saltation by requiring that saltating particles have some significant probability of reproducing themselves, either through successive saltation or replacement with an energetic bed particle. We designate the saltating population as consisting of those particles which, having left the surface with vertical momentum p_i, impact the surface after acceleration by the wind, and so lead to a passel of particles whose total vertical momentum Π_i satisfies the relation $\Pi_i > cp_i$, with c a positive constant whose value determines the definition of saltating particles. The reptating population then comprises the remainder of the moving particles ($\Pi_i < cp_i$). Suppose we choose $c = 1$. Then, according to this definition, the particles which,

upon impact, more than reproduce their previously outgoing vertical momentum in the rebound and the ejecta, are to be considered saltating particles. A greater value of c makes the definition more strict, a smaller value less strict. We are, in essence, distinguishing between those particles which are "moving on up" and those which are declining in potency. This definition requires a calculation involving the wind, and will not depend on impact and bed properties alone. It is likely that this definition, or a similar one, will prove useful in theoretically separating the reptating and saltating grain populations.

Progress in elucidating the mechanics of grain-bed impacts necessitates further simulations. The rapidly expanding computer power available to the research scientist suggests that investigating the effect of adding a third dimension, and following the evolution of a surface in two and three dimensions will be possible in the near future. Work on three-dimensional simulations has already begun.

Experimental Measurement of the Splash Function

It is important, on occasion, to abandon the comforts and confinements of one's office, and to set out to investigate the question: does the way in which Nature behaves have anything at all to do with those endless scribblings cluttering up my chalkboard and filling the reams of papers stacked on and around my desk? With respect to the motion of individual sand grains in saltation, researchers often have turned to a wind tunnel for an answer. White and Schultz (1977) measured liftoff and impact velocities and angles of saltating grains in a wind tunnel, but without relating the two. Willetts and Rice (1985a) measured the splash function for incident sand grains from three size fractions striking unsieved dune sand by observing individual grain-bed collisions in a wind tunnel with a high-speed movie camera. They found that a variety of rebound and ejecta characteristics were sensitive to incident angle and the size of the incident grain.

There is, however, a certain lack of control in a wind tunnel experiment to investigate grain-bed impacts. Requests for certain incident velocities or angles may go unheeded. The individual sand grains in a wind tunnel are not well-attuned to the desires of the experimenter.

On the other hand, duplication of conditions in Nature are effected more readily in a wind tunnel than elsewhere.

By measuring the splash function, we hope to augment and confirm our fundamental theoretical studies of the mechanisms operating in the grain-bed impact process. As described in the next chapter, a detailed measurement of the splash function also is required as input data for a model of steady-state saltation.

The task at hand is to devise a means of propelling sand grains at velocities of hundreds to thousands of centimeters per second and low incident angles onto a bed of sand grains accurately and repeatably. In addition, the velocities of the rebounding and ejected grains must be detected.

Common to the possible designs of this apparatus will be a means of accelerating the sand grain, and a projectile tube, down which the sand grain travels, to collimate its velocity. We consider three basic design philosophies. One involves accelerating the grains with an air blast in a confined tube, similar to a pea-shooter. This technique was used by Mitha, et al., (1986) for measurement of the splash function of BBs successfully. However, because sand grains are not generally spherical, in

this scheme, the velocity they attain is not likely to be as regular as that achieved by Mitha, et al. Also, the air blast would affect grains on the surface of the sand bed.

The second technique involves accelerating the grains in circular motion and then letting go of them, a sort of catapult. Preliminary investigations of this method revealed two problems: it is difficult to aim the sand grains, and, since the acceleration is perpendicular to the velocity, the grain will sit at one side of the projectile tube, and if the particle is irregularly-shaped, it will slide out of the tube unpredictably, and with a potential for an unknown spin.

The third method involves linear acceleration. The projectile tube is accelerated along its axis with the sand grain at one end. Then the tube is brought to a stop, but the grain continues moving down the tube on a collision course with the sand bed. This technique was judged best suited to fulfill our needs.

Detection of the rebounding and ejected sand grains was a thorny issue. We considered detection schemes ranging from observing the sand grains with a CCD camera to collecting them in segmented boxes in order to determine their range, along with placing a sticky plate at varying

heights to allow the determination of the distribution of grain trajectory heights. We rejected those possibilities in favor of photographing the sand grain trajectories illuminated by a stroboscope. This method was used by Mitha, et al. (1986) for BBs, but we had thought initially that capturing sand grains on film would present insurmountable difficulties. Photographing sand grains in the low light level of a stroboscope is not easy, but it is possible.

We discuss an experiment to measure the splash function for coarse sand. The apparatus, experimental procedure, data analysis and preliminary results are described below. The detailed design of the sand grain accelerator (dubbed the "sand gun"), much of the machining, and the debugging and maintenance of the sand gun are the work of S.W. Stryker.

Apparatus

The centerpiece of the experimental apparatus is the sand gun, which propels sand grains onto a sand bed, and is pictured in Figure 3.20. The intent was to assure smooth acceleration of the sand grains to repeatable speeds ranging from one to fifteen meters per second, and to achieve a sufficiently narrow cone of trajectories that it would be possible to hit a sand bed of modest size at low angles.

The gun is powered by a Parker air piston with 3" bore and 13" stroke. The sand grain is transported in a carriage attached to the exposed end of the piston rod. Lateral movement of the piston rod/carriage assembly is prevented by two polished steel rods, to which the carriage is secured by linear bearings (Figure 3.21).

Prior to shooting the gun, the piston rod is held by a trigger at approximately the midpoint of its stroke. Air at elevated pressure is supplied behind the piston to create a pressurized reservoir. The trigger is then released, and the pressurized air behind the piston expands, pushing against the air (initially at atmospheric pressure) in front of the piston (which is vented), and the friction in the bearings, as well as accelerating the piston rod and carriage. At the pressures and velocities with which we were working in this study (15-40 psi, 600-1200 cm/sec), the final-velocity-initial-pressure relation was compatible with a square root dependence, as would be expected theoretically if the force of the air behind the piston was channeled entirely into acceleration of the mass. At lower pressures, bearing and piston friction cannot be ignored.

The trigger arms hold the piston rod/carriage against the force of the air pressure with the trigger assembly in a metastable locked position

(Figure 3.22a). A solenoid pulls down on the trigger, releasing the carriage as the trigger arms swing out of the way (Figure 3.22b).

The gun fires the sand grain down onto the the sand bed; therefore, it was necessary to devise a scheme for keeping the grain from spilling out of the projectile tube before the acceleration commences. We accomplished this as follows. The carriage acts as a support for a swivelling grain carrier/projectile tube, shown schematically in Figure 3.21. Prior to the release of the trigger, the grain carrier hangs vertically; the sand grain is dropped down the projectile tube (0.12 cm in diameter for this study) and remains at the bottom of it. When the carriage begins to move, the swivel swings up, contacts a magnet, and is held in a position with the axis of the projectile tube along the direction of motion. The sand grain remains at the back of the projectile tube because the large "fictitious force" resulting from the acceleration along the axis of the tube more than balances the projection of the force of gravity onto this axis. The moving assembly is brought to a stop by an air cushion at the forward end of the cylinder. The sand grain continues to move, travels out the projectile tube and strikes the sand bed. Intermittently, the grain carrier will break away from the magnet when

the assembly comes to a stop; however, we rarely detected any effect on the grain's trajectory in the data set described here.

The air cylinder and steel rod guides are mounted on an aluminum plate, which in turn is secured to a piece of plywood with angle iron (for convenient adjustment of impact angle) through shock mountings. The plywood is liberally loaded with lead bricks.

The pressurization and venting of the cylinder are accomplished through solenoid valves, and the trigger is tripped by a solenoid as described above. The pressure behind the piston is regulated, and the air entering this reservoir is treated with oil mist for lubrication purposes.

The sand grain is aimed at a bed of sand contained in a box of dimensions 12.5x12.5x2.5cm; it was levelled with respect to gravity and situated on a table vibrationally isolated from the sand gun. The sand used in this study was collected at the western end of the Kelso Dunes (Sharp, 1966), and it was sieved to retain those grains which passed through a mesh of size 0.085 cm, but which would not pass through a mesh of size 0.071 cm. It was composed primarily of rounded quartz and feldspar grains, with smaller amounts of magnetite and other minerals.

The velocities of incident, rebounding and ejected grains were

detected through strobe photography. The camera, a Canon AE-1 with a Soligar macro-lens, was set up to point perpendicular to the plane containing the flight path of the sand grain and the vector defining the direction of the force of gravity; therefore, we were able to detect motion in this plane only. The center of the field of view was positioned at the level of the sand bed. A GenRad Strobotac stroboscope was emplaced to one side of the camera, and aimed at a point slightly above the sand bed. The data discussed here were photographed with the stroboscopeset at a frequency of 400 Hz. Kodak Ektachrome P800/1600 color slide film was used, and developed at ASA 1600 with "push processing."

This experiment was performed in a dark corner of the "dungeon" of the Basic and Applied Physics Tandem AcceleratorFacility in the Sloan Laboratory, Caltech. The sand used in the experiment was stored in glass bottles, but no special attempts to control its moisture content were undertaken.

Experimental Procedure

The purpose of the experiment was twofold: to measure the splash function for a variety of incident parameters, and to take our new

apparatus, the sand gun, through a "shakedown cruise," and thereby evaluate its potential for further grain-bed impact investigations. For the study reported here, we obtained many photographs (15-25) of grain-bed impacts for each of a number of combinations of incident velocity and angle. At the beginning of each roll of film, the sand gun, sand bed, and camera were positioned and a photograph of a scale was taken. The positions of the camera and gun were not changed thereafter until the end of the roll.

Because it was not always possible to see two stroboscopic images of the incident grain in the photograph of a splash event (particularly at high incident velocity), prior to photographing the splash events, a number of photographs of incident grain trajectories were taken, in the absence of the sand bed, to ascertain the incident velocity and angle. These were combined with data from those grain-bed impact events in which the incident grain was visible, in order to produce mean values for the incident grain velocity and angle.

The following procedure was executed in recording splash events. First, the incident sand grain was chosen with a tweezers from a container of sand of the same type as used in the bed, and carefully

dropped into the swivelling grain carrier, down into the projectile tube. Attempts were made to be unbiased in the choice of the grain, although, as in any human endeavor, one's own prejudices are likely to influence the result. The author believes he may have been more favorably disposed toward choosing grains which were easier to pick up with the tweezers, possibly preferring those which were tabular in shape.

Next, sand was poured onto the sand bed, and a straightedge, resting on the edges of the box, was dragged across the sand surface in the direction of the incident grain's velocity to sweep away excess grains. This had the effect of producing a surface which was level and, at least in character, repeatable. We do not know what the relation of this surface is to a natural surface undergoing saltation impacts. However, observations of the surface produced in this manner suggest that it is rough on the scale of one grain diameter. This difficulty points out one advantage of studying grain-bed impacts in a wind tunnel: the surface is automatically prepared to resemble surfaces experiencing saltation in Nature. Further, Willetts and Rice (1985b) have reported that most grains on surfaces undergoing saltation are in motion. With the apparatus described here, it will be possible (in the future) to study the effect of

surface preparation on the splash function.

Finally, the lights were extinguished, the stroboscope was turned on, the air cylinder was pressurized, the camera shutter was opened, the trigger was released, the gun fired, and the camera shutter was closed.

A peculiar human-physiological phenomenon was noted during the execution of this experiment. Once the tendency to react with panic at the firing of the gun was overcome (aided by ear-protectors), and with the sand surface at eye-level, we found that we could observe and record some details of the splash event illuminated by the stroboscope with the naked eye. It was possible, with sufficient concentration, to pick out, roughly, the the number and trajectories of the ejected grains, often the rebounding grain, and with more difficulty the incident grain, although almost never all of these for the same event.

Analysis

Having recorded the splash events on slide film, it was necessary to subject the slides to analysis in order to extract meaningful data. With the unavailability of a projection-digitizing table possessing the capability of resolving low-light sand grain images, a two-step analysis process was employed for this purpose. First, the slides were projected

onto a sheet of paper using a standard slide projector. The line defining the surface of the sand bed was recorded by marking several points along it; the points corresponding to the positions of the stroboscopic images (closest to the impact point) of the incident, rebounding, and ejected grains were recorded on the paper. Points along the parabolic trajectories of particles whose velocity was insufficient to produce separated strobe images were marked.

Second, the positions of the marked points were quantified with a high-resolution Tektronix 4957 digitizing tablet. J.E. Hart, of Maranantha High School, performed a significant portion of the digitizing labor.

Events in which the sand grain did not hit the bed, or hit the bed very close to its edge, were rejected. In addition, a number of events in which the rebounding particle's velocity could not be ascertained (because the velocity, and hence the spacing between the images, was large) were excluded from the data set. This might have caused a slight bias against low angle, high velocity rebounds; rejected events did not comprise more than about ten percent of the events for any of the classes of incident parameters we considered. For ejected grains with very small ranges along the surface ($\sim< 0.25$ cm), it was occasionally difficult to decide

whether the grain was moving forward or backward. Judgment was employed.

Because of the difficulty of precisely levelling the camera and sand bed, the apparent top of the sand bed in the photographs was above the actual surface. We determined the extent of this difference by finding the intersection point between the incident particle and the rebounding particle trajectories for events in which both were available. The true bed level (in the vertical plane of the incident grain) was typically a few grain diameters below the apparent surface. This number rarely varied by more than a grain diameter over a roll of film (recall that the bed and camera remained stationary); the variation may reflect measurement errors or bed roughness.

The digitized positions of the points for each event were converted to centimeters using the distance between intervals on the scale. The incident and rebounding grain velocities were determined by measuring the distance between the two images just before and just after the impact. The angle with respect to gravity was derived from the slope of the line connecting the points associated with the two images. We found the horizontal and vertical velocities of the ejected particles for

which separated strobe images were available by fitting these points to the kinematical relations (in gravity) between horizontal position and time, and vertical position and time, respectively. The velocities of particles whose individual strobe images were not discernible were determined by fitting to the parabolic relation between horizontal and vertical position in a gravitational field.

The effect of air drag was ignored in this investigation. Figure 3.23 is a comparison of trajectories in air and in vacuum of a spherical grain ejected at 100 cm/sec and 45°. The grains for which we relied on the shape of the parabola were generally moving at a slower velocity than this (and hence they experienced less drag).

The data from splash events at a particular gun angle and cylinder pressure were combined to yield various quantities of interest. The incident velocities and angles were averaged over the available data at that sand gun angle and pressure.

Uncertainties in the derived quantities are primarily statistical in nature at the present time, being due to the small number of events obtained thus far. Uncertainties in the measurement of individual velocities stem from a number of sources. Random errors primarily arise

from the imprecision involved in the digitization process. We find that redigitization of a splash event, even if done by two separate researchers, will reproduce the velocities to better than 10 cm/sec, and the angles to within about 1°. Systematic errors of measurement result from imprecise levelling of the various components, grains moving out of the focal plane, and imperfect camera optics. The "fisheye" effect for our macro-lens was found to be tolerable. Photographing and digitizing a piece of graph paper, we discovered that a horizontal straight line three-quarters of the way from the bottom of the field of view bent only about 0.10 cm at the edge of the photograph. Considering all of the sources of error, we estimate that our measurement of most grain velocities is uncertain at a level no more than 20 cm/sec, and that most angles can be measured to within one to two degrees.

Finally, we note that a problem which we have not considered is the detection efficiency, i.e., the probability of capturing an ejected or rebounding grain on film. Despite low light levels, we felt that we detected most grains coming off the bed. Grains moving at very low angles to the horizontal or grains which rose to only a few grain diameters might have been missed.

Preliminary Results

We analyzed grain-bed impact events, ranging between twelve and twenty-two in number, for nine incident angle/incident velocity combinations. Figure 3.24 is a photograph of one of the events analyzed. For this impact, it is possible to observe the rebounding particle and many ejecta.

The general nature of the experimental events agrees qualitatively with the simulations. A particle of generally high velocity, presumed to be the rebounding particle, leaves the surface; additionally, a number of other grains are observed to depart from the bed. Ejected particles with high velocity generally leave at large forward or backward angles to the vertical. The ejection angles of the lower energy particles are more closely clustered around zero, with a somewhat forward bias. Many of the particles come off with large velocity components transverse to the direction of the incident particle; however, we have quantitative data on two-dimensional motion of the grains only. The variation of the number of particles ejected and the rebound characteristics from event to event was significant.

Figure 3.25 shows a crater resulting from a grain-bed impact in

fine to medium Kelso Dune sand. Typically, such craters were created in the coarse sand bed for events involving high incident velocities or high incident angles.

The mean values and half-widths of distributions of various quantities related to the grain-bed impacts are presented in Tables 3.11 and 3.12. We discuss selected aspects of the data.

Dependence on Incident Velocity

We studied the dependence of the grain-bed impact characteristics on the incident velocity at a nominal incident angle α_i of 15 °; these data comprise the first six entries of Table 3.11 and Table 3.12.

The nature of the rebound appears to be roughly independent of incident velocity (Table 3.11), i.e., the outgoing velocity scales, and the outgoing angle does not vary, with incident velocity. This concurs with the results of our computer simulations. The third and fourth entries of Table 3.11, with incident velocities v_i = 910. and v_i = 1000., both include one event in which the incident grain rebounded backwards, decreasing the values of $\overline{\epsilon_{ix}}$, the ratio of mean rebounding horizontal velocity to mean incident horizontal velocity, and $\overline{\theta_i}$, the mean rebounding angle relative to

the vertical, significantly. Otherwise, the only notable rebound variations with incoming velocity are in the mean vertical velocity amplification $\overline{\epsilon_{iy}}$, occurring at v_i = 650. and at v_i = 1000. The former may be due to insufficient statistics. The rise in the mean vertical velocity amplification at the latter incident velocity is more difficult to explain. Whether it can be ascribed to statistics, or whether it is an indication of a general trend, can only be established by additional experimentation.

The reaction of the bed does not scale with incident velocity, as summarized in Table 3.12. The mean number of ejecta per event rises roughly linearly with incident velocity (Figure 3.26), in contrast to the dependence on the square of the velocity postulated by Ungar and Haff (1986). The mean reptation distance per event also has an approximately linear dependence on incident velocity, this effect being attributable to the increase in the number of ejected grains entirely, since the mean reptation distance per particle remains roughly constant.

Surprisingly, the mean vertical ejection velocity has only a very slight, if any, dependence on incoming velocity. This holds true for the vertical velocity distribution of the ejecta as well, as illustrated in

Figure 3.27, where we plot the outgoing vertical velocity distribution (note that this includes the rebound) for v_i = 760. cm/sec and v_i = 1200. cm/sec. The "peak" in the former distribution at velocity ≈ 100 cm/sec corresponds to the rebound, illustrating the following point concerning steady-state saltation: if ejection velocities are independent of incident velocities, grains with low incident velocity are much more likely to produce particles capable of replacing themselves in the saltating stream than grains with high incident velocities. This lends credence to the notion that the high velocity particles in the saltating stream arise from the successive growth of velocity of a particle originating in the low velocity population of grains, rather than by a dramatic ejection of a bed grain with a large vertical velocity component.

In Figure 3.28 we present the distribution of ejected angles θ_e for CASE G of the computer simulations, (dense bed, v_i = 3000 cm/sec, α_i = 15 °). A peak in the distribution corresponding to ejection of particles at a brink is clearly visible, as well as a larger peak corresponding to nearly vertical ejection. Figure 3.29 shows that the ejected angle distribution for the coarse sand experiment at v_i = 760. cm/sec and v_i = 1200. cm/sec.

is rather different. Moreover, the mean ejection angle decreases with increasing incident velocity (Figure 3.30). There is no corresponding variation in the simulations. We interpret the differences between simulation and experiment as arising from the roughness of the experimental sand surface versus the relatively smooth, close-packed simulation surface. For the experiment, at low incoming velocities, a large fraction (roughly half for v_i = 760. cm/sec) of the ejections have large forward ejection angles, reminiscent of brink particle ejection. As the incident velocity increases, it is possible that this brink ejection saturates; perhaps the radius of the "crater" created in the surface becomes larger than the mean distance between depressions in the surface. It may be that energy is becoming available to the layer of grains below the surface. These particles would be constrained to move nearly vertically. It is clear that both additional experiments and computer simulations would be helpful for further investigation of the unexpected dependences of the ejecta characteristics on incident velocity.

Dependence on Incident Angle

Our data on the effect of incident angle on the splash function are rather sketchy at present. We have obtained results for a nominal incident velocity of 900 cm/sec for α_i = 12 °, 16 ° and 21 °, and at incident velocity 1200 cm/sec for α_i = 10 ° and 16 ° (Tables 3.11 and 3.12).

The mean vertical velocity amplification varies as an inverse function of the incident angle, whereas the mean rebound angle is unaffected by α_i at these low incident angles. The mean number of grains ejected per event increases with incident angle, probably due to increased deposition of energy in the bed. The dependence of the mean ejection vertical velocity on α_i is apparently complicated, rising at angles both smaller and larger than 15 °, and the mean ejected angle is insensitive to incident angle. The mean reptation distance per particle (and per event) reflects the complex variation of vertical ejection velocity with α_i.

In summary, we have found no significant evidence that the rebound characteristics do not scale with incident velocity. The ejected

velocities are roughly independent of incident velocity, the number of ejecta increases approximately linearly with incident velocity, and the ejected angles decrease with v_i, probably reflecting a change from brink-dominated ejection to "cratering." The vertical velocity amplification decreases, and the number of ejecta increases with increasing incident angle. The dependence of vertical ejection velocity on incident angle will require more data to untangle. Finally, the nature of the surface appears to have affected our results. All of these conclusions are compatible with the general trends observed in the simulations and the conceptions and models derived from them. Thus, these three-dimensional experiments have verified the validity of using the two-dimensional simulations for a qualitative investigation of the grain-bed impact.

We believe that the questions raised concerning the effect of the surface on the bed-grain ejecta, as well as the data obtained from the preliminary experiment described here justify the effort expended in developing the sand gun experiment. It is anticipated that this apparatus will prove useful for future systematic investigations of fundamental aspects of the splash function.

APPENDIX III.1

The ratio of outgoing to ingoing velocities in the horizontal and vertical directions for the rebound model are provided, using variables defined in the body of this paper (these equations are derived following Goldsmith, 1960):

$$\epsilon_{ix} = \frac{c_2 cos(\beta) cos(\alpha_i+\beta)}{cos(a_i)} - \frac{c_3 cos(\beta) w_i r_i}{v_i cos(\alpha_i)} - \frac{c_4 sin(\beta) sin(\alpha_i+\beta)}{cos(\alpha_i)}$$

$$\epsilon_{iy} = \frac{c_4 cos(\beta) sin(\alpha_i+\beta)}{sin(a_i)} - \frac{c_3 sin(\beta) w_i r_i}{v_i sin(\alpha_i)} + \frac{c_2 sin(\beta) cos(\alpha_i+\beta)}{sin(\alpha_i)}$$

$$c_1 = 1/\kappa_i + (m_i/m_{beff})(1 - 1/\kappa_{beff})$$

$$c_2 = (\sigma + c_1)/(1 + c_1)$$

$$c_3 = (1 - \sigma)/(1 + c_1)$$

$$c_4 = (\epsilon - m_i/m_{beff})/(1 + m_i/m_{beff}) . \qquad (3.A.1)$$

SYMBOL DEFINITIONS: CHAPTER III

v_i	incident particle incoming velocity
α_i	incident particle incoming angle relative to horizontal
w_i	incident particle incoming angular velocity
r_i	incident particle radius
m_i	incident particle mass
I_i	incident particle moment of inertia
k_i	$= I_i/m_i r_i^2$
r_b	bed particle radius
m_b	bed particle mass
m_{beff}	bed particle effective mass
I_b	bed particle moment of inertia
κ_b	$= I_b/m_b r_b^2$
κ_{beff}	effective coefficient κ_b
Δ_b	horizontal gap between the surfaces of bed particles
β	angle (relative to vertical) defining point of contact between incident and target particles
μ	interparticle coefficient of friction
ϵ	two-body collisional coefficient of restitution
σ	friction restitution coefficient
ϵ_{ix}	incident particle outgoing to ingoing horizontal velocity ratio
ϵ_{iy}	same for vertical velocity (vertical velocity amplification)
ϵ_i	same for total velocity
θ_i	incident particle outgoing angle relative to vertical
w_o	incident particle outgoing angular velocity
ξ_i	$= w_o r_i/(\epsilon_{ix} v_i \cos\alpha_i)$

θ_e ejected bed particle angle relative to vertical

p_{ex} ratio of ejected bed particle horizontal momentum to incident particle horizontal momentum

ϵ_{bx} ratio of horizontal momentum transferred to the bed to the incident particle incoming horizontal momentum

ϵ_{by} same for vertical momentum

θ_b angle, relative to horizontal, of vector defining momentum transferred to the bed

$\mathcal{E}$ energy transmitted to the bed

ρ density of the bed

k interparticle force spring constant

d decay distance for accoustical wave in a bed

ℓ distance from impact point on the surface of the bed

v_e ejection velocity

R "crater radius"

δ_b roughness on bed is $\delta_b r_b$ in magnitude

g acceleration of gravity

$\overline{A}$ mean value of A

TABLES: CHAPTER III.

All numbers given in these tables are expressed in cgs units, unless otherwise specified, and represent mean values of distributions obtained from the computer simulations and the coarse sand experiment. Angles are presented in degrees. The numbers in parentheses represent the calculated half-widths of the distributions.

TABLE 3.1 Simulation Parameters

CASE	v_i	α_i	μ	Type of Bed	r_i
A	3000.	15.	0.5	Loose	1.0
B	3000.	25.	0.5	Loose	1.0
C	3000.	70.	0.5	Loose	1.0
D	3000.	15.	0.0	Loose	1.0
E	1000.	15.	0.5	Loose	1.0
F	4000.	15.	0.5	Loose	1.0
G	3000.	15.	0.5	Dense	1.0
H	6000.	15.	0.5	Loose	0.5
I	8100.	15.	0.5	Loose	0.5

TABLE 3.2 Simulation Results for the Rebounding Particles

CASE	$\overline{\epsilon_{ix}}$	$\overline{\epsilon_{iy}}$	$\overline{\epsilon_i}$	$\overline{\theta_i}$	$\overline{\xi_i}$	$\overline{\beta}$
A	0.59	1.12	0.65	62.	0.85	17.
	(0.08)	(0.29)	(0.04)	(9.)	(0.18)	(5.)
B	0.53	0.68	0.58	57.	0.88	16.
	(0.16)	(0.22)	(0.10)	(16.)	(0.31)	(12.)
C	0.54	0.25	0.37	30.	0.85	-4.
	(0.64)	(0.07)	(0.07)	(37.)	(0.72)	(19.)
D	0.85	1.07	0.87	71.	0.	17.
	(0.07)	(0.32)	(0.04)	(7.)		(5.)
E	0.60	1.06	0.66	64.	0.82	13.
	(0.11)	(0.39)	(0.05)	(12.)	(0.23)	(9.)
F	0.55	1.26	0.63	58.	0.87	18.
	(0.06)	(0.21)	(0.03)	(7.)	(0.18)	(10.)
G	0.67	0.85	0.70	70.	0.74	7.
	(0.14)	(0.46)	(0.08)	(14.)	(0.26)	(9.)
H	0.53	1.39	0.69	53.	1.14	16.
	(0.25)	(0.78)	(0.08)	(26.)	(0.58)	(13.)
I	0.47	1.66	0.63	46.	1.28	21.
	(0.09)	(0.32)	(0.01)	(11.)	(0.14)	(5.)

TABLE 3.3 Simulation Results for the Bed: Transfer of Momentum

CASE	$\overline{\epsilon}_{bx}$	$\overline{\epsilon}_{by}$	$\overline{\theta}_b$	$\overline{m_{beff}/m_b}$
A	0.41 (0.08)	2.12 (0.29)	54. (2.)	1.9 (0.3)
B	0.47 (0.16)	1.68 (0.22)	60. (5.)	1.9 (0.3)
C	0.46 (0.64)	1.25 (0.07)	83. (10.)	2.3 (0.2)
D	0.15 (0.07)	2.08 (0.32)	75. (5.)	1.3 (0.2)
E	0.40 (0.11)	2.06 (0.39)	55. (3.)	2.2 (0.3)
F	0.45 (0.06)	2.26 (0.25)	54. (2.)	1.8 (0.3)
G	0.33 (0.14)	1.85 (0.46)	57. (4.)	2.0 (0.3)
H	0.47 (0.25)	2.39 (0.78)	44. (13.)	-
I	0.53 (0.09)	2.66 (0.32)	53. (1.)	-

TABLE 3.4 General Results for Ejected Particles

CASE	Ejection Velocity	Ejection Vertical Velocity	Ejection Angle*	Reptation Distance per Event	Number Ejected per Event
A	185.0 (90)	160.0 (30)	17.0 (20)	120.0 (85)	6.0 (2)
B	180.0 (85)	165.0 (85)	9.0 (25)	55.0 (35)	7.0 (2)
C	185.0 (125)	175.0 (125)	8.0 (20)	65.0 (100)	8.0 (2)
D	150.0 (95)	135.0 (85)	14.0 (25)	105.0 (100)	8.0 (4)
E	110.0 (40)	110.0 (45)	15.0 (15)	2.0 (3)	0.4 (0.5)
F	215.0 (130)	195.0 (115)	10.0 (20)	250.0 (180)	9.0 (2)
G	120.0 (60)	100.0 (50)	8.0 (30)	45.0 (65)	7.0 (4)
H	160.0 (95)	155.0 (95)	2.0 (14)	4.0 (50)	2.0 (2)
I	190.0 (130)	175.0 (130)	9.0 (25)	80.0 (90)	6.0 (3)

* relative to the vertical

TABLE 3.5 Ejected Momenta Per Event

CASE	Horizontal Incident Momentum	Vertical Incident Momentum	Horizontal Ejected Momentum	Vertical Ejected Momentum
A	18200.0	4900.0	2100.0 (1100)	5900.0 (1500)
B	17100.0	8000.0	1300.0 (800)	7400.0 (2600)
C	6400.0	17700.0	1200.0 (1300)	8200.0 (1300)
D	18200.0	4900.0	2000.0 (1100)	6400.0 (3300)
E	6100.0	1600.0	50.0 (85)	270.0 (390)
F	24300.0	6500.0	2800.0 (1500)	11300.0 (1500)
G	18200.0	4900.0	950.0 (1100)	4700.0 (2900)
H	9100.0	2400.0	110.0 (690)	2240.0 (2000)
I	12300.0	3300.0	1100.0 (200)	6600.0 (2200)

TABLE 3.6 Ejected Energies per Event*

CASE	Incident Kinetic Energy	Ejected Kinetic Energy	Ejected Rotational Energy
A	28000.0	790.0 (310)	100.0 (60)
B	28000.0	890.0 (380)	90.0 (80)
C	28000.0	1170.0 (300)	60.0 (30)
D	28000.0	760.0 (450)	0.0
E	3100.0	20.0 (30)	10.0 (20)
F	50000.0	1860.0 (430)	220.0 (120)
G	28000.0	400.0 (320)	70.0 (60)
H	57000.0	240.0 (260)	40.0 (40)
I	100000.0	960.0 (240)	210.0 (190)

*all energies in 10^3 ergs

TABLE 3.7 Ejected Angles and Momenta Ratios by Particle Type

CASE	Target Particle		Brink Particles		All Other Particles	
	θ_e	p_{ex}	θ_e	p_{ex}	θ_e	p_{ex}
A	0.4	0.005	44.	0.100	4.8	0.015
	(9.0)	(0.020)	(15.)	(0.055)	(15.)	(0.025)
B	-2.2	-0.005	50.	0.065	1.6	0.010
	(5.3)	(0.010)	(10.)	(0.060)	(15.)	(0.040)
C	0.3	0.001	45.	0.200	1.3	0.050
	(4.0)	(0.030)	(14.)	(0.180)	(13.)	(0.110)

TABLE 3.8 Reptation Distance per Event by Particle Type

CASE	Target Particle	Brink Particles	All Other Particles
A	13. (54.)	96. (74.)	12. (27.)
B	-5. (14.)	48. (49.)	13. (35.)
C	-1. (21.)	51. (65.)	15. (31.)

TABLE 3.9 Ejected Particle Location Relative to the Impact Point

CASE	Horizontal Distance from Impact Point	Vertical Distance from Impact Point	Total Distance from Impact Point
A	3.4 (4.4)	-1.3 (0.7)	4.4 (3.7)
B	3.1 (4.6)	-1.4 (0.8)	4.6 (3.4)
C	-2.1 (6.9)	-1.2 (0.8)	5.5 (4.9)
D	0.9 (10.1)	-1.1 (0.7)	7.5 (6.9)
E	1.3 (2.0)	-1.0 (0.01)	1.8 (1.7)
F	2.5 (5.7)	-1.4 (0.9)	5.2 (3.8)
G	6.2 (13.0)	-1.1 (0.7)	8.5 (11.3)
H	1.8 (2.4)	-1.2 (0.6)	2.7 (1.8)
I	3.3 (5.1)	-1.2 (0.7)	4.6 (4.1)

TABLE 3.10 Rebound Model Parameters

CASE	r_i/r_b	m_i/m_{beff}	Δ_b	α_i	w_i	k_i	k_b	ϵ	σ
1	1.0	0.5	0.	15.	0.	0.5	0.5	0.6	1.0
2	1.0	0.5	0.	15.	0.	0.5	1.0	0.85	0.

TABLE 3.11 Basic Data for Coarse Sand Splash Function Measurement

$\overline{v_i}$	$\overline{a_i}$	total # events	total # ejecta†	$\overline{\epsilon_{ix}}$	$\overline{\epsilon_{iy}}$	$\overline{\theta_i}$
650. (40.)	15. (2.)	12	33	0.58 (0.13)	0.80 (0.43)	68. (13.)
760. (50.)	16. (1.)	22	51	0.55 (0.24)	0.71 (0.36)	64. (18.)
910. (20.)	16. (1.)	20	81	0.48 (0.27)	0.72 (0.36)	58. (34.)
1000. (40.)	15. (1.)	18	90	0.49 (0.25)	0.74 (0.30)	62. (18.)
1100. (80.)	15. (1.)	18	102	0.54 (0.25)	0.68 (0.31)	64. (24.)
1200. (50.)	16. (1.)	19	109	0.58 (0.17)	0.86 (0.36)	66. (13.)
880. (50.)	12. (1.)	17	50	0.61 (0.17)	0.94 (0.46)	69. (13.)
1200. (60.)	10. (1.)	12	59	0.61 (0.17)	1.27 (0.48)	67. (12.)
920. (60.)	21. (1.)	17	80	0.50 (0.18)	0.48 (0.24)	66. (14.)

† all events

TABLE 3.12 Ejecta Data for Coarse Sand Splash Function Measurement

$\overline{v_i}$	$\overline{\alpha_i}$	$\overline{E_{ke}/E_{ki}}^{\dagger}$ *	mean ejecta *	mean reptation distance *	mean reptation distance **	$\overline{v_{ey}}^{\dagger\dagger}$ *	$\overline{\theta_e}$ *
650. (40.)	15. (2.)	0.42 (0.12)	2.8 (1.1)	12. (10.)	4.3 (5.9)	48. (28.)	34. (17.)
760. (50.)	16. (1.)	0.40 (0.21)	2.3 (1.8)	10. (14.)	4.4 (9.2)	50. (28.)	27. (18.)
910. (20.)	16. (1.)	0.36 (0.15)	4.1 (2.6)	17. (21.)	4.2 (11.)	49. (29.)	23. (26.)
1000. (40.)	15. (1.)	0.36 (0.23)	5.0 (2.1)	20. (20.)	4.1 (11.)	49. (34.)	19. (22.)
1100. (80.)	15. (1.)	0.42 (0.18)	5.7 (3.1)	27. (26.)	4.7 (10.)	58. (46.)	17. (24.)
1200. (50.)	16. (1.)	0.43 (0.16)	5.7 (3.2)	22. (17.)	3.8 (8.6)	54. (37.)	17. (27.)
880. (50.)	12. (1.)	0.47 (0.17)	2.9 (2.4)	20. (25.)	6.9 (16.)	62. (42.)	18. (23.)
1200. (60.)	10. (1.)	0.49 (0.17)	4.9 (2.4)	43. (46.)	8.7 (25.)	72. (57.)	20. (22.)
920. (60.)	21. (1.)	0.35 (0.20)	4.7 (2.2)	37. (46.)	7.9 (23.)	59. (38.)	22. (24.)

* per event ** per particle

† outgoing kinetic energy divided by incident kinetic energy

†† mean ejected vertical velocity

FIGURE CAPTIONS: CHAPTER III

Figure 3.1 Nine frames from a simulation of a saltation impact: CASE G. The first frame has the incident grain about to impact the surface; the second grain shows the incident grain rebounding from the surface. The frames run in time sequence from left to right and from top to bottom, at times (in seconds) 0.000, 0.0021, 0.0049, 0.0070, 0.0170, 0.0270, 0.0370, 0.0570 and 0.0700.

Figure 3.2 Definition of variables for the simulations and the rebound model (before, during and after the collision).

Figure 3.3 Arrows represent velocities of particles at four times (t in seconds) close to the simulated impact of a particle on the dense particle bed. (a) $t = 0$. (b) $t = 6.4 \times 10^{-5}$ (c) $t = 1.6 \times 10^{-4}$ (d) $t = 2.2 \times 10^{-4}$.

Figure 3.4 Arrows represent interparticle forces corresponding to the time snapshots of Figure 3.3 Arrows are parallel to the interparticle force.

Figure 3.5 The distribution of vertical velocities for particles (ejected and incident rebound) leaving the surface for CASE A.

Figure3.13 Mean vertical velocity amplification as a function of mass ratio for CASE 1 of Table 3.10.

Figure 3.14 Mean vertical velocity amplification as a function of frictional coefficient of restitution for CASE 1 of Table 3.10.

Figure 3.15 Mean vertical velocity amplification as a function of incident angular velocity for CASE 1 of Table 3.10. The amplification depends fairly strongly on incident spin rate, being greater for spins oriented in the rolling sense.

Figure 3.16 Comparison of mean vertical velocity amplification versus incident angle for the rebound model-solid line- (CASE 2 of Table 3.10) and the computer simulations-three points.

Figure 3.17 Time snapshots of particle velocities for simulated impacts on the dense bed for an impact (a) roughly equidistant from brink and anti-brink, (b) close to the brink and (c) close to the anti-brink.

Figure 3.18 Distribution of vertical velocity amplification for the rebound model of CASE 1 of Table 3.10.

Figure 3.19 Mean vertical velocity amplification as a function of bed inclination for CASE 1 of Table 3.10, with $\alpha_i = 15.°$.

Figure 3.20 Sand grain accelerator: the "sand gun."

Figure 3.21 Schematic illustration of the sand gun components. The drawing is not to scale and does not show details.

Figure 3.22 Sand gun trigger mechanism (after S. Stryker, 1985: unpublished drawing): (a) Locked and ready to fire. (b) A pull from the solenoid releases the trigger arm.

Figure 3.23 Calculated trajectories of a sand grain of radius 0.079 cm ejected at velocity 100 cm/sec and angle 45° moving in vacuum (dashed line) and in air (solid line).

Figure 3.24 Grain-bed impact event for coarse sand. Incident particle strikes the bed from the left at velocity 1100 cm/sec and angle 15 ° to the horizontal.

Figure 3.25 "Crater" produced in medium to fine sand from the Kelso Dunes by a grain-bed impact.

Figure 3.26 Dependence of the mean number of ejecta on the incident velocity at incident angle 15 ° for the coarse sand experiment. Error bars give the half-width of the distribution of the number of ejecta at each point.

Figure 3.27 Distribution of vertical velocity for grains leaving the

surface (including the rebound) for incident angle 15 ° and incident velocities 760 cm/sec and 1200 cm/sec for the coarse sand experiment.

Figure 3.28 Distribution of ejection angle θ_e for computer simulation events, CASE G (Table 3.1).

Figure 3.29 Distribution of ejection angle θ_e for coarse sand experiment with incident angle 15 ° and incident velocities 760 cm/sec and 1200 cm/sec.

Figure 3.30 Mean ejection angle versus incident velocity at incident angle 15 ° for the coarse sand experiment. Error bars show the half-width of the distribution in angle at each point.

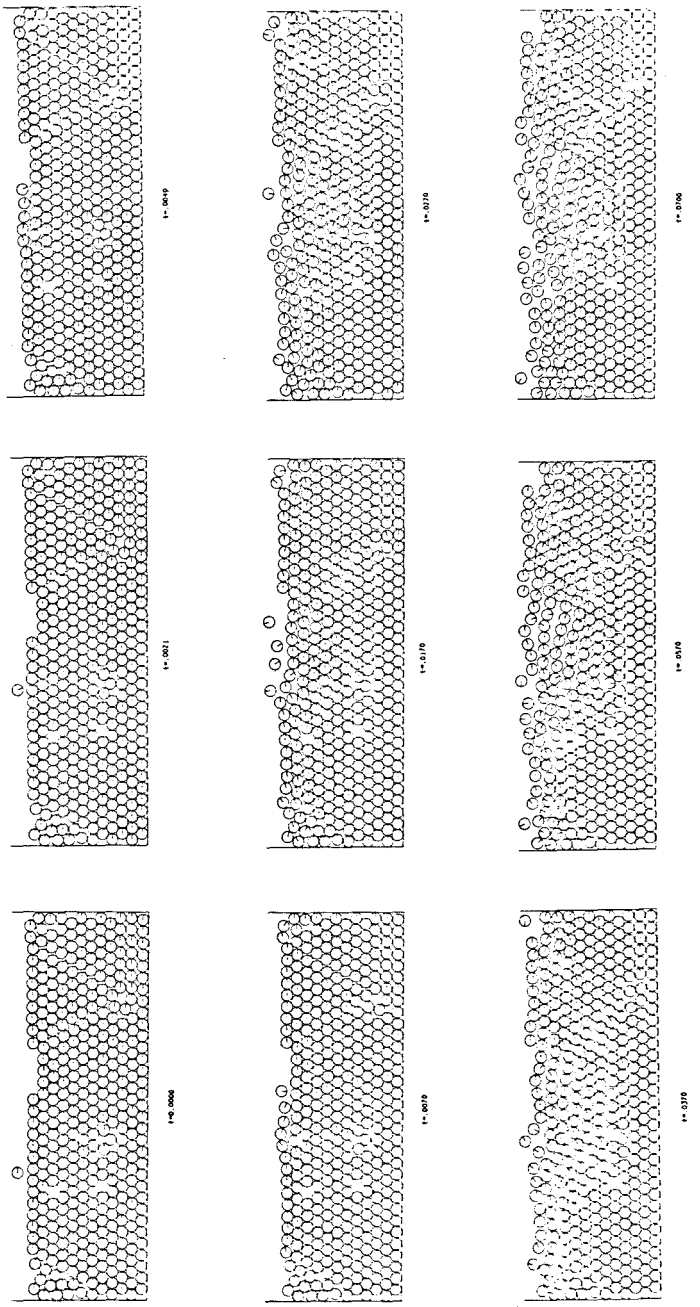

Figure 3.1

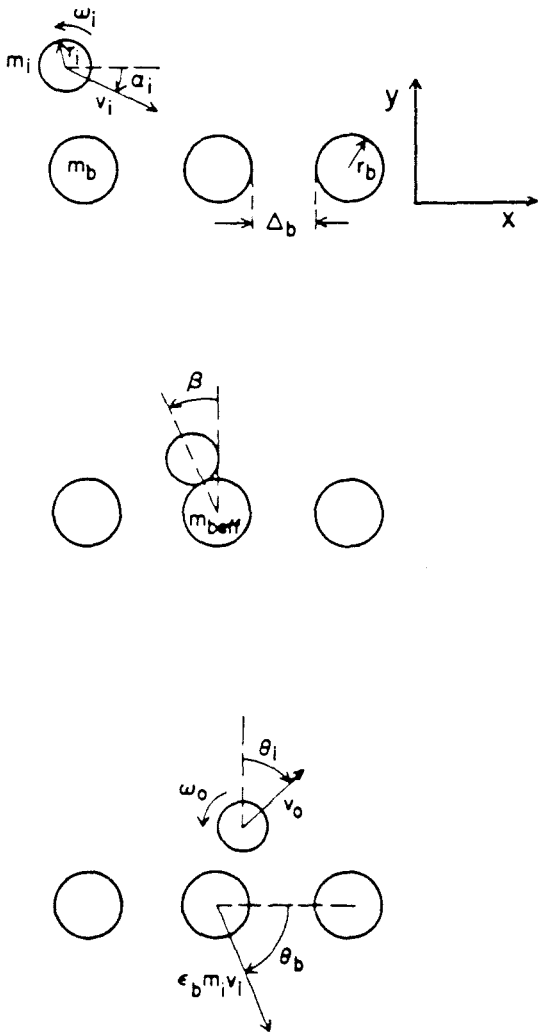
ω_i
m_i
r_i
a_i
v_i
m_b
r_b
Δ_b
y
x
β
m_{beff}
θ_i
ω_o
v_o
θ_b
$\epsilon_b m_i v_i$

Figure 3.2

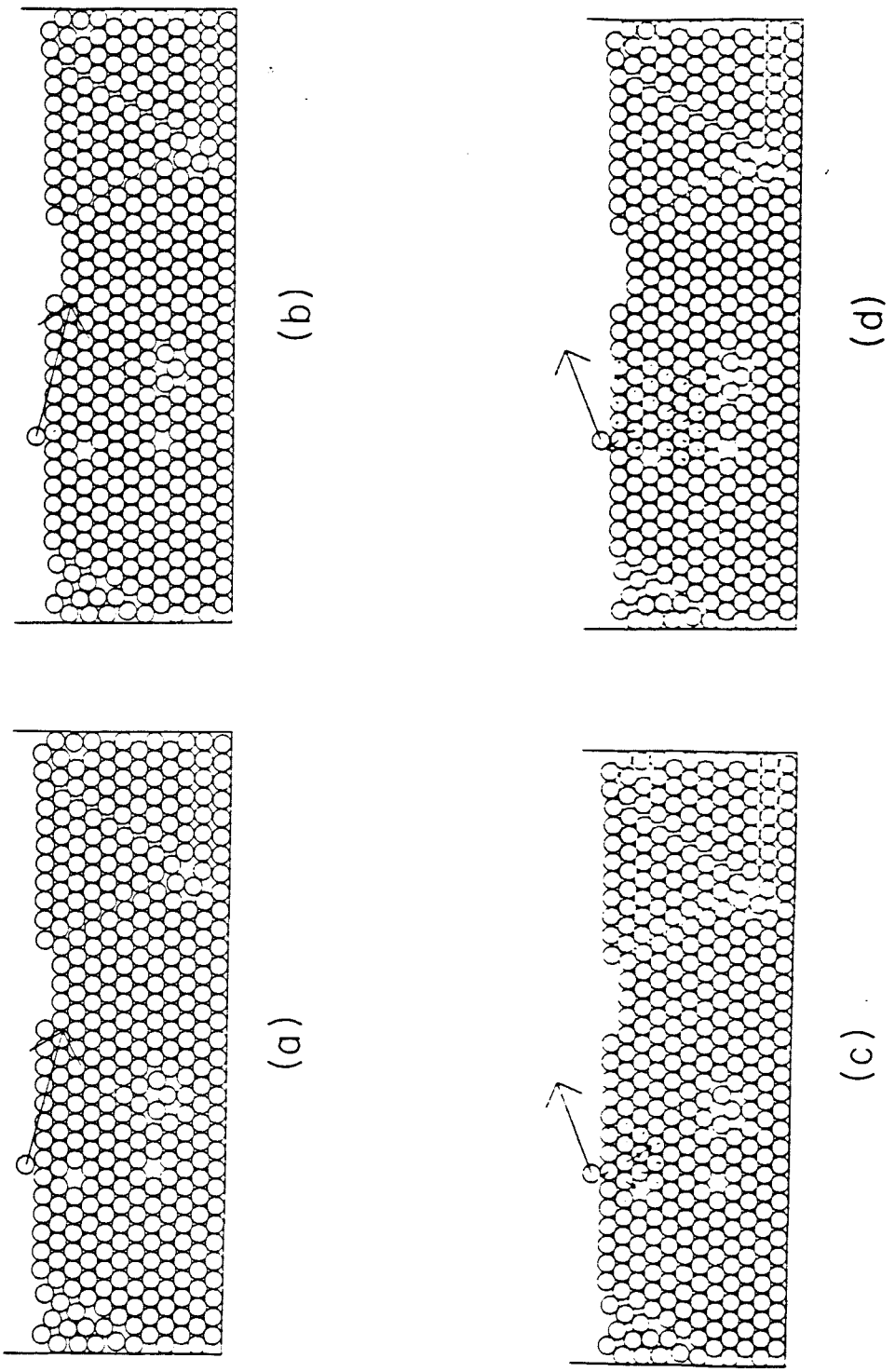

Figure 3.3

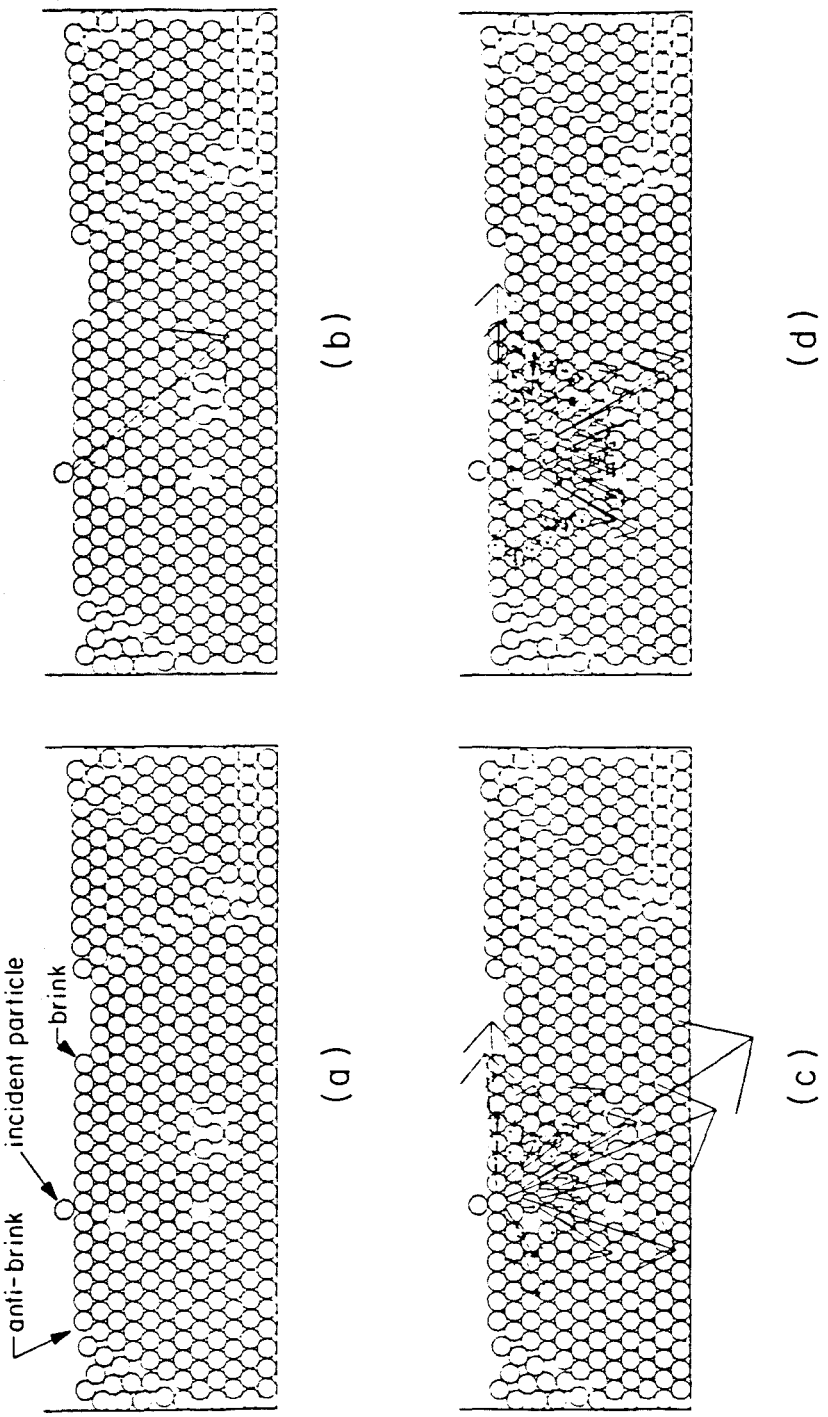

Figure 3.4

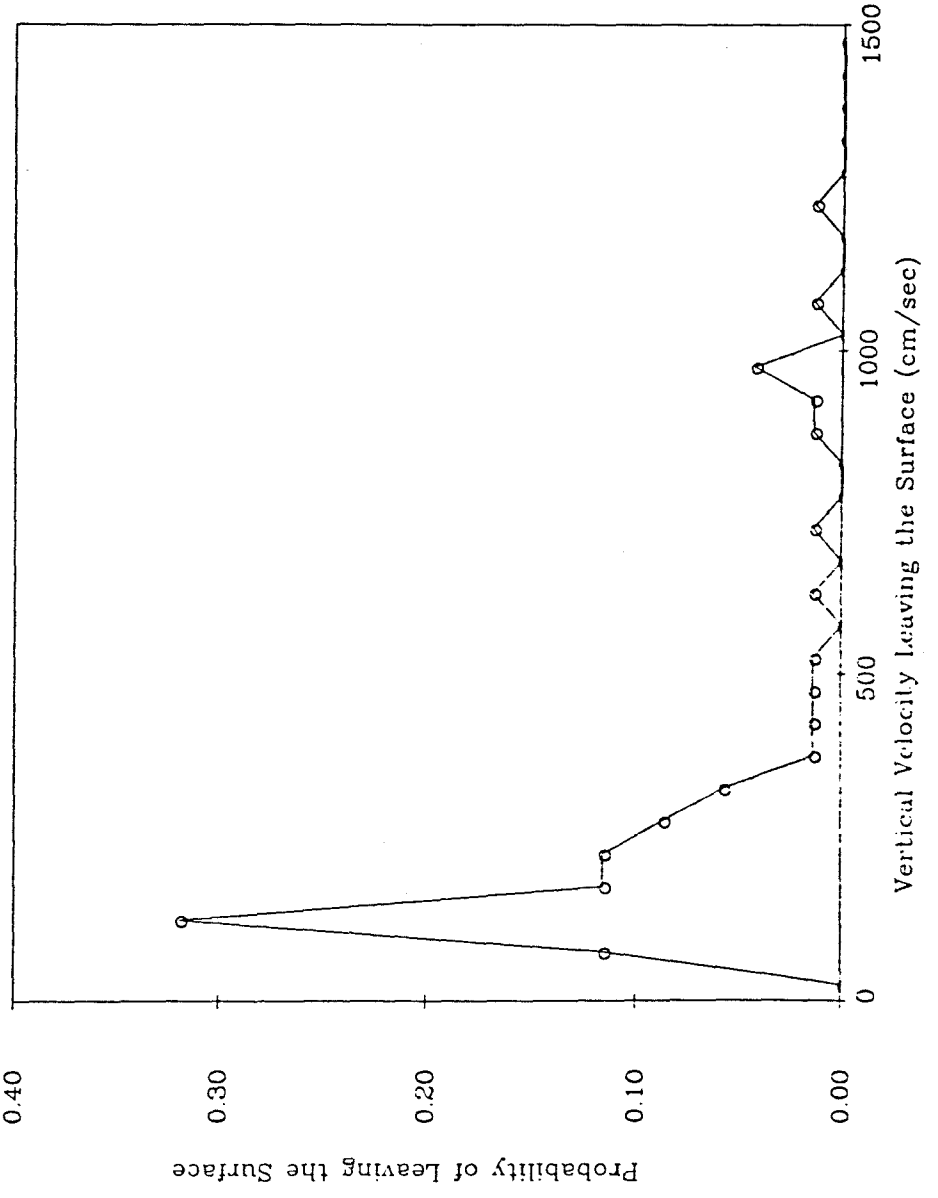
Probability of Leaving the Surface
0.00
0.10
0.20
0.30
0.40
0
500
1000
1500
Vertical Velocity Leaving the Surface (cm/sec)

Figure 3.5

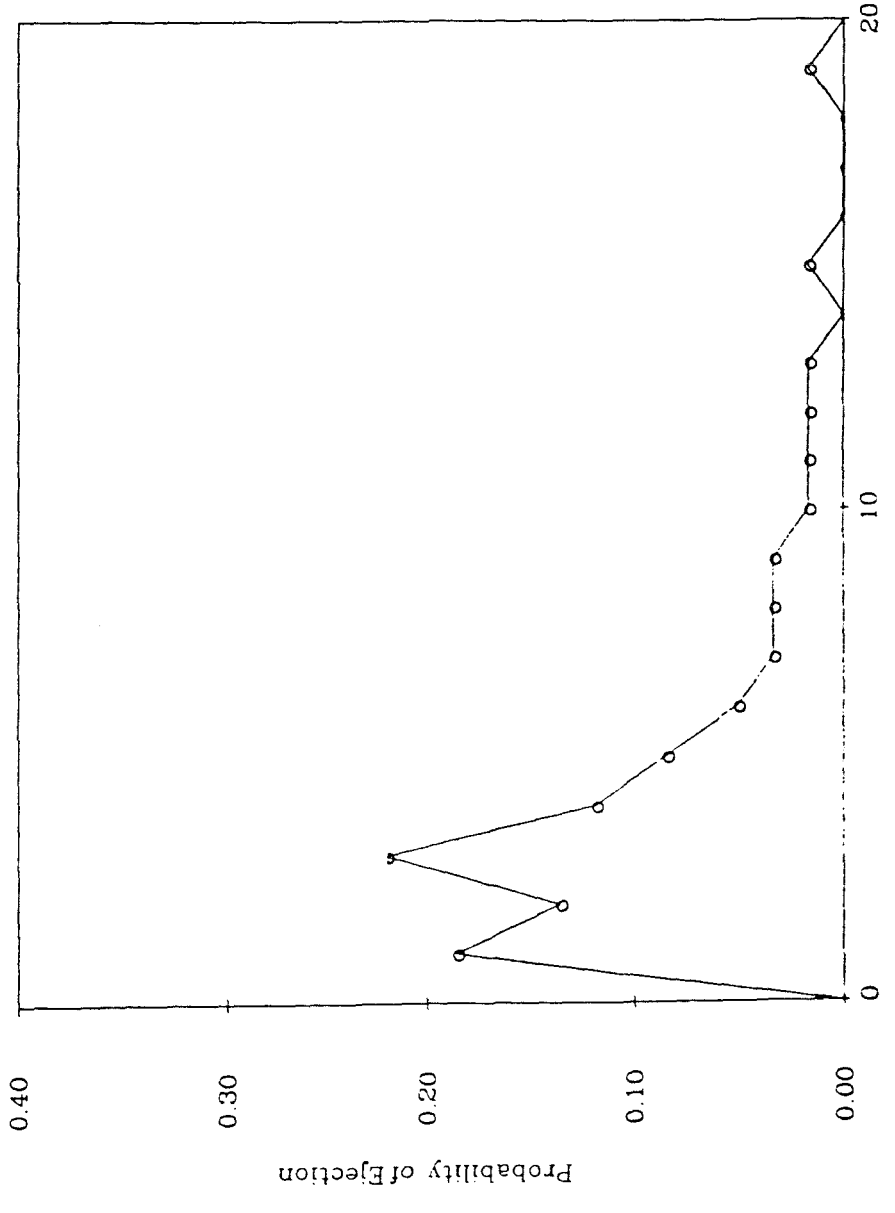
0.40
0.30
0.20
0.10
0.00
Probability of Ejection
0
10
20
Total Distance from Contact Point (cm)

Figure 3.6

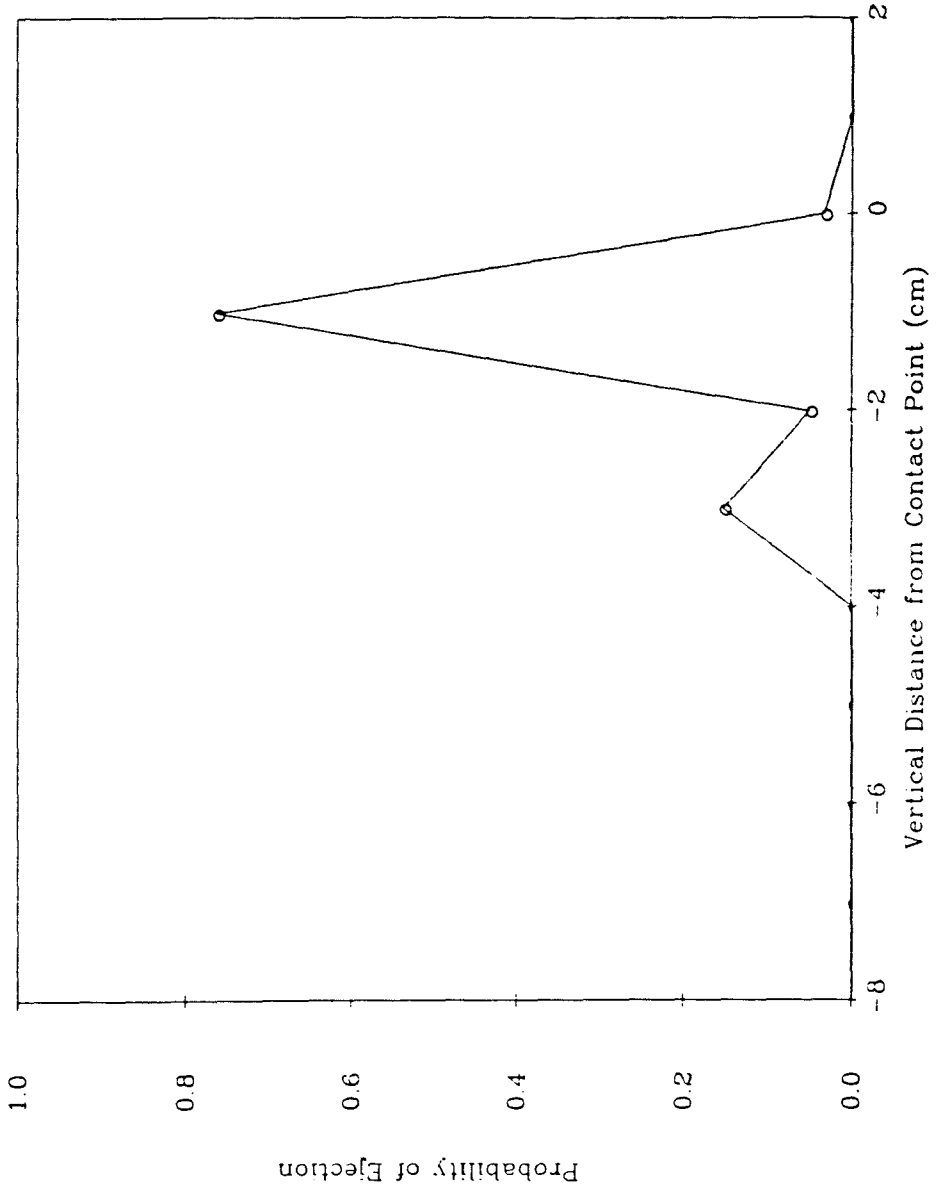
Probability of Ejection
1.0
0.8
0.6
0.4
0.2
0.0
-8
-6
-4
-2
0
2
Vertical Distance from Contact Point (cm)

Figure 3.7

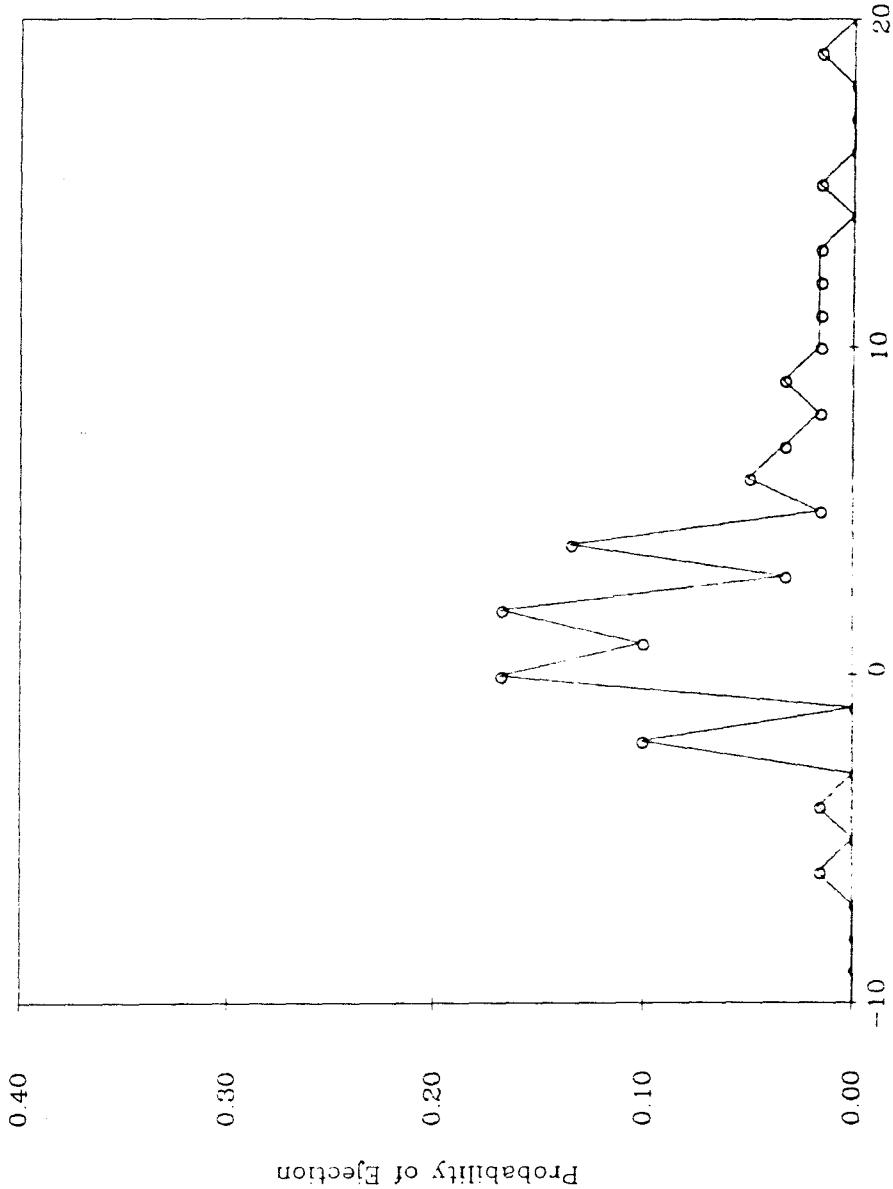
Probability of Ejection
0.00
0.10
0.20
0.30
0.40
-10
0
10
20
Horizontal Distance from Contact Point (cm)

Figure 3.8

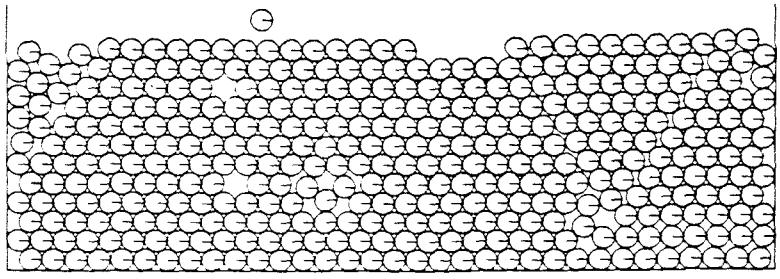

t=0.0000

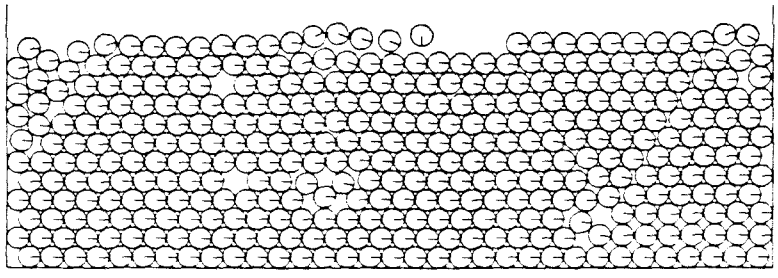

t=.0070

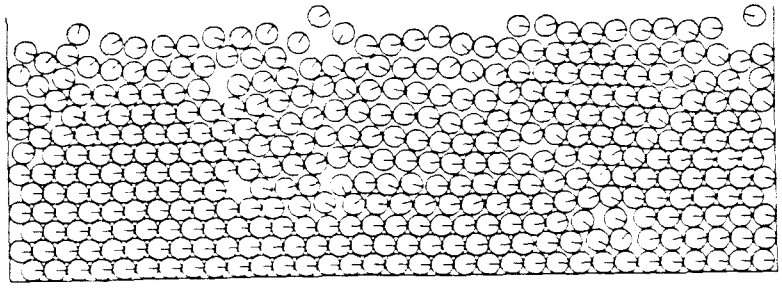

t=.0370

Figure 3.9

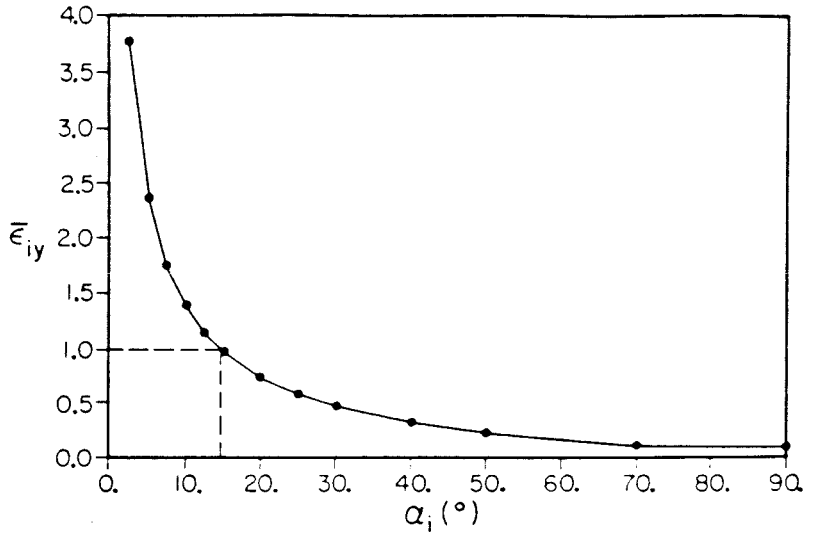

(a)

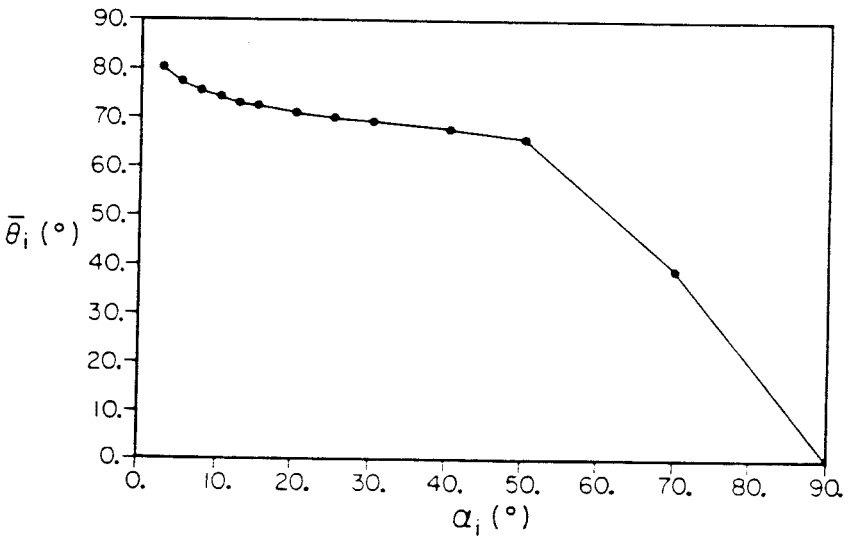

(b)

Figure 3.10

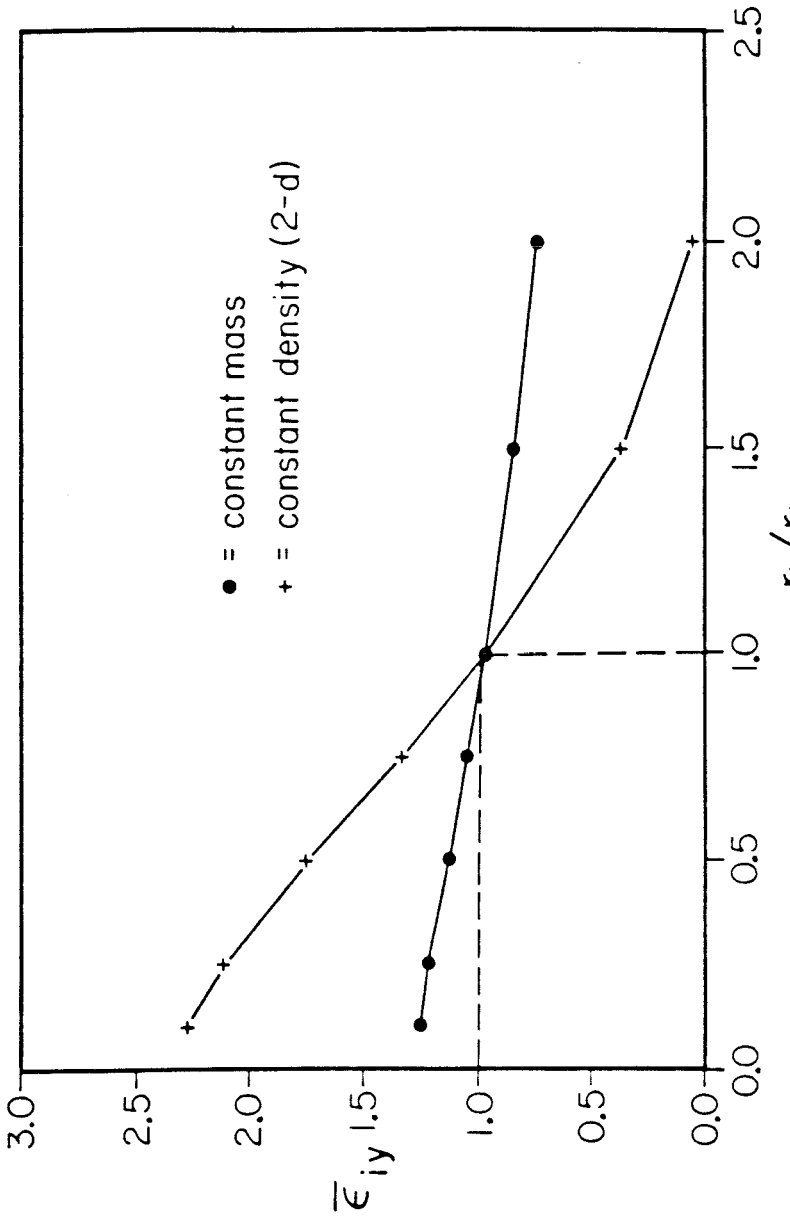
● = constant mass
+ = constant density (2-d)
$\bar{\epsilon}_{iy}$
r_i/r_b
3.0
2.5
2.0
1.5
1.0
0.5
0.0
0.0
0.5
1.0
1.5
2.0
2.5

Figure 3.11

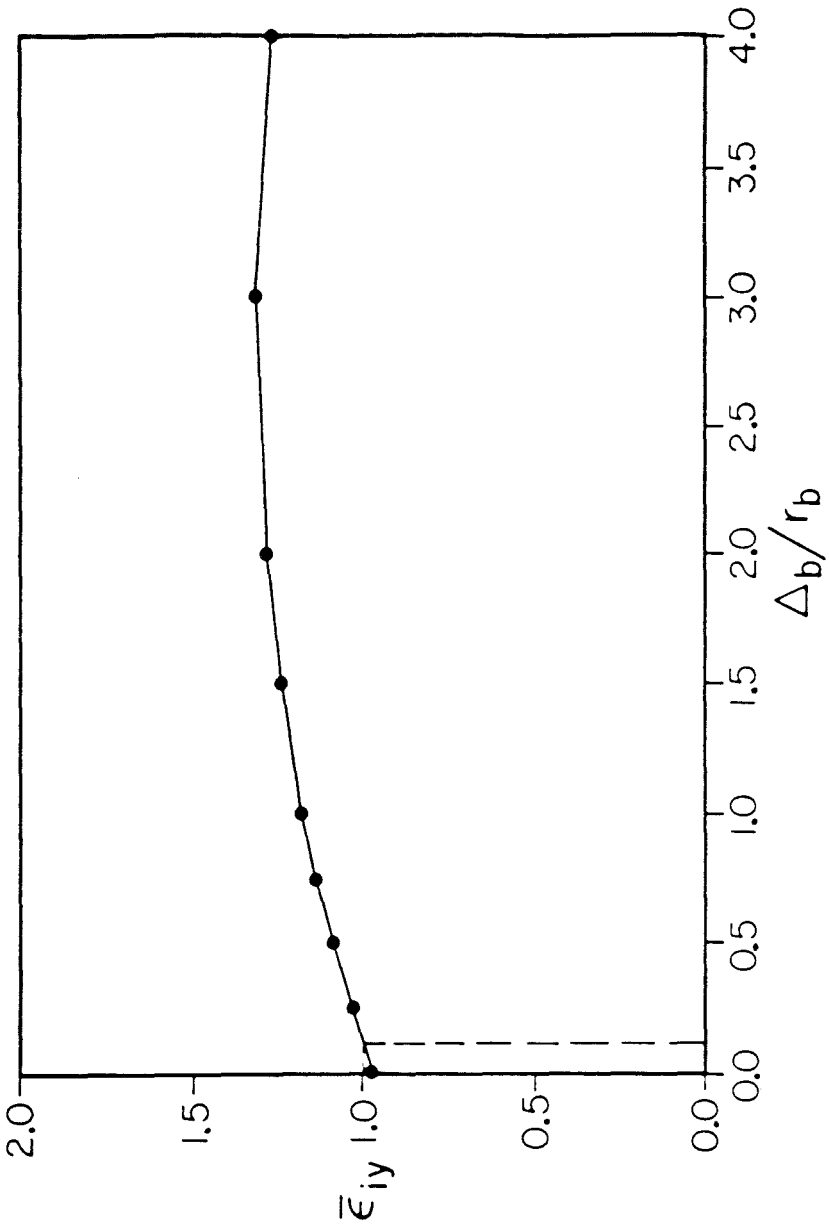

Figure 3.12

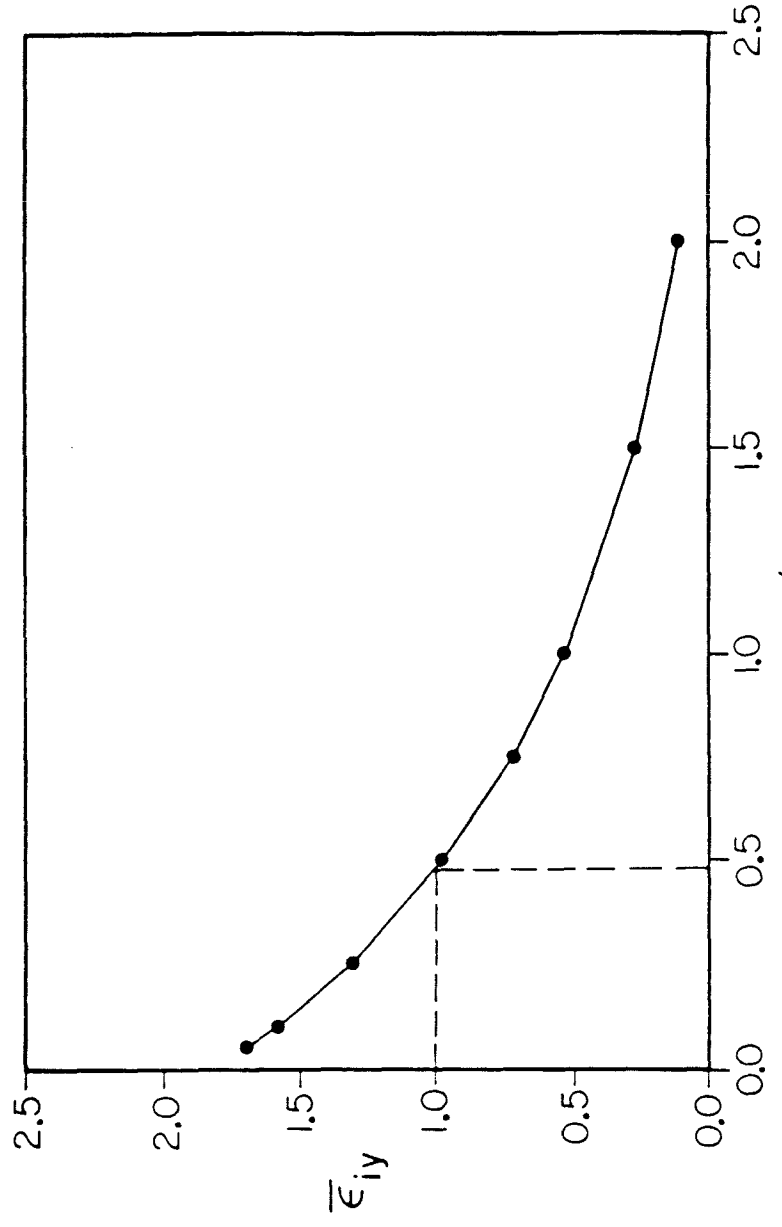

Figure 3.13

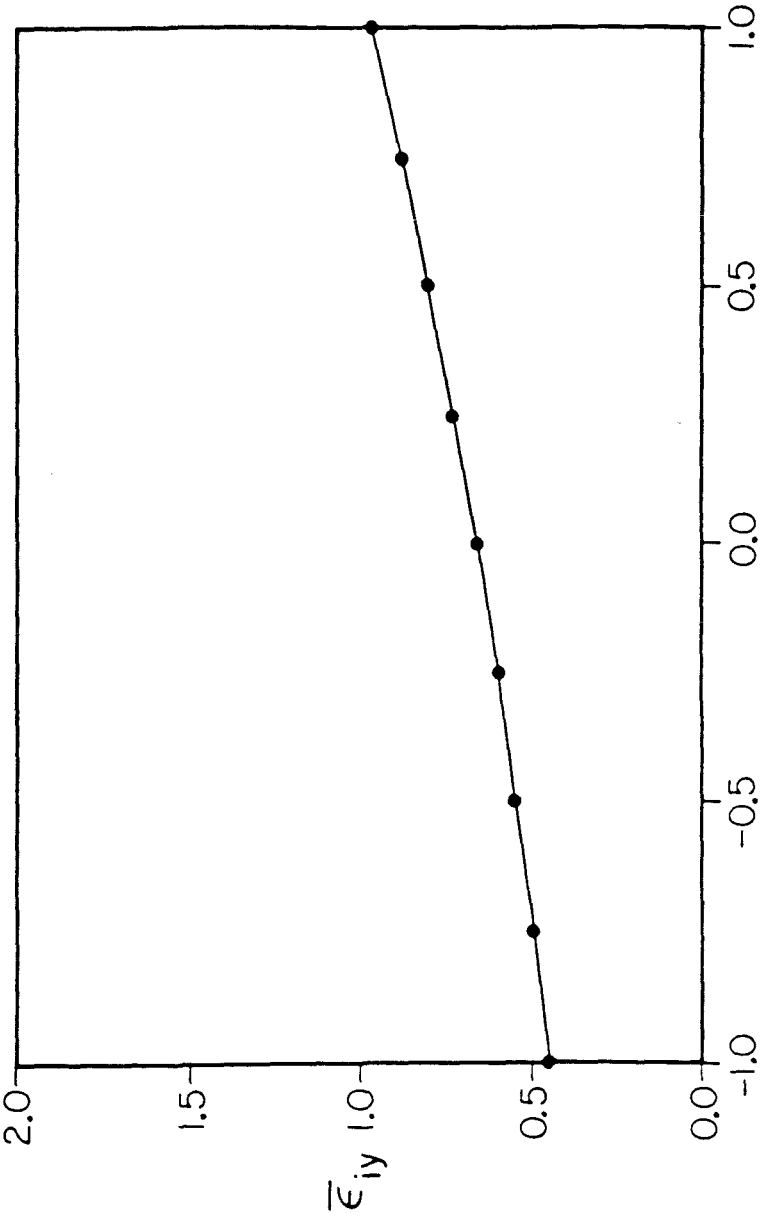

Figure 3.14

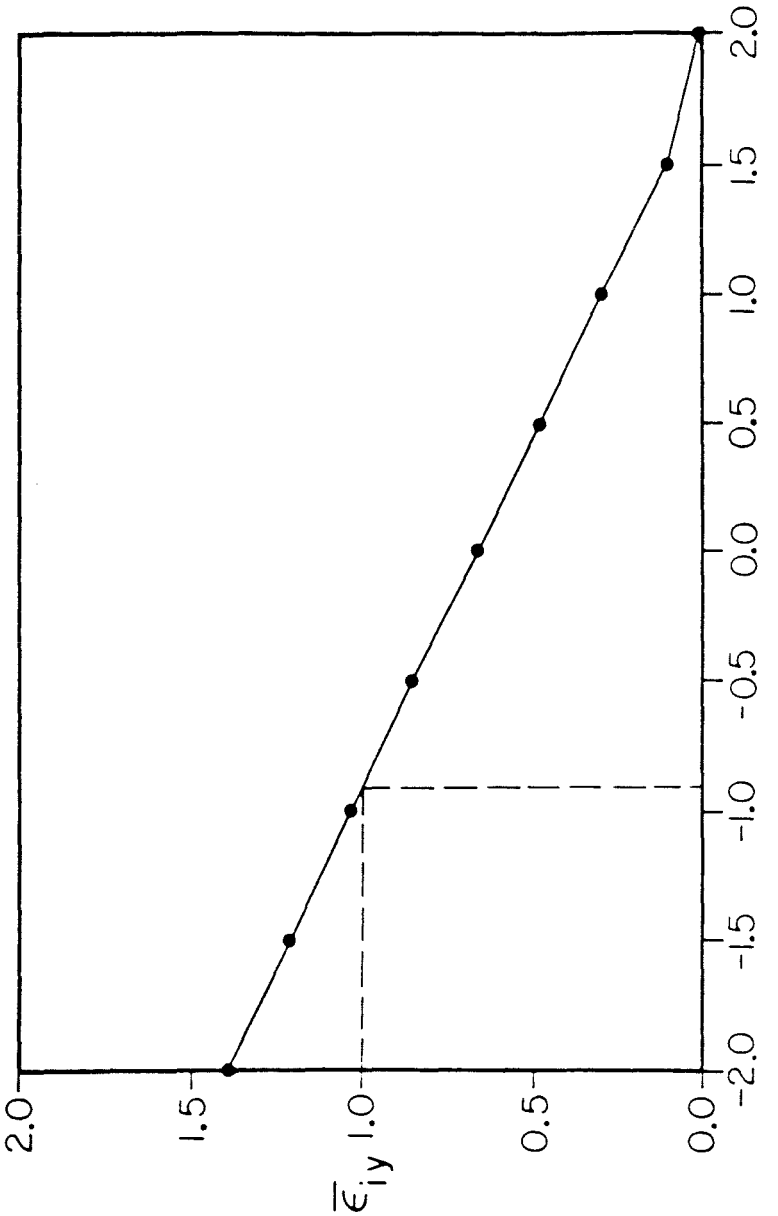
2.0
1.5
1.0
0.5
0.0
$\overline{\epsilon}_{iy}$
-2.0
-1.5
-1.0
-0.5
0.0
0.5
1.0
1.5
2.0
$\frac{\omega_i r_i}{v_i}$

Figure 3.15

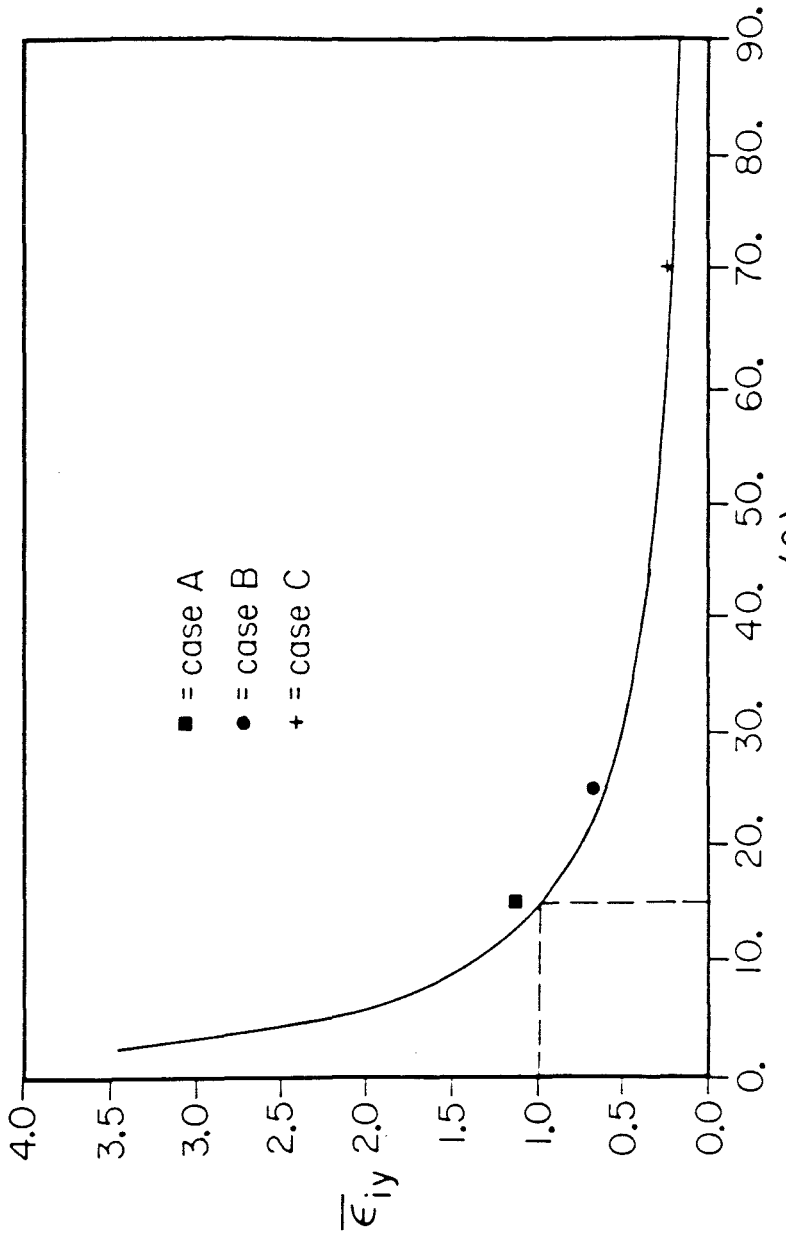
■ = case A
● = case B
+ = case C
$\overline{\epsilon}_{iy}$
α_i (°)
0.0
0.5
1.0
1.5
2.0
2.5
3.0
3.5
4.0
0.
10.
20.
30.
40.
50.
60.
70.
80.
90.

Figure 3.16

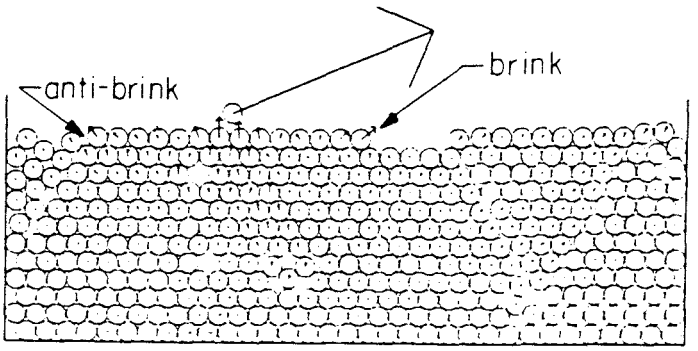

(a)

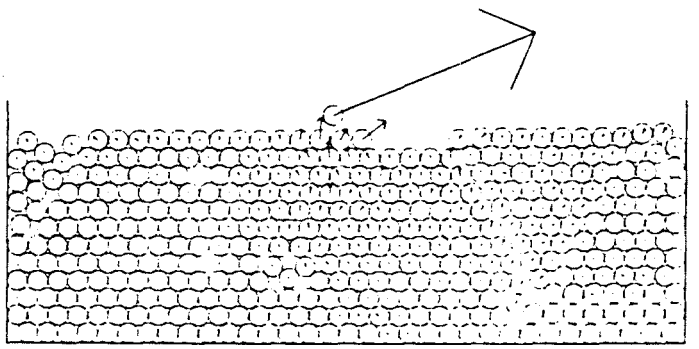

(b)

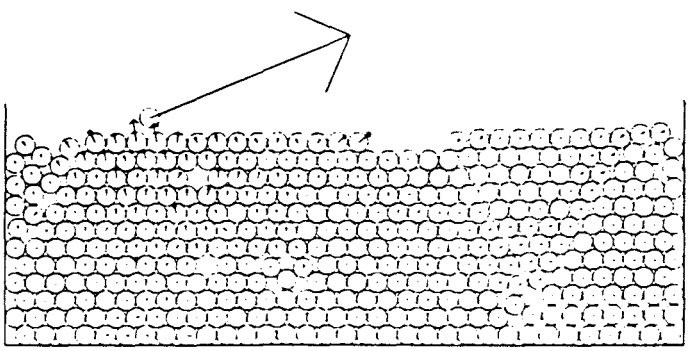

(c)

Figure 3.17

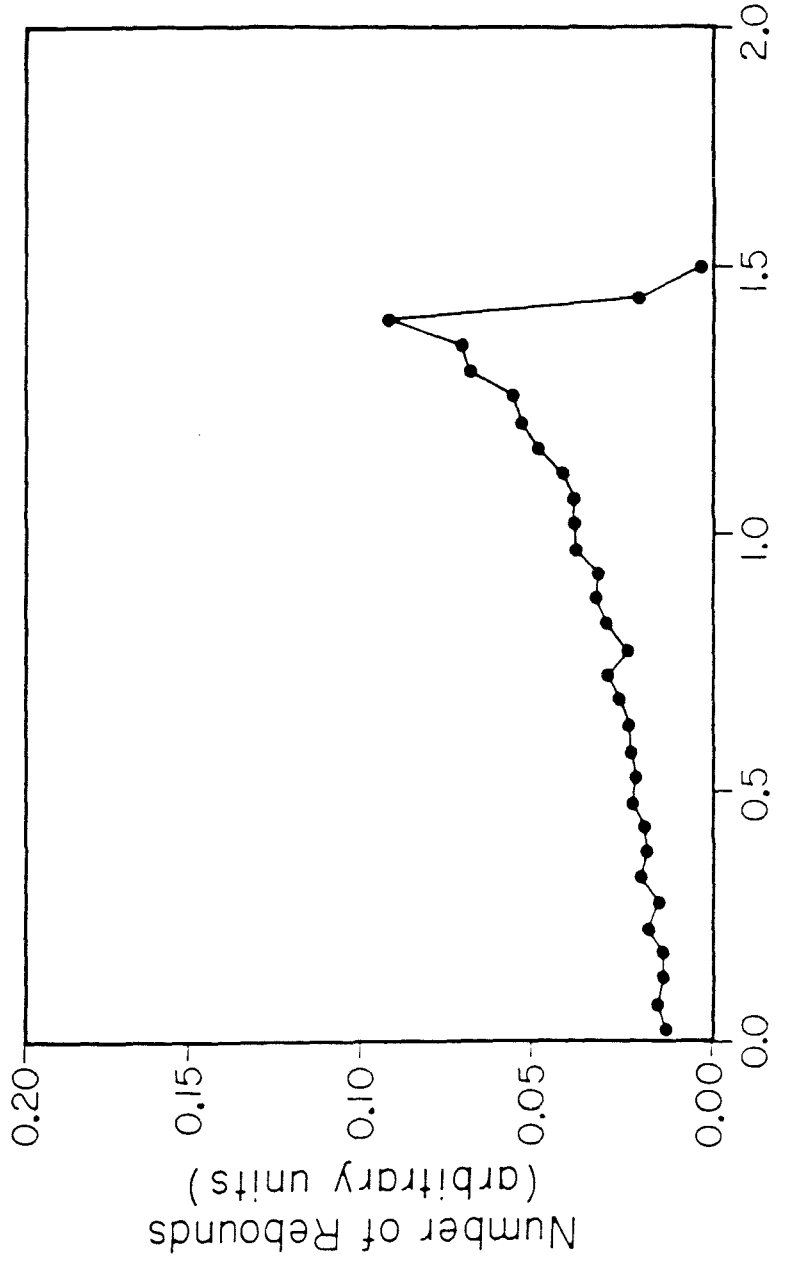
Number of Rebounds
(arbitrary units)
0.20
0.15
0.10
0.05
0.00
0.0
0.5
1.0
1.5
2.0
ϵ_{iy}

Figure 3.18

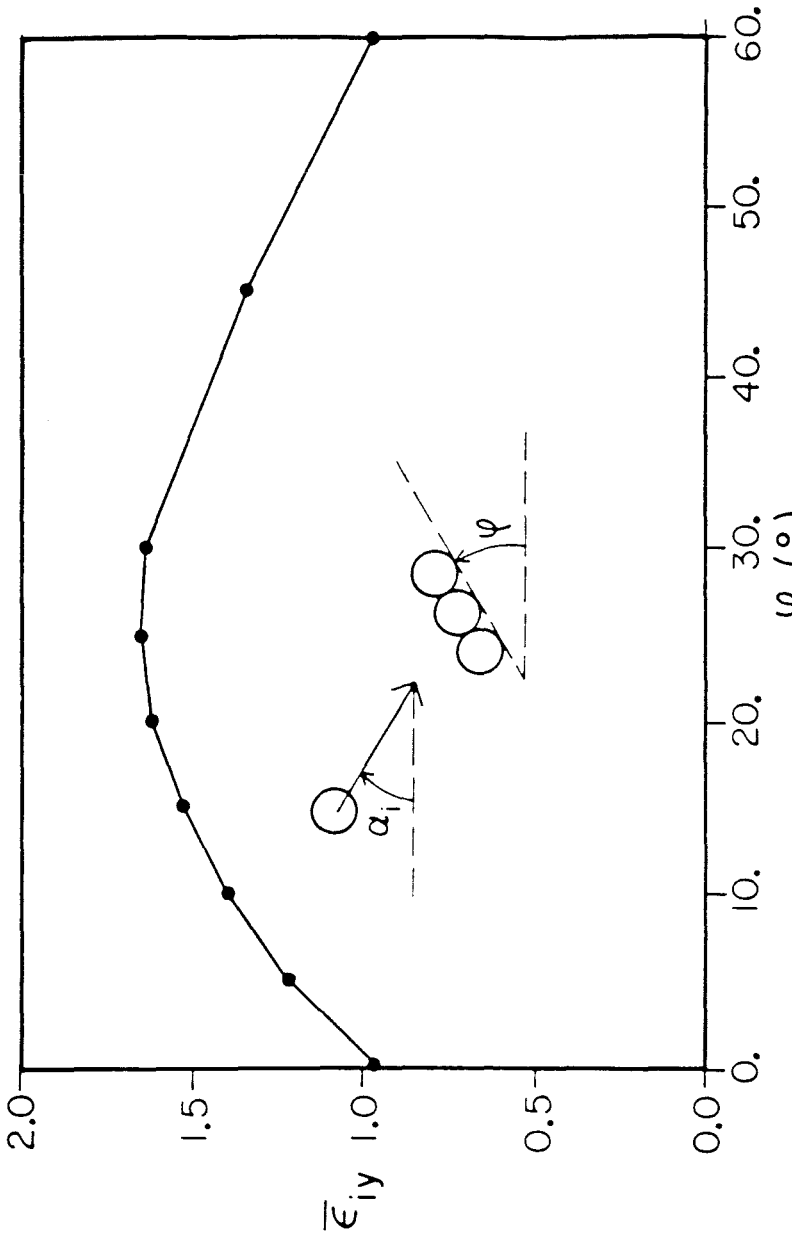

Figure 3.19

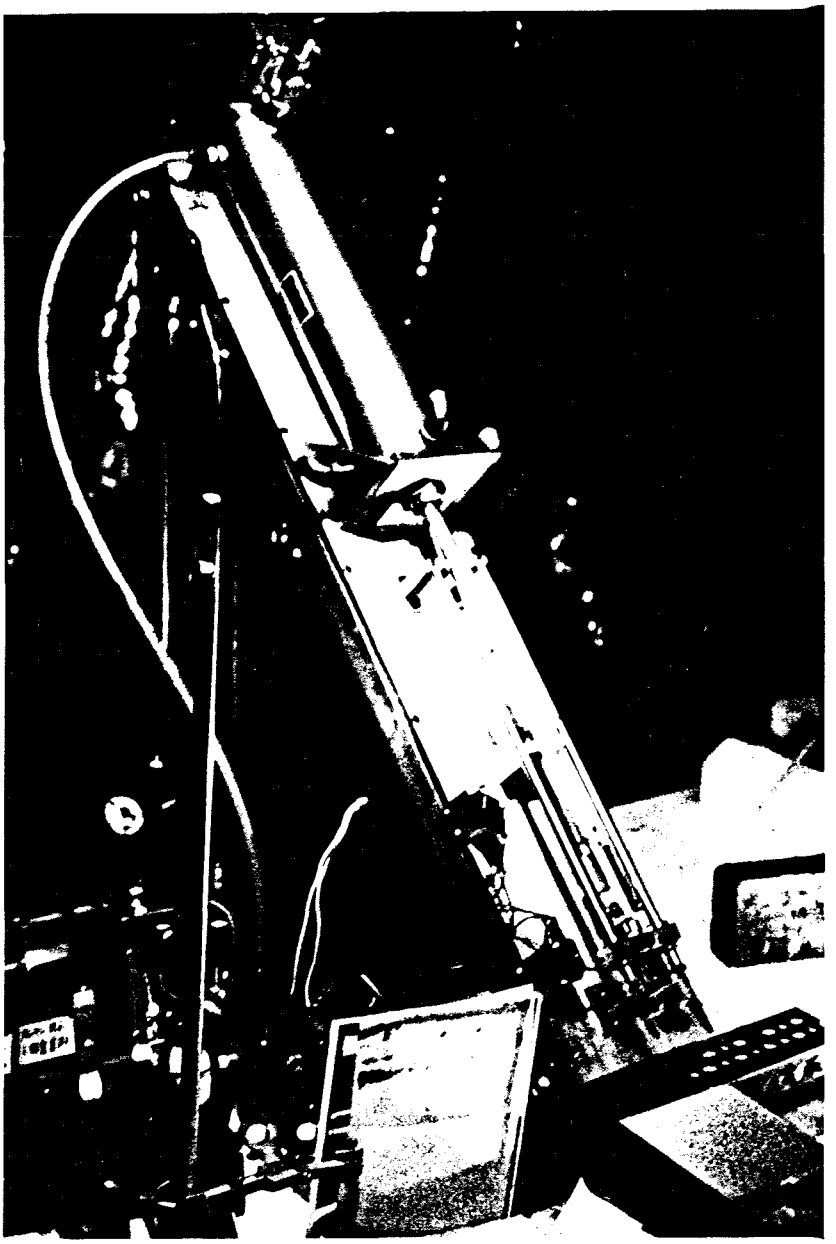

Figure 3.20

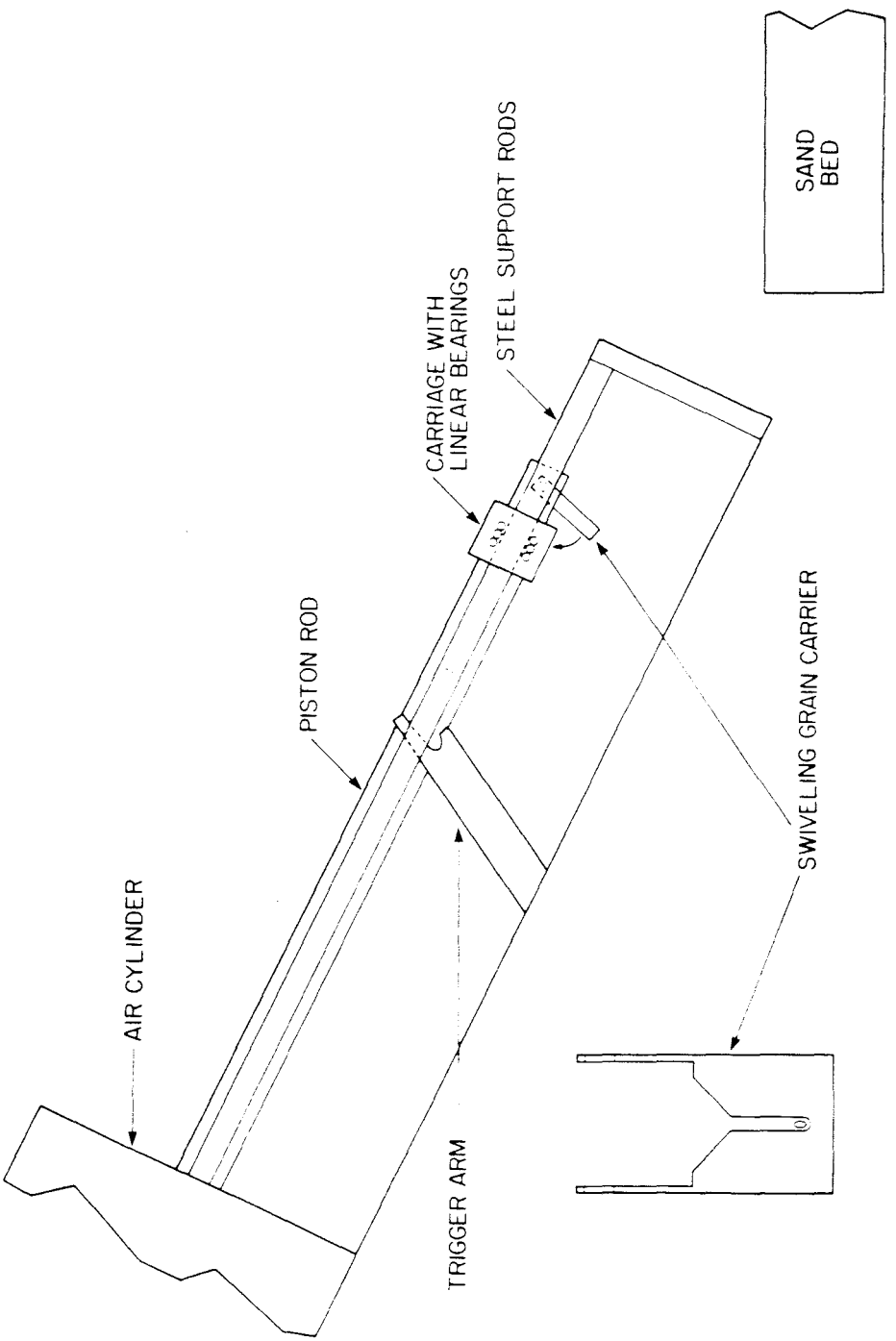
SAND BED
STEEL SUPPORT RODS
CARRIAGE WITH LINEAR BEARINGS
PISTON ROD
AIR CYLINDER
SWIVELLING GRAIN CARRIER
TRIGGER ARM

Figure 3.21

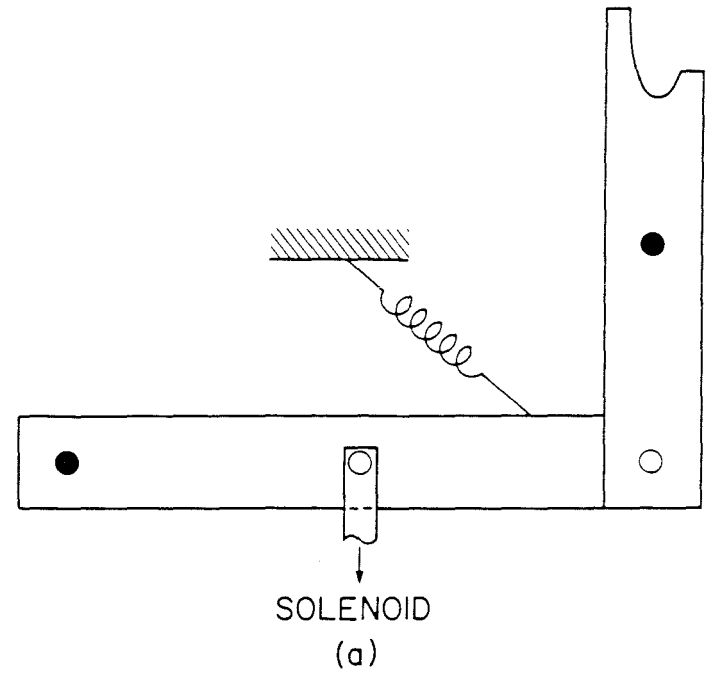

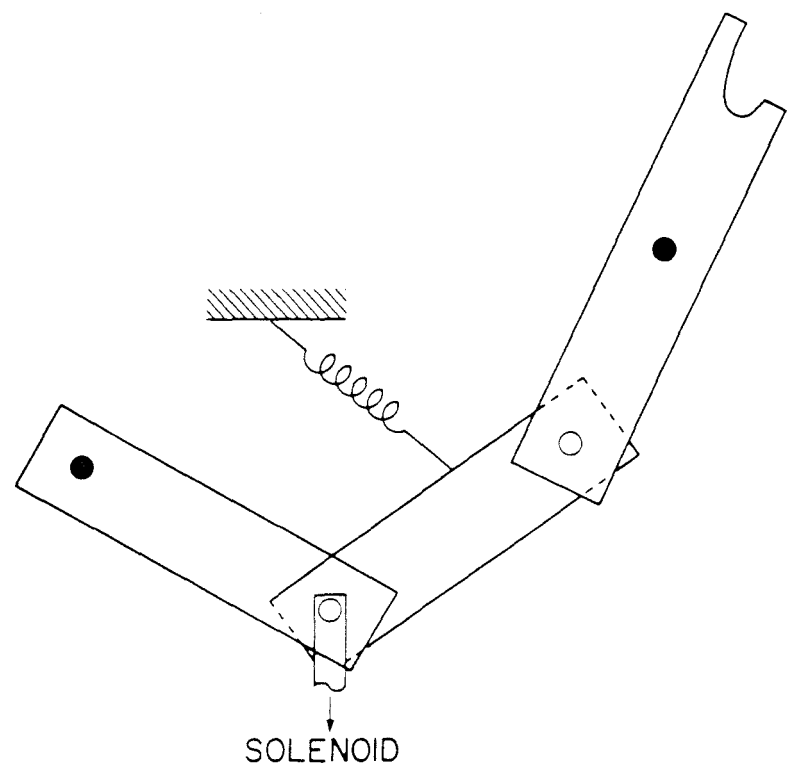

Figure 3.22

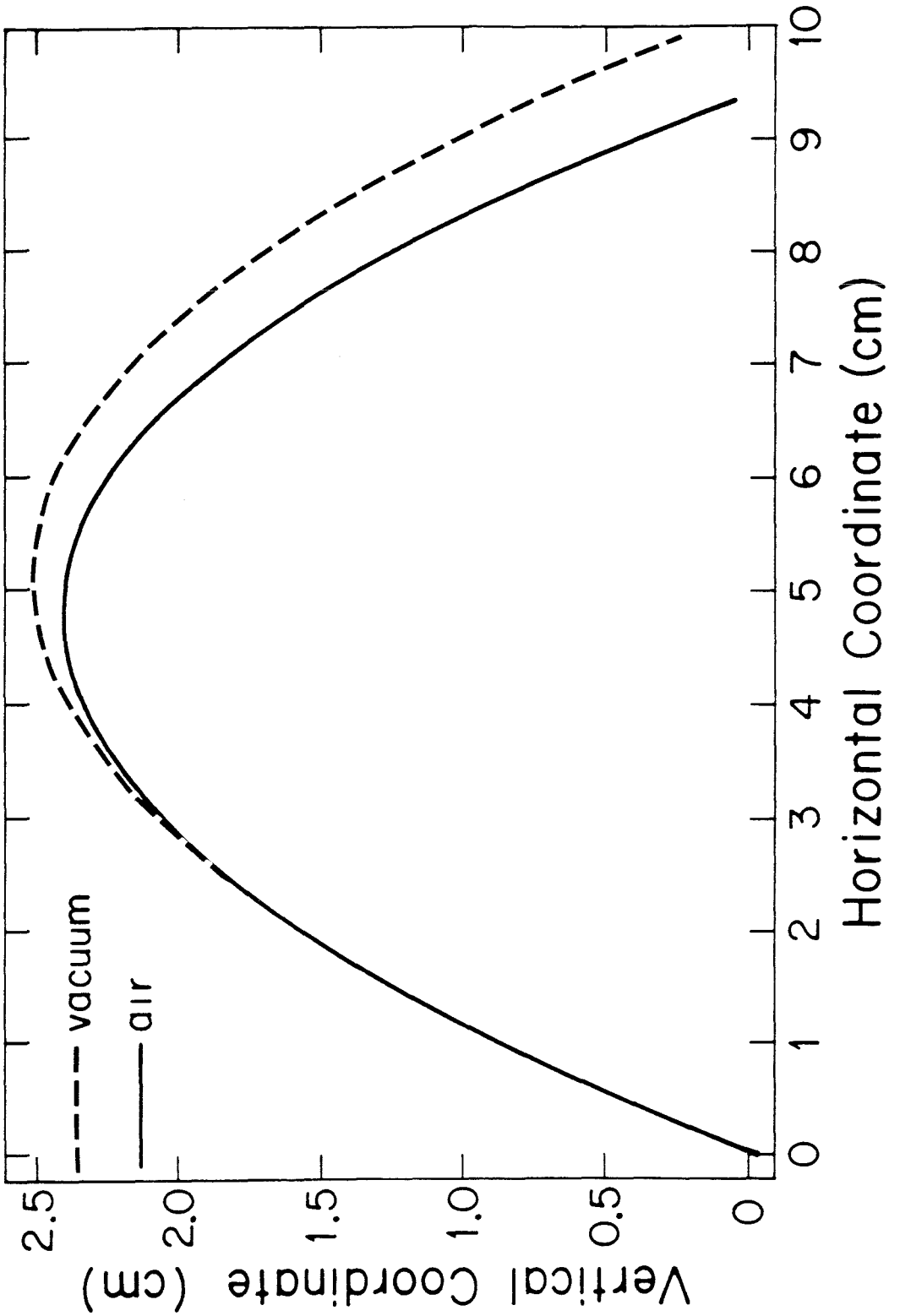
Vertical Coordinate (cm)
Horizontal Coordinate (cm)
vacuum
air
0
0.5
1.0
1.5
2.0
2.5
0
1
2
3
4
5
6
7
8
9
10

Figure 3.23

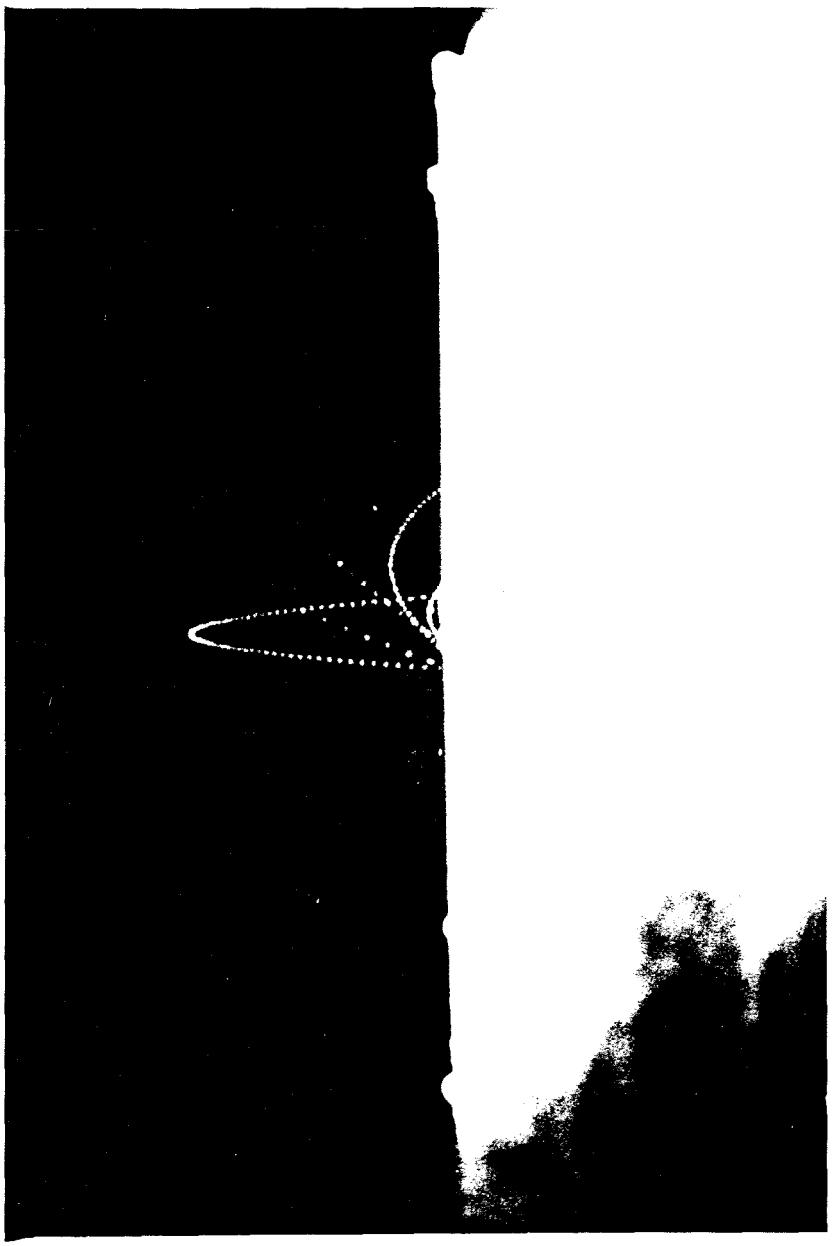

Figure 3.24

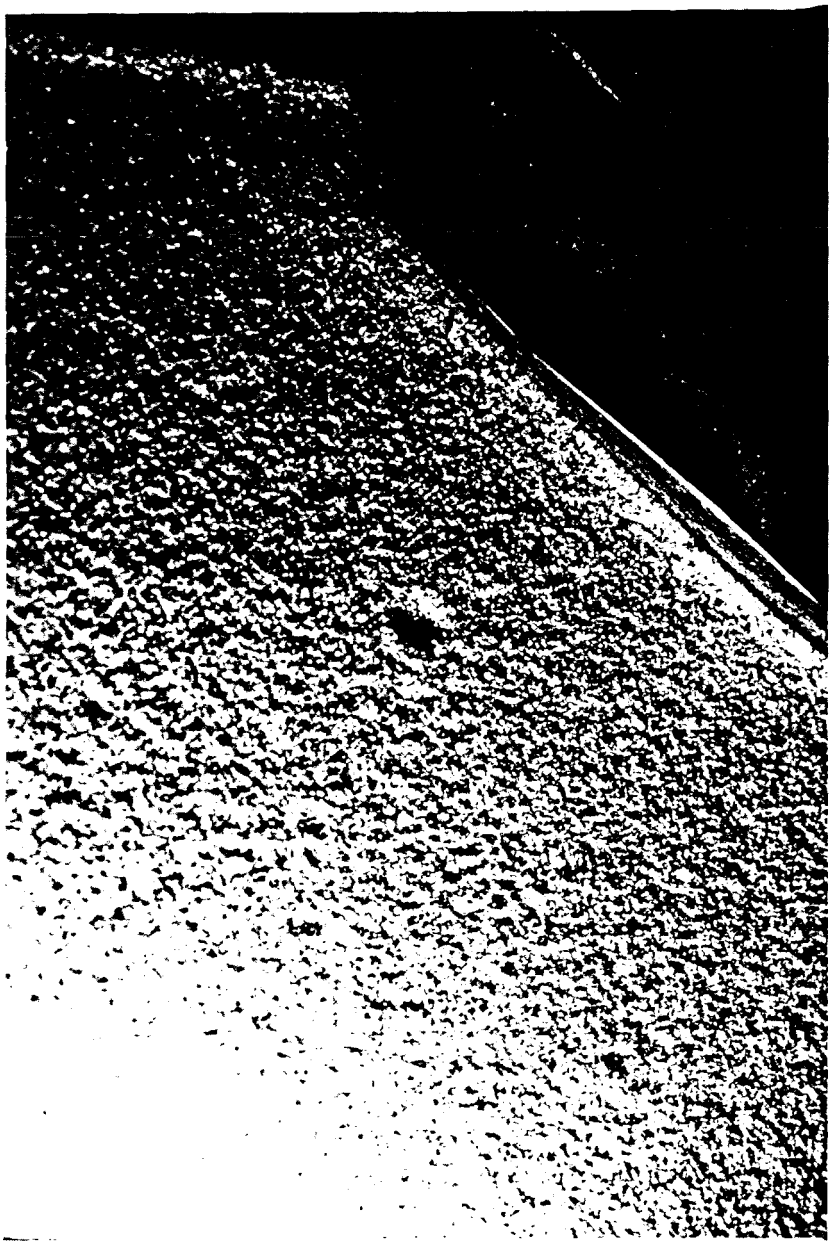

Figure 3.25

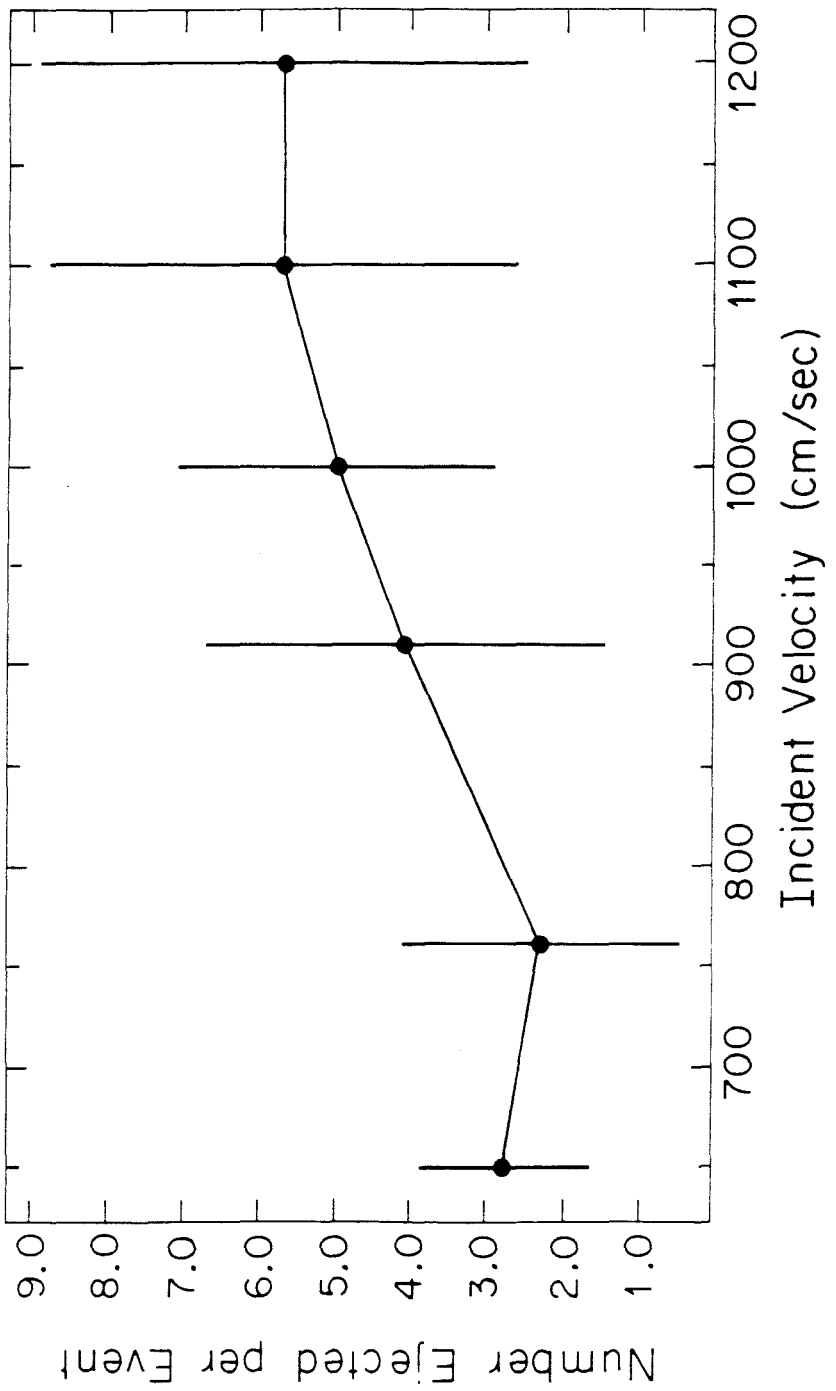
Number Ejected per Event
9.0
8.0
7.0
6.0
5.0
4.0
3.0
2.0
1.0
700
800
900
1000
1100
1200
Incident Velocity (cm/sec)

Figure 3.26

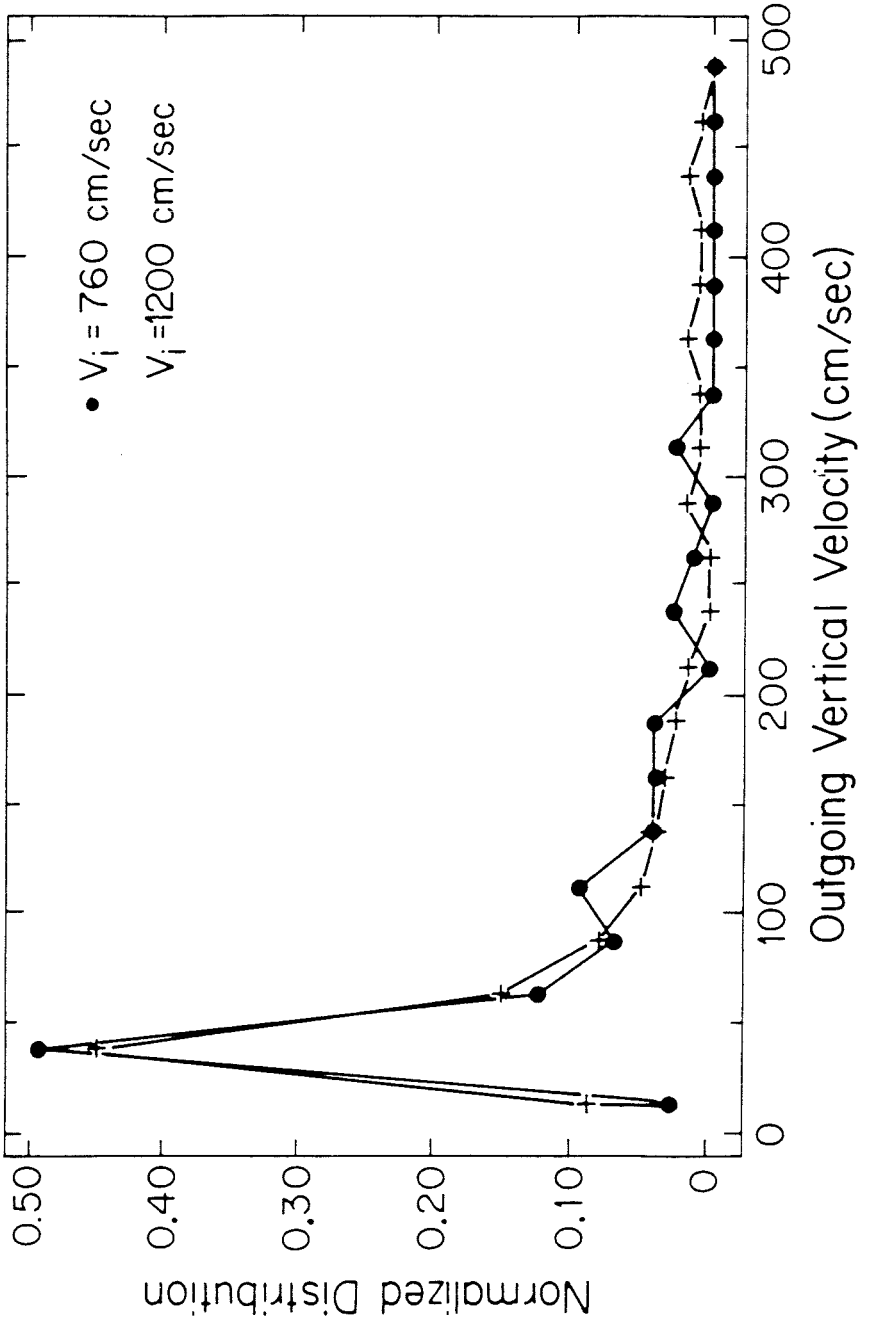
• V_i = 760 cm/sec
V_i =1200 cm/sec
Normalized Distribution
0.50
0.40
0.30
0.20
0.10
0
0
100
200
300
400
500
Outgoing Vertical Velocity (cm/sec)

Figure 3.27

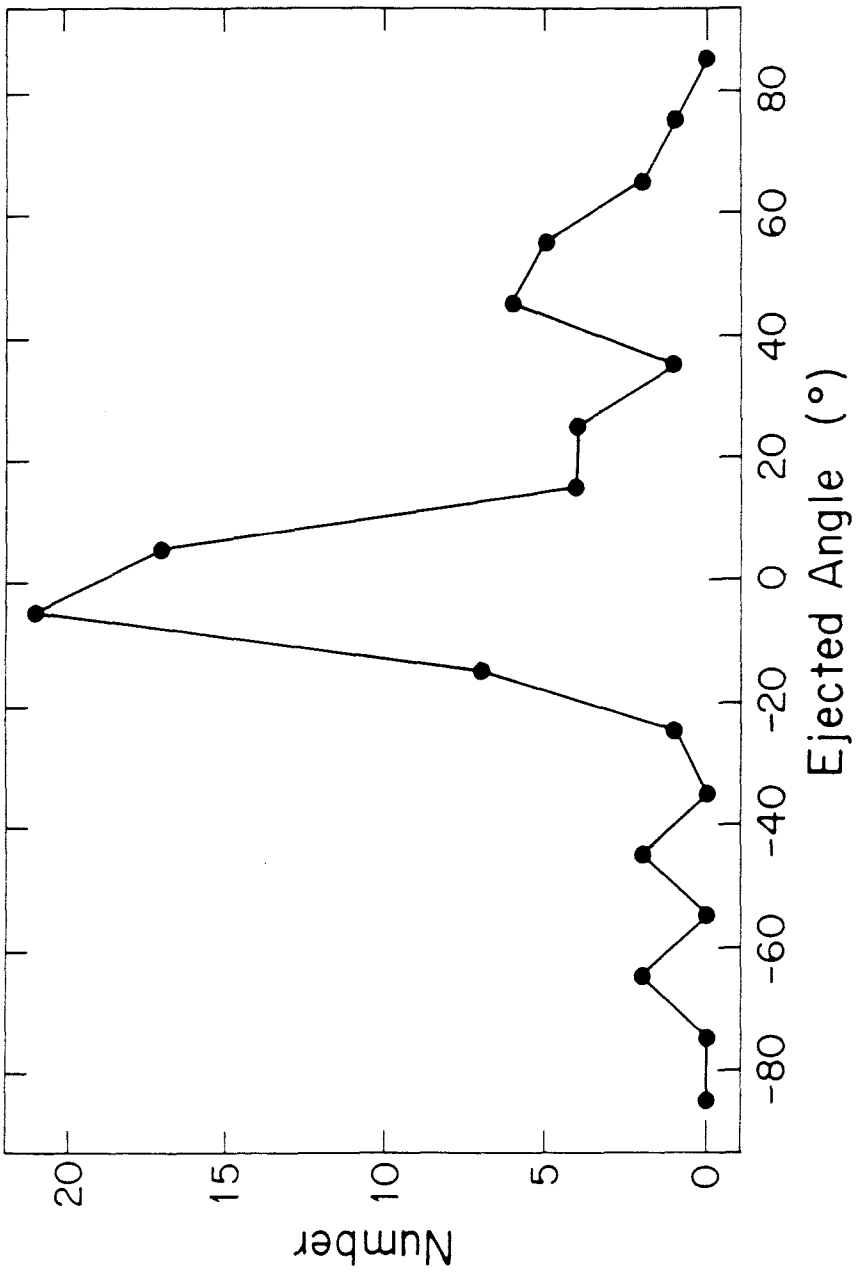

Figure 3.28

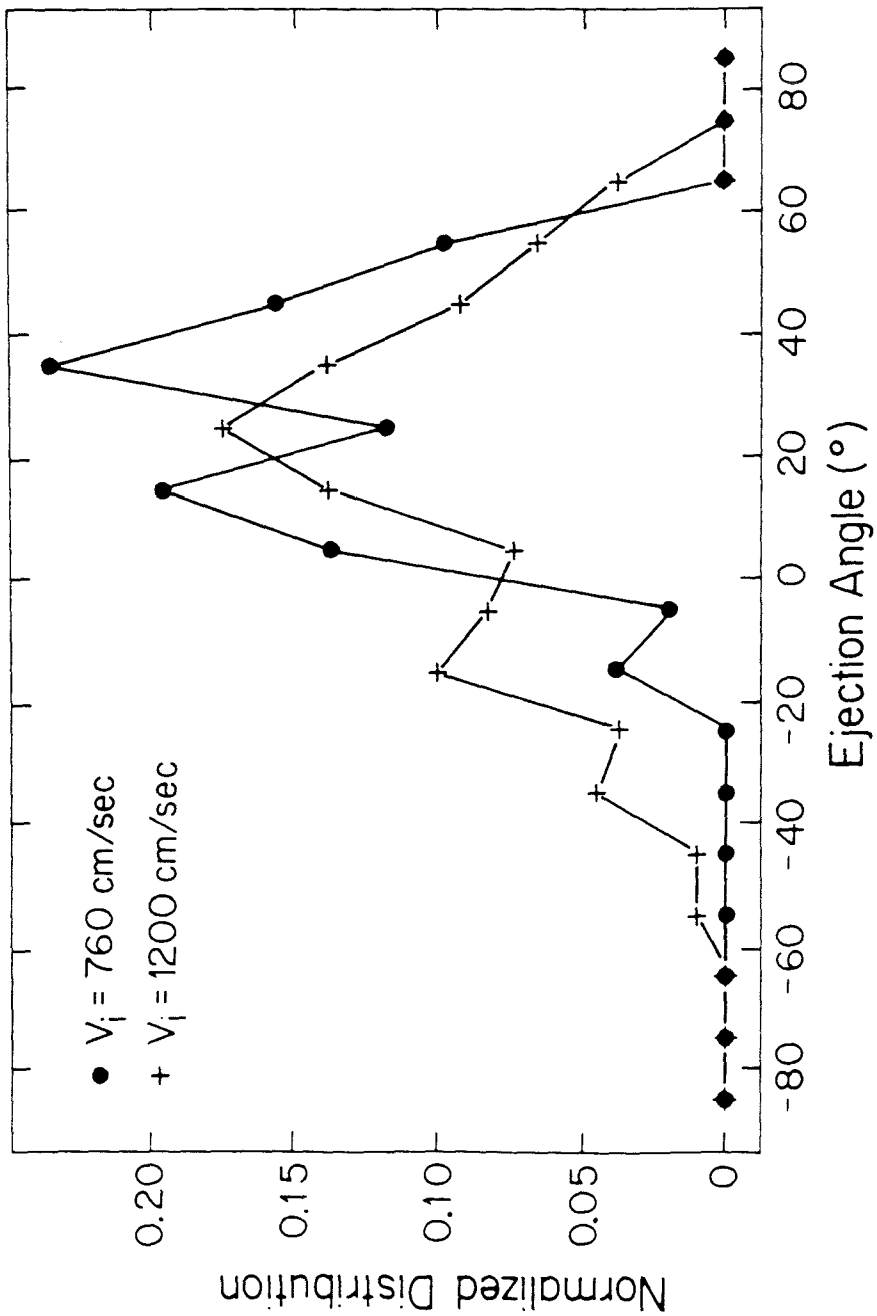
Normalized Distribution
0.20
0.15
0.10
0.05
0
-80
-60
-40
-20
0
20
40
60
80
Ejection Angle (°)
● V_i = 760 cm/sec
+ V_i = 1200 cm/sec

Figure 3.29

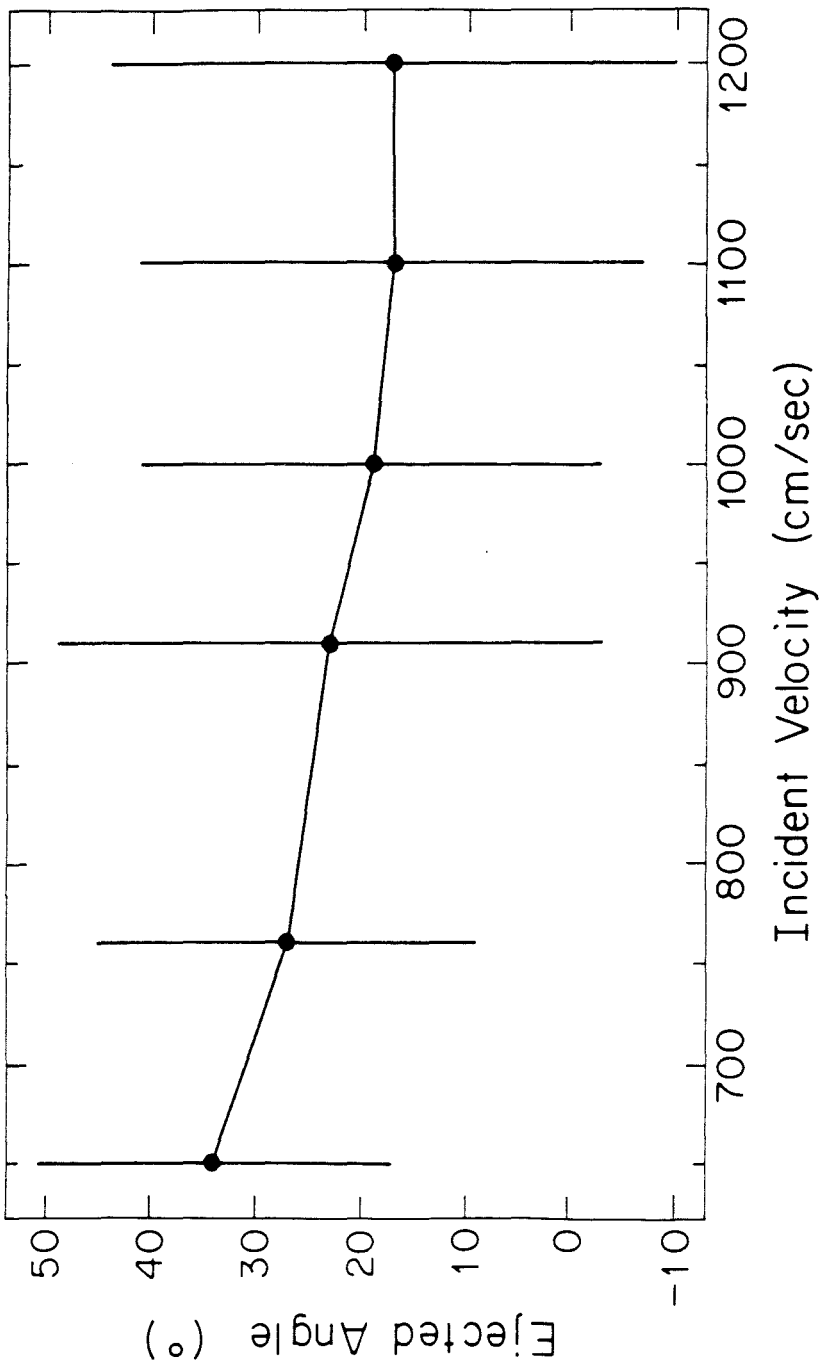
Ejected Angle (°)
50
40
30
20
10
0
-10
700
800
900
1000
1100
1200
Incident Velocity (cm/sec)

Figure 3.30

CHAPTER IV. A MODEL FOR STEADY-STATE EOLIAN SALTATION

> "The shifting sands! Slowly they move, wave upon wave, drift upon drift, but by day and by night they gather, gather, gather. They overwhelm, they bury, they destroy. . . With little or no restraint upon them they are transported hither and yon at the mercy of the wind."
>
> -John C. Van Dyke

Grain-bed impacts constitute one important component of the eolian saltation process. Having learned something about the character of these impacts, as detailed in Chapter III, presently, we would like to combine this knowledge with aerodynamical considerations to produce an algorithm describing sand transport unchanging in time, i.e., steady-state eolian saltation.

Our aim is to construct a model which is both self-consistent and self-contained. Recent attempts at modeling eolian saltation save one (Ungar and Haff, 1986) have relied on empirical data on blowing sand as input for their calculation (e.g., Sorenson, 1985; Anderson and Hallet, 1986). As a natural extension of this work, it is of interest to seek a model of eolian saltation which allows us the ability to predict results of experiments which have not been performed, without reference to data on blowing sand. It might be of particular use for applications involving

conditions difficult to reproduce in the laboratory, such as those found in planetary environments, or the hypervelocity conditions characteristic of sediment transport resulting from a nuclear detonation.

Ungar and Haff (1986) generated a model of saltation capable of making independent predictions. Their primary advance was the inclusion of a boundary condition on the grain population, which states that an average grain leaving the surface, through acceleration by the wind, and impact with the surface, must reproduce itself. They employed a simple relation between incoming and outgoing grains at the bed: the incident particle gives rise to a passel of particles ejected vertically from the bed with identical ejection velocity. The number of ejected particles in their model is proportional to the square of the incident velocity. As we discuss below, this conception of the splash function can be characterized mathematically in terms of a delta-function.

Ungar and Haff's formulation of the grain-bed impact resembles a cratering event, where an incident high-velocity grain leads to the expulsion of a number of lower-energy grains. This ignores the fact that the incident particle usually rebounds with a significant fraction of its incident energy, and the detailed features of the ejection process,

primarily brink particle ejection. It is our intention to extend the formalism of Ungar and Haff to include a more realistic model of the grain-bed impact, with the results of Chapter III as our guide.

In this chapter, we focus on the following three topics: (1) the feedback principles involved in steady-state saltation, (2) a computational algorithm for computing the characteristics of steady-state saltation employing realistic splash functions, and (3) the implications of the predictions of this model for saltation in Nature.

Feedback in Eolian Saltation

It is often a useful exercise to make simplifying assumptions for a complex problem, to elucidate better the physical features of the process. In eolian saltation, the aerodynamical processes constitute a difficult aspect of the problem. As will be seen below, one can reproduce the general dynamical characteristics of saltation without reference to the difficulties attending a fluid-mechanical calculation. In particular, we replace the wind with a more easily analyzed driving force, a conveyer belt, which accelerates and reflects the grains ejected from the sand bed. Within this simplified model, we show how the formalism of Ungar and Haff (1986) leads to a solution of the steady-state problem for two types

of grain-bed interactions: a single impact rule, in which a particle striking the bed produces a number of outgoing grains with a single velocity (similar to the Ungar-Haff splash function), and an impact distribution rule describing collisions with the bed that give rise to a distribution of outgoing velocities. Implicitly, we are assuming that the fine details of the fluid-mechanical behavior of the air are unimportant in determining the general conduct of the system; rather, the overall role that the wind plays in accelerating the grains, something akin to the mean aerodynamical drag on a particle over its trajectory, dominates its influence on the system dynamics.

The conveyer belt is aligned parallel to the bed and is supplied a power per unit area P_T from an external source (see Figure 4.1). Dissipative forces on the belt, which we take to be proportional to the velocity of the belt, v_c, lead to power dissipation $P_F = \zeta(v_c)^2$, with ζ a constant. Gravity and the vertical wind drag are replaced by inelastic collisions with the belt, so that the velocities of the grains remain constant in traveling between the conveyer belt and the bed. Upon impact with the conveyer belt, the grains reflect in the vertical direction with

constant coefficient of restitution ϵ and are accelerated horizontally according to

$$v_{cox} = v_c v_{ciy}/(v_c+v_{ciy})$$
$$v_{coy} = -\epsilon v_{ciy}, \qquad (4.1)$$

where $\vec{v}_{ci}$ and $\vec{v}_{co}$ are the velocities before and after striking the conveyer belt, respectively. Here the positive x direction is parallel to the conveyer belt and in the direction of its motion. The y axis runs from the sand bed to the conveyer belt. The fraction of the conveyer-belt velocity that the particle picks up in the horizontal direction on impact, $v_{ciy}/(v_c+v_{ciy})$, increases with greater impact velocity on the belt; analogously, a sand grain propelled higher into a wind stream will pick up more of the wind's energy, by virtue of having been exposed to higher wind speeds. We make the approximation that the sand grains come off the bed vertically, i.e., $v_{cix} = 0$. This simplifies the algebra and has no bearing on our exposition of the feedback mechanism in saltation. Finally, we assume that the flux of grains striking the conveyer belt is uniform along its length and breadth.

Delta-Function Splash Function

We consider the case of a definite relation between the incoming ($\vec{v}_{bi}$) and the outgoing ($\vec{v}_{bo}$) velocities at the bed:

$$v_{box} = 0$$
$$v_{boy} = (-\epsilon v_{biy} + f v_{bix})/\sqrt{N}, \qquad (4.2)$$

with N the number of particles splashed up per impact. Here, all of the grains emerge from the bed with this same velocity. The coefficient of restitution at the bed is ϵ (identical to that with the belt) and momentum is converted from the horizontal to the vertical direction through the factor f. The motivation for this form of the grain-bed coupling is to approximate the successive saltation model, with the addition of the dependence of the number of grains ejected on the impact velocity accomplished in a simple manner.

In this simple model, the outgoing energy is shared equally among the N grains. A specific form for N must be adopted, with the physical requirement that N increase with increasing impact velocity. We choose $N = (v_{bix})^2/(v_{girl})^2$ (after Ungar and Haff, 1986), where v_{girl} is a constant having the dimensions of velocity and is related to the bed

properties. The dependence of the number of grains ejected per incident grain on the incident velocity, coupled with the limited power available to the conveyer belt, provides feedback to force a stable, calculable particle flux.

We may proceed to a solution for the steady state either through intuition or the Ungar-Haff formalism. We first apply intuition. As previously stated, in steady-state saltation, by definition, each particle must, on the average, reproduce itself on collision with the bed. Since there is a definite relationship between ingoing and outgoing velocities at the bed, and these velocities are coupled directly to v_c, there can be only one impact velocity and thus each incoming grain, being identical to all others, must result in exactly one outgoing grain; hence N = 1. This sets $v_{bix} = v_{girt}$. The remaining particle velocities and the conveyer-belt velocity may be found by applying the conditions of steady state, i.e., $\vec{v}_{ci} = \vec{v}_{bo}$ and $\vec{v}_{co} = \vec{v}_{bi}$, as shown in Figure 4.1, leading to the results

$$v_{bix} = v_{girl} \qquad v_{biy} = -\epsilon f v_{girl}/(1-\epsilon^2)$$

$$v_{box} = 0 \qquad v_{boy} = v_{girl} f/(1-\epsilon^2)$$

$$v_c = v_{girl}/\left(1 - (1-\epsilon^2)/f\right). \tag{4.3}$$

Notice that v_c and the particle velocities are independent of the power supplied. They depend only on the impact law at the bed through the constants v_{girl}, f and ϵ.

We next calculate the mass flux (mass per unit area) of grains F hitting the conveyer belt. The force per unit area on the conveyer belt due to its effort in accelerating impacting sand grains is $F \cdot (v_{cox} - v_{cix}) = F\, v_{cox}$, and the power dissipated per unit area, P_g, will be this times v_c:

$$P_g = F \cdot (v_c)^2 \left(1 - (1-\epsilon^2)/f\right). \tag{4.4}$$

By setting $P_T = P_g + P_F$, we arrive at the relation between the power supplied per unit area and the flux:

$$F = \left(P_T/(v_c)^2 - \zeta\right)/\left(1 - (1-\epsilon^2)/f\right). \tag{4.5}$$

The formal approach to finding the steady state involves the solution of the integral equation (Ungar and Haff, 1986):

$$F(v_{boy}) = \int S(v_{boy}, \vec{v}_{bi})\, B(v'_{boy}, \vec{v}_{bi}; v_c) F(v'_{boy})\, dv'_{boy}\, dv_{bix}\, dv_{biy} \quad (4.6)$$

with $S(v_{boy}, \vec{v}_{bi}(v'_{boy}, v_c))$ the number density of particles ejected with vertical velocity v_{boy} from an impact by a particle with vector velocity $\vec{v}_{bi}(v'_{boy}, v_c)$, v'_{boy} the previous ejected velocity of the impacting particle, and $B(v'_{boy}, \vec{v}_{bi}; v_c)$ the function which determines how the conveyer belt affects the particle velocities, i.e., the function B takes an ejected particle moving at velocity v'_{boy} and turns it into a particle impacting at velocity $\vec{v}_{bi}$. $F(v_{boy})$ now represents the velocity distribution of the particles coming off the bed. The limits on this integral in v'_{boy} are 0 to ∞, the limits on v_{bix} are $-\infty$ to ∞, and those on v_{biy} are $-\infty$ to 0. Definite integration over the full physical range of the variables will be assumed for all subsequent integrals in this section, unless otherwise indicated. In words, equation 4.6 states that, in steady-state saltation, a representative sample of ejected particles must, after acceleration by the conveyer belt and subsequent impact on

the bed, exactly reproduce itself. Although it might appear that we are engaged in an exercise in the manipulation of mathematical gobbledegook, the wisdom of applying this method to this modest case, which can be solved by other means, will be apparent when this formalism is required for the more general problem.

Within this model, we can express the functions S and B as follows:

$$S(v'_{boy},\vec{v}_{bi}) = \boldsymbol{\delta}(v_{boy} - f v_{bix} + \epsilon v_{biy})\cdot(v_{bix})^2/(v_{girl})^2$$

$$B(\vec{v}_{bi},v'_{boy};v_c) = \boldsymbol{\delta}(\, v_{bix} - (v'_{boy}v_c/(v'_{boy}+v_c))\,)\cdot\boldsymbol{\delta}(v_{biy} + \epsilon v'_{boy}). \quad (4.7)$$

Note that the symbol for the delta-function will be printed in bold type, to distinguish it from the constant δ to be introduced below. Integrating over v_{bix} and v_{biy} we can replace the components of $\vec{v}_{bi}$ by the values given in the delta-functions appearing in the expression for B and arrive at a more compact form for the splash function which incorporates the role of the conveyer belt. This new function we call $T(v'_{boy},v_{boy};v_c)$, with

$$T(v'_{boy},v_{boy};v_c) = \boldsymbol{\delta}(v_{boy} - f v'_{boy}v_c/(v'_{boy}+v_c) - \epsilon^2 v'_{boy})\cdot (v'_{boy}v_c)^2/(\, v_{girl}(v'_{boy}+v_c)\,)^2 \quad (4.8)$$

The integral over v'_{boy} gives the result:

$$F(v_{boy}) = F(v^*)\cdot(v_c v^*)^2/(\, v_{girl}(v_c+v^*)\,)^2 \qquad (4.9)$$

with v^* the solution of the equation

$$(v^*)^2 + v^*(\, v_c(1+(f/\epsilon^2)) - v_{boy}\,) - (v_c v_{boy}/\epsilon^2) = 0. \qquad (4.10)$$

This implies that $v^* = v_{boy}$ and leads to the identical results as for the intuitive approach, with

$$F(v_{boy}) = \delta(v_{boy} - (f v_{girl}/(1-\epsilon^2))\,)\cdot(P_T/(v_c)^2 - \zeta)/(1 - (1-\epsilon^2)/f), \qquad (4.11)$$

for $P_T > \zeta(v_c)^2$; otherwise, $F(v_{boy}) = 0$.

Two characteristics of the solution are important. First, the conveyer-belt velocity and the grain velocities are controlled completely by the nature of the grain-bed and grain-belt interactions, and are independent of the power applied. This is a consequence of the imposition of the steady-state requirement. Second, the flux of grains scales with the power supplied, and is zero below that power required to turn the conveyer belt at the necessary speed to sustain steady-state saltation. In other words, there is a threshold power required to maintain saltation. If the belt cannot turn at a sufficient velocity to

accelerate the grains to the velocity needed to reproduce themselves, the saltation flux must be zero. Despite the simplifying assumptions necessary for the above solution, it does have the advantage that it is analytically calculable.

Velocity Distribution Sand-bed Ejection Law

Real grain-bed impacts lead to grains coming off the surface with a distribution of velocities. In Chapter III, we saw that a particle impacting a bed of grains gives rise to a single rebounding grain with velocity given by a probability distribution peaked around a function of the incident velocity. The impacting grain also sires a number of ejected grains at smaller velocities distributed as an inverse function of velocity. An occasional impacting particle may not rebound with sufficient velocity to continue in saltation, but, on the other hand, one of the ancillary particles ejected from the surface may work its way into the saltating population. When the gains balance the losses, saltation has achieved steady state.

To investigate this more general process, we have replaced the delta-function in the function S of the Ungar-Haff integral equation equation by a distribution of outgoing velocities from the bed:

$$S(v_{boy},\vec{v}_{bi}) = \alpha\cdot\left(v_{bix}/(v_{bix}+\epsilon)\right) e^{-\left((v_{boy}-f v_{bix}+\epsilon v_{biy})^2/\beta\right)} + \gamma\cdot(v_{bix})^2\cdot e^{-(v_{boy}/\delta)}, \qquad (4.12)$$

where α, β, γ, δ and ϵ are parameters. This form of the number density impact function (the splash function) is pictured in Figure 4.2 for one choice of the parameter set and a particular incident velocity. It contains a gaussian peak centered around the outgoing velocity used in the last section and a dying exponential distribution at lower velocity. This splash function has the essential features of that found in experiments and simulations (Chapter III), including the probable incident particle rebound and the generally lower velocity particles ejected from the bed, whose velocity distribution is monotonically decreasing.

The effect of the conveyer belt on the grains, expressed by the function $B(\vec{v}_{bi},v_{boy}',v_c)$, is identical to that of the last section. We may therefore rename S as T, a function of the velocity at which the impacting particle had been ejected from the surface, v_{boy}', since B is composed only of delta-functions:

$$T(v_{boy}, v'_{boy}; v_c) = \alpha \cdot (v'_{boy} v_c / (v'_{boy} v_c + \epsilon(v'_{boy} + v_c))) \cdot$$

$$e^{-(((v_{boy} - f v_c v'_{boy})/(v_c + v'_{boy}) - \epsilon^2 v'_{boy})^2/\beta)}$$

$$+ \gamma \cdot (v_c v'_{boy}/(v_c + v'_{boy}))^2 \cdot e^{-(v_{boy}/\delta)}. \qquad (4.13)$$

We solve the problem by discretizing it in the M-dimensional space of ejected grain velocities $\{v_{boy}\}$ (Rumpel, 1985). $F(v_{boy})$, the differential mass flux of particles leaving the surface at velocity v_{boy}, then becomes an M-component vector and $T(v_{boy}, v'_{boy}; v_c)$ becomes an M×M matrix. The steady-state condition may be expressed as

$$\vec{F} = [T\{v_c(\vec{F})\}]\vec{F}. \qquad (4.14)$$

The requirement that constant power P_T is supplied to the belt is stated as follows,

$$P_T = v_c \sum_{i=1}^{M} (F_i \mu_i / (\mu_i + v_c)) - \zeta (v_c)^2, \qquad (4.15)$$

where $\vec{\mu}$ is the vector with components $\mu_1, \mu_2, \mu_3, \ldots, \mu_M$, the equally spaced velocities corresponding to the M outgoing flux components of $\vec{F}$.

The matrix element $[T\{v_c(\vec{F})\}]_{ij}$ is the number of particles splashed up with outgoing velocity μ_i per incident grain which resulted from a particle which had been ejected from the sand surface with velocity μ_j and accelerated by the conveyer belt. Note that this matrix represents a convolution of the splash (S) and conveyer-belt (B) functions. The elements composing the jth column of [T] constitute the velocity distribution of particles coming off the bed due to an impacting grain with velocity $v_c\mu_j/(v_c+\mu_j)$ and their sum is the number of particles splashed up due to that grain.

Nature herself supplies a physical method for the solution of this mathematical problem. When saltation is initiated on a sand dune, some number of grains are propelled into the wind, experience acceleration until they strike the bed where they spawn additional grains into the flow, at the same time affecting the wind profile near the surface. As the disturbance propagates downstream, we might expect that the grain velocity distribution and the wind profile will change less and less, until a steady state is reached, with the particle velocity distribution at that

point being entirely independent of the initial distribution of the grains entrained in the wind. (Exceptions to this scenario are brought up later.)

Likewise, in solving the conveyer-belt problem, we commence with an initial distribution of outgoing velocities given by the vector $\vec{F}(0)$, determine the conveyer-belt velocity from the power conservation equation, and then apply the matrix $[T\{v_c\}]$, which describes acceleration by the belt and impact with the surface, to produce a new representative sample of particles $\vec{F}(1)$. The process of adjusting v_c and reapplying the T-matrix is repeated

$$\vec{F}(n+1) = [T\{v_c(\vec{F}(n))\}]\vec{F}(n) \qquad (4.16)$$

until the components of the flux vector and v_c approach a constant value. This process is slightly different from that of actual saltation, as the particles are not moved "downstream", i.e., we assume that the flux is independent of postion. This amounts to applying periodic boundary conditions along the length of the conveyer belt. In addition, the high velocity grains are updated at the surface as frequently as the low velocity grains. In real saltation, the time to complete a trajectory corresponding to a particle coming off the surface at low vertical

velocity is less than the time it takes for a grain ejected at high velocity to return to the surface.

A number of observations should be made about this technique for determining the steady state. First, if the T-matrix were constant, repeated application of the matrix to an arbitrary nonzero flux vector would lead to a solution where $\vec{F}$ is the eigenvector with largest eigenvalue (Acton, 1970). In our case, by regulating the conveyer-belt velocity, we adjust the matrix [T] so that its largest "eigenvalue" is one. If the "eigenvalue" was greater than one, the magnitude of the flux vector $\vec{F}$ would grow exponentially with the number of iterations. If the "eigenvalue" was less than one, the magnitude would decay exponentially. The former is prevented by limited availability of power and the latter does not generally occur unless the power to keep the belt going at its steady-state velocity, $\zeta(v_c)^2$, exceeds the power supplied. (The third possibility, oscillation, is discussed below.)

Second, an infinite mass flux would be possible if the flux distribution diverged at zero ejection velocity in such a way as to keep the power supplied by the belt to the grains finite. By discretizing the

problem, we have implicitly imposed an "infrared cutoff" (Bjorken and Drell, 1964), located at the velocity corresponding to the first component of the flux vector. For impact distribution rules which generate low-energy particles, such a cutoff might have been necessary in solving the problem with the integral equation technique. The cutoff exists in natural saltation under the guise of gravity, which provides a natural cutoff vertical velocity, $\sqrt{2gd}$, i.e., a grain must rise to a least its own diameter (d) to actively participate in saltation; otherwise, it remains trapped in a surface "pocket" of typical depth d. Here g is the acceleration of gravity.

Third, although the splash function used in this study does not explicitly conserve energy (except on the average), egregious violations of energy conservation are prevented by the upper cutoff μ_M in the space of outgoing velocities.

We note that the equations describing this model contain no natural dimensional parameters (e.g., no gravity) to constrain the choice of units. Thus, the system of units used is arbitrary, and only relative values of the parameters are important.

For most combinations of the parameters α, β, γ, δ and ϵ in the matrix [T], the rate of convergence of this iterative procedure is rapid, rarely requiring more than twenty to thirty steps. Figure 4.3 shows the total outgoing flux versus mean outgoing velocity as a function of iteration step, n, for the parameters listed as CASE B in Table 4.1. In this example, as for all others in which we used the form of [T] given above, convergence to a single solution independent of initial conditions was achieved.

In terms of the nature of the steady-state solution, the parameter space can be divided into two regions: one where the gaussian term in the splash function dominates (α large) and the other where the low-energy dying exponential term overshadows that of the gaussian term (γ large). An example of the steady-state flux distribution and the corresponding T-matrix for a splash function with only a gaussian peak (CASE A of Table 4.1) are presented in Figures 4.4b and 4.4a, respectively. The elements of the T-matrix are normalized so that the largest element equals 99. The width of the flux distribution in Figure 4.4b is greater than the width, $\sqrt{\beta/2}$, of the gaussian in the T-matrix, since the flux is the weighted sum

of the columns of the T-matrix, whose gaussians peak at different velocities; therefore the peak in the velocity distribution gets smeared out. Figure 4.5 shows the results of a similar calculation in which a small dying exponential term has been added to the gaussian of the previous splash function (CASE B in Table 4.1). The shape of the flux distribution reflects the presence of the gaussian in the splash function. As illustrated in Figure 4.6, if the coefficient of the low-energy dying exponential term (γ) is large enough (CASE C in Table 4.1), the flux becomes monotonically decreasing with velocity. In this instance, even though the peak is still visible in the splash function, it has been overwhelmed in the velocity distribution.

In the last sub-section, the flux was found to vary linearly with the power for the single outgoing velocity problem. This is true for the more general case, as can be seen by examining equation (4.15), where if the power is increased, the overall flux can be scaled up without changing v_c or the shape of the distribution. The flux scaling factor is the same as that for the power if $\zeta(v_c)^2 \ll P_T$.

The Feedback Mechanism

One approach to considering feedback in the conveyer-belt saltation system is to consider the lower velocity ejected particles to be a small perturbation on the successive saltation solution. For this purpose, we return to a treatment of the problem in the continuous state space of ejection velocities. First, we note that should the convolution of the S and B functions be represented as a product of functions depending separately on v_{oy} and v'_{oy} (a separable kernel in the Ungar-Haff integral equation), $a(v_{oy})$ and $b(v'_{oy},v_c)$, then the steady-state solution for the velocity distribution of the flux must have the same functional form as $a(v_{oy})$:

$$F(v_{oy}) = a(v_{oy})\cdot c\{F\}, \tag{4.17}$$

with $c\{F\}$ a functional of F independent of v_{oy}. This separability has a physical basis in that the ejected grain velocity distribution was found to be roughly independent of incident velocity (Chapter III). Thus, if we set α in equation (4.12) for our splash function to zero, leaving only the term exponentially decaying in v_{oy}, $F(v_{oy})$ would decay as v_{oy} increases with

the same decay constant δ. Another example is the delta-function splash function leading to a flux distribution characterized by a delta-function. The point is that the shape of the splash function in outgoing velocity space is to some extent reflected in the shape of the outgoing velocity distribution of the flux. In the case of a gaussian, non-separable splash function, its peaked character shows up in the flux, although it is smeared out, as we found in the results for CASE A, Figure 4.4.

We consider the integral equation with a splash function consisting of the sum of a delta function and a separable, decaying exponential term:

$$F(v_{oy}) = \int dv'_{oy}\delta(v_{oy}-v(v'_{oy},v_c))N(v'_{oy},v_c)F(v'_{oy}) + \int dv'_{oy}e^{-(v_{oy}/\delta)}q(v'_{oy},v_c)F(v'_{oy}), \qquad (4.18)$$

with $v(v'_{oy},v_c)$, $N(v'_{oy},v_c)$ and $q(v'_{oy},v_c)$ arbitrary functions. What we have in mind here is to treat the delta-function as an approximation to a highly-peaked gaussian function. This may be rewritten as

$$F(v_{oy}) = N(v_{oy}^*,v_c)F(v_{oy}^*) + e^{-(v_{oy}/\delta)}\int dv'_{oy}q(v'_{oy},v_c)F(v'_{oy}), \qquad (4.19)$$

with v_{oy}^* the solution to the equation $v(v_{oy}^*,v_c) = v_{oy}$ If, taking the

Neumann approach (e.g., Mathews and Walker, 1970), we suppose that the magnitude of the first term greatly exceeds that of the second, the first order approximation to F, in the neighborhood of $v_{oy} = v_{oy}^*$, is

$$F(v_{oy}) \cong F_0 \delta(v_{oy} - v_{oy}^{**}), \tag{4.20}$$

with v_{oy}^{**} and v_c^* defined by

$$N(v_{oy}^{**}, v_c^*) = 1 \qquad v(v_{oy}^{**}, v_c^*) = v_{oy}^{**}, \tag{4.21}$$

and F_0 given by the power equation. Equation 4.20 embodies the notion that our delta-function represents a narrow gaussian. Putting the approximation of equation 4.21 into the second term of the integral equation 4.19, we find

$$F(v_{oy}) \cong N(v_{oy}^{**}, v_c^*) F_0 \delta(v_{oy} - v_{oy}^{**}) + e^{-(v_{oy}/\delta)} q(v_{oy}^{**}, v_c^*). \tag{4.22}$$

Equation 4.22 may be interpreted in the following manner. The proportion of the saltating flux which does not reflect from the bed, of magnitude $1 - N(v_{oy}^{**}, v_c^*)$, is replaced by the bed particles splashed up on impact. The peak in the saltating flux adjusts itself so that this ejected population can exactly balance the losses. The feedback of low

energy particles into the saltating population therefore plays a role in determining the steady state. This is what occurs in CASE B (Figure 4.5), where the low energy ejecta portion of the flux has very low magnitude. When this part of the splash function becomes larger in magnitude, the Neumann methodology breaks down, and the peaked splash function is not manifest in the velocity distribution of the outgoing flux, as for CASE C (see Figure 4.6).

Time Dependence in the Conveyer-Belt Model

The question of how feedback operates in saltation can be addressed by delving into the time-dependence of the conveyer-belt system; in particular, we examine how the system approaches the steady-state. The conveyer-belt model is of special usefulness in this regard, as the investigation of time-dependence is severely limited by computational power in the aerodynamical saltation problem (see later in this chapter). We limit our discussion of time-dependent phenomena to the single outgoing velocity case.

First we consider the iterative form of the single-velocity conveyer-belt problem as a special case of the iteration of a nonlinear mapping (e.g., Feigenbaum, 1983; Holmes and Moon, 1983):

$$v_{oy}(n+1) = v_{oy}(n)(\epsilon^2 + f v_c(n)/(v_c(n)+v_{oy}(n)))/\sqrt{N(n)}$$
$$F(n+1) = F(n)\cdot N(n)$$
$$N(n) = (v_c(n) v_{oy}(n)/(v_c(n)+v_{oy}(n)))^2/(v_s)^2$$
$$P_T = F(n) v_c(n)(v_c(n) v_{oy}(n)/(v_c(n)+v_{oy}(n))) + \zeta\cdot(v_c(n))^2, \quad (4.23)$$

where $F(n)$ is the value of the outgoing flux at iteration step n, etc. The state variables of the system generally approach the steady-state solution as an oscillating exponential decay, as can be seen in a Taylor expansion of equations 4.23 around the equilibrium point. A typical journey to the equilibrium point of this map is illustrated in Figure 4.7, with the parameters of CASE D of Table 4.2. We note that the approach to the steady state is generally more smooth when considering the velocity distribution splash function of equation 4.12.

More interesting behavior can be induced by considering two variations of the problem. (1) The coefficients ϵ and f are compelled to decrease with increasing impact velocity and (2) ϵ and f are chosen to decrease with increasing flux. The first case has as its physical basis the known dependence of the coefficient of restitution on impact velocity (monotonically decreasing), and the second arises from the notion that with large fluxes the "bed" grains will be in motion and therefore that saltating particles hitting them will retain less of their incoming energy.

These variations have the effect of changing the previously monotonic map into functions which possess extrema, and therefore they open up the possibility of limit-cycle behavior (Feigenbaum, 1983) (see Figure 4.8). The variation from monotonicity in our form of the map is small, and thus oscillatory behavior is difficult to achieve. A statement concerning the non-steady behavior of Nature's saltation resulting from the form of the splash function is beyond the scope of this study. However, our results suggest that such behavior is possible, given a splash function with the appropriate characteristics.

A Feedback Circuit

The conveyer-belt saltation problem contains two sources of feedback, one at the conveyer belt and one at the sand bed. This can be seen by examining the consequences of the absence of each of these two types of feedback. If the conveyer-belt velocity were fixed, the acceleration of the grains would be independent of the flux and would lead to geometrically increasing (or decreasing) fluxes when the conveyer-belt velocity was above (below) its correct steady-state value. Similarly, if the average number of grains splashed up per incident grain were independent of impact velocity, the flux of grains in saltation would

monotonically increase (or decrease) when the number of grains splashed up was greater than (or less than) one.

For the conveyer-belt problem, in the neighborhood of the steady-state solution, we may linearize the system to obtain a simple form of the feedback circuit. The derivative of the state vector of the system, $\vec{z}$, with respect to iteration step n, may be converted to the derivative with respect to time through division by the time for a grain to go from the conveyer belt to the surface and back, $h\cdot(\epsilon+1)/(\epsilon\cdot v_{oy})$, with h the distance between the conveyer belt and the bed. For the single velocity case, we define $\vec{z}$, and its time rate of change $d\vec{z}/dt$, as

$$z_1 = v_{oy} \qquad z_2 = F$$
$$d\vec{z}/dt = [Z]\vec{z}$$
$$Z_{11} = \left((\epsilon^2 + f v_c/(v_c+v_{oy}))/\sqrt{N} - 1 \right)(\epsilon v_{oy})/(h(\epsilon+1))$$
$$Z_{22} = (N-1)(\epsilon v_{oy})/(h(\epsilon+1))$$
$$Z_{12} = Z_{21} = 0. \tag{4.24}$$

The expression for $d\vec{z}/dt$ can then be simplified to the form (Cruz, 1972)

$$d\vec{z}/dt = [A](\vec{z}-\vec{z}^*) + [B](\vec{w}-\vec{w}^*) \tag{4.25}$$

when $\vec{z}$ and $\vec{w}$ are close to the steady-state values $\vec{z}^*$ and $\vec{w}^*$. Here $\vec{w}$ is the control vector with components $w_1 = v_c$ and $w_2 = N$. The

conveyer-belt velocity and the number of particles splashed up per incident particle, when expressed as a function of the state vector $\vec{z}$, provide feedback to allow stabilization of the system. The constant matrices [A] and [B] are (Cruz, 1972)

$$[A]_{ij} = \partial([Z]_{ik}z_k)/\partial z_j \Big|_{\vec{z}^*,\vec{w}^*}$$

$$[B]_{ij} = \partial([Z]_{ik}z_k)/\partial u_j \Big|_{\vec{z}^*,\vec{w}^*}$$

$$A_{11} = -\epsilon f(v_{oy}^*)^2 v_c^*/((\epsilon+1)h(v_c^*+v_{oy}^*)^2)$$

$$A_{12} = A_{21} = A_{22} = 0$$

$$B_{11} = ef(v_{oy}^*)^3/((e+1)h(v_c^*+v_{oy}^*)^2) \quad B_{22} = ev_{oy}^* F^*/((e+1)h)$$

$$B_{12} = -.5\epsilon(v_{oy}^*)^2/((\epsilon+1)h) \quad B_{21} = 0. \tag{4.26}$$

The progress of F towards the solution only depends on the control parameter N ($B_{22} \neq 0$), since F appears linearly in the derivative of the state vector. On the other hand, the expression for dv_{oy}/dt is nonlinear in v_{oy}, leading to a more complex expression describing its journey to the solution.

In Figure 4.9, we present a schematic of the linearized feedback system. The functions [B] and [C] provide the feedback control on the system input throught the parameters P_T and v_{girt}. If we were to

remove the feedback loop ("cut" the lines leading to the function [C]),i.e., invoke the open loop case, the function [A] would not be able to guide the system to the steady state. F would not change, and v_{oy} would either increase or decrease in time without bound, depending on the value of F.

Relation to Saltation in Nature

The replacement of the wind by the more easily described conveyer belt in a model for sand transport results in a system for which calculation is straightforward (and even analytical for a simple splash function), in which the dynamical feedback principles are directly observable, and which reproduces the basic features found in eolian saltation. For instance, the velocity distributions of flux and conveyer-belt velocity for the conveyer-belt model are insensitive to the power supplied above some threshold. The analog of this in nature would be that the wind velocity and the shape of the saltating-particle velocity distributions are independent of the free stream wind velocity. Ungar and Haff (1986) have found that, in their model, wind velocities within the saltating curtain stay constant at a certain height above the surface with increasing wind-shear velocity, and that the particle trajectories remain

roughly the same. Bagnold (1941) and Chepil (1945b) obtained this result experimentally. In addition, we found that a threshold existed for the power supplied to the conveyer belt for sand transport. This corresponds to the impact threshold in eolian saltation (Bagnold, 1941).

The conveyer belt system proceeds to the steady state by a damped oscillation of the system variables. The power supplied to the belt and the nature of the grain-bed impact act through the control variables (the conveyer belt velocity and the number of particles splashed up on impact) to provide closed-loop feedback to guide the system to the steady state. In true saltation, the splash function at the bed and the wind velocity profile will act as control variables. Our system oscillated with certain choices of the splash function; this may have implications for eolian saltation, and for the propriety of a steady-state description. In any case, the conveyer-belt model may be a convenient means of studying evolution of this type of dynamical system in time, which may be prohibitively computationally intensive for the aerodynamical case at present.

Finally, the iterative algorithm for solving the conveyer-belt problem, implemented in the discretized space of outgoing velocities,

will prove useful in our investigation of eolian saltation described in the following section.

Saltation with Wind as a Driving Force

We are now prepared to approach the task on which we have set our sights: the development of a model for transport of sand by the wind. In doing so, we will make a number of assumptions. Specifically, we take the sand transport to be unchanging in time, and to be occurring over a topographically flat surface; the bed roughness is defined by the grain size and ripples are absent. We also suppose that grain-bed impacts are the means of entraining surface grains in saltation during steady-state transport. As previously mentioned, the focus on grain-bed impacts conflicts with the notions of Owen (1964), who employed aerodynamical forces as the impetus for the entrainment of grains. The work presented in this document and elsewhere (Willetts and Rice, 1985; Mitha, et al., 1986) gives clear evidence that grain-bed impacts are capable of propelling bed grains into saltation. We will argue that fluid forces are unlikely to play a role in particle entrainment in steady-state eolian saltation.

The model described here follows the formalism of Ungar and Haff

(1986). Some of the general ideas inherent in the algorithm for finding the characteristics of the steady state were borrowed from Owen (1964). The unique quality of the model is that it does not require *a priori* appeal to data on wind-blown sand transport, and therefore may be independently tested by experiment. We describe the details of the model, its embodiment as a computational algorithm, the results for selected splash functions and wind conditions, and the manner in which the model may impact current views of natural eolian saltation.

Saltation Model

We divide our description of the saltation model into three portions: (a) the grain-bed impact, (b) the trajectories of the sand grains moving according to aerodynamical and gravitational forces, and (c) the solution of the Navier-Stokes equation for the wind.

The Grain-bed Impact

Recall that the number density of particles which emerge from the sand surface with velocity $\vec{v}_o$ due to the impact of a single grain with velocity $\vec{v}_i$ is termed the splash function $S(\vec{v}_o,\vec{v}_i)$ (Ungar and Haff, 1986). Also recall that the general picture emerging from studies of the splash function is that an incoming grain (on the average) rebounds from the

surface with some conversion of horizontal incident momentum to vertical outgoing momentum and transmits some momentum to the bed; the bed then reacts by ejecting a population of low energy grains predominantly in the vertical direction, but biased slightly downstream, as well as ejecting an occasional grain with a somewhat larger fraction of the incident energy, biased more strongly towards the forward direction. For the purposes of simplification, the velocities $\vec{v}_i$ and $\vec{v}_o$ are restricted to lie in the plane defined by the downstream (x) direction and the vertical (y) direction. In order to explore the effect of the splash function's form on saltation, a variety of analytical approximations to this general form are utilized, as well as a splash function derived from our experiment on coarse sand (Chapter III). We describe the detailed nature of these splash functions below.

Aerodynamics

In computing the wind velocity, we must consider the drag force the grains exert upon the wind. The mean wind velocity in the steady state is assumed to point in the $+x$ (downstream) direction, and to depend only on the height above the surface of grains y. Prandtl's mixing length hypothesis is used to effect the closure of the turbulent equation for the

mean wind velocity. The drag of the saltating grains on the wind is taken to be a body force acting in the horizontal direction. The equation for the mean wind velocity as a function of height, $u(y)$, is then (Ungar and Haff, 1986)

$$y^2(du/dy)\cdot(d^2u/dy^2) + y(du/dy)^2 = -0.5k^2 f_x/\rho \qquad (4.27)$$

where k (=2.5) is von Karman's constant, ρ (taken to be 0.00123 g/cm^3) is the density of air, and f_x is the spatially averaged force per unit volume applied to the air by the moving sand grains. The solution of this equation for $f_x = 0$ is the familiar logarithmic wind profile:

$$u(y) = ku^*\ell n(y/\ell), \qquad (4.28)$$

where u^* is a constant, termed the wind-shear velocity, which characterizes the free-stream wind-shear stress, τ (= ρu^{*2}), and ℓ is a constant related to the roughness of the surface. We shall solve the equation for the wind profile as a function of z, with $z = a\cdot\ell n(y/\ell)$ (a is a dimensionless constant). The equation for u as a function of z is then

$$(du/dz)\cdot(d^2u/dz^2) = -0.5 f_x \ell k^2 e^{(z/a)}/(\rho a^3). \qquad (4.29)$$

The advantage of these aerodynamical assumptions is that they correctly reproduce the logarithmic profile when the flux of saltating

grains is zero. Although the theoretical basis for the mixing length model has been shown to be unsound for systems with more than one length (or velocity) scale (Tennekes and Lumley, 1972), Prandtl's model has had empirical success with a single length (or velocity) scale, and has been used, either explicitly or implicitly, in most theoretical work on saltation (e.g., Bagnold, 1941; Chepil and Woodruff, 1963; Anderson and Hallet, 1986). In contrast to our assumptions, Owen (1964) introduced the idea that the turbulent length scale in the saltating layer was determined by the height of the saltating layer. While this assumption might be tenable in a flow with a very high concentration of grains, it is unlikely to be dominant at low or moderate wind speeds, where if the flux of grains is low, the problem must reduce to the case where no grains are moving. In any case, the saltation model presented here can be easily modified to accommodate any definite aerodynamical algorithm, should a sufficiently compelling alternative become available, with computation time being the primary issue. The engagement of difficulties in solving the fluid mechanical equations is not unique to students of saltation.

There are three physically appropriate choices for the two boundary conditions which must be applied to the wind velocity. One may

chooseamong specifying the wind velocity at a height above the saltating layer, the wind-shear velocity above the saltating layer and the wind velocity at or near the sand bed. The application of the first two conditions requires the utilization of empirical data on blowing sand (as in the models of Sorenson (1985) and Anderson and Hallet (1986)), since no fundamental relation between the wind speed and its derivative exists. Therefore, if we are to avoid a dependence on such data, it is necessary to set the wind velocity in the vicinity of the bed. This entails two difficulties. First, the mixing length model breaks down close to the bed, where one encounters small Reynolds numbers and viscosity begins to play a role (e.g., Schlichting, 1979; Tritton, 1977). The traditional setting of the wind velocity to zero at some fraction of the bed particle diameter is an empirical device to avoid a theoretical consideration of this difficulty, which for sediment-free problems may be a perfectly acceptable course of action. In addition, during saltation, the region close to the bed is likely to be heavily laden with sand grains, and in the absence of a detailed treatment, which is beyond the scope of this monograph, we are compelled to adopt the same strategy of fixing the height at which the wind velocity drops to zero. Thus, we specify that

the wind velocity vanishes at one-thirtieth of the bed grain diameter, in accordancewith empirical extrapolations: $\ell = r/15$ (Schlichting, 1979).

The second problem encountered in applying the boundary condition at the bed is that the surface itself might be difficult to define if the density of reptating grains is high. Our boundary condition on the wind should be valid at low saltation fluxes. Its validity beyond that will have to be determined by experiment. The results presented here were obtained by specifying the wind-shear velocity above the saltating layer, u^*. (Specifying the wind velocity at a particular height above the saltating layer is equally valid, and simple to accomplish in our model.)

Sand Grain Trajectories

The trajectories of the sand grains are determined by integrating their equations of motion under gravitational and wind-drag forces from an initial velocity $\vec{v}_0$ at the surface. This yields the impact velocities of the grains, $\vec{v}_i$, which are necessary for evaluating the splash function, and the force per unit volume on the wind as a function of height, which is used for determining the wind profile. We ignore the possibility of collisions between saltating grains above the surface. The drag force on

the grains $\vec{f}_{drag}$ is calculated assuming that the grains are spheres (non-spherical grains can be assigned an equivalent diameter: see Bagnold, 1941), and ignoring lift forces due to particle rotation (see White and Schultz, 1977) with the form (Ungar and Haff, 1986):

$$(\vec{f}_{drag}\cdot\hat{x}) = -0.5c_d\rho v_{rel}(\vec{v}_{rel}\cdot\hat{x})\pi r^2$$
$$(\vec{f}_{drag}\cdot\hat{y}) = -0.5c_d\rho v_{rel}(\vec{v}_{rel}\cdot\hat{y})\pi r^2. \qquad (4.30)$$

The relative velocity between grains and air is $\vec{v}_{rel}$ the radius of the grains is r, the unit vectors in the horizontal and vertical directions are $\hat{x}$ and $\hat{y}$, and the drag coefficient c_d is given by (White, 1974: referenced by Ungar and Haff, 1986)

$$c_d = (24./Re) + 6./(1. + \sqrt{Re}) + 0.4,$$
$$Re = 2.rv_{rel}/\upsilon. \qquad (4.31)$$

The kinematic viscosity of air, υ, is taken to be 0.146 cm^2/sec. Because the grains contribute the most to the drag on the wind at the tops of their trajectories, and because these tops of the trajectories are separated in y, due to our calculating only a finite number of them (see below), it is necessary to average this drag force over a vertical distance on the order of the difference between the heights of the trajectories.

Computational Algorithm

The steady-state condition for saltation may be stated as follows (Ungar and Haff, 1986): if a collection of grains coming off a representative sample of the sand surface has velocity distribution $F(\vec{v}_o)$, then through accleration by the wind and impact with the surface, these grains must lead to the same velocity distribution $F(\vec{v}_o)$ of outgoing particle velocities. Mathematically, this requirement may be represented by an integral equation.

The solution of this integral equation is most easily effected through a discretization of the problem in the space of outgoing velocities $\vec{v}_o$. The technique is similar to the approach taken for the conveyer-belt model. The discussion of the method here is facilitated by assuming that the splash function is such that the outgoing velocities are constrained to lie in the vertical direction ($\vec{v}_o \rightarrow v_{oy}$). In this case, the outgoing velocity distribution becomes a vector in v_{oy}-space, $\vec{F}$, where F_j (the jth component of $\vec{F}$) is the number of grains per unit area per unit time per unit velocity emerging with velocity $v_j = (.5+j)\Delta v$, with Δv the

velocity spacing in the discretized space. (Note that here we have defined $\vec{F}$ as a number flux, rather than as a mass flux, as was done in the conveyer belt analysis.) The splash function is not explicitly defined within this space, since it depends on the incident velocities of the grains, which have components in both horizontal and vertical directions. However, for a given wind profile, because there is a one-to-one correspondence between $\vec{v}_o$ and $\vec{v}_i$, a matrix [T] can be constructed, whose components $[T]_{jk}$ represent the number of grains of velocity v_k coming off the surface due to the impact of a grain which, prior to accleration by the wind, came off the surface with velocity v_j. (Here we have essentially replaced the single parameter v_c, the conveyer-belt velocity, of earlier in the chapter, with a function, $u(y)$, the wind profile.) The steady-state condition is then represented by the matrix equation (see equation 4.14 above)

$$\vec{F} = [T\{u\}]\vec{F}. \qquad (4.32)$$

Generalizing to a two-component outgoing velocity involves expressing F as a matrix in (v_{ox},v_{oy})-space, and expressing T as a generalized matrix with four indices in a manner analogous to the above discussion.

The iteration method used to solve for the steady state is illustrated schematically in Figure 4.10. The wind-shear stress u^*, the splash function, and initial guesses for $\vec{F}$ and the wind profile are supplied as input. The trajectories of the particles lifting off with velocities v_j are computed, while recording the force per unit volume (weighted by F_j) that each exerts on the wind as a function of height. The wind profile is then adjusted to account for these forces, and the trajectories recomputed. This process is repeated until the wind profile and the trajectories converge. Then the matrix [T] is applied to $\vec{F}$ to determine a new distribution of outgoing velocities, and the wind-trajectory loop is repeated. The iteration over the outgoing velocity distribution (numbered by n)

$$\vec{F}(n+1) = [T(u)]\vec{F}(n) \qquad (4.33)$$

is repeated until $\vec{F}$ converges, signalling the arrival at the steady state. Given the steady-state value of $\vec{F}$, any other characteristics of the steady state, such as the mass flux profile, may be calculated.

A variety of internal self-consistency checks, as well as a direct comparison of our results with those of Ungar and Haff (1986) for a

delta-function splash function, have convinced us that errors in the computer code implementing the above algorithm have been eliminated.

Results

Rather than attempt detailed comparisons between this model of saltation and experiment (as we argue below, the proper experiments have not been performed yet), we will discuss some aspects of the model of a more abstract nature. Of particular interest are the manner in which the character of saltation depends on wind velocity and the form of the splash function.

To investigate these dependences, we employed a splash function describing the vertical velocity distribution of rebounding and ejected grains, resulting from the impact of a single grain, as a sum of a gaussian and a declining exponential distribution (both of which are functions of the incident velocity components). The grains could also be ejected at definite horizontal velocities which depended on the incident velocity (at no extra computational cost). Note that this incorporation of a horizontal ejection velocity component into the splash function is not the same as having the horizontal outgoing velocity described by a distribution, as is the case for the vertical outgoing velocity component.

The outgoing flux of grains can still be described within the space of outgoing vertical velocities. The mathematical form of the splash function is similar to the one used for the conveyer-belt model (equation 4.12), and is given by

$$S(\vec{v}_o,\vec{v}_i) = \{(c_1/(c_2\sqrt{2.\pi}))\cdot(v_{ix}/(v_{ix}+c_5))\,e^{-0.5((v_{oy}-fv_{ix}+\epsilon v_{iy})^2/c_2^2)} + c_3\cdot(v_{ix}^2+v_{iy}^2)\cdot e^{-(v_{oy}/c_4)}\}\delta(v_{ox} - c_6\epsilon(1.-f)v_{ix}). \qquad (4.34)$$

Here the subscript "o" denotes outgoing velocities, the subscript "i" refers to the incident velocity, and c_{1-6} are constants. The rebounding part of the splash function (the gaussian) is peaked around a function of the ingoing velocity components, $fv_{ix}-\epsilon v_{iy}$, and the ejected grain portion of this splash function has an outgoing vertical velocity distribution which declines exponentially, with magnitude proportional to the square of the incident velocity. The horizontal outgoing velocity of all particles ejected as a result of the impact is identical, being a definite function of the incident horizontal velocity: $c_6\epsilon(1.-f)v_{ix}$ This form of the splash function is not designed to imitate precisely natural grain-bed interactions, but rather to provide a convenient means of investigating general attributes of steady-state saltation.

Several cases will be considered. The various constants for each of these cases are presented in Table 4.3. The grains are assigned a radius 0.0125 cm and a density 2.6 g/cm^3. First, the consequences of employing a purely gaussian splash function with vertical ejection only will be examined (CASE 1). Then, varying magnitudes of the exponentially decreasing part of the splash function will be added (CASES 2-3), ending with a purely exponential splash function (CASE 4). Horizontal ejection of grains will be considered as well (CASES 5-6). Finally, the data on coarse sand reported in Chapter III will be used to derive a splash function for the purpose of studying the features of steady-state saltation when both horizontal and vertical outgoing velocities are given by distributions.

The data reported below satisfy the requirement that no components of the vector of outgoing flux from the bed $\vec{F}$ and no point on the wind profile $u(y)$ shall change by more than one percent from one iteration to the next before we terminate the program and accept the current state of the system as the steady state. Satisfaction of this requirement with an initial $u(y)$ and $\vec{F}$ somewhat different from their steady-state values generally takes twenty to thirty full iterations of the

algorithm. Some portion of the slow convergence may result from the discretization of the calculation.

Rebound Splash Function

An analysis of the results of a gaussian splash function used in our saltation algorithm provides an opportunity to discuss their relation to the findings of Ungar and Haff (1986) and to the solutions of the conveyer-belt system. Our gaussian term is a smeared-out approximation to Ungar and Haff's delta-function (with vertical ejection of the grains), but the amplitude used here is much more weakly dependent on the incident velocity. We studied the dependence of the saltation on the wind-shear velocity u^* for the parameters shown in Table 4.3, CASE 1.

The distribution of vertical velocities of grains leaving the surface in the steady state is illustrated in Figure 4.11 for three values of u^*. The half-widths of the distributions are about 45 cm/sec, somewhat larger than the intrinsic half-width of the gaussian splash function, 35 cm/sec (this being the width of a distribution which would result if there were a single impact velocity). The broadening of this distribution results from the spread in the impact velocities. The same effect was seen in the conveyer-belt model.

Eolian researchers since the time of Bagnold have noticed that the wind profile is altered by the presence of moving sand grains (e.g., Bagnold, 1941; Chepil, 1945b); in particular, with increasing u^*, the wind velocity decreases close to the surface and the wind velocity increases well above the surface, whereas, in the absence of moving grains, the wind velocity increases at all heights for larger u^*. Figure 4.12 (after Bagnold) displays wind profile data which demonstrates this concept. Bagnold noted that there is a height ($\approx$ 0.2 cm in his data) at which the wind velocity remains roughly constant with varying u^*. He believed this height to be related to the amplitude of sand ripples.

Ungar and Haff (1986), in their steady-state saltation model with a delta-function splash function, found that there is a certain height at which the wind velocity remains constant with changing wind-shear velocity; the wind profiles cross at this point, termed the focus. This feature of their model can be attributed to the fact that since the incident velocity must remain fixed in order to satisfy the steady-state requirement, the mean drag force exerted on the particles over their trajectory must not change, and hence the mean wind velocity the particles see must stay fixed also. Therefore, as u^* is increased, the

wind velocity at the top of the particle trajectories increases, and correspondingly the wind velocity close to the bottom of the trajectories must decrease. No reference to ripple amplitudes is necessary. In short, according to Ungar and Haff's model, this crossing of the wind profiles is due to the steady-state requirement on the grain-bed interaction.

Steady-state saltation involving a relaxation of the delta-function splash function to a gaussian retains this feature: the wind profiles for different free-stream wind-shear velocities cross at a particular height above the bed, as shown in Figure 4.13. However, a new twist to Ungar and Haff's argument is discovered when considering a gaussian splash function. A distribution of grain trajectories results: some grains go higher than others. As u^* is increased, those grains travelling above the focus height will feel additional acceleration over this part of their trajectory; those grains whose trajectories are entirely or mostly below the focus height will experience less acceleration due to the decrease in wind velocity at those heights. Therefore, increasing u^* has the effect of extending the variety of particle trajectories. The precise manner in which the system adjusts the trajectories and the wind profile to correspond to changes in the free-stream wind-shear velocity is

complicated. It is an intricate averaging process geared (both on the computer and in nature) toward satisfying the steady-state condition, that, on the average, each incoming grain reproduces itself, and that the force the wind exerts on the grains is equal and opposite to the force the grains exert on the wind.

For our gaussian splash function (CASE 1 of Table 4.3), the mean value of the trajectory height is about 3.5 cm, and the mean trajectory length is roughly 40. cm. The horizontal and vertical mean impact velocities are 320. cm/sec and 70. cm/sec respectively. In going from u^* = 35. cm/sec to u^* = 125. cm/sec, the half-widths of the distributions of these quantities increase by ten to thirty percent, reflecting the stretching of the grain trajectories due to the bifurcation of the wind profile change at the focus height.

Wind tunnel and field measurements have focussed on measuring various quantities related to the mass transport and abrasion power as a function of height (and on measuring the wind velocity). These quantities may be related to the number density of grains (number per unit volume) at a particular height y, $N(y) = \sum_i n_i(y) = \sum_i \sum_j F(\Delta v(i+0.5))/\dot{y}_{ij}(y)$, where the first sum is over the ejected vertical velocities (indexed by i

and going from 0 to M), $\dot{y}_{ij}(y)$ is the vertical velocity at height y on the trajectory of the grain ejected at velocity $\Delta v(i+0.5)$, and $j = 0$ (= 1) correspondsto $\dot{y}_{ij}(y) > (<) 0$. The horizontal number flux corresponding to the ith trajectory at height y is then the number density, $n_i(y)$, times the horizontal velocity at that height. The kinetic energy flux, important for erosion by moving sand, is proportional to the square of the horizontal velocity times the number density (summed over each trajectory). The horizontal force per unit volume exerted on the wind measures a slightly different quantity, being roughly proportional to the square of the velocity of the grains ***relative to the wind***.

In Figure 4.14, we plot height versus the number flux of grains for three values of u^* (CASE 1). While the maximum in the number density occurs at about 0.5 cm off the surface, we expect that the number flux and kinetic energy flux will peak at a greater height, since the horizontal velocity of vertically ejected grains does not become large until well into its trajectory. In Table 4.4, we list the heights at which the flux, the kinetic energy flux, and the forceper unit volume reach a maximum as a function of u^*. The height at which the flux is a maximum rises

gradually with increasing wind-shear velocity. For the gaussian splash, the kinetic energy peak follows the flux peak until high velocities.

This behavior may be understood by considering that the number flux (kinetic energy flux) is the product of the number density and the horizontal velocity (the square of the horizontal velocity). The horizontal velocity is an increasing function of height along a particle trajectory, and the number density (above 0.5 cm for CASE 1) decreases with height. Thus, their product must peak above the surface. The square of the horizontal velocity is a stronger function of height than the first power, and thus its product with the number density (proportional to the kinetic energy flux) will peak higher above the surface than the flux peaks. At greater wind velocities, the horizontal velocity (and its square) become even stronger functions of height, because the wind velocity increases above the focus and decreases below the focus. Therefore, as u^* is increased, we expect the peaks to become more widely separated and to rise to greater heights. The horizontal drag force profiles peak at lower heights, because the high vertical velocity near the surface (used in calculating the drag force) partially compensates for the lower horizontal velocities there.

The flux profiles of Figure 4.14 may be integrated over height and multiplied by the mass of each grain to obtain a vertically integrated mass flux. Our results (for all types of splash functions) are consistent with the mass flux being related to the square of the wind-shear velocity, as advocated by Ungar and Haff (1986), but appear to be inconsistent with the cubic relations usually postulated (e.g., Bagnold, 1941; White, 1982). The cubic dependence has its genesis in the postulate that the impact velocity of saltating grains is proportional to the wind-shear velocity; this assumption is in clear conflict with our steady-state requirement. Additional data on the mass flux versus u^* curve are needed to settle definitively this question within our model. (We have at most five points for any one splash function.) However, Ungar and Haff derived this relation on rather general principles, which will undoubtedly apply for most types of splash functions.

The free-stream wind-shear velocity may be related to the derivative, with respect to the logarithmic height z, of the wind profile (above the saltating layer) as follows: $du/dz = ku^*$. An effective wind-shear velocity may be defined at the surface in an analogous fashion: $u^*_{eff} = (du/dz)|_{z=0}/k$. This is a direct measure of the stress

transmitted by the fluid forces directly to the surface ($\tau_{eff} = \rho(u^*_{eff})^2$). As previously mentioned, two types of threshold wind-shear velocities have been utilized in descriptions of eolian saltation (Bagnold, 1941): a fluid threshold, u^*_f, which is the minimum imposed wind-shear velocity required to initiate movement of grains on a previously stationary bed through fluid forces, and an impact threshold, u^*_i, the minimum imposed wind-shear velocity required to maintain saltation once it has begun. Empirically, researchers have found that $u^*_i < u^*_f$; once saltation has been initiated and is in progress, the wind-shear velocity may be decreased to u^*_i, without terminating the grain movement. When $u^*_i < u^* < u^*_f$, entrainment of particles must be occurring through grain-bed impacts, and not by virtue of fluid-drag or -lift forces, since the fluid stress at the surface is below that required to entrain particles.

In our model (for all splash functions), we find that as we turn up the free-stream wind-shear velocity, u^*_{eff} at the surface decreases, as is detailed in Table 4.5. This means that the fluid stress being exerted on

the surface grains is decreasing with increasing u^*. A general argument for why fluid stresses are unlikely to play a dominant role in the entrainment of grains in steady-state eolian saltation will be presented in the Discussion section later in this chapter.

Splash Function Including Low-Energy Ejecta

The primary consequence of adding an exponentially decreasing outgoing velocity distribution term to the splash function ($c_3 \neq 0$) is to create a population of grains moving close to the surface at low velocity. The number density of grains $N(y)$ (for CASES 2-4) decreases monotonically with height (above a grain diameter). However, the horizontal number flux, the kinetic energy flux, and the horizontal drag force per unit volume have maxima at heights above the surface. These heights decrease as the strength of the decaying exponential term increases relative to the gaussian term (CASES 2 → 3 → 4 of Table 4.4). The kinetic energy flux everywhere peaks above the number flux for CASES 2 to 4. In Figures 4.15 and 4.16 we display the flux profiles and kinetic energy flux profiles (respectively) for CASE 2 of Table 4.3, with three different values of u^*.

A focus height at which the wind profiles cross exists for the

splash functions which include the exponentially declining term. However, the "point" at which the profiles intersect actually becomes spread over a difference in heights of up to about 0.25 cm for our data.

The splash functions incorporating a gaussian (rebound) term are characterized by rather abrupt cutoff in height of the flux and kinetic energy flux, as well as a sharp bend in the wind profile. In contrast, the purely exponential splash function (CASE 4) leads to flux and wind profiles changing much more gradually with height, and, for the parameters considered, the calculation becomes difficult at high wind-shear velocities, as the saltation layer becomes highly dispersed.

Ejection of Grains with a Horizontal Velocity Component

Two types of splash functions involving horizontal ejection of grains ($c_6 \neq 0$) were examined: one involving a gaussian splash (CASE 5) and one involving both a gaussian term and an exponentially decreasing term (CASE 6). Typical high-velocity grains in these cases are incident at about 10° and rebound at about 30°. The same qualitative features occurring in the vertical ejection cases were observed with these splash functions: the heights at which maxima in the flux and kinetic energy flux occur grow with increasing u^*, and the peaks in kinetic energy occur

above those in flux, which in turn are above the peaks in the horizontal body force acting on the wind.

It is interesting to note that horizontal ejection of grains does not influence the steady decline of the effective wind-shear velocity at the surface u^*_{eff} with increasing u^* above the impact threshold u^*_i (Table 4.5).

Coarse Sand Splash Function

The extension of the computational algorithm from the restriction to a vertical ejection velocity distribution to ejecting grains with velocities distributed in both horizontal and vertical components is straightforward. The splash function becomes a matrix in four dimensions (two impacting velocity components and two outgoing velocity components), $[S]_{ijkl}$ and the outgoing velocity distribution is defined by a matrix in two dimensions (two outgoing velocity components) $[F]_{ij}$. Trajectories of particles along a grid in horizontal and vertical ejection velocity space must be computed. To reduce computation time, only trajectories involving grains which make up a significant fraction of the grains coming off the surface are computed,

except at the beginning and near the end of the calculation, when all trajectories are computed. Caution is necessary in eliminating trajectories, so that feedback is retained.

The splash function was derived from the data on grain-bed impacts of coarse sand described in Chapter III. The velocity dependence of the splash function was fairly well-specified by these data, with linear interpolation employed within the range of experimental measurement (v_i = 650-1200 cm/sec) and linear extrapolation used outside this range. The data were smoothed using an algorithm employing gaussian weights due to Tombrello (see Chapter V). The paucity of information on the angular variation of the coarse sand splash function forced us to use some simple transformations on the data obtained at $\approx 15°$ incident angle to account for variations with incident angle. Specifically, we modified the rebound portion of the splash function so that the vertical velocity amplification sharply increased with decreasing incident angle, and we modified the bed ejecta part of the splash function to incorporate the trend that the number of ejecta increases slightly with increasing incident angle. These modifications were made to be consistent with what little data we have. No other dependences on angle were included.

The error criterion on the change in each outgoing flux bin being less than 1% from one iteration to the next was relaxed to include only those bins which contained more than 1% of the flux. In addition, the data on coarse sand saltation given here have not been checked by changing the outgoing velocity bin sizes to date.

The wind profiles, number flux profiles and kinetic energy flux profiles for three values of the wind-shear velocity u^* (50, 100 and 125 cm/sec) are shown in Figures 4.17-4.19. The height of the wind velocity focus is about 1 cm (Figure 4.17). The wind velocities below the focus height are relatively insensitive to u^*, as compared with the wind velocities resulting from our analytical forms for the splash function. This could be a consequence of the fact that the number of ejecta is not strongly dependent on incident velocity for the coarse sand splash function (Chapter III). Therefore, as u^* is increased, the grains which go to higher heights in the saltating curtain impact with greater velocity, but the increase in the number of grains ejected by the high-energy impacts is lessened, and thus the need to compensate for them by lowering the velocity of the low-flying grains, and hence the wind velocity near the bed, is correspondingly lessened.

The flux profiles display some interesting structure, with peaks at 0.25 cm and 1.25 cm, and a general increase in flux closer to the surface. This structure is probably at least partially an artifact of our calculational procedure (the discretizing of the outgoing vertical velocities). The kinetic energy profiles extend rather high above the surface, but the details of the profile may be due to the discretization. Further work will allow definite predictions to be made for this type of sand. In particular, a better definition of the splash function will be necessary.

The effective wind-shear velocity at the surface decreases with increasing u^*, Table 4.5 The decline is gentle, reflecting the weak dependence of the splash function on velocity, as discussed above.

Finally, in Figures 4.20 and 4.21 we show the steady-state outgoing horizontal/vertical velocity distribution and impacting velocity/angle distribution for u^* = 100 cm/sec for coarse sand. The discretized distribution is normalized so that the largest element is equal to 9999. The outgoing flux is dominated by low-velocity grains ejected vertically, with some backwards ejections, but mostly skewed toward grains coming off the bed in the forward direction. The grains which are

ejected vertically at low velocity impact at high angle relative to the horizontal, and they are preponderant in the impacting grain distribution. Most other grains impact at low angles.

Discussion

Natural saltation over sand surfaces is likely to resemble the characteristics of saltation computed using our model with the splash function chosen from our coarse sand grain-bed impact experiment (appropriately scaled for grain size). However, it is of interest to consider conditions under which one can obtain splash functions of a different character. For instance, desert travellers are familiar with the sight of sand saltating across an asphalt roadway. Unless sand is accumulating, every grain hitting the surface of the road is ejected back into the saltating stream, with a velocity distribution probably not unlike that of our gaussian splash, except that the number of grains coming off the surface per incident grain is precisely one, independent of the impact velocity. Thus, there is no particle flux feedback in this system. The system steadies itself by an adjustment involving loss of energy due to aerodynamic drag over the grain trajectories, and via the variation of the vertical velocity amplification with incident angle (à la Rumpel, 1985).

Because saltating grains retain a larger fraction of their energy in collisions with the road than they do in collisions with the bed, one sees the height of the saltating layer rise as the sand crosses the road. R.S. Anderson and P.K. Haff (1987: unpublished work) have addressed the saltation of grains over a hard surface quantitatively.

Sharp (1964) collected data on mass flux profiles of sand moving over a bouldery alluvial plain surface in the Coachella Valley of California. A curious conclusion derived from his data was that larger saltating grains rebound to greater heights than do smaller saltating grains. We do not believe that an explanation of this rise in rebound height with grain size is to be found in the nature of the grain-bed impact. If anything, our results suggest that larger grains will rebound with a lesser vertical velocity amplification, because they "see" a smoother surface than do smaller grains. Rather, it may be possible to interpret Sharp's data by reference to the effect of aerodynamical drag on saltating grain trajectories. Smaller particles attain lesser heights for the same vertical ejection velocity because of their smaller mass to cross-sectional area ratio.

We examined the trajectories of spherical grains ejected into a

sediment-free wind blowing over a surface characterized by grains of roughness 1. cm, with the wind speed being about 40 mph at a height of 100 cm (u^* = 160 cm/sec). These conditions were chosen to correspond roughly to those described by Sharp (1964) at his experimental plot. Sand grains of diameter 0.025 cm and 0.1 cm were ejected vertically and at angle 60° to the vertical for a number of ejection velocities. Their trajectories were computed using the mean wind profile (equation 4.28) and the drag force equations 4.30 and 4.31. In Figure 4.22, we plot the height attained by the grains versus the vertical ejection velocity. It is clear that the height of the smaller-sized sand grains "saturates." This suggests that the explanation for the greater heights attained by larger particles is due to aerodynamical drag. Further, the lesser height achieved by the smaller grains will result in a smaller velocity on the subsequent impact. However, other factors should be considered, such as the distribution of incoming angles of the various grain sizes; since the vertical velocity amplification is sensitive to incoming angle, a larger incident angle for the larger grains could defeat the effect of the wind drag. A proper calculation would necessarily consider the trajectories of the grains in steady-state saltation. A minor modification of our

steady-state saltation computer program (defining a separate population of grains corresponding to each grain size and assigning each such population its own outgoing flux vector), with a proper specification of the splash function for a mixed-grain size bed, will allow us to perform this calculation.

Another modification which we would like to make in the saltation algorithm is to consider time dependence of the system. Time dependence is of interest both for examining the path (in phase space) the saltating system takes to the steady state, and for investigating the stability of the sand-wind system. Observations of saltation on dunes suggest that saltation can be unsteady. This may be due to imposed variations in the free-stream wind-velocity (wind gusts), or to intrinsic properties of the saltating sand system.

In altering our program, we would make the assumption that the response time of the wind is sufficiently small that the mean wind velocity could be treated as remaining in the horizontal direction and that it could be calculated at any instant from the instantaneous horizontal drag forces. A steady-state condition would no longer apply. However, assuming that the flux of grains was independent of horizontal position,

an expression for the outgoing flux from the bed at a particular time t, $F(v_{oy},t)$, may be formulated as follows:

$$F(v_{oy},t) = \int S(v_{oy},\vec{v}_i)\cdot W(\vec{v}_i,v'_{oy},t-\tau,\{u(y(v'_{oy},t-\tau),t-\tau)\})\cdot F(v'_{oy},t-T)dv'_{oy}dv_{ix}dv_{iy}d\tau. \quad (4.35)$$

S is the splash function, W is a function which describes the transformation of a grain ejected with velocity v'_{oy} at time $t-T$ through a wind profile changing with time into a grain impacting at velocity $\vec{v}_i$ at time t, T is the flight time of the trajectory, and τ is the time before the impact of a grain which impacts at velocity $\vec{v}_i$, and varies from T to zero over the course of a particle trajectory. We note that W would still be a delta-function, albeit one with a very complicated argument, and that this argument would be determined in practice by computing particle trajectories. A practical implementation of this algorithm requires discretizing time and treating it in a manner similar to the treatment of v_{oy}; F then becomes a matrix defined in v_{oy}-t space. This means that another loop is added to the calculation and computation time becomes large. Investigations with the conveyer-belt model may provide some

guidance as to how to proceed with this calculation.

Additionally, in theory, variations of saltation with downstream distance can be treated in a similar manner. For example, one could examine the change in the nature of saltation at the junction between a sand bed and a road. However, considering downstream variations introduces the difficulty that the wind velocity is now a function of both height and horizontal position.

For all of the preceding calculations, we have assumed that the sand bed is flat and immobile. In reality, for a significant flux of sand, a substantial fraction of the sand grains on the surface may be moving (Willetts and Rice, 1985b), although the author has witnessed saltation conditions in the field in which most of the surface grains were stationary, and effects of individual grain-bed impacts on the bed could be observed. Two consequences of the motion of a large number of the surface grains can be identified: the wind profile might be altered and the splash function might be changed.

If a sizable fraction of the surface grains are in motion, we can imagine the entire bed to be moving downstream at the mean forward velocity of the grains comprising the "surface." In this case, setting the

boundary condition on the wind at the surface to be zero is only an approximation; rather, setting the wind velocity at the bed to be equal to this mean forward surface velocity seems more appropriate, and is easy to do in our computational algorithm. In any case, this is unlikely to have a significant effect on the wind profile, since the velocities of grains remaining near the surface are only a small fraction of the saltating particle velocities, and hence of the wind velocities above the surface. Our coarse-sand data imply that most low-energy grains are ejected nearly vertically, and those which remain within a few grain diameters of the surface will have forward velocities of less than on the order of 25 cm/sec (for this grain size).

The consequences of a mobile bed will be far greater for the nature of the splash function than for the boundary condition on the wind. Our simulation and experimental data on the splash function were collected for stationary beds. The effect of moving bed grains on the saltating grain-bed impact is probably to reduce the effective mass of the bed grains; if the bed grains are not in contact with other grains, their effective mass will equal their true mass. The upshot will be a decrease in the vertical velocity amplification, leading to a change in the

characteristics of the steady-state saltation (i.e., mass fluxes will be smaller than they would have been otherwise). This phenomenon can be investigated with the techniques at hand by shaking our experimental sand bed container (on the computer or in the laboratory) so that the surface grains are in motion.

We have assembled in this document evidence to suggest that grain-bed impacts play a role in entraining particles in steady-state saltation, an idea which dates back to Bagnold (1941). It is appropriate at this time to address the question of whether fluid forces also fulfill the function of a means of sand grain entrainment in steady-state saltation. Prior to this discussion, it is necessary to define in clear terms what we mean by the word "entrainment." A particle is entrained in saltation when, being at or close to the surface, it acquires vertical velocity from an external agency so that it becomes clearly separated from the surface and its subsequent motion can be described in terms of the gravitational and fluid forces acting upon it (i.e., no intergranular forces). The source of the vertical momentum the entrained grain receives defines the means of entrainment. Thus, entrainment is a process exemplified by the application of forces in the vertical direction

exceeding gravitational forces.

We divide the processes which can lead to entrainment into impact processes and fluid-force processes. Two classes of impact generated entrainment can be identified: the multiplication of a low-energy moving grain's vertical velocity through an impact with a surface grain (vertical velocity amplification >> 1), and the ejection of a surface grain by the impact of a high-energy grain with the sand bed. We note that the grain in the former process is, in the sense of our definition of Chapter III, already in saltation, since its ratio of outgoing to incident momentum in a collision is already large. Fluid stresses acting on bed particles can lead to entrainment either by direct aerodynamical lift forces, or by the conversion of horizontal drag forces, through contact with a neighboring grain, into vertical momentum. Such a particle would be rolled out of a pocket by the fluid forces.

It is not appropriate to include particles which skip along the surface, impact a protruding bed grain, and enter the saltating stream under the heading of fluid-force entrained grains, simply because the impetus for their movement along the surface was a fluid force. Under this notion, all grains would be entrained by fluid forces, since all energy

in the system can ultimately be traced back to the wind. This definition would merely confuse the situation, and thus we will promptly discard it.

Chepil (1958) concluded that lift and drag fluid forces on surface grains are roughly equivalent, whereas Hunt and Napalis (1985) argued that horizontal drag forces will dominate over lift forces in the fluid-force entrainment of grains. Iversen, et al., (1976) reviewed the issue of fluid entrainment of particles in great detail. In any case, below, we assert that fluid forces play no role in particle entrainment during steady-state saltation, although they clearly will be important in considering the initiation of saltation.

We begin by making two assumptions (these assumptions will be examined in greater detail later): (1) the ability of fluid forces to entrain particles (for a given size and type of grain) depends on the fluid shear-stress at the surface only, and (2) the ability of saltating particles to reproduce themselves through impact with the surface increases directly with their velocity and inversely with their incident angle. This "reproductive capacity" of saltating grains is meant to include some combination of their vertical velocity amplification, and their ability to splash out bed grains, and it is intended as a measure of whether, on the

average, a grain coming off the bed, through acceleration and impact with the surface, can reproduce itself. The number of other particles ejected into the saltating stream is also a measure of reproductive capacity.

We argue that the shear stress at the surface, related to the effective surface wind-shear velocity, decreases with free-stream wind-shear velocity u^*. This may be seen by considering an experiment in which we start with steady-state saltation over a sand bed and increase the value of u^*. On physical grounds, the wind velocity near the top of the saltating layer must increase. According to our second assumption, the ability of particles traveling through the top of the saltating layer, whose impact velocities would be correspondingly greater, to reproduce themselves would increase. This could be accomplished through ejecting additional numbers of particles, or through an increase in vertical velocity amplification. In order to maintain a balanced steady-state condition at this new u^*, the system is forced to compensate for this increase in reproductive ability of the high-flying grains by decreasing the reproductive capacity of other grains. This may be accomplished only through a decrease in wind velocity, which again on physical grounds, must take place near the surface. If the wind velocity near the surface

decreases, the derivative of the wind velocity must go down as well, and therefore the shear stress the wind exerts on the surface, as well as the value of u^*_{eff}, declines. Since this experiment may be started in a region where we know that u^*_{eff} is below the fluid threshold wind-shear velocity (since $u^*_i < u^*_f$), the value of u^*_{eff} remains below the threshold for fluid-force entrainment of particles for all u^*. Considering our first assumption, this means that grains cannot be entrained by fluid forces in steady-state saltation.

We now consider the viability of our two assumptions. One might suggest that a mobile bed might be more conducive to entrainment of particles by fluid stresses, so that the fluid threshold shear stress would go down as the bed mobilized (B.B. Willetts, 1986: communicated at the ASU Aeolian Symposium, September 30-October 4, Tempe, Arizona). The fact that the grains are somewhat dispersed would tend to work against the fluid-drag method of entrainment, which requires a neighbor to define the fulcrum of the particle to be entrained. Grains which have been knocked off the bed by impacts are not eligible for fluid entrainment; therefore, if the majority of the surface grains are in motion, and

consequently not in contact with the solid bed, fluid entrainment, as defined above, will not occur.

An impact of a saltating grain with the bed may result in the ejection of a number of surface grains, clustered around the impact point. If the saltating flux is low, at the periphery of the resulting "crater," the grains will be momentarily jostled from their static positions. This would lessen the effect of particle cohesion and facilitate fluid entrainment. However, working against this effect, the region in which the jostling takes place is likely to have a local drop in the wind velocity, due to the drag on the wind of the grains ejected around the impact point. Moreover, unless cohesive forces far exceed the gravitational force on a grain, the lift force at the fluid threshold shear stress (which is above the actual surface shear stress during sediment transport) can only propel a jostled grain to heights on the order of several grain diameters in height, since the lift force is significant only within the first few grain diameters above the surface, and, by definition, at threshold, the lift force just barely overcomes gravitational and cohesive forces. (A similar argument can be made for fluid-drag entrainment.) The grain-bed impacts propel surface grains to an order of magnitude greater height,

with a correspondingly higher chance of becoming part of the saltating population. Thus, the disruption of cohesive forces will not lead to a prominent role for fluid entrainment, unless cohesive forces are very strong (>> gravitational forces).

Second, we examine the assumption that higher velocity or lower angle particles are more likely to reproduce themselves. Experimental evidence (Willetts and Rice, 1985a; Chapter III) suggests that this will be so for conventional situations. One can imagine scenarios where the assumption will break down. For instance, a very high velocity incident particle might vaporize or bury itself in the bed, but this is outside the realm of conventional saltating grain speeds. Also, if the raising of the velocity of the particle is accompanied by the mobilization of the bed, one could imagine that, although the number of ejecta might rise due to increased transfer of energy to the bed, the concomitant decrease in vertical velocity amplification would result in an overall lowering of the particle's reproductive capacity. In this regime, the system would experience a positive feedback condition; higher impact velocities result in lower numbers of grains in saltation resulting in even higher impact velocities, etc. Of course, the system would eventually saturate, and

might go into an oscillatory mode. This does not mean necessarily that the range of the oscillation would venture into the regime where fluid forces at the surface could participate in entrainment. If the system were to be in such an oscillating mode, the steady-state assumption would have been violated.

In conclusion, we believe that the above arguments, made independent of the results of our saltation calculations, but supported by those calculations, are sufficiently compelling to regard grain-bed impacts as the overwhelmingly dominant mechanism for particle entrainment in steady-state saltation. In view of this, we expect that increased attention to grain-bed impact mechanics would be beneficial for the advance of our understanding of eolian saltation.

Finally, we note that an experimental test of the model we have proposed is necessary to evaluate properly its validity as a quantitative description of saltation. Such an experiment would require, at minimum, the measurement of the splash function for a given sand, and the measurement of wind profiles and mass flux profiles as a function of free-stream wind velocity or wind-shear velocity for saltation involving this sand. To our knowledge, such an experiment has not been performed.

The saltation model presented here is theoretically self-consistent, and self-contained. In addition, the known qualitative features of saltation have been reproduced by the model: the wind velocity increases above a focus height, and decreases below that height, with increasing wind-shear velocity, and the flux and kinetic energy flux profiles behave in a manner consistent with experiment and field experience. The model predicts that the mean impact velocity of the sand will remain roughly constant with u^*, but that the velocities of grains higher in the saltating stream will increase, while the velocities of grains lower in the saltating stream (and less accessible to experimental observation) will decrease with increasing u^*. We expect that the computational model presented here will be beneficial to researchers in interpreting existing data, for gaining insight into saltation and processes involving saltation, and as a predictive tool.

SYMBOL DEFINTIONS: CHAPTER IV.

x, y	horizontal and vertical coordinates
t	time
g	accleration of gravity
d, r	grain diameter, radius
$\vec{v}_i, \vec{v}_o$	incident and outgoing velocities of grains
$F(\vec{v}_o), \vec{F}$	differential outgoing flux from the bed
$S(\vec{v}_o, \vec{v}_i)$	splash function: number density of grains coming off the bed with velocity $\vec{v}_o$ due to impact of grain with velocity $\vec{v}_i$
v_c	conveyer belt velocity
$\vec{v}_{ci}, \vec{v}_{co}$	incident and outgoing velocities of grains striking the conveyer belt
$\vec{v}_{bi}, \vec{v}_{bo}$	incident and outgoing velocities of grains striking the sand bed
P_T	power supplied to the conveyer belt
P_F	$= \xi v_c^2$ power going into dissipation in the conveyer belt
P_g	power supplied to grains impacting the conveyer belt
$B(\vec{v}_o', \vec{v}_{iz}; v_c)$	function which transforms a grain impacting the conveyer belt at velocity $\vec{v}_o'$ to a grain coming off the belt at velocity $\vec{v}_i'$
$T(\vec{v}_o', \vec{v}_{iz}; v_c)$	convolution of functions S and B
N	$= (v_{bix})^2/(v_{girl})^2$ number of particles ejected per incident particle
ϵ	coefficient of restitution
f	fraction of incident horizontal velocity converted to outgoing vertical velocity
$\alpha, \beta, \gamma, \delta, \epsilon$	parameters describing the splash function of equation 4.12
μ_i	discrete outgoing vertical velocity of grains in the space $\{\vec{v}_o\}$

M	number of elements in discretized space $\{\mu_i\}$
h	conveyer belt - bed distance
$\vec{z}$	state vector: $z_1 = v_{oy}$, $z_2 = F$
$\vec{w}$	control vector: $w_1 = v_c$, $w_2 = N$
[Z]	matrix transforming $\vec{z}$ to $d\vec{z}/dt$
[A], [B]	constant matrices relating $\vec{z}$ to $d\vec{z}/dt$
$u(y)$	wind velocity profile
k	= 2.5, von Karman's constant
ρ	density of air
f_x	spatially averaged force per unit volume on wind
u^*	wind-shear velocity
u^*_{eff}	effective wind-shear velocity at the surface
u^*_i	impact threshold wind-shear velocity
u^*_f	fluid threshold wind-shear velocity
τ	wind-shear stress
$\vec{f}_{drag}$	drag force on particles due to wind
c_d	drag coefficient
v_{rel}	relative velocity between wind and grains
υ	kinematic viscosity of air
Re	Reynolds number
c_{1-6}	parameters describing the splash function of equation 4.34

TABLES: CHAPTER IV.

TABLE 4.1 † Conveyer Belt Model Velocity Distribution Splash Parameters

CASE	f	ϵ	α	β	γ	δ	ϵ	P_T	ζ
A	0.8	0.6	1.6	0.5	0.	-	3.0	1000.0	0.05
B	0.8	0.6	1.6	0.5	0.004	0.2	3.0	1000.0	0.05
C	0.8	0.6	1.6	0.5	0.2	0.5	3.0	1000.0	0.05

†CASES A-C have M = 40 and the velocity interval between elements of the M element differential flux vector F is 0.25

Table 4.2 Conveyer Belt Model Delta-Function Splash Function Parameters

CASE	f_{max}†	f_{min}†	ϵ	P_T	ζ	v_{girl}
D	0.8	0.8	0.6	1000.0	0.	1.
E	0.8	0.6	0.6	1000.0	0.	1.

†f varies from f_{max} to f_{min} with increasing velocity.

TABLE 4.3 Aerodynamic Saltation Splash Function Parameters

CASE	c_1	c_2	c_3	c_4	c_5	c_6	ϵ	f	u^*
1	2.	35.	0.	-	275.	0.	0.7	0.1	35,75,125
2	2.	35.	$2.\cdot10^{-7}$	40.	275.	0.	0.7	0.1	35,75,125
3	1.	35.	$2.\cdot10^{-7}$	40.	275.	0.	0.7	0.1	35,75,125
4	0.	-	$2.\cdot10^{-7}$	80.	-	0.	0.7	0.1	35,50,75
5	2.	35.	0.	-	275.	1.	0.3	0.1	50,100,150
6	2.	35.	$2.\cdot10^{-7}$	40.	275.	1.	0.3	0.1	50,100,150

TABLE 4.4 Peak Heights in Flux, Kinetic Energy Flux, and Drag Force per Unit Volume Profiles

CASE	u^*	Height at which profiles peak (cm): flux	kinetic energy flux	drag force
1	35.	3.0	3.0	1.2
1	75.	3.0	3.0	1.6
1	125.	3.4	5.0	3.0
2	35.	1.0	2.0	0.2
2	75.	1.6	2.5	1.0
2	125.	1.8	4.0	1.6
3	35.	0.6	1.5	0.2
3	50.	1.1	3.5	0.2
3	75.	0.6	2.5	0.2
4	35.	0.6	3.4	0.2
4	50.	1.4	3.4	0.2
4	75.	2.0	5.0	0.2
5	50.	0.8	2.0	0.6
5	100.	0.8	2.0	0.6
5	150.	1.4	3.0	1.2
6	50.	1.6	2.0	0.2
6	100.	1.0	2.0	0.2
6	150.	1.0	4.0	1.0

TABLE 4.5 Effective Wind-shear Velocities at the Surface

CASE	u^*_{eff} for $u^* =$ †		
	u^*_1	u^*_2	u^*_3
1	33.1	29.0	24.8
2	25.1	20.1	13.9
3	35.0	30.6	24.2
4	26.4	24.6	20.9
5	40.6	35.7	31.1
6	28.0	20.4	12.1
7(coarse sand)	25.6	25.1	21.5

† for CASES 1-3, $u^* = 35,75,125$; for CASE 4, $u^* = 35,50,75$; for CASES 5-6, $u^* = 50,100,150$; for CASE 7 (coarse sand), $u^* = 50,100,125$.

FIGURE CAPTIONS: CHAPTER IV.

Figure 4.1 A sketch of the conveyer-belt model.

Figure 4.2 The splash function for CASE B, with incoming velocity = 7.375. This is the thirtieth column of the T-matrix of Figure 4.5.

Figure 4.3 Total flux versus mean outgoing velocity as a function of iteration step for CASE B.

Figure 4.4 (a) T-matrix and (b) steady-state flux distribution for CASE A.

Figure 4.5 (a) T-matrix and (b) steady-state flux distribution for CASE B.

Figure 4.6 (a) T-matrix and (b) steady-state flux distribution for CASE C.

Figure 4.7 Flux versus outgoing velocity as a function of iteration step for CASE D. The two lines represent the locus of points in the $F-v_{oy}$ plane for which $F(n+1) = F(n)$ and $v_{oy}(n+1) = v_{oy}(n)$.

Figure 4.8 Flux versus outgoing velocity as a function of iteration step

for CASE E. The system approaches $(F, v_{oy}) \approx (20., 1.)$ from the upper left as if it were a fixed point; however, on arrival the system instead encounters a saddle leading to an oscillation between the two circled solutions.

Figure 4.9 A schematic of the linearized feedback system for the single outgoing velocity case. [A] and [B] are defined explicitly in the text. [C] is the function which computes v_c and N from F and v_{oy}

Figure 4.10 Schematic illustration of algorithm for calculating the characteristics of steady-state saltation.

Figure 4.11 Outgoing vertical velocity distributions for the gaussian splash function (CASE 1) at three wind-shear velocities: u^* = 35, 75, 125 cm/sec.

Figure 4.12 Mean wind profiles (after Bagnold, 1941) over a sand bed composed of 0.025 cm diameter grains experiencing saltation at four values of the wind-shear velocity (from Ungar and Haff, 1986).

Figure 4.13 Mean wind profiles for the gaussian splash function (CASE 1)

Figure 4.20 Outgoing vertical/horizontal velocity distribution for the steady state with the coarse sand splash function. The discretized distribution is normalized so that the largest element is 9999.

Figure 4.21 Impact velocity/impact angle distribution for the steady state with the coarse sand splash function. The discretized distribution is normalized so that the largest element is 9999.

Figure 4.22 Height attained by grains of size 0.025 cm and 0.1 cm in a 40 mph sediment-free wind profile. The grains are ejected vertically and at 60° to the vertical.

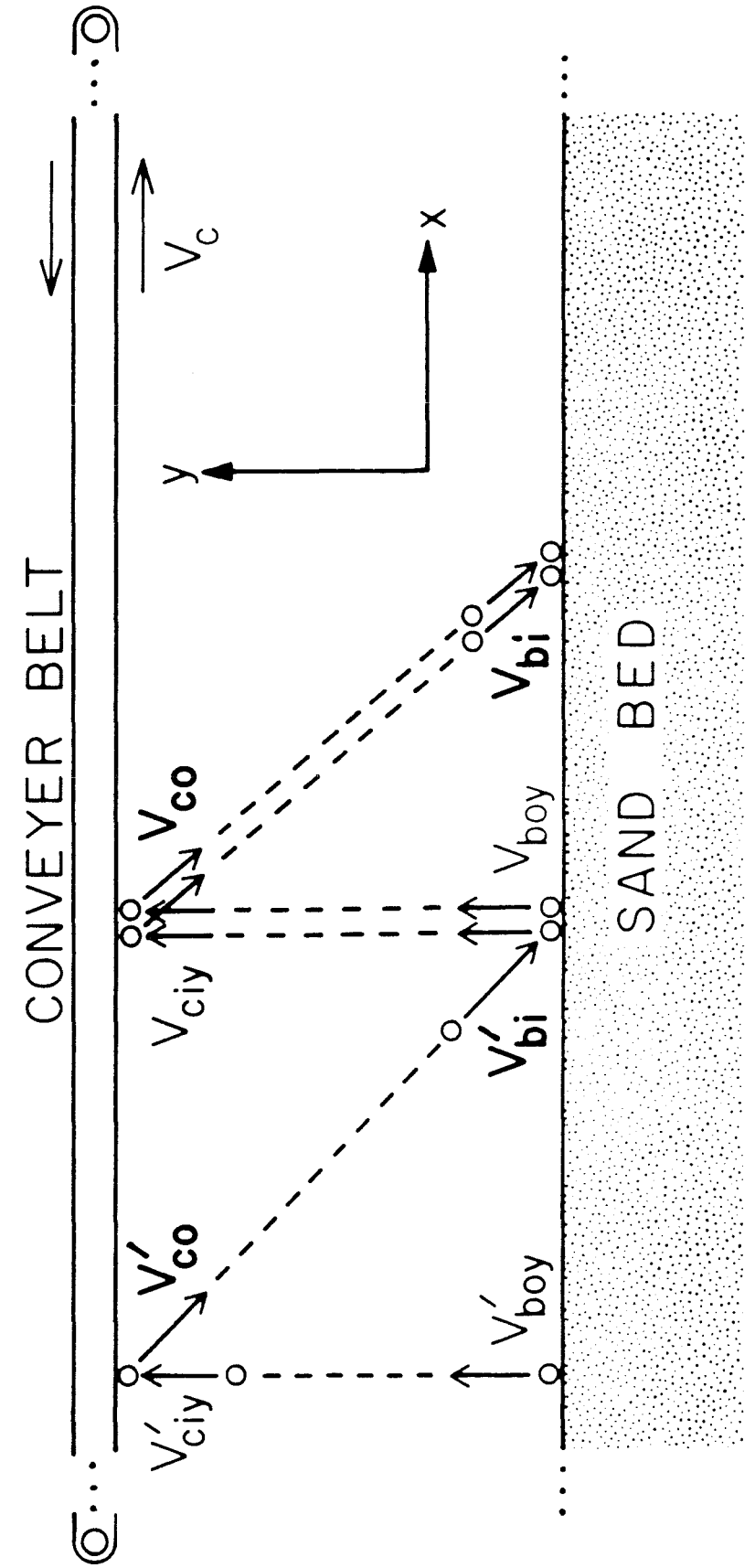
CONVEYER BELT
SAND BED
V_c
x
y
V_{co}
V_{ciy}
V_{boy}
V_{bi}
V'_{co}
V'_{ciy}
V'_{boy}
V'_{bi}

Figure 4.1

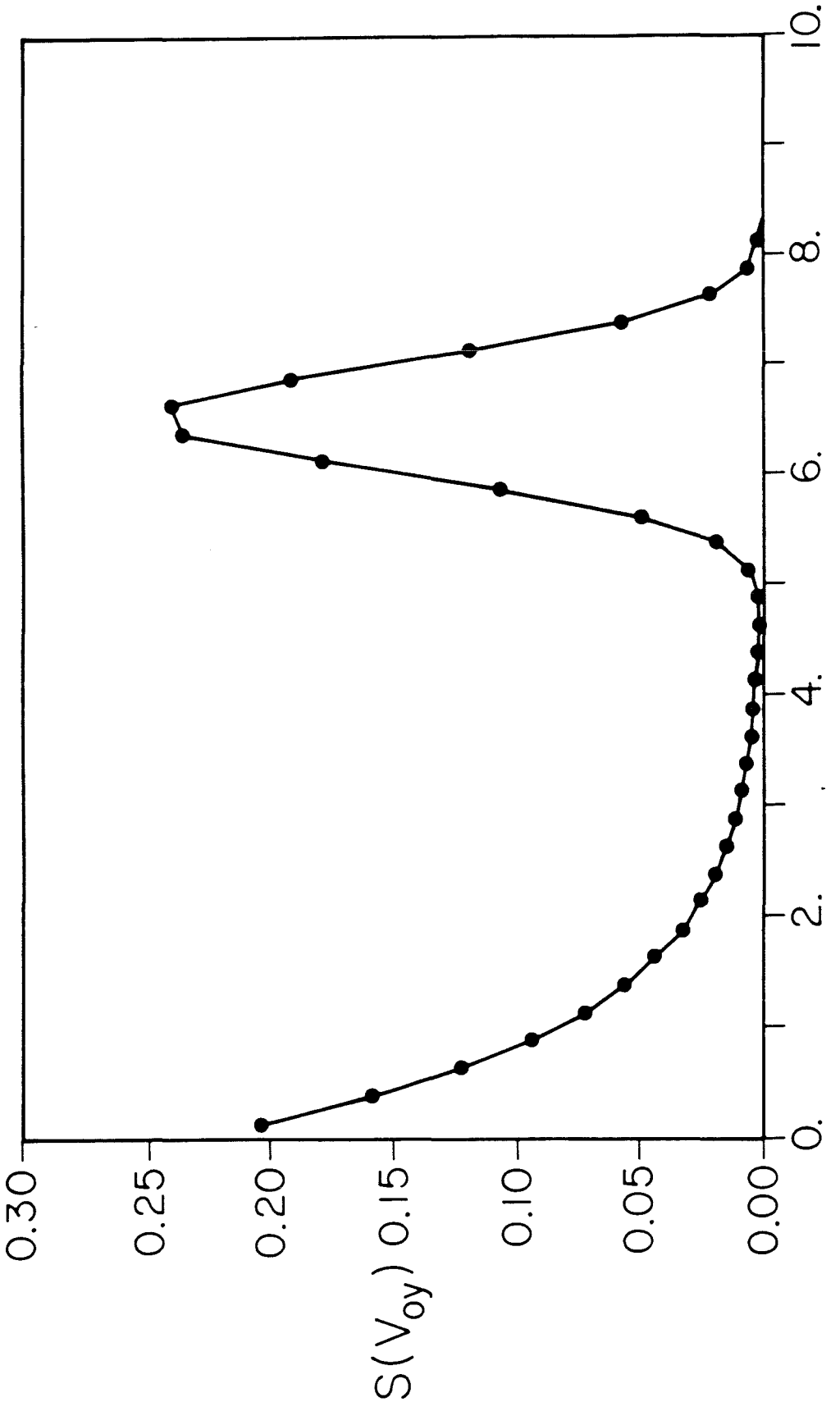

Figure 4.2

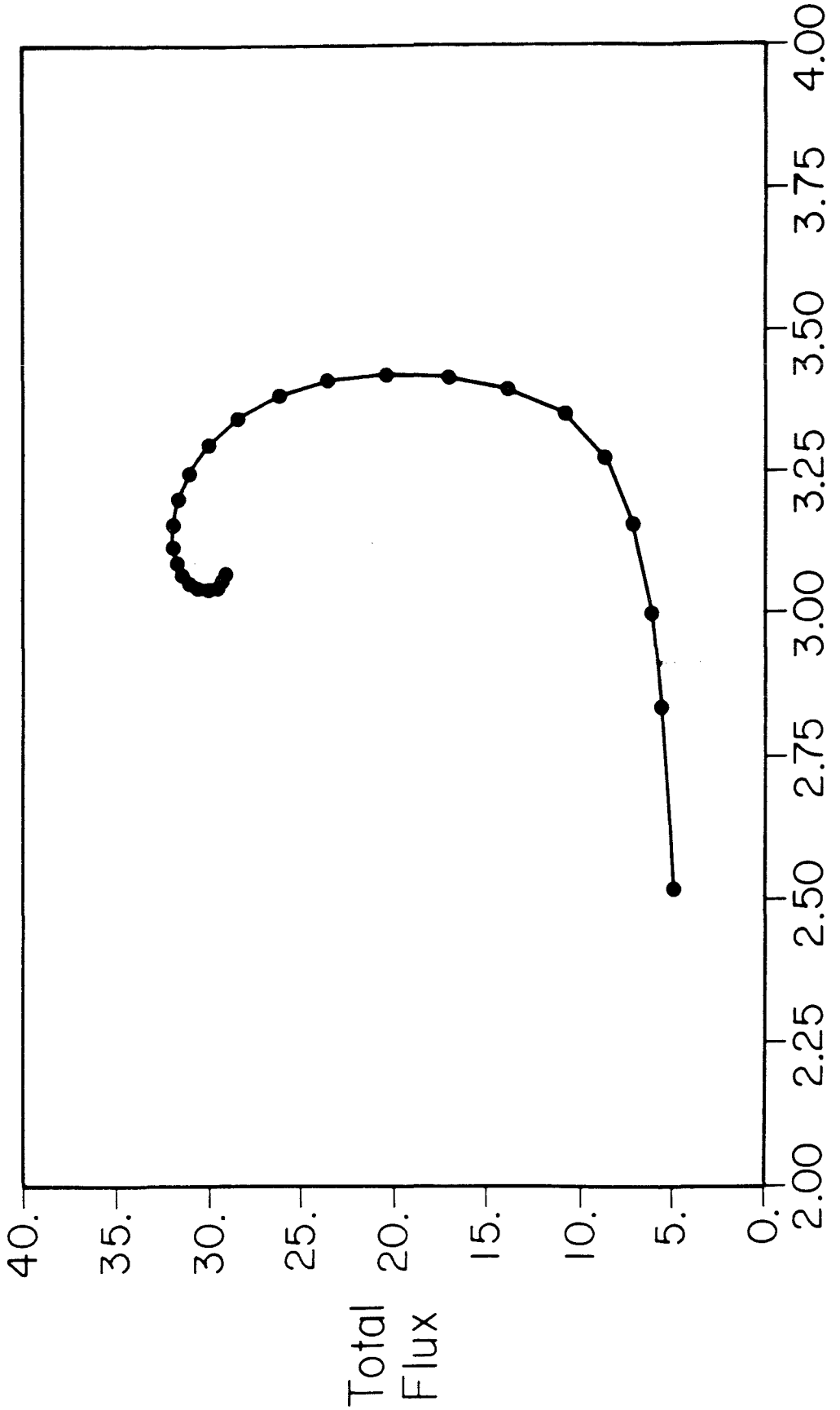
Total Flux
40.
35.
30.
25.
20.
15.
10.
5.
0.
2.00
2.25
2.50
2.75
3.00
3.25
3.50
3.75
4.00
Mean Outgoing Velocity

Figure 4.3

(a)

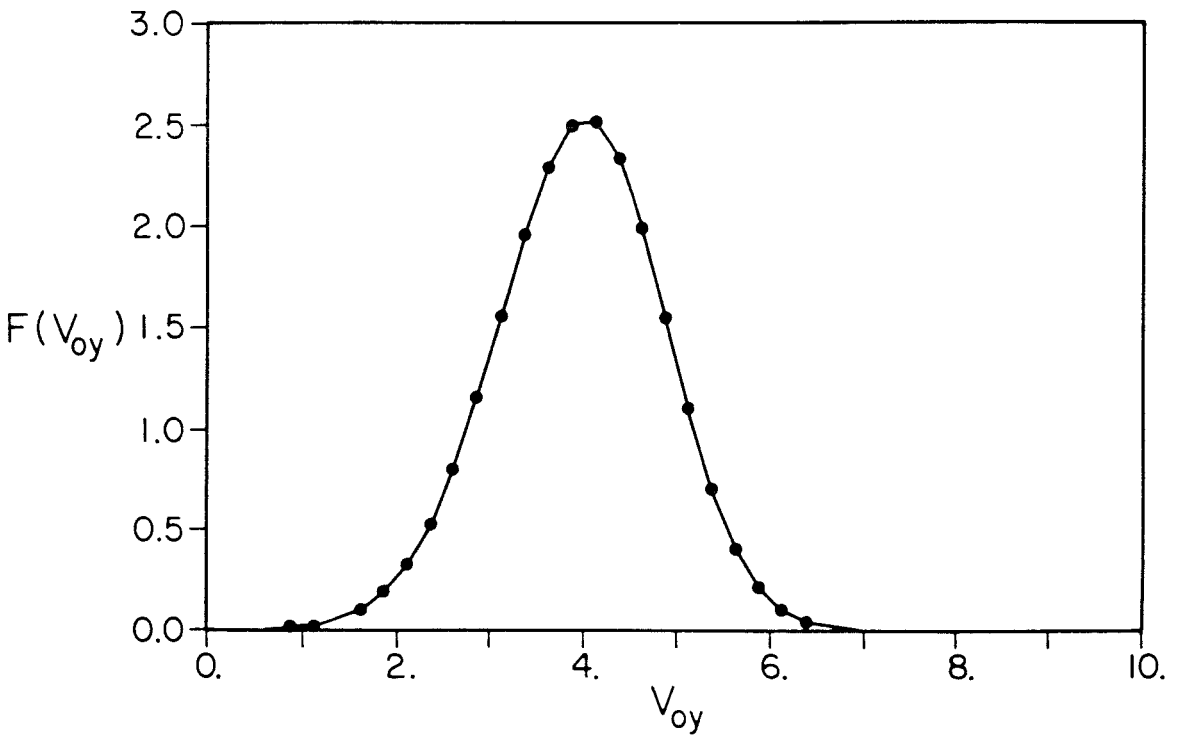

(b)

Figure 4.4

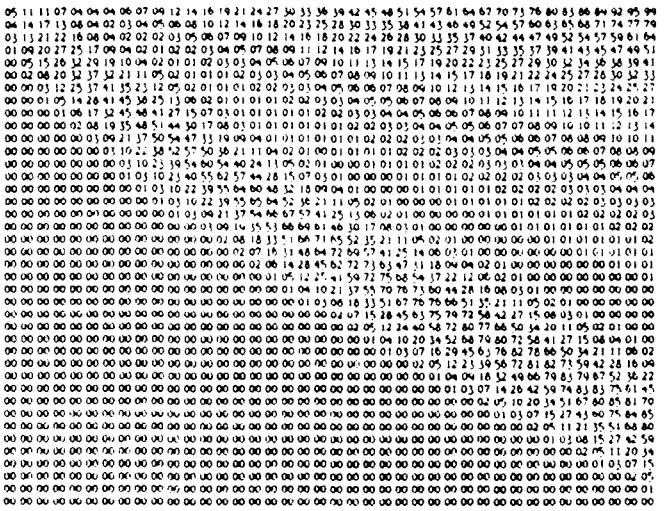

(a)

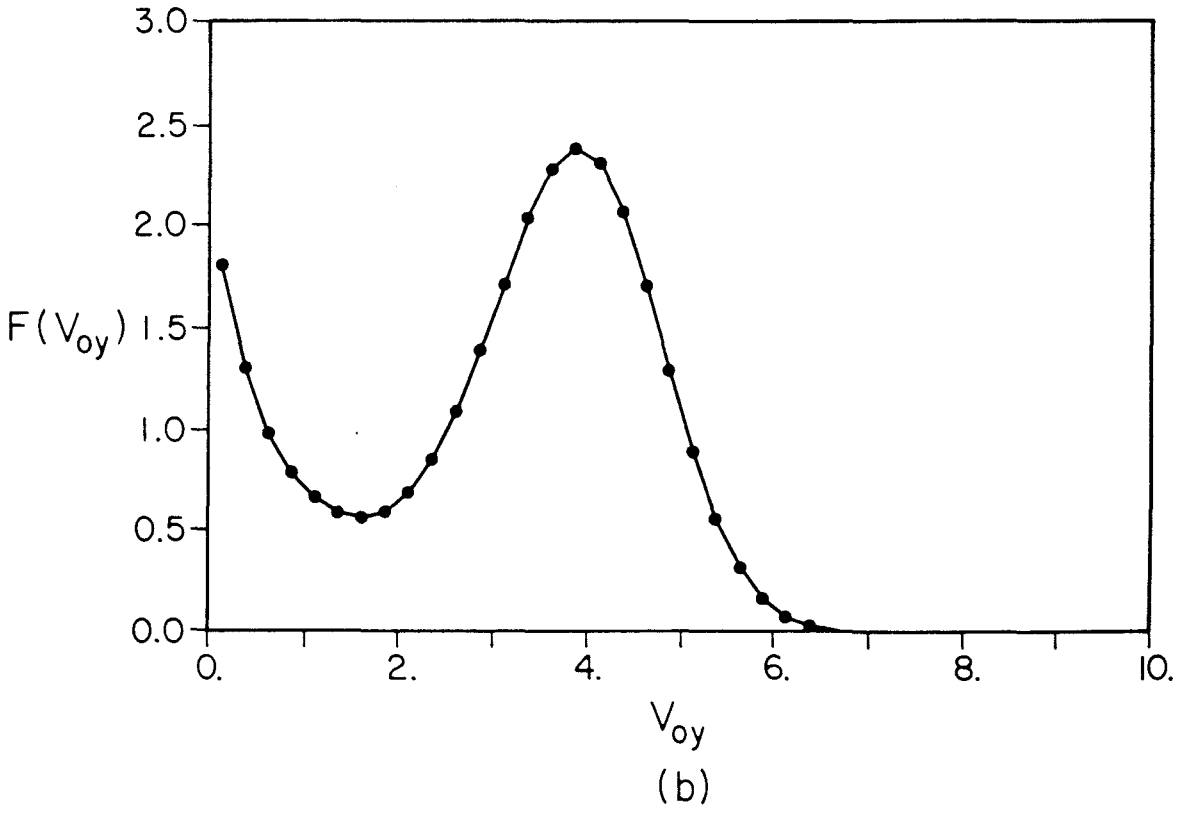

(b)

Figure 4.5

(a)

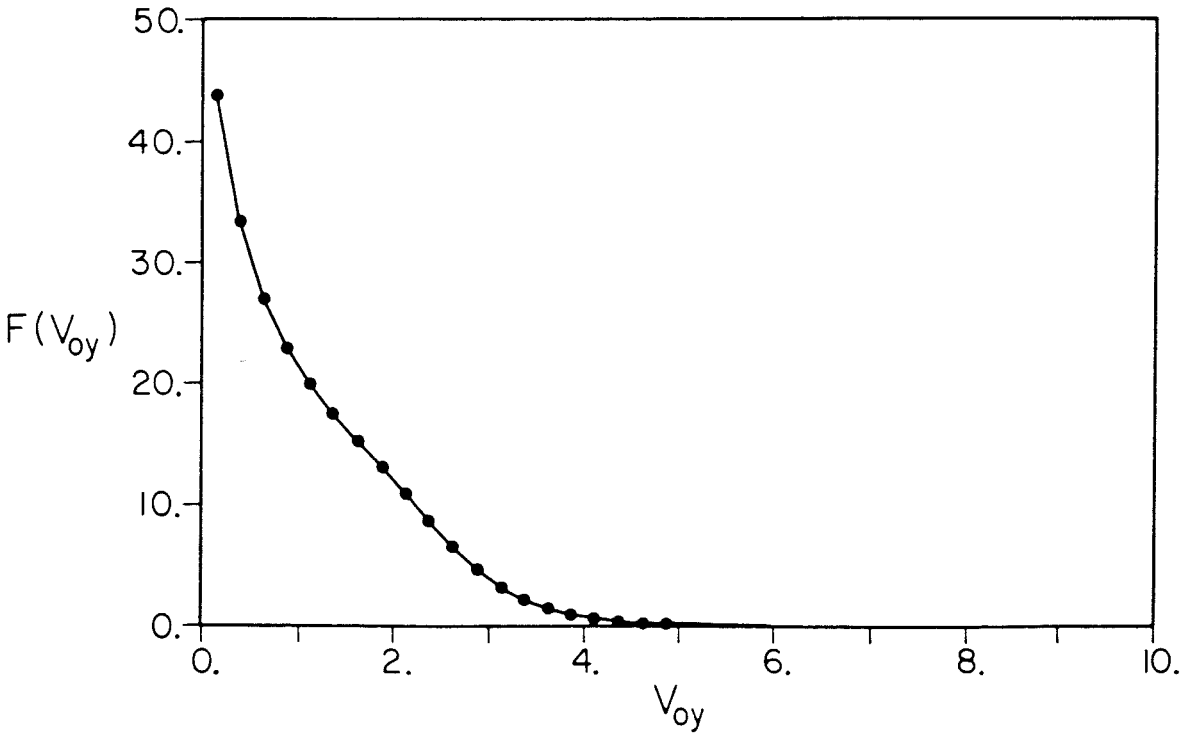

(b)

Figure 4.6

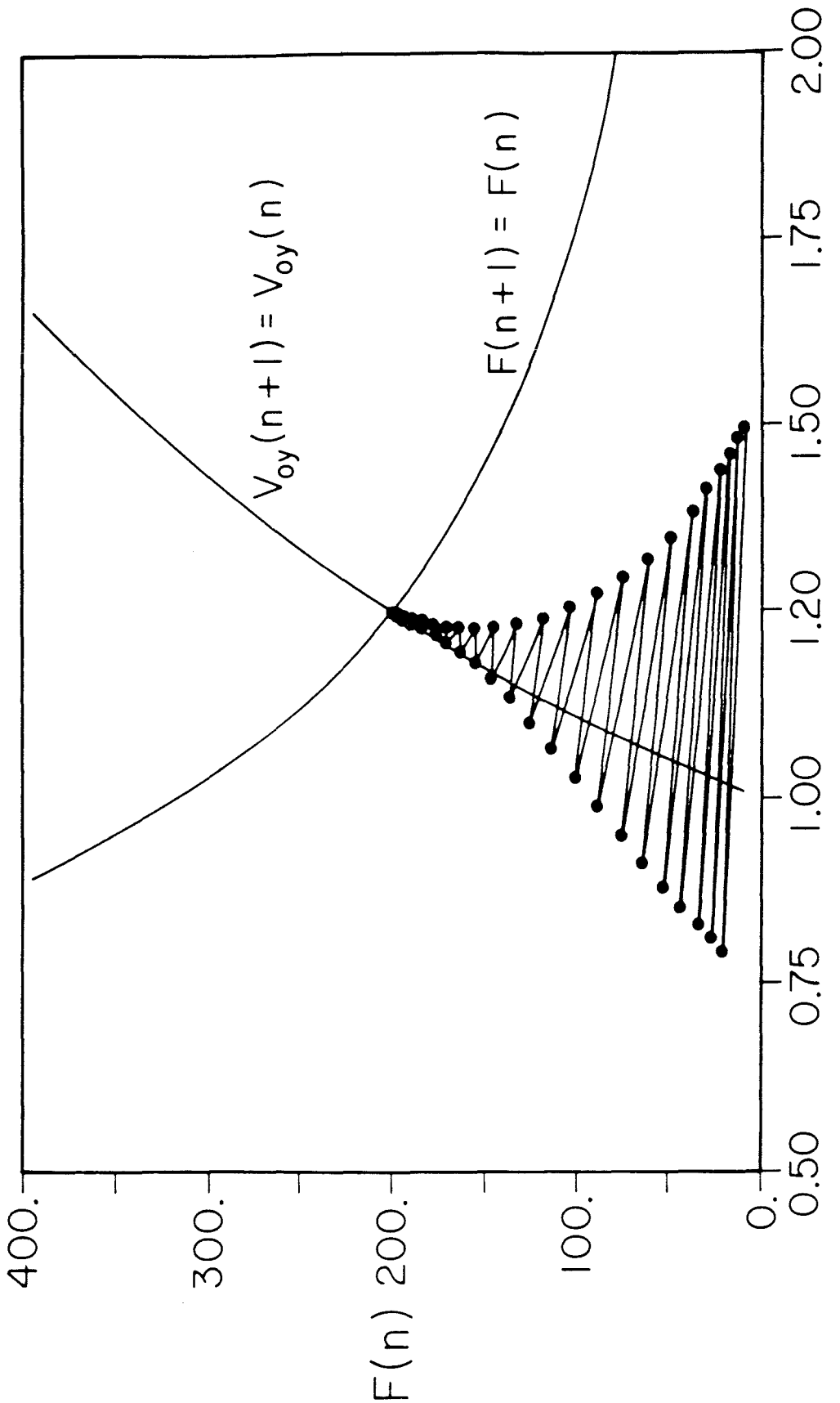
$V_{oy}(n+1) = V_{oy}(n)$
$F(n+1) = F(n)$
F(n)
400.
300.
200.
100.
0.
0.50
0.75
1.00
1.20
1.50
1.75
2.00
$V_{oy}(n)$

Figure 4.7

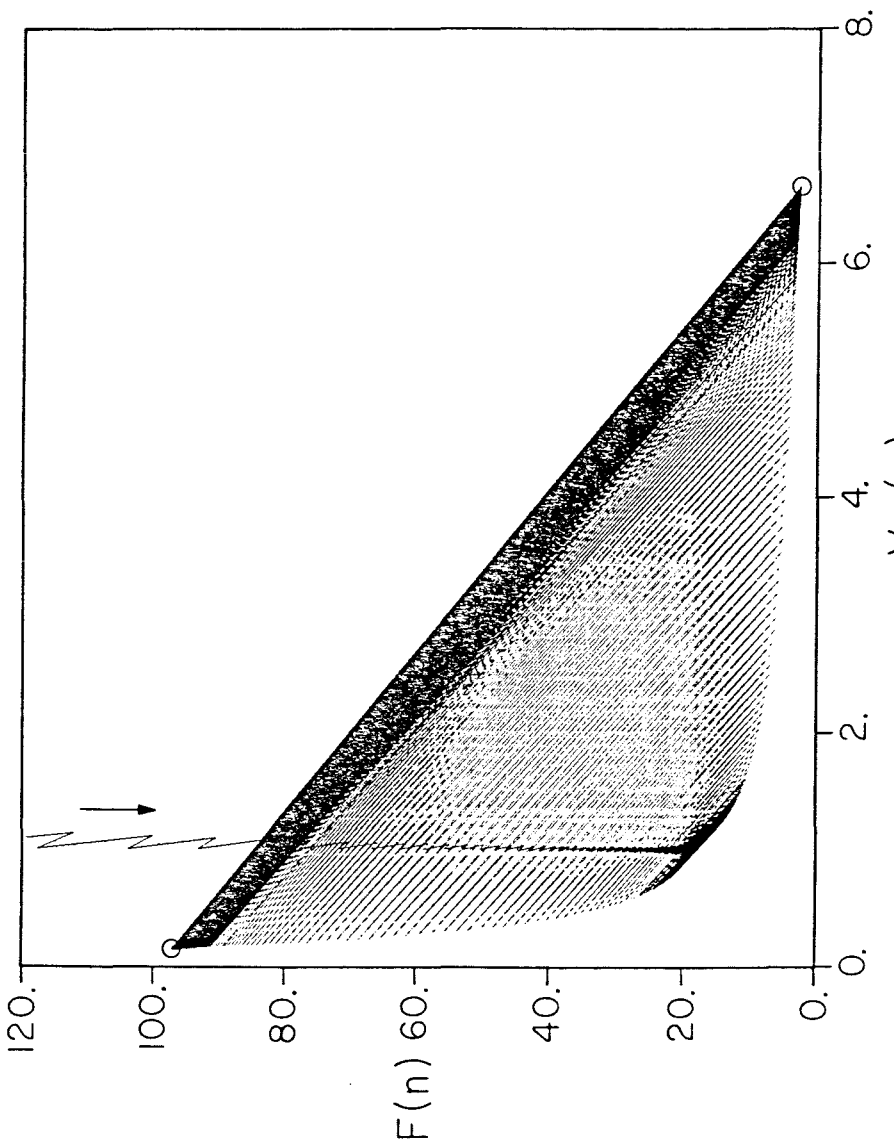

Figure 4.8

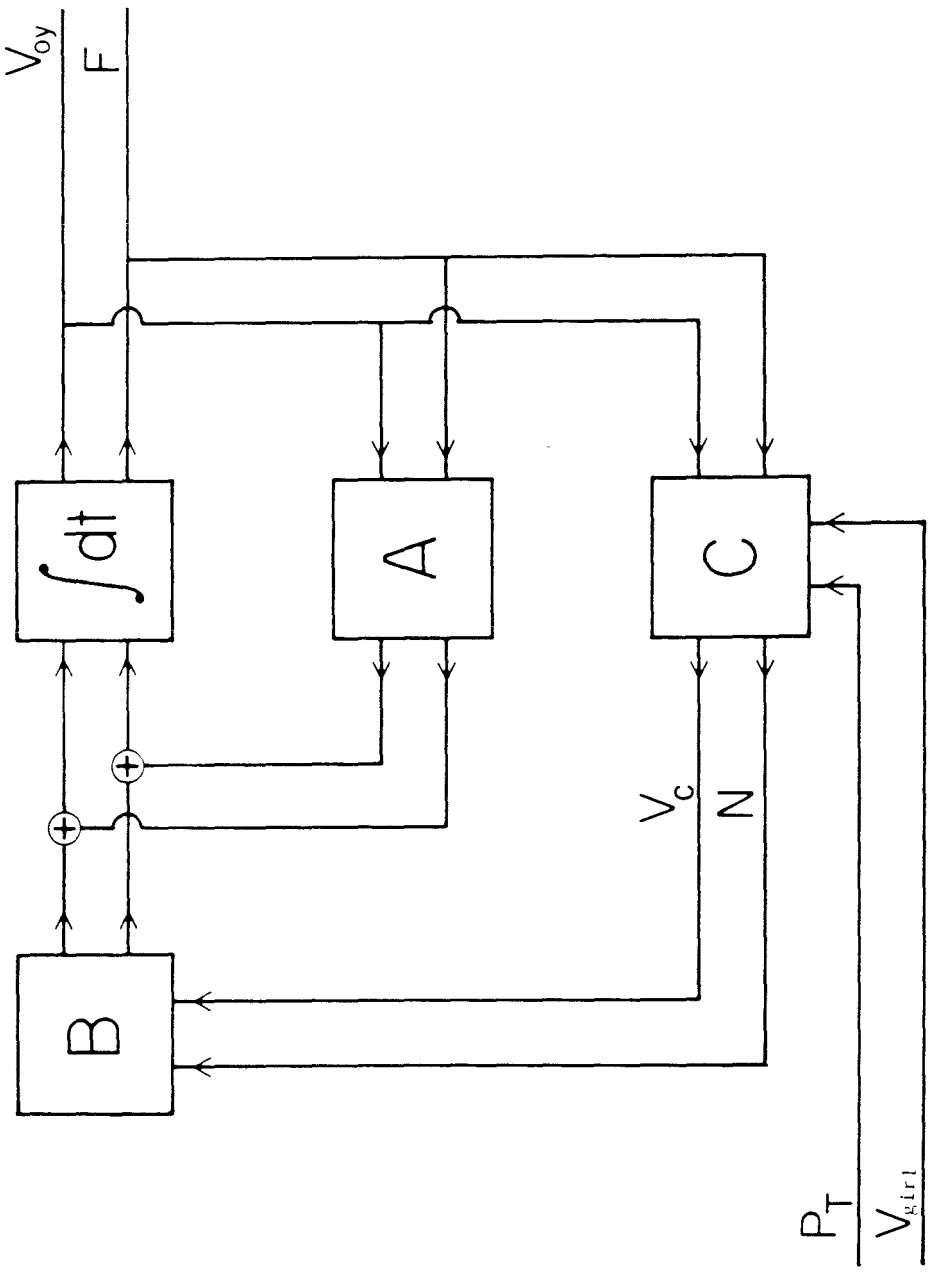

Figure 4.9

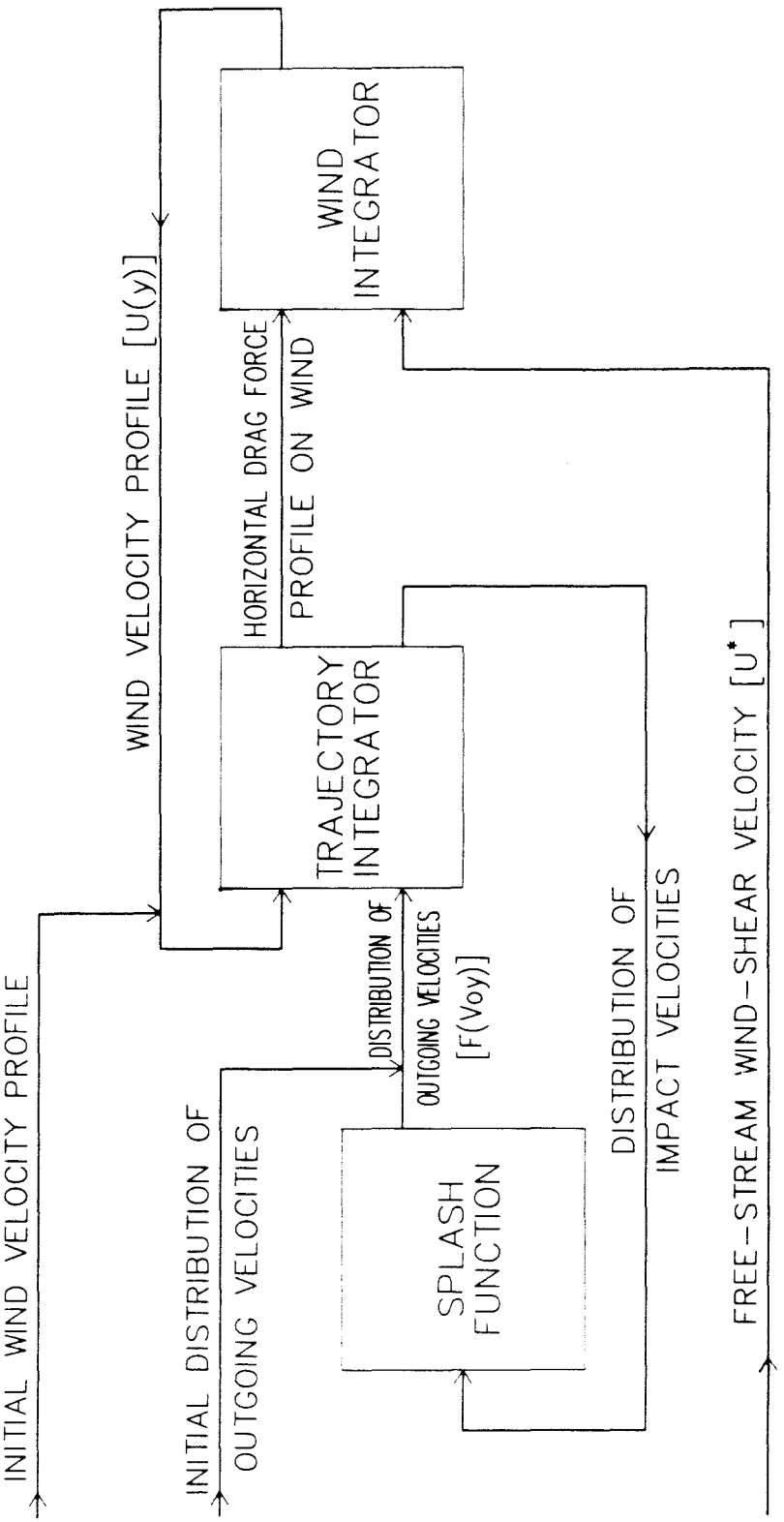
INITIAL WIND VELOCITY PROFILE
WIND VELOCITY PROFILE [U(y)]
INITIAL DISTRIBUTION OF OUTGOING VELOCITIES
TRAJECTORY INTEGRATOR
HORIZONTAL DRAG FORCE PROFILE ON WIND
WIND INTEGRATOR
DISTRIBUTION OF OUTGOING VELOCITIES [F(Voy)]
SPLASH FUNCTION
DISTRIBUTION OF IMPACT VELOCITIES
FREE-STREAM WIND-SHEAR VELOCITY [U*]

Figure 4.10

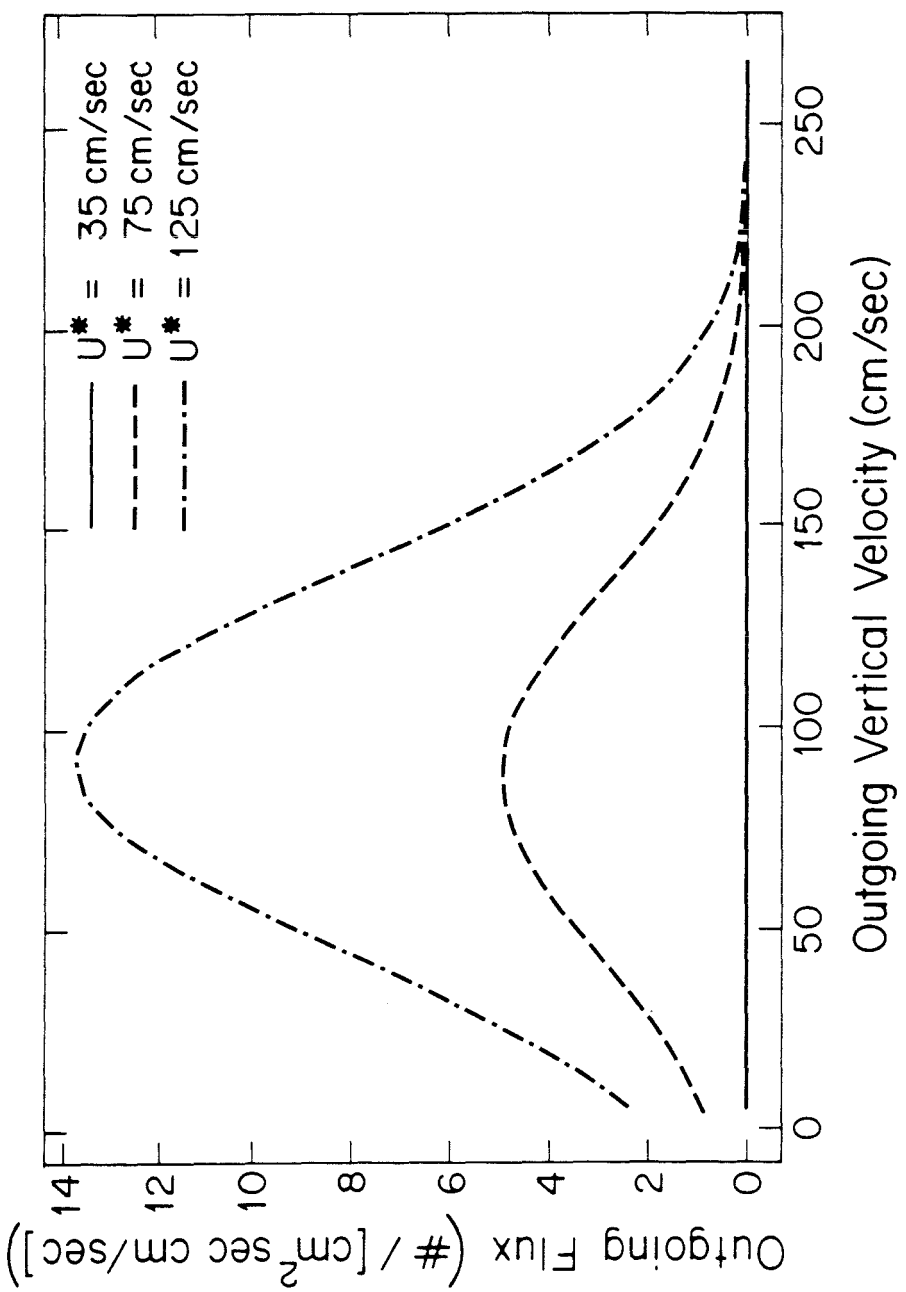
Outgoing Flux (# / [cm² sec cm/sec])
Outgoing Vertical Velocity (cm/sec)
U* = 35 cm/sec
U* = 75 cm/sec
U* = 125 cm/sec
0
2
4
6
8
10
12
14
0
50
100
150
200
250

Figure 4.11

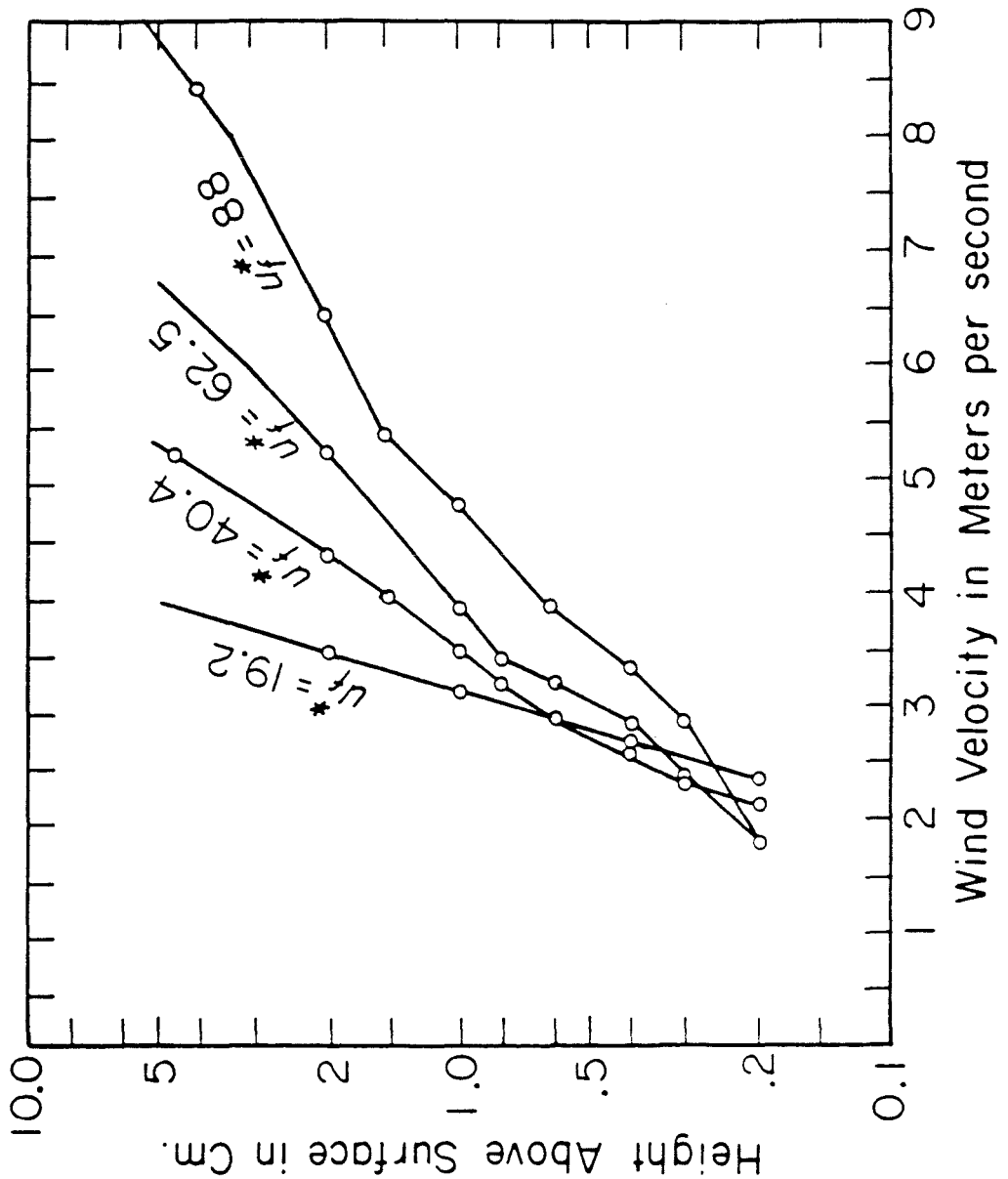
Height Above Surface in Cm.
10.0
5
2
1.0
.5
.2
0.1
1
2
3
4
5
6
7
8
9
Wind Velocity in Meters per second
$u_f^* = 19.2$
$u_f^* = 40.4$
$u_f^* = 62.5$
$u_f^* = 88$

Figure 4.12

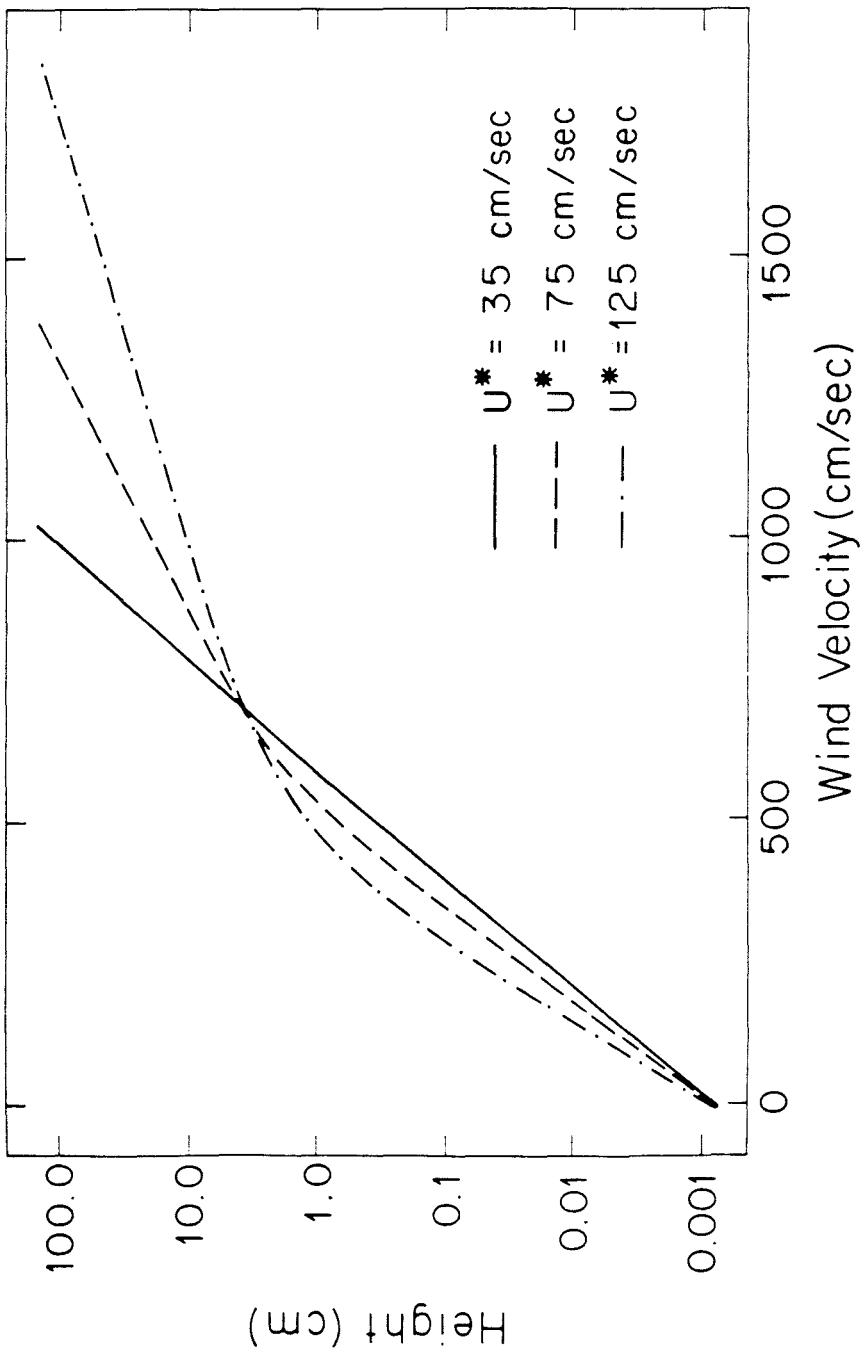
100.0
10.0
1.0
0.1
0.01
0.001
Height (cm)
0
500
1000
1500
Wind Velocity (cm/sec)
U* = 35 cm/sec
U* = 75 cm/sec
U* = 125 cm/sec

Figure 4.13

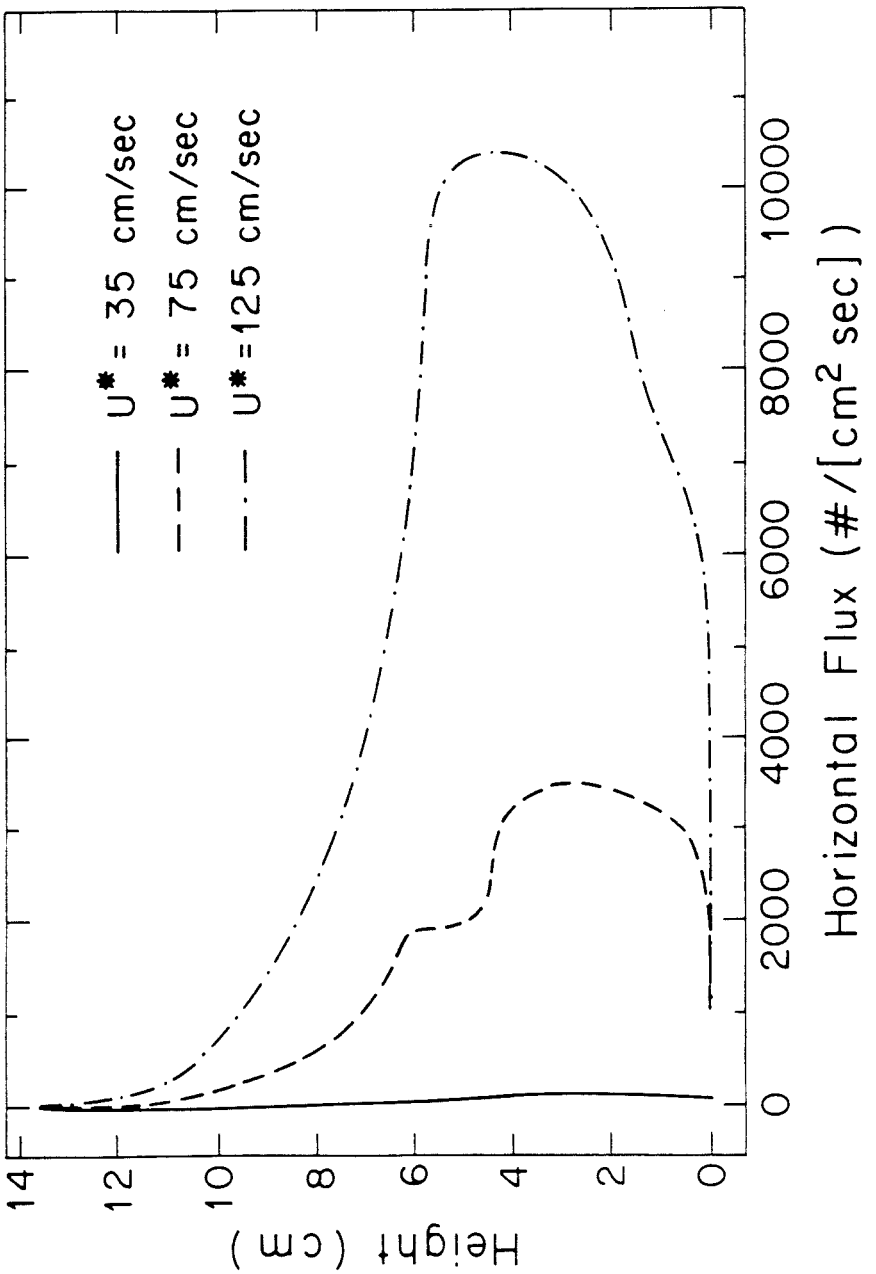
U* = 35 cm/sec
U* = 75 cm/sec
U* = 125 cm/sec
Height (cm)
Horizontal Flux (#/[cm² sec])
0
2
4
6
8
10
12
14
0
2000
4000
6000
8000
10000

Figure 4.14

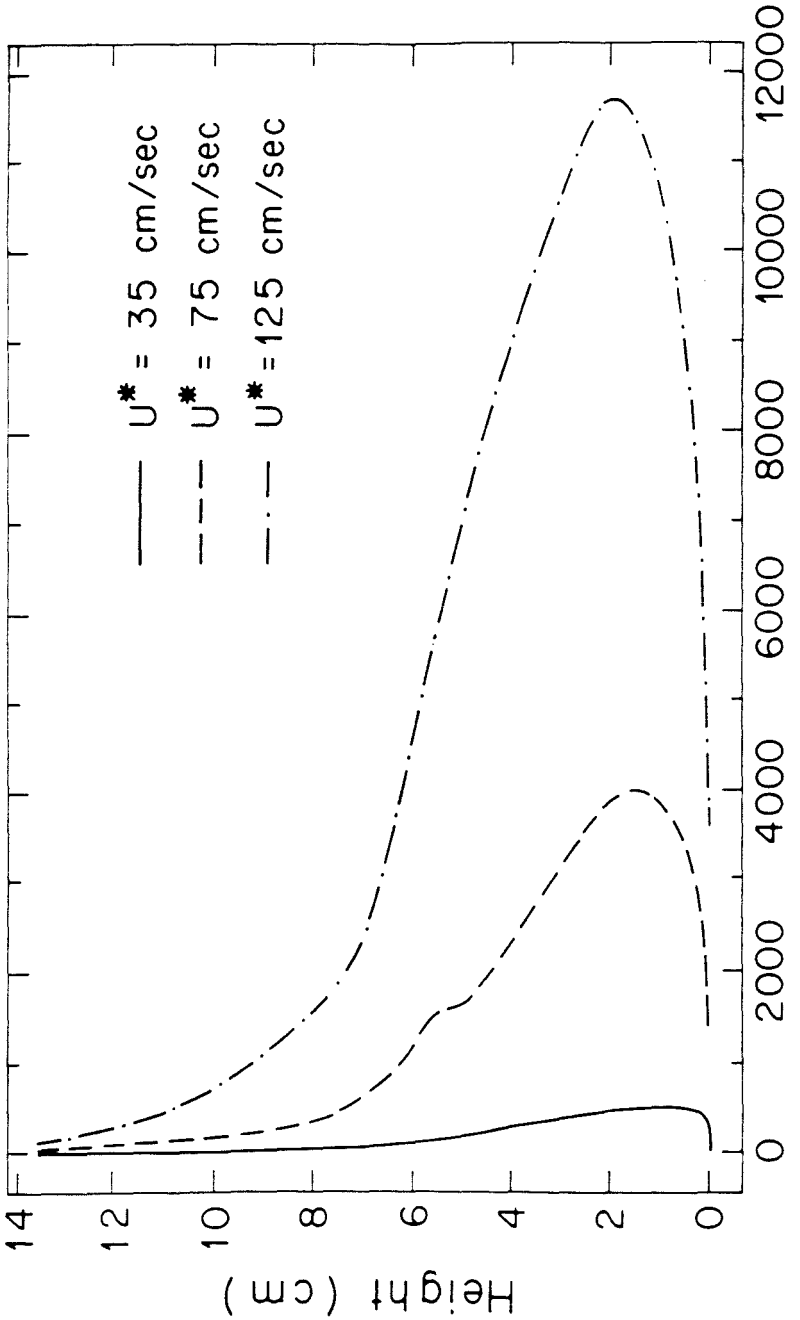
U* = 35 cm/sec
U* = 75 cm/sec
U* = 125 cm/sec
Height (cm)
Horizontal Flux (#/[cm2 sec])
0
2
4
6
8
10
12
14
0
2000
4000
6000
8000
10000
12000

Figure 4.15

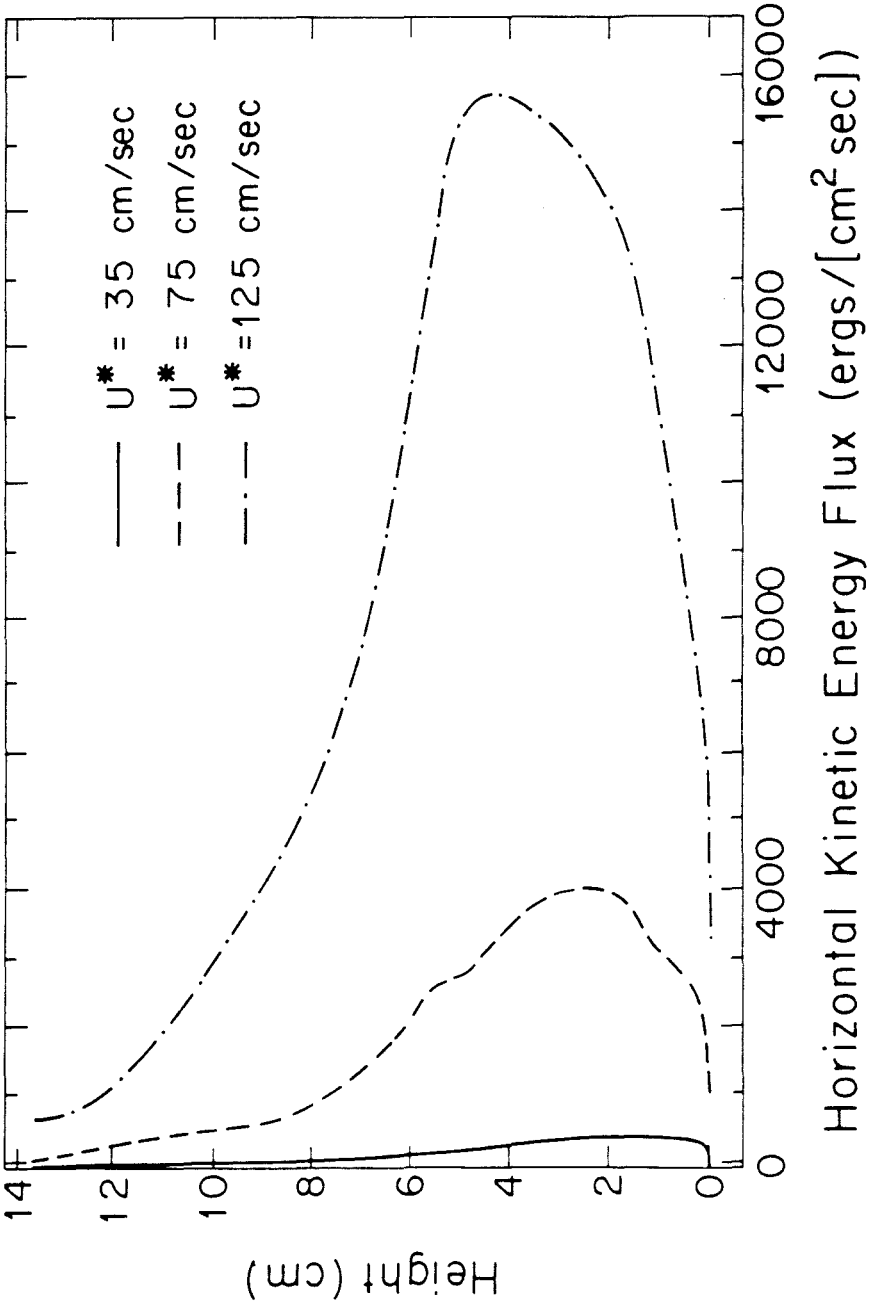
U* = 35 cm/sec
U* = 75 cm/sec
U* =125 cm/sec
Height (cm)
Horizontal Kinetic Energy Flux (ergs/[cm² sec])
0
2
4
6
8
10
12
14
0
4000
8000
12000
16000

Figure 4.16

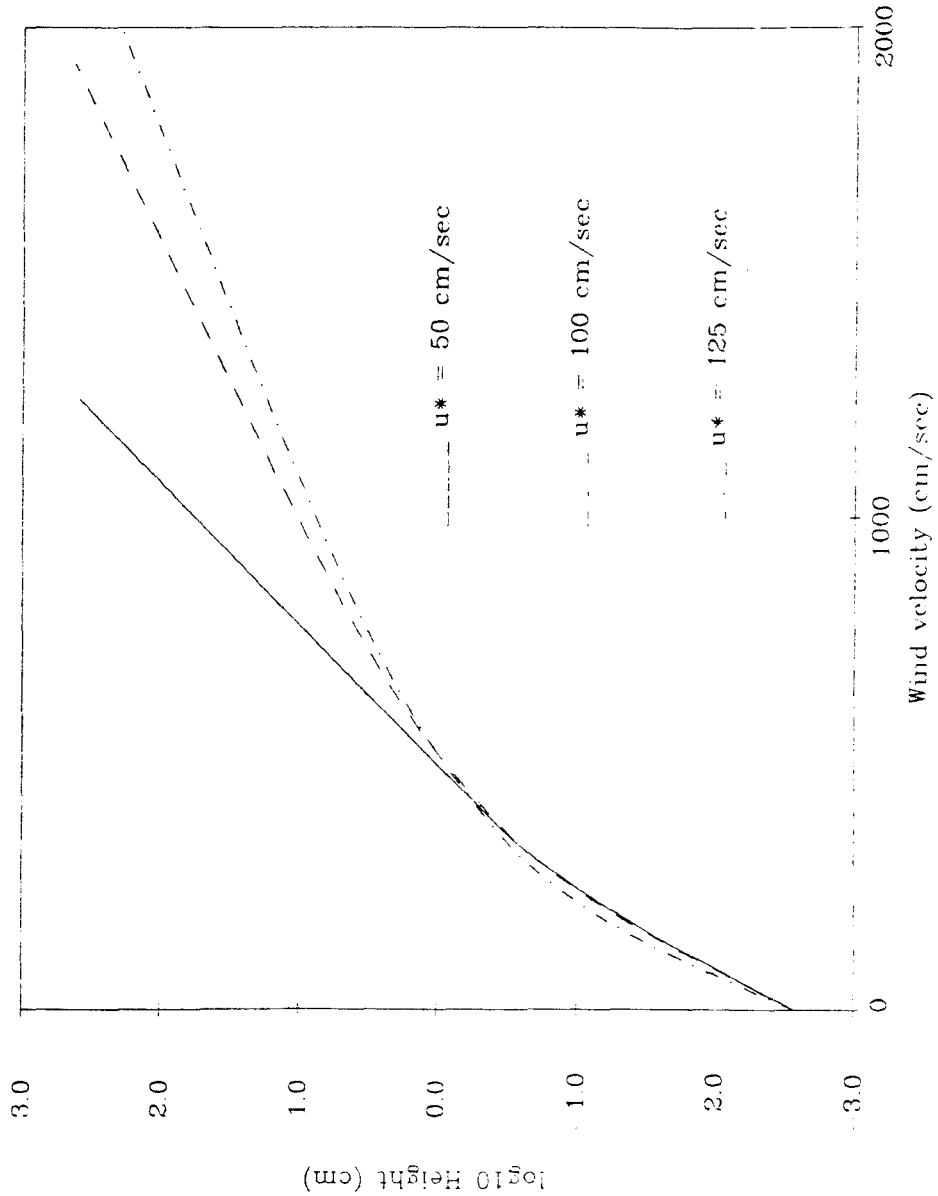
3.0
2.0
1.0
0.0
1.0
2.0
3.0
log10 Height (cm)
0
1000
2000
Wind velocity (cm/sec)
u* = 50 cm/sec
u* = 100 cm/sec
u* = 125 cm/sec

Figure 4.17

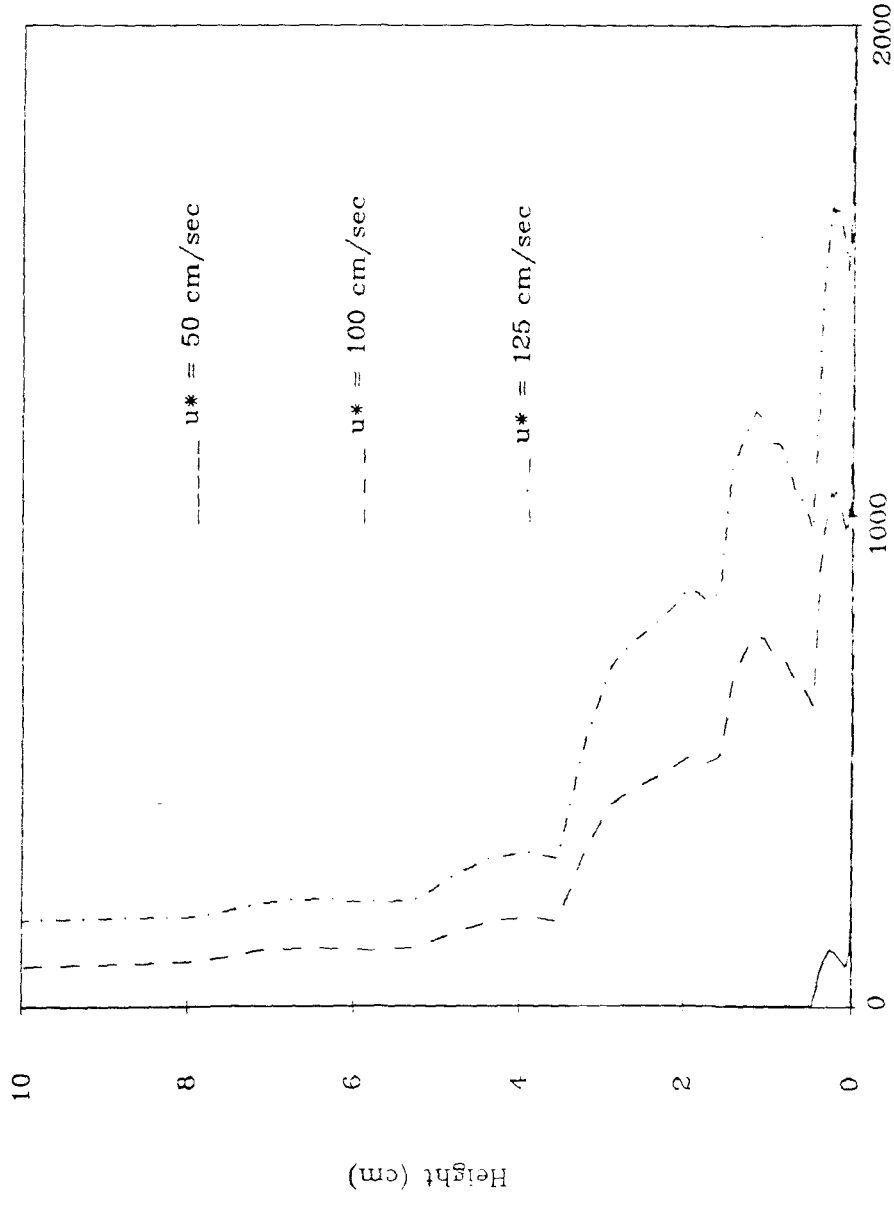
u* = 50 cm/sec
u* = 100 cm/sec
u* = 125 cm/sec
Height (cm)
0
2
4
6
8
10
0
1000
2000
Flux (#/[cm**2sec])

Figure 4.18

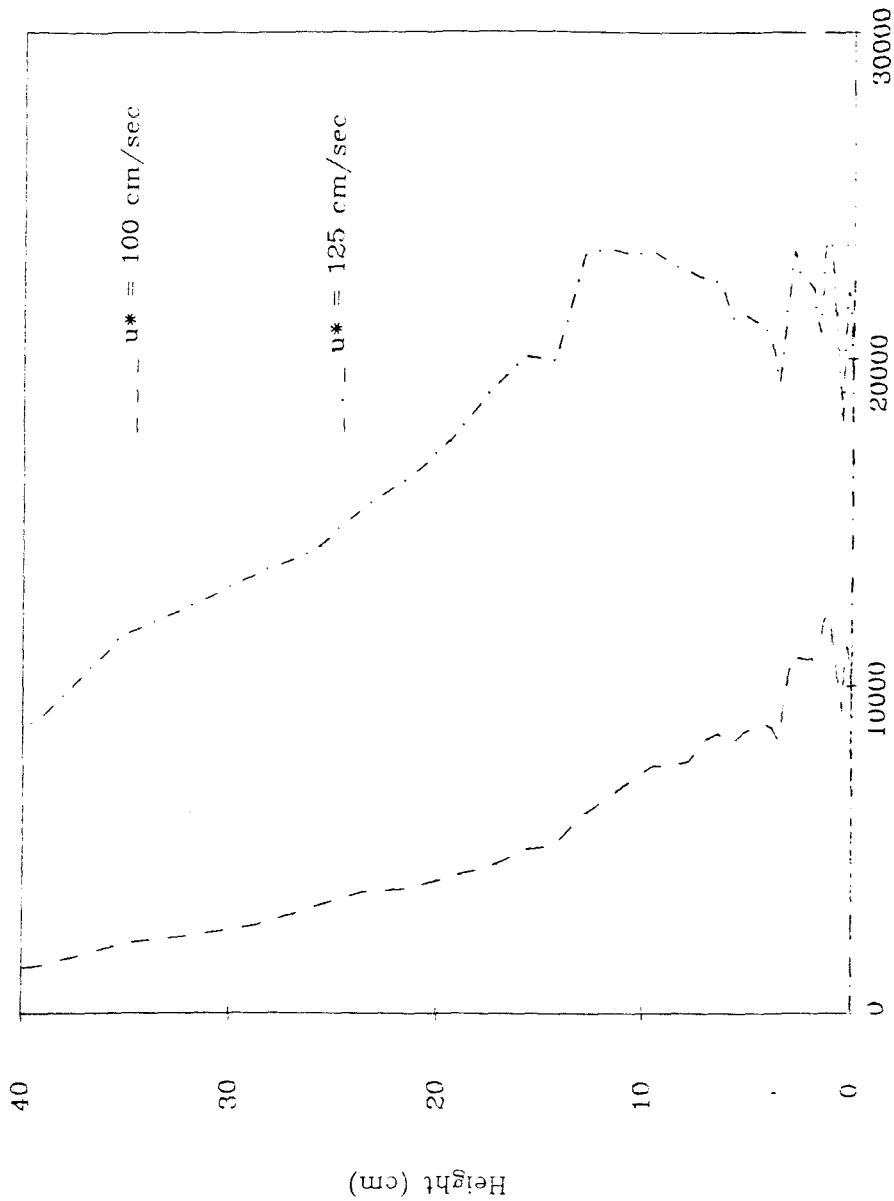
u* = 100 cm/sec
u* = 125 cm/sec
Height (cm)
0
10
20
30
40
0
10000
20000
30000
Kinetic energy flux (ergs/[cm**2sec])

Figure 4.19

Horizontal Outgoing Velocity (cm/sec)

Vertical Outgoing Velocity (cm/sec)	-200.	-100.	0.	100.	200.	300.	400.	500.	600.	700.
12.5	0000	0000	9999	0673	0028	0003	0002	0001	0001	0000
37.5	0000	0002	0178	0683	0131	0005	0002	0002	0001	0000
62.5	0000	0004	0255	0471	0138	0008	0004	0001	0001	0000
87.5	0000	0001	0056	0182	0034	0006	0004	0001	0001	0000
112.5	0000	0001	0004	0025	0011	0003	0007	0001	0001	0000
137.5	0000	0001	0004	0008	0009	0005	0005	0001	0001	0000
162.5	0000	0000	0004	0009	0012	0005	0003	0001	0000	0000
187.5	0000	0000	0001	0003	0006	0003	0002	0001	0000	0000
212.5	0000	0000	0000	0001	0003	0001	0001	0000	0000	0000
237.5	0000	0000	0000	0000	0001	0001	0001	0000	0000	0000
262.5	0000	0000	0000	0000	0001	0001	0000	0000	0000	0000
287.5	0000	0000	0000	0000	0000	0000	0000	0000	0000	0000
312.5	0000	0000	0000	0000	0000	0000	0000	0000	0000	0000
337.5	0000	0000	0000	0000	0000	0000	0000	0000	0000	0000
362.5	0000	0000	0000	0000	0000	0000	0000	0000	0000	0000

Figure 4.20

Impact angle (degrees)

Impact Velocity (cm/sec)	3.5	10.5	17.5	24.5	31.5	38.5	45.5	52.5	59.5	66.5
50.	0000	0000	0000	0000	0000	0178	0000	0004	0000	9999
150.	0673	0000	1074	0000	0257	0000	0000	0000	0000	0000
250.	0032	0269	0107	0057	0000	0000	0000	0000	0000	0000
350.	0007	0014	0077	0000	0000	0000	0000	0000	0000	0000
450.	0006	0012	0033	0000	0000	0000	0000	0000	0000	0000
550.	0006	0026	0024	0000	0000	0000	0000	0000	0000	0000
650.	0001	0014	0011	0000	0000	0000	0000	0000	0000	0000
750.	0000	0006	0010	0000	0000	0000	0000	0000	0000	0000
850.	0000	0002	0005	0000	0000	0000	0000	0000	0000	0000
950.	0000	0000	0004	0000	0000	0000	0000	0000	0000	0000
1050.	0000	0000	0001	0000	0000	0000	0000	0000	0000	0000
1150.	0000	0000	0000	0000	0000	0000	0000	0000	0000	0000
1250.	0000	0000	0000	0000	0000	0000	0000	0000	0000	0000
1350.	0000	0000	0000	0000	0000	0000	0000	0000	0000	0000
1450.	0000	0000	0000	0000	0000	0000	0000	0000	0000	0000

Figure 4.21

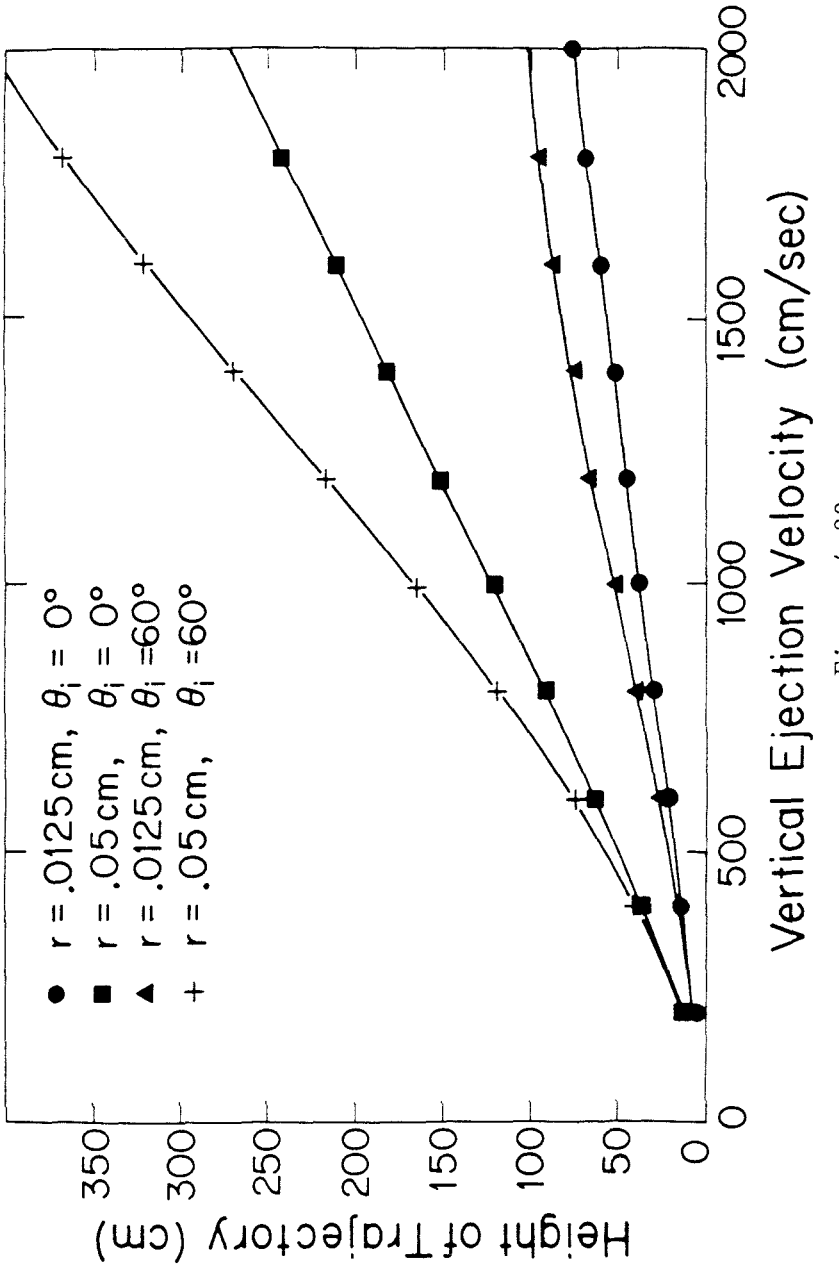
Height of Trajectory (cm)
Vertical Ejection Velocity (cm/sec)
0
50
100
150
200
250
300
350
0
500
1000
1500
2000
● r = .0125 cm, θi = 0°
■ r = .05 cm, θi = 0°
▲ r = .0125 cm, θi = 60°
+ r = .05 cm, θi = 60°

Figure 4.22

CHAPTER V. THE EVOLUTION OF A SAND SURFACE UNDER EOLIAN SALTATIONIMPACTS: RIPPLE FORMATION

> "I also noticed, on an occasionwhen sand was accumulating and at the same time being rippled by the wind, that the surface was not continuous, but composed of scattered sand-grains which darted hither and thither as ants when the nest is disturbed."
>
> -Vaughn Cornish

Under the low light of early morning or late afternoon, a traveller of arid lands cannot fail to notice the beauty of the sand dunes that dot the desert. An adventurous sort might even stop his vehicle to admire the form and the shape that Nature has so meticulously sculptured out of mere sand grains. A far greater reward awaits those "wanderers of the wasteland" (Zane Grey) who venture out onto the dunes. A new level of detail is revealed. The backs of the dunes, so smooth in appearance from a distance, are found to possess regular undulations of no less beauty than the dunes themselves: the sand ripples.

In bold mockery of human inquiry, Nature has chosen to make the molding of these seemingly simple objects a complicated matter, thereby closely guarding the secret of why ripples form. In attempting to make progress toward solving this mystery, we will make a number of simplifying assumptions. We decouple the saltation process from the

evolution of the bed. Thus, we assume that surface particle transport is driven by saltating grain-bed impacts, and that the flux of saltating grains impacting an imaginary *flat* surface, parallel to the mean elevation, is, on the average, independent of position, even in the presence of small-scale topographical bed features (ripples) upstream. These assumptions are in accordance with the results of Chapter IV, where we found that fluid stresses are unlikely to play a role in moving surface grains during steady-state saltation, and that the distribution of particle trajectories and impact velocities is broad (meaning that variations in flux resulting from the changing slope of surface topography are smeared out). This contradicts Bagnold's (1941) picture of saltation, in which the grains move along paths which are characterized by a certain length so that small flux differences onto surfaces of different slopes manifest one characteristic path length downstream (however, see observations later in this chapter). Thus, the surface grains are pictured as being compelled to reptate by an externally controlled driving force: the impacting saltating grains.

The influence of small fluctuations on a dynamical system can sometimes assume a dominant role in determining its future evolution.

For instance, consider the example of a perfectly round marble placed at the very top of a perfect, levelled hemisphere. In the absence of any thermal or aerodynamic variations, the ball will (at least within the realm of classical mechanics) remain at the top. However, the slightest fluctuation in the temperature of some portion of the ball will cause it to change shape, leading to an imbalance which will drive the motion of the marble in some direction, eventually leading it to fall off the hemisphere. On the other hand, a marble placed at the bottom of a hemispherical bowl will stay put. The former case constitutes an unstable equilibrium, the latter a stable equilibrium.

Likewise, treating the sand in a continuum sense, a perfectly uniform flux of saltating grains (of infinitesimal size) striking a flat bed of like grains and transporting a certain fraction of them at each impact a definite distance will result in the maintenance of the flat bed. However, simply by introducing the discrete nature of the impacts and the surface, there will be fluctuations in the surface slope and the surface grain transport rate. Further, there will be statistical fluctuations in the saltation flux due to wind gusts. The question then arises as to whether the sand surface is stable or unstable under these various fluctuations,

i.e., is the sand surface analogous to the marble on the top or the bottom of the bowl? The transition of a flat surface to one composedof ripples in Nature suggests that the surface is initially unstable under saltation impacts.

Bagnold (1941) analyzed the stability of a sand grain surface in saltation and came to the conclusion that a perturbation to the surface would grow, because upstream-facing portions of a hole or a bump receive increased impact flux, due to their increased exposure to the low-angle impacting grains; therefore more material would be evacuated and the disturbance would increase in size. The depression created presumably would be subject to increased capture of reptation flux; however, reptating grains are incident at greater angles to the horizontal than saltating grains, and so the change in the flux of captured reptating grains will be less relative to the change in saltating grain flux experienced by the surface perturbation. Indeed, we will show that simple assumptions concerning the transport rate of ejected bed grains will lead to the conclusion that regions confined to saltation impact transport alone can, in steady-state, assume either a flat or monotonically increasing shape only. The gentle slopes of ripples imply

that there is a competing process which tends to smooth surface roughness.

We will adopt the point of view that statistical fluctuations play a large role in governing ripple formation, from initial disturbances in a flat sand bed, to the development of periodic topography. This idea was arrived at and developed in conjunction with P.K. Haff. Further, we will find that the form of ripples is dictated by a balance between surface roughening, and surface smoothing processes.

It is not our intention to provide a detailed model of ripple formation. We assert that sufficient information concerning the reaction of surfaces to saltating grain impacts (see Chapter III) is not yet in hand to do this. However, we will, through experiment and theoretical considerations, identify what we believe to be the important physical components of the ripple formation process, and describe a framework for placing these components into a predictive model.

Before delving into the particulars of the problem, we first journey to a sand dune west of the Salton Sea in Imperial County, California, to perform some qualitative observations on ripple formation (see also Sharp, 1963, for a description of evolving ripples). A westerly

wind is blowing at about 15-25 mph, with occasional gusts up to roughly 40 mph. Much of the Salton Sink is engulfed in an intense dust storm, and sand is saltating with vigor on our dune. An experimental plot on a stretch of the dune near the top has been artificially flattened and smoothed in a manner described later in this chapter, and the sand surface is observed by redirecting the sun's rays (with a mirror) nearly parallel to the bed. Initially, the surface of the plot appears rather flat; however, after about five to ten seconds of intense saltation, the bed, as viewed between wind gusts, takes on a mottled appearance: the surface has become decidedly rougher, leading to a somewhat random pattern of illuminated grains and shadows. The length scale of this topography appears to be about 0.5 cm. The surface remains in a similar state for slightly over a minute. Then the eye gradually begins to perceive the formation of ordered groupings of grains. Some of these piles of grains, particularly the small ones, seem to disappear for no apparent explanation; others augment their cache of grains. As the groupings of grains grow in size, and acquire some coherence transverse to the wind, they start to resemble smaller versions of the ripples surrounding our experimental area, and may be termed "proto-ripples." It is then possible

to observe directly what the proto-ripples are doing: smaller ripples, by virtue of the fact that they travel faster, overtake larger ones ahead of them. The two ripples seem to merge together. In many cases, this agglomerated ripple moves off as a single entity. In other cases, the ripple which began in front moves off with a smaller size than previously. The ripple behind had "eaten" part of the larger ripple. Eventually, through merging and exchange of material between ripples of disparate size, the proto-ripples become relatively uniform in wavelength, approaching the size of the surrounding ripples. At this particular site, during the period we observed the process, including occasional episodes of sporadic saltation, this final merging required a rather long time: about thirty minutes.

In this chapter, we will concentrate on understanding the physical mechanisms operating in the process described above. We begin with a means of quantifying the shapes of sand ripples, then utilize this method for the measurement of evolving surface topography during saltation, and finally apply theoretical and computational methods in an attempt to elucidate the mechanics underlying ripple formation.

The Measurement of Eolian Sand Ripple Cross-Sectional Shapes

One critical parameter that must be considered in any theory of ripple formation is the cross-sectional shape or profile of the ripples in the direction perpendicular to the ripple crest, i.e., along the motion of the ripples. This direction will be defined as the ripple axis. The ripple wavelength (trough-to-trough distance) and ripple index (wavelength divided by maximum height-or-amplitude), commonly used to characterize sand ripples, are a subset of the information obtained when measuring the profile. Several questions concerning the nature of ripples cannot be answered without detailed knowledge of the ripple shape. For instance, the influence of the apparent dip of the dune surface along the ripple axis (subsequently referred to as the apparent dip) on the slope angle of the ripple relative to the mean dune surface can only be determined by a complete measurement of the profile. Note that, in our definition, the apparent dip is negative for ripples moving upslope and positive for ripples moving downslope (see Figure 5.1).

Various techniques have been employed by previous investigators to determine the shapes of ripples in sand. Cornish (1935) stretched a thread from crest to crest and measured downward to obtain the height.

Sharp (1963) placed a piece of Plexiglas across the ripple crests and measured the depth of the sand surface; he also impregnated sand ripples with a Glyptol solution for scrutiny in the laboratory. Plaster of paris molds were obtained by Allen (1969) to examine shapes of fluvial ripples. Seppala and Linde (1978) used stereophotography to produce topographic maps of eolian ripples in a wind tunnel. This last procedure is perhaps too delicate for field work, and requires a large amount of data reduction. In fact, although all these techniques produce useful information, they place a strain on the patience of the investigator; therefore, only a small number of ripple shapes may be obtained in practice.

We have designed and implemented a method for measuring sand-ripple profiles which is characterized by its ease of use in the field and its high accuracy. The method is based on the fact that a straightedge suspended over a surface whose profile is unchanging in one direction will, when properly illuminated, cast a shadow of length proportional to the perpendicular distance between the surface and the straightedge. For ripples, we require only that the cross-sectional shape be constant over the distance parallel to the ripple crests between the maximum and minimum shadow length, a distance which is typically only a fraction of a

centimeter. By aligning the path of the illumination along the crest of the ripples and the straightedge perpendicular to this, ripple profiles are easily obtained directly from the shadow lengths. A schematic illustration of the method is presented in Figure 5.2. The shadow lengths can be photographed, even under adverse dune field conditions, and brought back to the laboratory for careful measurement. We note that this technique may be adapted to the study of fluvial ripple formation, with the added difficulty of obtaining a collimated source of illumination under water. All field measurements described in this section on static ripple profiles were performed at the Kelso Dunes in the Mojave Desert of eastern California (described by Sharp, 1966). The idea to use shadows to measure ripple profiles originated with R.P. Livi, initial tests of the apparatus were carried out with the aid of R.S. Andersonand R.P. Livi, and the data reported here were obtained with the field assistance of P.K. Haff.

Field Procedure

The apparatus used in measuring the ripple profiles consists of a straightedge with support, a mirror mounted on a tripod to direct the sun's rays in the desired direction, a Brunton Compass to determine the

inclination of the straightedge relative to the horizontal plane and a Canon AE-1 35 mm camera. A post of known height was fastened onto the straightedge and its shadow used to measure directly the angle of the incoming illumination. In addition, a scale was affixed to the straightedge for accurate conversion of the ripple profiles to centimeters. Figure 5.3 shows this equipment deployed in the field.

After choosing a particular site, approximately one to two minutes are required in order to set up the apparatus and photograph the ripple shadow. The first step is to align the straightedge perpendicular to the ripple crests. This can be done to within 1°-2°. The straightedge supports are pushed into the sand until the straightedge is close to, but does not touch, the ripple crests. The straightedge need not be parallel to the plane in which the ripples lie. Then, using the shadow-casting post as a guide, the mirror is positioned to direct the sun's rays perpendicular to the straightedge. Finally, the camera is positioned directly over the straightedge and the shadow is photographed onto slide film This records the ripple shapes relative to the straightedge slope. A Brunton Compass is placed upon the straightedge to record its inclination with respect to the horizontal. The apparent dip of the surface upon which the

ripples lie can later be determined by adding to this the slope angle between the straightedge and the line connecting successive ripple-trough minima, which is a product of the analysis.

Analysis

The slides are projected onto a digitizing table for analysis and the ripple shadows are analyzed to obtain the ripple height as a function of the distance along the line connecting successive troughs. The coordinates of the divisions on the scale, of the post shadow and of the edge of the straightedge give the scale of the picture, the angle of illumination and the base line from which ripple shadow lengths will be measured, respectively. The uncertainty in digitizing the coordinates of the scale and the straightedge leads to an error in ripple profile of less than ten percent of the mean surface sand-grain diameter encountered in our studies. This mean grain size was about 0.027 cm. The uncertainty in the illumination angle led to a systematic error in the ripple profile of no more than half of the mean grain size.

The shadow cast by the straightedge is reproduced with great clarity in the photographs (see Figure 5.4). The typical roughness of the surface of the ripples is observed to be about one grain diameter. This

roughness introduces some difficulties in defining the edge of the shadow. For instance, a grain will often protrude from the shadow and be partially illuminated, like lunar mountains at the terminator, creating a double shadow terminus. At each point along the ripple, we chose the approximate mean of the two possible extreme edges of the shadow. The difference in the ripple profile between digitizing the same ripple at both upper and lower extrema (on the average) is no more than about one-half of a grain diameter.

Careful examination of the shadow terminus also reveals that focus is somewhat critical in these studies. Although through the center of the photograph the details were quite sharp, the shadow became slightly fuzzy close to either side of the photograph. Individual grains were distinguishable throughout the shadow terminus, but a higher quality lens would ensure a sharp focus along the entire length of the shadow. The errors introduced by this effect were somewhat less than those arising from the other uncertainties in this investigation. Approximately one hundred points on each ripple were recorded.

The digitzed data are automatically conveyed to a computer for further study. Prior to any additional analysis, the shadow lengths were

smoothed using a technique due to Tombrello (1985). In order to smooth a data set $y(x_i)$, Tombrello's algorithm takes a weighted average of the data in the vicinity of x_i, with the weight being determined by the normal distribution function of the difference between the datum at x_i and that at the nearby points. The smoothed data set $y_S(x_i)$ can be expressed as

$$y_S(x_i) = \frac{\sum_{j=i-n}^{i+n} y(x_j)\, e^{-[y(x_i)-y(x_j)]^2/2\sigma^2}}{\sum_{j=i-n}^{i+n} e^{-[y(x_i)-y(x_j)]^2/2\sigma^2}} \qquad (5.1)$$

where n is the number of points to each side of x_i which are considered in the smoothing process and σ is the level of noise which is to be eliminated from the data. For our data, y is the length of the shadow as a function of x, the distance along the straightedge. The quantity σ for the ripple profile data was chosen to be one grain diameter. Thus, we did not consider the structure of the ripple surface below the scale of the individual grain, although this topic would be worthy of further study and the ripple shadow technique is well-suited to it. Four-point Lagrangian

interpolation was employed for further definition of the curve to facilitate the analysis. Multiplication by the tangent of the illumination angle converted the shadow lengths to ripple heights.

The ripple profiles were defined from trough to trough. The extent of a ripple is defined by the two points, on either side of the maximum height on the ripple, at which the tangents to the profile are colinear. For each ripple, we obtained the height and slope angle as a function of distance along the ripple axis. Comparison between ripples was hampered by the variations in wavelength. To emphasize the importance of the ripple shape, all of the ripples to be compared in this study were scaled to their mean wavelength, while keeping the shape constant, i.e., the ripple height was multiplied by the same factor by which the wavelength was altered. For most ripples, this changed the wavelength by less than ten percent.

Tests

The ripple shadow apparatus was tested to ascertain the accuracy with which ripple profiles could be measured by this technique. There are three contributions to the uncertainties which must be considered: those due to analysis, those due to intrinsic problems in the method and those

caused by the deviation from the assumption that the ripple profile is constant over the variation of the length of the shadow. The uncertainties in analysis have already been found to be about one-half of the mean grain diameter, primarily due to roughness of the surface. In this section we demonstrate that no uncertainties from other sources approach this level.

The intrinsic contribution to the error was evaluated by measuring the profiles of two objects of known shapes: a copper half-cylinder and a ripple in a hand specimen of fine sandstone. The shape of the sandstone ripple was determined by the use of a dial-indicator mounted in the head of a milling machine; the mill table was fed to vary the position along the ripple axis. The shapes as measured by the shadow technique for both the sandstone ripple and the copper half-cylinder differ by less than half the uncertainty attributed to the analysis from the known shapes.

Profiles of single ripples at the Kelso Dunes were measured as a function of the angle of illumination without moving the position of the straightedge. Here we probed the uncertainties in the measurement of the illumination angle as well as the variation of the ripple cross-section

over distances on the order of the shadow length along the crest, since the position of the shadow changes as the angle varies. The differences in ripple profile for three illumination angles ranging from 26° to 53° were no more than approximately one-half grain diameter, comparable to the variations due to the roughness of the surface. We conclude that the ripple profiles may be measured to better than a grain diameter using this technique.

Preliminary Results and Discussion of Method

The results presented here are not intended primarily as a study of the nature of ripple shapes, but rather as an illustration of the usefulness of the ripple-shadow technique. A representative example of the ripple profiles measured in this study is shown in Figure 5.5a and the corresponding slope angle is displayed in Figure 5.5b. A typical ripple (among those we studied) exhibits a concave-up profile over only the first twenty-five percent of the ripple, and rises to a maximum slope angle of between 5° and 15°. A relatively flat, slightly convex shape covers the next fifty percent of the ripple, followed by a small "slipface" at an angle varying between 8° and 35° degrees and then a gentle concave slope to the trough. This general profile agrees well with the drawing in

Sharp's (1963) paper describing ripples at the Kelso Dune complex. We found that many of the ripples display some bump-like structures on the windward side (see Figure 5.5). These were often well above the noise level, so they represent collections of a number of grains. Possible explanations include uneven dumping of the saltation load and the formation of "mini-ripples" on the backs of the larger ripples.

The extent to which the shape of ripples varies in a region of presumed uniform saltation conditions was investigated by measuring profiles of a single ripple at several different positions along the ripple crests; the profiles of successive ripples along the ripple axis were also studied. Seven measurements of the profiles of two adjacent ripples at intervals of approximately 5 cm along their crests were compared. The standard deviation of the profiles for each ripple was about equal to the roughness level of one-half of a grain diameter. Thirteen consecutive profiles along a length of 94.5 cm parallel to the ripple axis were procured. The mean standard deviation of these ripple shapes (averaged over the length of the profile) was somewhat greater than that for a single ripple: approximately one grain diameter.

The dependence of the ripple profile on the apparent dip of the

dune surface is of interest because it may influence the theory of ripple formation. If the lee-side "slipface" angle of the ripple is determined by the angle of repose of the sand, one would expect that the "slipface" angle, relative to the surface of the dune, would become smaller in magnitude for increasing apparent dip. To investigate this, we observed ripple profiles at different locations on a single dune. The dune was approximately 40 m in length and 5 m high. The ripples climbed up the stoss side of the dune and over the crest to the brink of the dune slipface. Six to eight profiles of different ripples were obtained at each of four different sites with mean apparent dips: -10.4 °, -3.3 °, +0.7° and +6.1 °. The four sites were within thirty meters in lateral distance and three meters in height of one another. Sand samples were collected at each site by scooping across the crest and troughs of the ripples and these were later sieved to obtain size distributions.

The mean ripple profiles for the four sites are plotted in Figure 5.6 and the mean slope angles are shown in Figure 5.7. Taking the mean values of the slope angles tends to reduce the "slipface" angle to less than the maximum value on any one ripple since the "slipface", localized in position, may occur at slightly different positions on the ripple. The

ripples of longest wavelength occurred at the -10.4 ° site, followed by those at the sites at +0.7°, -3.3 ° and +6.1 ° (see Table 5.1). The ripples on the stoss surface of the dune (at -10.4 ° and -3.3 °) were characterized by shallow slopes (relative to the dune surface) on both the ripple stoss and ripple lee surfaces, whereas the ripples at and beyond the top of the dune (+0.7° and +6.1 °) had somewhat steeper slopes (see Table 5.1). The mean grain size (by mass) at the sites was 0.0272 cm. All four sites had a mean grain size within two percent of this value and the distributions were almost identical. We conclude that at our test sites ripple "slipface" angles (relative to the dune surface) follow the trend opposite that to be expected if the orientation of the dune surface with respect to gravity were the controlling factor. In fact, at the -10.4 ° site, the ripple "slipfaces" are actually inclined upward relative to a horizontal plane. The ripple stoss angles also have a complex dependence which will require further work to understand. In view of the ease of recording and analyzing accurate ripple profiles, the ripple shadow technique would be suitable to use in conjunction with detailed wind-shear measurements at specified locations on the surface of a dune in order to correlate ripple shapes with dune morphology and wind regime.

The ripple profile measurement technique described here provides easy access to accurate information about ripple shapes. The idea is simple, the apparatus is inexpensive and easy to construct, deployment under field conditions is not onerous and the data reduction effort required is only modest. We anticipate that this technique will prove useful to others interested in the origin and nature of eolian sand ripples, and, with modifications, to investigators studying the formation of fluvial sand ripples.

Field Study of the Evolution of Ripple Profiles During Saltation

The manner in which a bed of sand evolves under saltation impacts will be strongly related to the asymptotic state of the surface, i.e., the ripples. Earlier in this chapter, we saw that simple observations can reveal a great deal about the process of ripple formation. However, the human eye and brain cannot assimilate all of the essential data concerning this process. Thus, it is desirable to quantify the shape of the bed as the ripples form, both to confirm qualitative information obtained by direct observation, and to provide additional details which might influence the theory of ripple formation. The technique described in the last section, the measurement of ripple cross-sectional shapes through casting a

straight shadow across the rippled surface, may be adapted to dynamic meaurements of surface topography. We describe a method for making such measurements, and some preliminary findings concerning ripple development.

Method and Analysis

The technique used for observations on a dynamic bed is similar to that described above for a static bed; here, we highlight the differences. A longer straightedge (approximately 60. cm) was employed to facilitate following the development of surface features as they moved downstream. It was suspended approximately 10. cm above the sand surface, and oriented parallel to the wind direction. Direct sunlight was utilized (rather than mirror-redirected sunlight) for simplicity. As pointed out by R.S. Anderson, the illumination need not be oriented perpendicular to the straightedge.

In order to study the evolution of a bed experiencing saltation impacts, it is desirable to be able to create a repeatable, flat surface from which to begin. This was accomplished by burying two thin metal rails, parallel to the wind, about 50. cm apart, and so that their tops were flush with the sand surface. The shadow-casting straightedge was placed

near the downstream end of the rails and parallel to them. A quantity of sand was then heaped onto the surface between the rails, and a straightedge attached to a driveway asphalt applicator was dragged from a spot just upwind of the rails across the rails to create a surface which, from close observation, appeared to be smooth at least to the level of a grain diameter. We note that this surface probably resembled the surface created for the sand gun experiment, as the surface levelling techniques were similar. A view of the smoothed surface and the position of the straightedge is supplied in Figure 5.8.

The purpose of this experiment is to record the surface profile in time starting from an initially flat bed, and continuing through the formation of ripples, while the sand is saltating. After smoothing the surface, a photograph of the straightedge shadow is taken as soon as is practical (usually about 15-30 seconds) and at fixed time intervals thereafter. The profiles were recorded on color slide film using the now weathered Canon AE-1 camera. It is important to remember that this photography is being performed in an environment of high winds, and that the surface itself is obscured by the movement of saltating and reptating grains. Thus, one's expectations for photographic quality must be

appropriately reduced. In addition, we are not necessarily recording a direct surface cross-section, since the assumption that the surface is unchanging in the direction transverse to the wind no longer holds. Figure 5.9 is a typical photograph of the shadow cast by the straightedge onto the evolving surface.

Despite the fact that the straightedge was only roughly 10 cm in lateral distance from the shadow terminus, we feel confident that its effect on ripple formation was minimal, as no significant wind scour was observed around the apparatus after long periods of saltation, and mature ripples were only slightly distorted in moving past the experimental plot (see Figure 5.10).

A 45 cm span of the surface profile was digitized, with a point on the profile recorded about every 0.2 cm. The data were not smoothed, but interpolation was employed to standardize the spacing of the profile data in the downstream direction. Considering the various uncertainties involved, the error in the profile is estimated to be in the range 0.05-0.10 cm, significantly greater than for the static case, primarily because of the difficulty in defining the shadow terminus.

One goal of this effort was to quantify the interactions between

the forming collections of sand which we had observed directly. This may be accomplished through examination of the surface profile. Another purpose we had in mind was to test how the length scale of the surface roughness (i.e., of the proto-ripples) parallel to the wind changed with time. For this, a quantity which we termed the length-scale distribution was employed. The length-scale distribution, $f(\lambda)$, measures how likely it is that, choosing a point of the surface profile and then looking a distance λ downwind, the elevation at the point chosen, and the elevation λ downstream from there, are "close." In the spirit of Tombrello's (1985) algorithm for smoothing, for a given distance λ, we average the gaussian function of the difference in elevations over the entire profile, with the half-width of the gaussian, σ, chosen to be the presumed noise level of our profile. We measure the lengths λ in units of the constant downstream distance interval Δx ($\lambda=\ell\Delta x$) between points on the profile $h(i\Delta x)$. Then, mathematically speaking, the length-scale distribution is defined as follows:

$$f(\ell\Delta x) = \frac{[N/(N-\ell)]\sum_{j=1}^{N}\sum_{k=j}^{N-\ell} e^{-[h(j\Delta x)-h(k\Delta x)]^2/2\sigma^2}}{\sum_{\ell=1}^{m}[N/(N-\ell)]\sum_{j=1}^{N}\sum_{k=j}^{N-\ell} e^{-[h(j\Delta x)-h(k\Delta x)]^2/2\sigma^2}} \quad (5.2)$$

The number of points on the profile is N and the number of lengths considered is m. (ℓ varies from 1 to m, λ varies from Δx to $m\Delta x$) The denominator is included only as a normalization factor. Other techniques for detecting the length scales of the profile are available. For instance, R.S. Anderson is characterizing surfaces using the more conventional power spectrum derived from a Fourier Transform.

Preliminary Results

Several developmental tests of this technique were undertaken, including one with the assistance of T. Drake. Preliminary data were obtained at the barchan dunefield mostly contained in the Salton Sea Naval Test Base, west of the Salton Sea, in Imperial County, California. An experimental plot was established on a partially vegetated dune 40 m in length and 3 m high. The plot was situated on the downwind side of the dune (local slope $\approx 5°$), where a clear fetch of approximately 10 m was

located. The sand here has a wide distribution of sizes, with mean size 0.039 cm, calculated by dividing the sand sample into size bins through sieving and weighting the bins according to the mass of grains in that bin. On this day, data recording was occasionally interrupted by the passage of a blowing stick or tumbleweed across the plot. When this occurred, the plot was resmoothed and the experiment was restarted.

For this study, a series of 28 (uninterrupted) photographs of the shadow cast by the straightedge, taken over a period approaching one-half hour (during which saltation was occurring most of the time), were digitized. The first four frames were taken at 30 second intervals, the remaining 24 at one minute intervals. (These time intervals are approximate: $\approx \pm 10$ seconds.) The first few minutes of this experiment were characterized by moderate winds (15-20 mph) and fairly uniform saltation. For a period of about ten minutes, very strong winds (exceeding 30 mph), accompanied by occasional powerful gusts, prevailed. Thereafter, the winds died down and saltation was sporadic, occasionally ceasing altogether.

Figures 5.11 and 5.12 show the surface profiles (vertical scales magnified by a factor of five) and the corresponding length-scale

distributions for selected times during this series of photographs. In Figure 5.11, the wind is blowing from left to right. Figures 5.11(a) and 5.12(a) correspond to the first photograph of the series. There, the profile is characterized by a large variety of length scales and no clear order. In the length-scale distribution, there is a distinct rise at low lengths, as well as a suggestion of a rise in the distribution at approximately 11 cm and 23 cm (which may be a multiple of the 11 cm peak). The surface has developed topography of amplitude 0.2 cm in less than 30 seconds.

The second surface profile and the corresponding length-scale distribution (Figures 5.11(b), 5.12(b)), taken 2.5 minutes after the first photograph, unmistakably illustrate the formation of surface undulations of "wavelength" around 5 cm. The third profile shown (c) was recorded 4.5 minutes into the experiment, after the wind velocity had substantially increased. The ripples are not as well-defined as in the previous view, and a broader distribution of length scales has appeared. Presumably, the surface is attempting to adjust to the changing wind conditions, which directly affect the nature of the saltating grains impacting the surface.

The fourth through sixth profiles (Figures 5.11(d)-(f), 5.12(d)-(f))

show the state of the surface 13.5, 14.5 and 15.5 minutes after the first photograph. They record the evolution of the bed in the later portion of the period of high wind velocities, and show the ripples assuming a relatively uniform wavelength of roughly 7 cm (still less than half of the wavelength of surrounding ripples). The fluctuating saltation conditions existing over the remainder of the experiment lead to ripples of varying sizes, Figures 5.11(g) and 5.12(g).

In Figure 5.11, it is clear that in many cases the measured ripple shapes bear little resemblence to traditional ripple shapes. This is particularly evident in Figure 5.11(c), where the stoss slopes appear to be steeper than the lee slopes. One explanation for this is the experimental uncertainties of the ripple-shape observation technique, as we have thus far implemented it. The angles on the slopes range from a few degrees to about ten degrees, occasionally up to fifteen degrees, but our angular resolution was no better than roughly five degrees for some of the photographs during intense saltation. In addition, one must remember that these are forming, merging ripples, and the shapes cannot be expected to be well-defined. Evidence for this is found in that the most uniform wavelength ripples we observed, shown in Figure 5.11(f), are also the best

developed shapes from our data set.

The disappearance of small ripples can be seen in the length-scale profile. The peak at 4 cm in Figure 5.12(b) migrates to the higher length-scale peak at 7 cm as a small ripple climbs the back of a larger ripple: see arrow in Figures 5.11(d)-(f). This agglomerated ripple moved out of the field of view before we could ascertain whether the two ripples had definitely merged.

A more distinct example of the merging of two ripples is shown in Figure 5.13 (see arrows). The ripples are clearly separated in Figure 5.13(a). The smaller ripple becomes spread out on the stoss slope of the larger ripple in Figure 5.13(b), and in Figure 5.13(c) they become indistinguishable. Subsequent photographs (not shown) confirm the coherence of this new ripple. In contrast, two larger ripples of roughly equal size (Figure 5.14(a)) begin to merge, as shown in 5.14(b)-(c), but then repel each other in 5.14(d). Perhaps the difference between this case and the previous one is that the windward ripple of Figure 5.14 appears to maintain a saltation shadow zone in its lee, a location in which surface grains reptating over the crest of the ripple can be kept safe from the impacts of saltating particles and later incorporated into the body of the

ripple (see Sharp, 1963), whereas, the windward ripple of the ripple-collision in Figure 5.13 seems to lose its shadow zone. (Note that the trajectory of a saltating grain impacting at 11 ° to the horizontal would appear as a 45° line on the profile plots.) Since these details are on the edge of our resolution limit, we cannot say with certainty that the small ripple lost its shadow zone. However, we will comment on this general idea in our theoretical discussion.

Discussion

In the surface profiles of the single series of observations recounted here, we discerned a number of examples of two ripples merging, two ripples "colliding", but repelling each other, and also an apparent single ripple breaking into two ripples. Our observations indicate that the dynamics of ripple collisions play a substantial role in the evolution of a surface toward ripples of uniform size. Furthermore, our results confirm that the length scale characterizing the surface is an increasing function of time, as observed by Bagnold (1941), Sharp (1963) and Seppala and Linde (1978). After the initial smoothing, the length scale very rapidly becomes a significant fraction of the final ripple size, and then grows slowly by ripple mergers. A refined experimental

technique and a bit of luck with respect to wind and illumination conditions should allow better definition of the evolution of the length scale of the bed with time.

Our preliminary results appear to conflict directly with the notion of the ripple wavelength being determined by a characteristic path (Bagnold, 1941). In particular, the existence of relatively stable ripples (Figure 5.11(f)) in the presence of stable ripples with somewhat larger wavelength in the region surrounding our plot is difficult to explain under Bagnold's model. These surrounding ripples were responding to the changing wind conditions, but, through the course of the experiment, were of a larger size than the ripples on our plot. Furthermore, Bagnold's correlation between ripple hop lengths and ripple wavelengths were based on calculated, not measured trajectories (see page 64 of Bagnold, 1941) Further experiments in a variety of wind conditions and locations will be required to confirm the preliminary results we have reported here.

While we feel that Bagnold's characteristic path (hop) length for saltating grains is not directly related to ripple formation, we do not deny that such a characteristic length exists. While the results of Chapter IV suggest that the distribution of saltating grain hop lengths

will be broad, the grains which impact the surface at highest velocity, and which presumably lead to the greatest amount of forward reptation per impacting particle, are likely to be characterized by a relatively narrow distribution of path lengths. Indeed, one windy day at the Kelso Dunes, the author smoothed a patch of sand on a dune where saltation was occurring and made a rather deep furrow transverse to the wind direction in the middle of the smoothed area. (This furrow was created inadvertently, and was originally regarded as an annoyance.) Roughly 10 cm downstream, a shallow, broad depression formed. However, the furrow was much steeper topographically than the slope found on the upstream side of a ripple. Also, a similar furrow placed in the Salton Sea dunes experimental plot during conditions of gusty winds and ripple formation, had no corresponding effect on the topography downstream.

As the dynamic observation technique described here appears to be a viable means of obtaining detailed information on the formation of wind-blown sand ripples, a number of improvements to increase its usefulness toward this end are in order. A stand to hold the camera over the smoothed plot in a fixed position (and to protect it from the elements) should be built. This will probably have a positive effect on

resolution, and will allow the investigator to record photographically the state of the bed immediately after smoothing it. The late spring months are the most reliable times for finding the critical combination of sunlight and high wind speeds in the Mojave Desert. However, the sun is rather high in the sky for most of the day at this time of the year. Thus, a large mirror to redirect the sunlight at a more desirable angle, as was used in the measurement of static ripple shapes, would be useful. With these improvements, dynamic ripple-shadow measurements should provide useful data for the formulation and testing of models of ripple formation.

A Theoretical Analysis of Possible Mechanisms of Ripple Formation

The experimental results of this chapter and the observations of ripple formation in a wind tunnel by Seppala and Linde (1978) quantify the growth with time of the length scale of a sand bed under saltation impacts, as envisioned by Sharp (1963). They also confirm that the manner in which ripples attain a final asymptotic, relatively uniform wavelength is through ripple-ripple collisions which may involve mergers or exchange of material. In this picture, the transport of surface grains

in reptation, and thereby the translation of the ripples, is considered to be driven by the impacts of saltating grains, which bounce off the surface and continue in saltation. In this approximation, we assume that saltating and reptating populations are decoupled. As we showed in the last chapter, fluid stresses will be unlikely to be involved in the entrainment of surface grains. While this argument was made in the context of a flat surface, ripples represent only a minor aerodynamical obstruction, due to their large length to height ratio (ripple index); therefore, the argument probably applies to a rippled surface also.

In this section, we will concentrate on the analysis of two aspects of eolian bedform development: the evolution of the surface under a variety of rules for moving surface grains in reptation and the interaction between developing surface undulations, i.e., collisions between proto-ripples.

Elementary Considerations on Surface Evolution

We begin with a continuum-like approximation, in which the grain size and the reptation length are assumed to be small compared to the length scale of the surface topography. Our aim is to derive an equation for the shape of the surface, $h(x,t)$ (as a function of downstream distance

x and time t), which propagates at a constant velocity v in the positive x direction. To do this, we first relate the surface profile to the vertically integrated reptation flux passing above the point x, $R(x,t)$ (measured in number of grains per second). Note that we are using the number flux here, not the mass flux, $q(x,t)$. Also note that we are working in two dimensions, considering a surface one grain thick in the transverse direction. The two-dimensional approximation will be continued throughout this chapter. We take the x direction to be binned with bin width Δx, and take the grains to have a diameter d (this is actually the effective diameter, which includes the effect of porosity), the number of grains which must be placed into a bin to raise its height by an amount d is then $\Delta x/d$ (see Figure 5.15). In a time interval Δt the change in height Δh will be determined by the difference in the number of grains entering the bin and the number of grains leaving the bin: $[\Delta t R(x-\Delta x/2,t) - \Delta t R(x+\Delta x/2,t)]$. This relation may be written as follows

$$(\Delta h/\Delta t) = [R(x-\Delta x/2,t) - R(x+\Delta x/2,t)]d/(\Delta x/d), \qquad (5.3)$$

or, in the limit of small Δt and Δx,

$$(\partial h(x,t)/\partial t) = -d^2 \cdot (\partial R(x,t)/\partial x). \qquad (5.4)$$

This is basically a mass conservation equation. (Recent investigators using variants of this time-honored equation in the field of eolian sediment transport include Hunter, et al., 1977 and Anderson, 1986.) By demanding that the surface shape propagate at velocity v in the positive x direction, i.e., $h(x,t) = h(x-vt)$, we may state that $\partial h/\partial t = -v(\partial h/\partial x)$. Combining this with equation 5.4, we find that the surface height (above a baseline h_0) is proportional to the reptation flux at that point:

$$h(x-vt) = (d^2/v)R(x-vt) + h_0. \qquad (5.5)$$

This equation relies on the assumption that the reptation distance per particle (i.e., the horizontal range of a reptating particle) is small compared to the size of ripples or other topography existing on the surface. The results of the coarse sand experiment (Chapter III) imply that the mean reptation length per grain, for coarse sand, is on the order of 4 cm. The wavelength of ripples in such coarse sand may be about 20 cm. Thus, the assumption would seem to break down. However, the actual distribution of reptation lengths in saltation does not necessarily reflect this data. One must do the steady-state calculation, carefully define the reptating population, and consider the effect of ripple inclines on the grain-bed interaction. In addition, this reptation distance was

obtained by shooting coarse sand at coarse sand. A more likely scenario is that finer sand grains will impact larger bed particles, with less momentum transfer to the surface and consequently a smaller mean reptation length. However, our data appear to be the only quantitative information on reptation lengths available. Anderson (1986) has employed the reptation length for a direct determination of the ripple wavelengths, within the context of a stability calculation.

For the purpose of computing the surface profile, we adopt a specific form for the reptation flux, which is assumed here to be a function of slope angle, β ($tan\beta = \partial h/\partial x$), Figure 5.15(a). Related to the saltation flux of grains impacting at a constant angle α onto a flat surface F_x, the corresponding flux onto a slope of angle β is

$$F_\beta = F_x[1 + (tan\beta/tan\alpha)]/\sqrt{1 + tan^2\beta}\,. \qquad (5.6)$$

Furthermore, we set the reptation flux proportional to the impacting flux, $R(x,t) = aF_b(x,t)$, where a which may be likened to the (assumed constant) reptation distance (see Anderson, 1986). Assuming that the slope is sufficiently small that the denominator of equation 5.6 may be set equal to 1 (a good assumption up to $\beta = 30°$), and using $tan\beta = \partial h/\partial x$, we may

write a differential equation for the surface profile using equations 5.5 and 5.6:

$$\partial h(x-vt)/\partial x = (h(x-vt)-h_0)/\lambda - tan\alpha$$
$$\lambda = ad^2F_x/(vtan\alpha). \qquad (5.7)$$

The solution to equation 5.7 is a function which rises exponentially with downstream distance and propagates with velocity v:

$$h(x,t) = Ce^{(x-vt)/\lambda} + \lambda tan\alpha + h_0, \qquad (5.8)$$

with C a constant. Thus, when saltating impacts (whose frequency is determined by the local surface slope) move surface grains a "short" distance forward in reptation, in the above model, the topography will steepen. If the reptation flux is proportional to the height in steady propagation, and the reptation flux is also proportional to the impact flux, a surface, once it has a positive slope, must continue to grow in slope, in order to try to keep up with this requirement. Under this model, a continuous surface has no other choice, excluding the trivial flat bed solution ($h = h_0$).

It is also worth noting that equation 5.7 may be written as a diffusion equation by taking its partial derivative with respect to distance and employing the notion that the surface propagates with

constant velocity. P.K. Haff (1986: personal communication) has pointed out that this is a diffusion equation with negative diffusion constant, an "anti-diffusion" equation. Thus, instead of levelling the profile function in time, as the usual diffusion equation would, this equation tends to steepen the surface.

Nature does not seem to conform to this model. She employs processes on surface slopes which we have not included, including the slope-lessening gravitational influence. In addition, natural ripples contain a region outside the domain of this simple model. The region in the lee of a ripple where no saltating grains impact was termed the shadow zone by Sharp (1963), who first recognized its importance in ripple formation. Grain transport in the shadow zone (Figure 5.15(b)) differs from impact generated transport.

The effect of a finite reptation length has been considered by Anderson (1986). He argued that the lag caused by a finite reptation transport length would allow the portion of the ripple getting the most flux (roughly half-way up the stoss side) to contribute to the large reptation flux needed by the ripple at its apex, in order to satisfy the requirement that the reptation flux is proportional to height.

Statistical Fluctuations and Ripple Interactions

If we are to entertain the idea that the development of ripples involves the growth of length scales, we are forced to the conclusion that the only way for the mean ripple wavelength to grow across a fixed stretch of sand (e.g., a dune) is for ripples to merge, since the mean ripple wavelength is the total fetch divided by the number of ripples. Such mergers have been observed and correlated with an increase in wavelength in the wind tunnel (Seppala and Linde, 1978) and the field (Sharp, 1963; this chapter).

Further progress is facilitated by focussing on two questions: why do ripples merge, and why do they cease merging when they attain a certain wavelength? The answers to these questions may provide clues as to the mechanisms for ripple formation and the determination of ripple wavelength.

The problem of ripple merger is complicated by the fact that the ripples are underlain by an infinite supply of grains. If two roughly equal-sized ripples merge and subsequently assume the same shape as that of the previous two ripples, the composite ripple must mine the bed for additional grains, eventually incorporating about twice as many grains as

constituted the two antecedent ripples.

However, ripples have been observed to form on hard surfaces. For instance, at Tule Wash Dune of Imperial County, California, the author observed ripples forming in the troughs of ripples which had been moistened (and therefore immobilized) by a recent rain. The wind was blowing along the crests of the relic ripples and bringing in a supply of sand from an area upwind which had dried. The ripples moving in the relic troughs were shaped like barchan dunes, uncorrelated with the ripples in the adjacent trough, but they collided and merged in a fashion similar to that seen on dry sand. Unless the mechanisms operating there were completely different from those which lead to ripples in dry sand, it is both reasonable and convenient, for the moment, to consider ripple interactions to occur on hard surfaces, where the total number of grains in the ripples is conserved.

Before approaching the problem of ripple mergers, it is appropriate to study why ripples collide. One explanation is that they differ in size. A small ripple moves faster than a large ripple because the reptation flux on its stoss surface is proportional to its profile height through the constant v, the velocity of the ripple (equation 5.5).

Assuming that the saltation flux and hence the reptating flux is identical on ripples of the same shape, the smaller ripple must have a larger propagation velocity to compensate for its lesser height. Therefore, the small ripples overtake the larger ones. One might imagine that the smaller ripple will begin "eating" its chubbier downstream neighbor. However, when the smaller ripple has gorged itself to the extent that it becomes larger than the now slimmer preceding neighbor, it slows down and ceases feeding. Thus it would seem there is a natural "repulsive" force between ripples of differing sizes. If a repulsive force exists between adjacent ripples, how does merger occur? It may be related to statistical fluctuations in the reptation flux, and hence to fluctuations in the velocity of the ripples as they collide. To investigate the consequences of adding a stochastic element to the ripple motion, we first consider a one-dimensional analogue for ripples feeding on each other.

P.K. Haff (1985: unpublished notes) conceived of a model in which entities he termed worms of various discrete sizes (number of "links") were placed on an annulus (Figure 5.16). The worms could move forward at specified time intervals one link at a time with certain probabilities.

When a worm moved forward, he could occupy the just vacated position of the last link of the worm ahead of him if that worm moved at that time, or, if his preceding neighbor did not move, the worm would eat its last link, digest it, and place it in the spot vacated by his own posterior link. The worms can be defined by the position of their heads, and their worm-length, ℓ_i, measured in units of worm-links.

Haff took the mean worm velocity to be inversely proportional to the worm-length, $v_i = A/\ell_i$ with $A \leq 1$, so that smaller worms moved faster, on the average, than larger worms, but the actually velocity at any step in time was to be determined by a random variable varying from 0 to 1, ζ_i. Thus, the distance a worm moved forward during that step (measured in worm-link units) would be $1-H(\zeta_i - A/\ell_i)$, with $H(x)$ the Heaviside Function. Were there no stochastic element to the problem, a worm could never eat completely the worm ahead of him, since the velocity depends on length; once a worm becomes larger than the worm ahead of him, he can no longer continue eating. The fluctuations in the velocity of a worm around the mean allow a larger worm to temporarily continue feeding on a preceding worm, with the potential for consuming

him to the last link.

Haff simulated this model of worms on a computer and found that, starting from an initial configuration with all worms having two segments only, the worms gradually merged until the mean worm-length was on the order of ten links, with a rather broad distribution. Thereafter, a very long number of steps forward in time was required for any other worm mergers to take place.

An analytical analysis of Haff's worm model is sticky. The difficulty stems from the fact that the number of objects (worms) is not conserved, and that the rate at which the objects move, and the fluctuations thereof, are determined by a state of the object which has no *a priori* correlation with position. As suggested by S. Spicklemire, the evolution of the worm annulus can be described by the theory of finite Markov chains (Kemeny and Snell, 1960). The worms form a Markov chain in the sense that their current state can be expressed as a function of their previous state only. Thus, for a simple model with two worms, one can form a transition matrix [T] whose element $[T]_{ij}$ describes the transition probability from the ith to the jth state. The form of the

matrix is given by $[T]_{ii-1} = \{A/(L-i)\}\{1 - A/i\}$, $[T]_{ii} = A^2/\{i(L-i)\}$ + $(1 - A/i)\{1 - A/(L-i)\}$, $[T]_{ii+1} = \{A/i\}\{1 - A/(L-i)\}$ and all other $[T]_{ij} = 0$, with the sum of the number of links on the two worms equal to L and the worm lengths, measured in number of links, given by i.

The so-called "absorbing states" in this formulation (Kemeny and Snell, 1960) are those configurations which result from the merger of two worms. Once the worms have merged, the number of worms becomes permanently decreased by one increment. The ijth element of the nth power of the matrix [T] gives the probability of going from state i to state j in n steps. This means of calculating transition probabilities can be generalized to m worms by employing a $m+1$-dimensional matrix, with obvious computational difficulties as m becomes large.

Using the form of the transition matrix [T] given above, we have computed some transition probabilities for the two-worm case. Our results indicate that sizes of worms greater than about five links are very stable; two worms of equal length of five links will merge with a probability of about .05 after they have moved about ten times their initial size (50 links). The mean "stable" length for our case is somewhat

lower than from Haff's simulations for the following reason: two worms on a ring forces a strong correlation between the worm lengths, precluding the possibility that exists in the computer simulations, where several smaller worms might be lined up in a row, with the corresponding increase in probability that a merger will occur.

In Nature, a typical sand ripple is about 200-300 grain diameters long. If the stable length of 10 links derived from the worm model is to be applicable, the links or statistical packets involved in ripple movement would have to be many grain diameters in size. To compare the two cases, we consider what the percentage fluctuations in the distance moved by a worm and a ripple are in the time it takes to move a distance equal to their respective worm-and-wave-lengths. For the stable worm of length $\ell = 10$ links, with $A = 1$, the mean distance moved is 10 links but the standard deviation of this distance is about 3 links, or 30% of the mean. Here the mean distance travelled is An/ℓ and the standard deviation of the distance travelled is $\sqrt{(nA/\ell)(1-A/\ell)}$, with $n = 100$ the number of discrete steps. The ripple calculation is more complicated. Consider a ripple of coarse sand, with grain diameter chosen for simplicity to be 0.1 cm. Suppose the wavelength is 200 grains, and the

height is 10 grain diameters. Our coarse sand data imply that in a moderately strong wind ($u^* = 100$ cm/sec), the number of high-energy impacts per cm^2 per second will be on the order of 5. We will take the back of the ripple to be 10 cm long and consider a 1 cm wide strip of it. We have assumed implicitly that reptating grains typically move on the order of a maximum of 1 cm in the transverse direction, which, for an order of magnitude calculation, is probably in the right ballpark. Further, we will take the total reptation distance per impact to be about 20 cm (see Chapter III). The number of impacts on the back per second is 50, and the total reptation resulting from these fifty impacts is 1000 cm. Thus, the average grain in the ripple (there are 10,000 of them in the 1 cm wide strip) moves forward 0.1 cm in a second, and the speed of the ripple is about 6 cm/min. The time to translate a ripple through the distance equal to its wavelength is about 200 seconds, during which there will be 10000 impacts, with a standard deviation, according to the Poisson statistics we assume to apply to saltation impacts, of 100 impacts, or 1% of the mean. This is considerably less than for the stable worms. We note that the corresponding percentages for worms of length 5 and 2 links are 45% and 70%, and the percentages for ripples of wavelength 100

grains and 40 grains (with constant ripple index) are about 3% and 10%.

The outlook for statistical fluctuations determining asymptotic ripple wavelengths looks rather bleak in light of this calculation. However, being a two-dimensional phenomenon, ripples interact in ways which are not contained within the context of the worm model. In addition, in the above calculations, we have not considered the effect of a distribution of reptation distances.

Collisions between Ripples

Collisions between two-dimensional ripples will involve aspects different from the interactions between the worms described in the last section. We take the ripples to be triangularly shaped, inclined at angle β to the horizontal on the stoss side and angle α on the lee side. The "lee slope" is intended to correspond to the shadow zone of grains impacting at angle α, rather than to the material actually contained within the ripple, which will lie slightly below this line. The ripples are propagated forward by removing a strip of material from the stoss side and placing it on the lee side of the ripple, as illustrated in Figure 5.17(a). This is done in a continuous manner, with no fluctuations.

Now consider the details of the grain transport. One way in which

the material can be moved is to reptate a single grain of diameter d, situated on the ripple stoss, forward a distance D for every impacting grain; the flux onto the back of the ripple is F_β. The velocity of an isolated ripple, v, is then

$$v = F_\beta d^2 D/(L_1 tan\beta), \qquad (5.9)$$

where L_1, the length of the ripple stoss, is related to the ripple wavelength λ by $L_1 = \lambda/(1 + tan\beta/tan\alpha)$. An alternative hypothesis is that the grains move up the slope one at a time. A grain waits in position until the grain in front of it has moved all the way up the slope. This results in a propagation velocity inversely proportional to the wavelength squared:

$$v = 2F_\beta D d^3 cos\beta/(L_1^2 tan\beta). \qquad (5.10)$$

The former method of moving the sand grains corresponds to the ejection of target particles from the bed, the latter is an extreme version of brink particle transport, in which only one grain is moved up the slope before the next is started. It is likely that transport on true ripples lies somewhere between the two.

Within this model, the grain transport during the interaction

between two ripples can be formulated in a similar manner, as shown in Figure 5.17(b). The material taken off the stoss side of the upstream ripple is placed on its lee slope, but, in a collision, the lee slope is shortened, and thus the collision has the effect of initially accelerating the forward speed of the upstream ripple, as well as increasing its height. Conversely, the downstream ripple loses a part of its stoss slope when the two ripples are interacting, and its velocity is initially slowed. In this sense, during the first part of the collision, the ripples act as if there is an attractive force between them. Collisions between two ripples are shown in Figures 5.18 and 5.19 for target ejection transport, and brink ejection transport, respectively. Further into the collision, the upstream ripple grows to be larger than its downstream neighbor, and this allows the downstream ripple to escape. With no fluctuations, this continuous model predicts that ripples of any two sizes, interacting under any of the impact-ejection mechanisms we have discussed, will not merge. Thus, we will have to invoke fluctuations or some other means to relate the collision model to ripple agglomeration.

While our model is a highly simplified picture of ripple interactions, it suggests two points which may be of some importance in

ripple formation. First, ripples interacting under the target ejection law come apart having exchanged sizes precisely: the downstream ripple moves off with the original size of the upstream ripple and vice versa (see Figure 5.18). This result is a consequence of the symmetry of the interaction around the point at which the two ripples have the same height. On the other hand, the brink ejection transport law results in the ripples separating with less disparity between their sizes than prior to the collision (Figure 5.19). In this case, due to the inverse square dependence of the transport rate on stoss length, the smaller ripple initially gorges itself on the larger one, and then is left too massive to take its fill as the collision progresses.

If the transport law embodies some combination of target ejection and brink ejection, a ripple collision will result in a tendency to lessen differences between ripple sizes. We envision that the interaction mechanism for mature ripples, which assumes a relatively narrow range of sizes, is collisional and that the accompanying exchange of grains brings the colliding ripples closer in size.

Second, as can be seen in Figures 5.18 and 5.19, the ripple collision causes the upstream ripple to be "plastered out" on the back of

the downstream ripple, the degree of "plastering" depending on the size ratio of the two ripples. During a collision, we define the shadow zone length to be the horizontal distance from the apex of the upstream ripple to the intersection of its lee slope with the stoss slope of the downstream ripple. Similarly, the effective height of the ripple is defined to be the corresponding vertical distance. When the ripples overlap, the shadow zone length and effective height of the upstream ripple become reduced to a fraction of their freestanding values, causing the ripple to become more susceptible to statistical fluctuations. If the effective height gets low enough, the potential for a statistical variation in the impact flux causing the disappearance of the shadow zone, and even the crest of the ripple, is significant.

The shadow zone, in some sense, defines a ripple. This is where the ripple stores away grains for future use. They are recycled through the ripple as it moves downstream as described by Sharp (1963). If the shadow zone disappears, the ripple has no zone of protection against saltation impacts, although a slope inclined nearly parallel to the impacts would insure a low flux there. The greatest consequence of losing or reducing the shadow zone length could be the loss of reptating grains to

the downstream ripple. If the length of the shadow zone is less than the reptation length, the grains reptating off the crest of the upstream ripple will strike the downstream ripple stoss slope. If the smaller ripple is losing grains in this way, its shadow zone is decreasing, which will cause the loss of additional grains. In other words, the system is then in a region of positive feedback, from which it is unlikely to recover. Thus, the upstream ripple will disappear, merged with the downstream ripple. These models suggest that ripple mergers are effected through the combination of statistical fluctuations and the loss of reptating grains through the reduction in the shadow zone length. For instance, statistical fluctuations and the "plastering out" during a collision might combine to lessen the shadow zone length sufficiently that the upstream ripple begins to lose grains and eventually its identity.

In Figure 5.20, we plot the minimum effective ripple height versus the initial size ratio of the colliding ripples for triangular ripples with $\beta = 5°$ and $\alpha = 10°$ and for both target and brink ejection transport models. These values for α and β were derived from the ripple shapes obtained experimentally earlier in this chapter, where α ranged from 10° to 15°, and beta ranged from 3° to 5°. The triangles representing ripples contain

about 80% of the ripple cross-sectional area, and extend from the end of the shadow zone of one ripple to the end of the shadow zone of the next ripple. The maximum percentage decrease of the effective ripple height increases with decreasing upstream to downstream size ratio, and it is larger for brink ejection transport. While the effect appears to be small for ripples of similar sizes, it is rather considerable for size ratios on the order of 2: the effective ripple height can be reduced by 40%.

The collisional model for ripple merger proposed here depends on the existence of a wide distribution of ripple sizes, as is present during the early stages of saltation occurring on an initially flat surface. Mature ripple fields are characterized by a narrow distribution of sizes. However, mature ripples usually do not merge. It is in the evolution of the surface to stable ripples where we witness ripple merger. Here, our preliminary data on developing ripple shapes presented earlier in this chapter suggest that the distribution of sizes can be large, Figure 5.12. Further data will allow quantification of the evolution of the distribution of ripple sizes with time. We note that Seppala and Linde (1978) found that the distribution of ripple wavelengths did not significantly narrow with time, and in fact increased in some cases of ripple development

studied in their wind tunnel. However, even their mature ripples had a large range of ripple wavelengths.

Surface Evolution and Ripple Growth: Computer Simulations

Up to this point, the complexity of the ripple growth process has impelled us to examine the various pieces of the problem separately, without combining them together into a coherent model. One way in which to approach piecing together the component parts into a model is through a computer simulation of surface transport on a bed composed of loose grains.

Computer simulation of ripple formation was first studied by P.K. Haff. On a computer, he took a two-dimensional bed of grains and binned the bed in the downstream direction. Grains were shot at the surface at a fixed angle individually from random points above the surface; a grain from the bin corresponding to the point on the surface which the incident grain strikes was removed from that bin and placed in the bin a fixed horizontal distance downstream (target ejection). The incident grain was eliminated from the simulation and the process was repeated. After each shot, the surface slope angles between adjacent bins were checked to insure they were under the angle of repose. If the slope angle exceeded

the angle of repose, the grains in the higher bin were redistributed until the slope angle decreased below the angle of repose.

Haff found that this simple algorithm led to the development of surface undulations which, through collisions and mergers, resulted in the formation of a relatively uniform-sized population of ripples. Under his model, the stoss slope angle of the ripple rose to the angle of repose. Haff argued that the stoss angle might be limited by the nature of grain-bed impacts, and thus artificially ceased grain transport from a bin when the slope angle there exceeded a certain value. This resulted in ripples which resembled ripples in Nature. R. Fätland also observed the formation of ripples with a similar but independently generated computer code.

It is of interest to inquire about the evolution of a bed on the level of individual grains, where the geometrical factors of finite grain size and the influence of different types of grain-bed interactions are taken into account. To approach these questions, the author has extended Haff's algorithm to a bed composed of independently acting circular grains which are constrained to lie on a regular two-dimensional lattice. The grain layers rest one on top of each other in a close-packed type of

configuration in the vertical direction, but are stretched in the horizontal direction so that the maximum angle relative to the horizontal at which grains can lie, the angle of repose, is 30°, as shown in Figure 5.21.

Circular grains which represent saltating grains are propelled at the surface at a fixed angle. Within this algorithm, there are two possible grain-bed interactions: target ejection and brink ejection. For target ejection, the bed grain which the incident particle strikes is moved forward a fixed distance (the reptation length) if the incident grain contacts it on its upstream side; the bed grain is moved backward for a contact on the downstream side (recall that for low incident angles, the upstream side is struck at a far greater frequency). The ejected grain is then "dropped" onto the surface at this new location; if it falls into a pocket, it stays there; if not, it continues to move laterally until it finds a pocket on the surface. For brink ejection, instead of moving the target particle, the program looks forward (backward) along the surface (for a limited distance) if the incident grain-target grain contact is on the upstream (downstream) side of the target particle until it encounters a brink (an anti-brink) grain, which is then ejected a fixed distance forward (backward), and settled into a pocket utilizing an identical algorithm to

that for settling target ejecta.

Here we will highlight a few of the results of studies undertaken with this ripple formation simulation code, which are still in progress. Under target ejection, the slopes do not become as steep (starting from a smooth surface) as in the Haff simulation, nor as predicted by the simple model at the beginning of this section, equation 5.8. This is probably related to the requirement that ejected grains be placed in a stable pocket on the surface, which tends to have a smoothing effect. Ripples form under target ejection in much the same way that ripples were observed to form in natural sands: initially mottled topographic features undergo collisions and mergers until a relatively stable population of undulations resembling ripples are formed. The mean slope angle is roughly 10° on the stoss side and 15° on the lee side of these "ripples," created by target ejection alone. Local variations in those slopes can be significant, which is likely at least partially explainable by the discrete bed particle positions.

Ejecting bed particles from brinks (and anti-brinks) has a somewhat different effect on the surface topography. This type of ejection causes, on the average, smoothing of surface topography. This is

because there is no possibility of creating a brink/anti-brink pair on a close-packed, smooth surface. Thus, a simulation with a sufficient number of impacts will finish with the surface nearly completely smoothed.

We can imagine how a surface might evolve under the action of target and brink ejections. An initally smoothed surface will not allow brink ejections, so that target ejections will dominate until the surface became sufficiently rough that brinks and anti-brinks exist aplenty. Then, the smoothing due to brink ejections will prevent the local surface topography from becoming rougher, while the other mechanisms we have discussed in this chapter will lead to organization of the surface grains into ripples. The final shape of the stoss surface of a ripple could represent a balance between the competing processes of roughening (target ejection) and smoothing (brink ejection).

A ripple profile computed with our algorithm resulting from the combination of brink and target ejection is displayed in Figure 5.22. The forward reptation length was 15 lattice grain spacings, and the backward reptation length was 5 lattice grain spacings. The ripples attained wavelengths on the order of 200 lattice spacings and heights of about 8

lattice spacings after about 10 ejections per surface grain. They resemble natural ripples.

Earlier we came upon the question of what the relative importance of reptation length and statistical fluctuations is in determining the ripple wavelength. To study this, we examined the asymptotic length scales for two reptation lengths with target ejection only: 4 and 8 lattice grain spacings. The surface came to a stable length scale of about 50 lattice spacings for the smaller reptation length case. The larger reptation length case, after the same number of ejections per surface particle (about 20) appeared to be growing in wavelength, with a peak ranging from 50 to 75 lattice spacings. The length scale distributions (as defined earlier in the chapter: equation 5.2) for the two cases are given in Figure 5.23. This result seems to suggest that the wavelength is correlated with the reptation length. However, we feel that by increasing the reptation length per impact, one is changing the statistics as well, in effect giving greater import to the impact through a larger transport distance. In short, the "fluctuation" associated with the impact has increased. To test this, for a reptation length of 4 lattice spacings, after impacting a randomly chosen spot on the surface, instead

of going to another random spot, we impacted this same spot once more. Thus, the reptation length was still four, but the statistics more closely resembled the case for the larger reptation length. The length scale distribution resulting from this calculation is plotted in Figure 5.23(c), and possesses a maximum at about 100 lattice spacings! This implies that reptation length is not likely to be the sole factor to be considered in computing the ripple wavelength within the context of the lattice-bed algorithm, and gives direct evidence of the importance of fluctuations. We anticipate that future work on this question and others utilizing the lattice ripple model will be of some use in elucidating the mechanisms for ripple formation.

Discussion

Here we summarize our ideas on ripple formation mechanics, discuss their relevance to natural ripples, and then provide some numerical predictions for wavelengths based on simplistic calculations emanating from these ideas. The main points we have made concerning ripple formation follow:

(1) Initially smooth sand surfaces experiencing saltation impacts become mottled and steepened by ejections of target bed particles. The

roughness of the topography is regulated by ejection of particles at brinks or anti-brinks created by the target ejections; brink ejections have a smoothing effect.

(2) Ripples are the end product of a gradual process of collision and merger of proto-ripples.

(3) Proto-ripples and ripples collide because of variations in propagation velocity caused by variations in size. Also, small ripples may collide because of statistical fluctuations in their velocity. In collisions, the upstream (smaller) ripple becomes "plastered out" on the back of the downstream (larger) one to an extent determined by the size ratio of the ripples.

(4) Ripples merge for two main reasons related to the vulnerability of the upstream ripple when it is "plastered out" onto the back of the downstream ripple:

(a) Statistical fluctuations in saltation impact flux might shear off the upstream ripple apex.

(b) The upstream ripple's shadow zone may become small enough during the collision that a significant fraction of its reptating grains are lost to the downstream ripple, resulting in a runaway

decrease in the size of the upstream ripple.

Our lattice ripple model implies that both processes might be important. (5) A mature ripple field achieves a narrow distribution of wavelengths by exchange of grains in gentle collisions between ripples of slightly different sizes.

The qualitative aspects of our ripple formation mechanisms agree with those seen in Nature. The colliding and merging found in our model agree with direct observations of sand surface evolution. All of our calculations scale with grain size, which corresponds to the increase in wavelength for larger grains.

Higher wind velocities lead to longer sand ripples. As we stated in Chapter IV, the range of saltating grain impact velocities increases with wind velocity. This will result in a broader distribution of reptation lengths, and would likely lead to a greater propensity for ripples to merge. The shadow zone, and hence the wavelength, will increase in length due to the lowering of the saltating grain impact angle (Sharp, 1963). We have not considered the effect of large scale eddies or wind gusts, which may cause significant fluctuations in the saltating impact

flux, and ultimately affect the asmptotic ripple size. These effects will rise with increasing wind velocity.

Finally, we present some numerical predictions for ripple wavelengths derived from the ideas presented above. We calculate the largest wavelength ripple which can result from the merger of two ripples of specified size ratio for two different merger hypotheses: (1) the ripples merge if the mean reptation length is greater than the minimum shadow length during the collision, (2) the ripples merge if statistical fluctuations could spread out the portion of the upstream ripple above the intersection between upstream lee and downstream stoss in the time it takes to transfer those grains forward the shadow zone length. The grain diameter is 0.1 cm, the reptation length is 4. cm, the number of impacts per cm^2 per second is 5, the stoss slope angle is 5° and the lee slope angle is 10° and the closest-approach collision data are gotten by averaging the two curves (brink and target ejection) of Figure 5.20. The statistical fluctuation model finds that the effective height of the upstream ripple (at its closest approach to the larger ripple) must not fall below 0.23 cm (about 2.5 grain diameters) or the ripples will merge. For the reptation model, the shadow zone must remain longer than the

reptation length of 4 cm to avoid merger. The results (Figure 5.24) lie close to wavelengths expected for sands of this diameter, keeping in mind that this is an order of magnitude calculation.

SYMBOL DEFINITIONS: CHAPTER V.

$f(\lambda)$	Length scale distribution of surface
σ	noise level for smoothing
x	downstream coordinate
t	time
$h(x,t)$	surface profile
$R(x,t)$	vertically integrated reptation flux
v	propagation velocity of ripples or worms
d	diameter of sand grains
α	impact angle of saltating grains
β	surface slope angle
F_x	number flux onto horizontal surface
F_β	number flux onto a surface inclined at angle β to the horizontal
D	reptation distance
ℓ_i	length of ith worm
$\mathcal{H}(x)$	Heaviside Function
ζ_i	random number between 0 and 1
$[T]$	transition matrix for worms
L_1	stoss length of ripple

TABLE: CHAPTER V.

TABLE 5.1. Variation of Ripple Shapes for Different Apparent Dips

Mean Apparent Dip	Mean Wavelength	Maximum Stoss Angle†	Mean Maximum "Slipface" Angle†
-10.4	8.1	6.3	-6.4
-3.3	6.8	6.5	-16.8
+0.7	7.3	11.4	-23.5
+6.1	6.7	10.0	-20.9

†relative to the dune surface

FIGURE CAPTIONS: CHAPTER V.

Figure 5.1 The apparent dip of a dune surface along the ripple axis, Θ, is the angle from the horizontal, defined in such a way that Θ is negative for ripples moving upslope and positive for ripples moving downslope. The slope angle of the ripple relative to the dune surface, φ, is also defined in this figure.

Figure 5.2 A schematic illustration of the ripple shadow technique. The sun's rays, redirected by a mirror, fall upon the straightedge, casting a shadow on the rippled sand surface. The perpendicular length of the shadow from the straightedge is proportional to the distance between the straightedge and the surface. This shadow can be photographed for careful analysis.

Figure 5.3 The ripple shadow apparatus deployed in the desert.

Figure 5.4 A photograph used for analysis of a typical ripple shadow. The effect of the individual sand grains is observable along the shadow terminus.

Figure 5.5 An example of a smoothed ripple profile: (a) the shape (the

scale is given by the horizontal line which is ten centimeters) (b) the slope angle.

Figure 5.6 Mean ripple profiles for different apparent dips on a single dune: (a) -10.4 degrees (b) -3.3 degrees (c) +0.7 degrees (d) +6.1 degrees. The horizontal lines correspond to a length of ten centimeters.

Figure 5.7 Mean ripple slope angles, relative to the local dune surface, for different apparent dips on a single dune: (a) -10.4 degrees (b) -3.3 degrees (c) +0.7 degrees (d) +6.1 degrees.

Figure 5.8 The shadow-casting straightedge and the smoothed experimental plot for dynamic surface profile measurements.

Figure 5.9 A surface profile shadow for dynamic ripple formation measurements.

Figure 5.10 Mature ripples form around the dynamic ripple-shadow apparatus without significant perturbation.

Figure 5.11 Sand surface profiles. The horizontal line is 45 cm in length and the vertical scale is exaggerated fivefold. The wind blows from left to right. Time into experiment (minutes): (a) 0. (b) 2.5 (c) 4.5 (d) 13.5 (e) 14.5 (f) 15.5 (g) 27.5. The

arrows in (d), (e), (f) document the disappearance of a ripple.

Figure 5.12 The length scale distribution arising from the profiles given in Figure 5.11. The arrow in (d) corresponds to the ripple which disappears in Figure 5.11(d)-(f).

Figure 5.13 The merger of two ripples (see arrows): (a) The ripples are separate. (b) The smaller ripple is spread out on the stoss slope of the larger ripple. (c) The ripples have merged.

Figure 5.14 Two ripples approach each other (see arrows) (a)-(c), but then repel each other (d).

Figure 5.15 (a) Definitions for the relation of flux to height on a ripple. (b) Saltation impact and saltation shadow zones (after Sharp, 1963).

Figure 5.16 P.K. Haff's worm model for the study of fluctuations in ripple formation.

Figure 5.17 The triangular ripple collision model. Grains are removed in slices off the ripple stoss slope and placed on the ripple lee slope. (a) Isolated ripple. (b) Colliding ripples.

Figure 5.18 The collision between two ripples of size ratio 0.6 in the target ejection model of grain transport. The ripples

separate having exchanged sizes.

Figure 5.19 The collision between two ripples of size ratio 0.6 in the brink ejection model of grain transport. The ripples separate closer in size to each other than prior to the collision.

Figure 5.20 Ratio of the effective upstream ripple height during a collision to the freestanding upstream ripple height versus ripple size ratio in the collision model for target and brink transport.

Figure 5.21 Lattice bed ripple model: brink ejection, anti-brink ejection, target ejection and angle of repose. Incident grains are shaded.

Figure 5.22 Profile of a single ripple from the lattice bed ripple model with both brink and target ejection.

Figure 5.23 Length-scale distributions for (a) reptation length =4, (b) reptation length = 8 and (c) reptation length = 4 with two hits per random point on the bed.

Figure 5.24 Ripple wavelength versus ripple size ratio for the statistical fluctuation model, and also the grains reptating beyond the saltation shadow model.

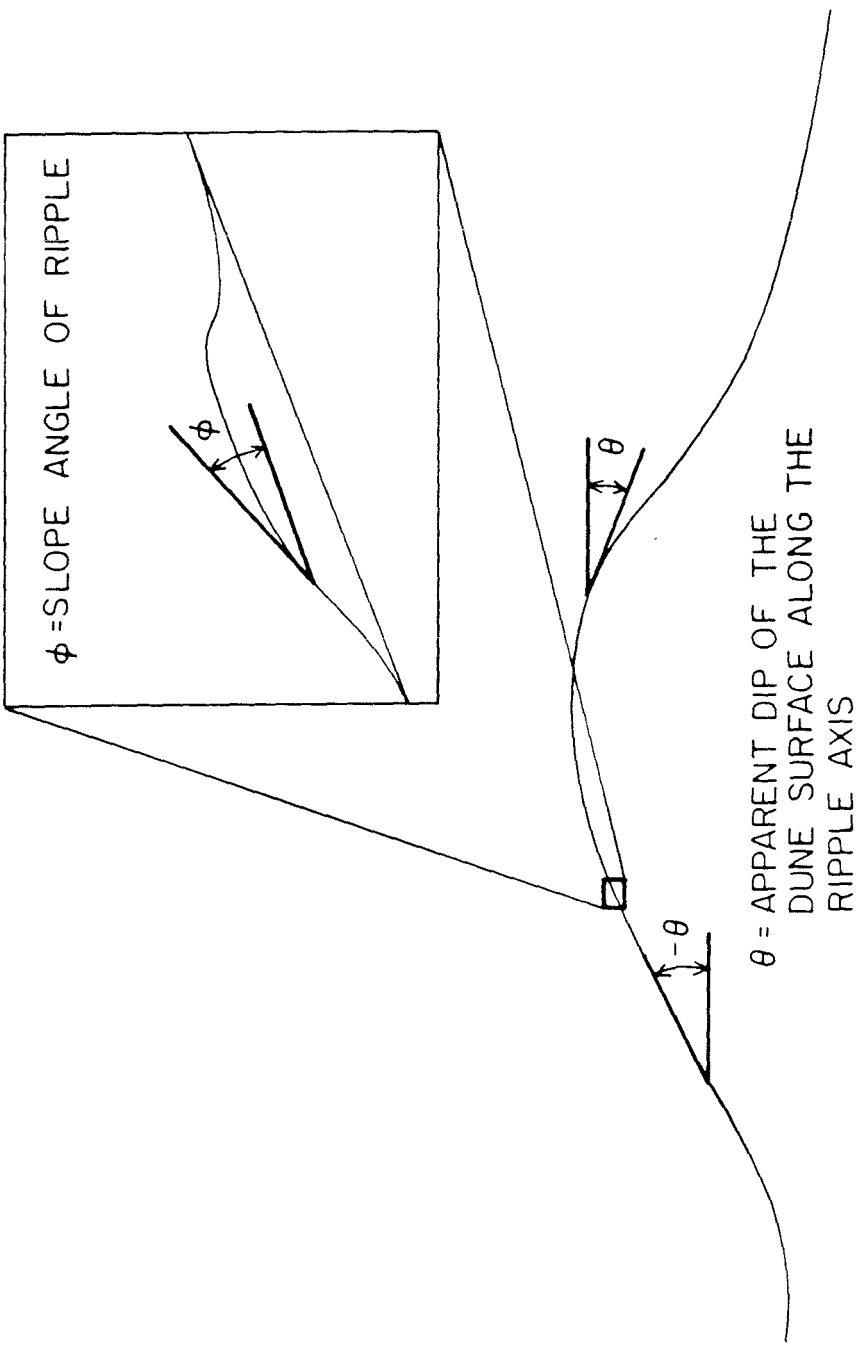
ϕ =SLOPE ANGLE OF RIPPLE
ϕ
θ
$-\theta$
θ = APPARENT DIP OF THE DUNE SURFACE ALONG THE RIPPLE AXIS

Figure 5.1

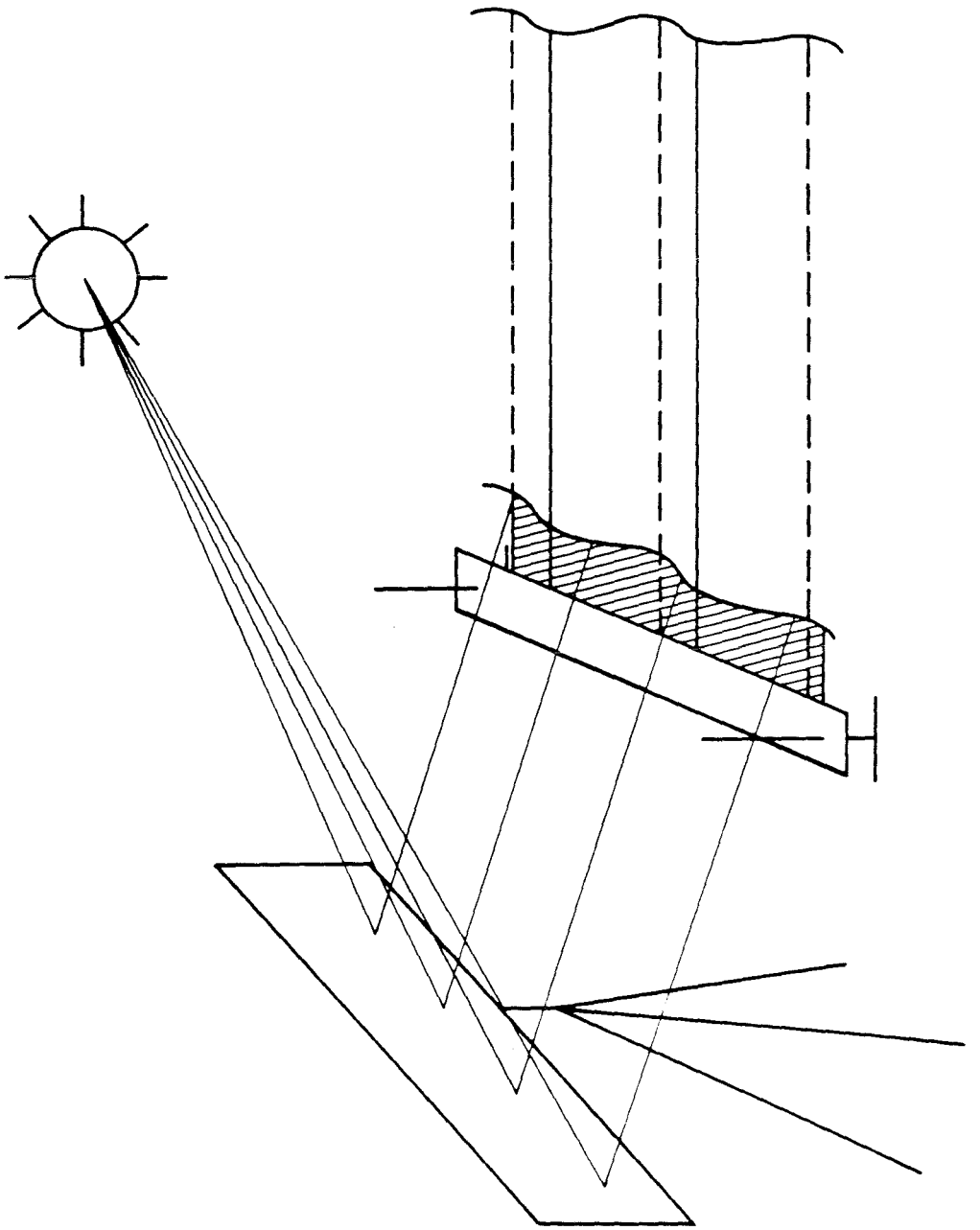

Figure 5.2

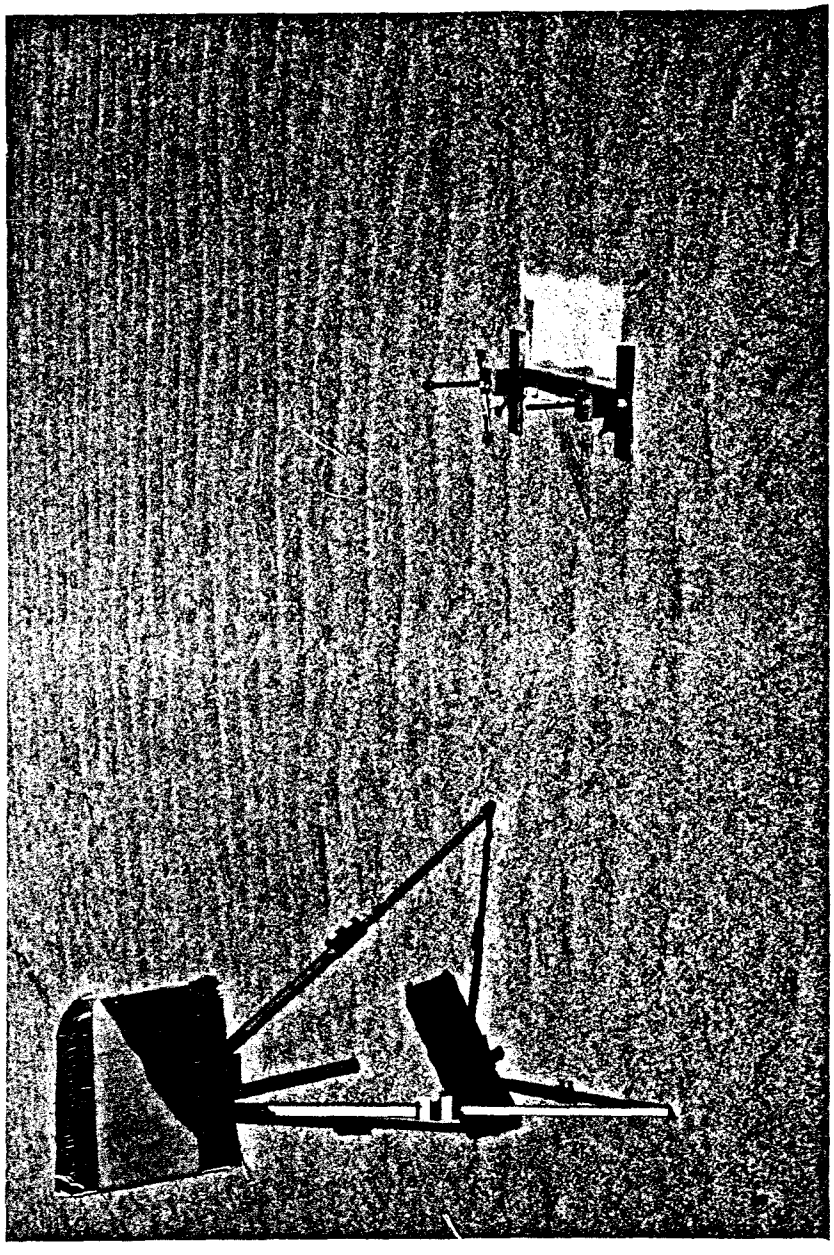

Figure 5.3

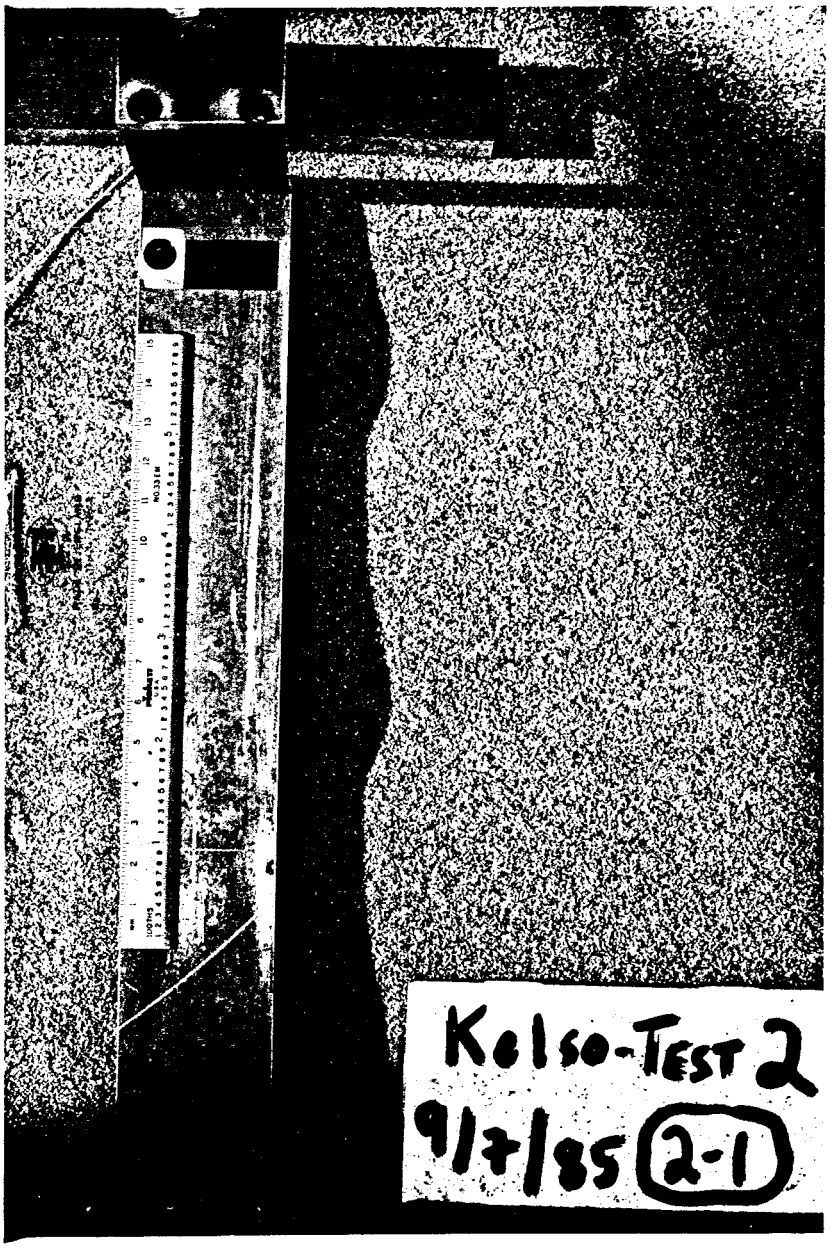

Figure 5.4

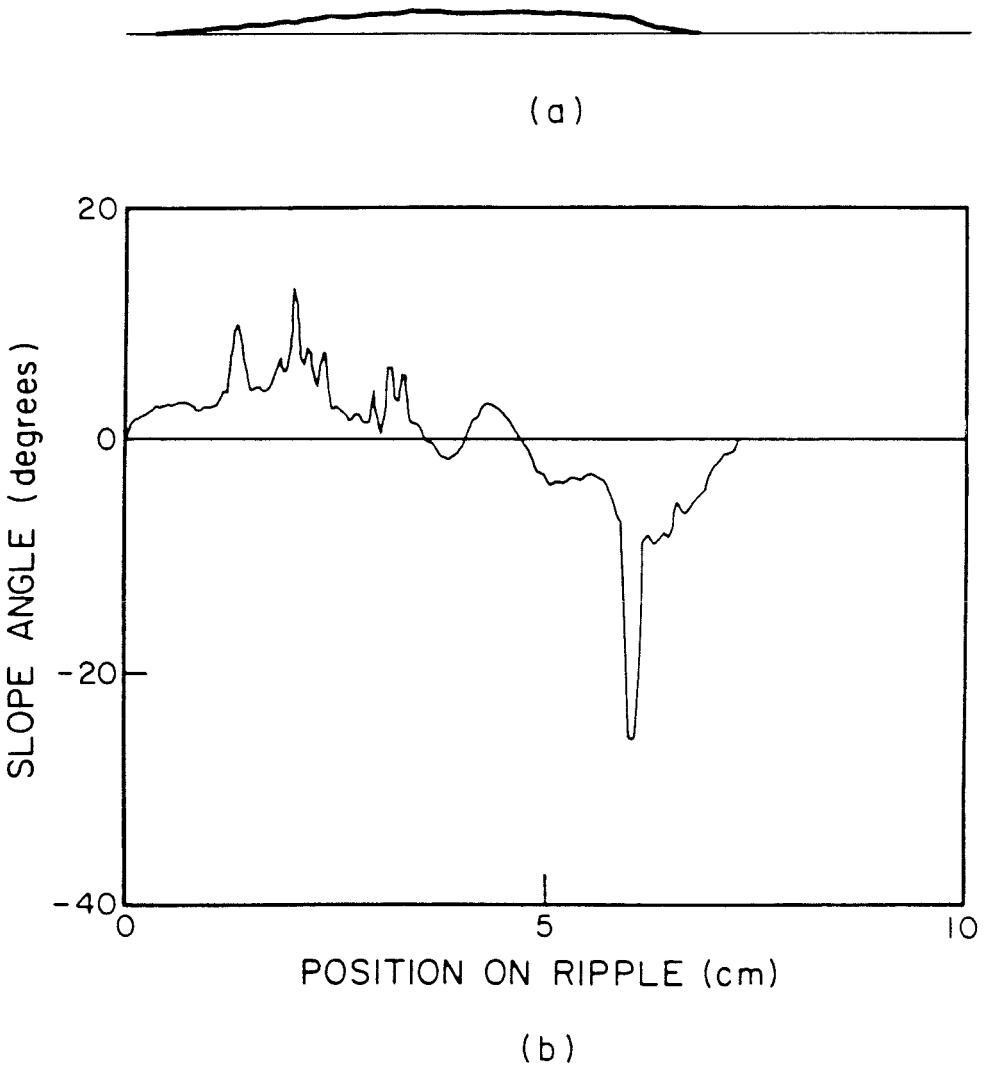

Figure 5.5

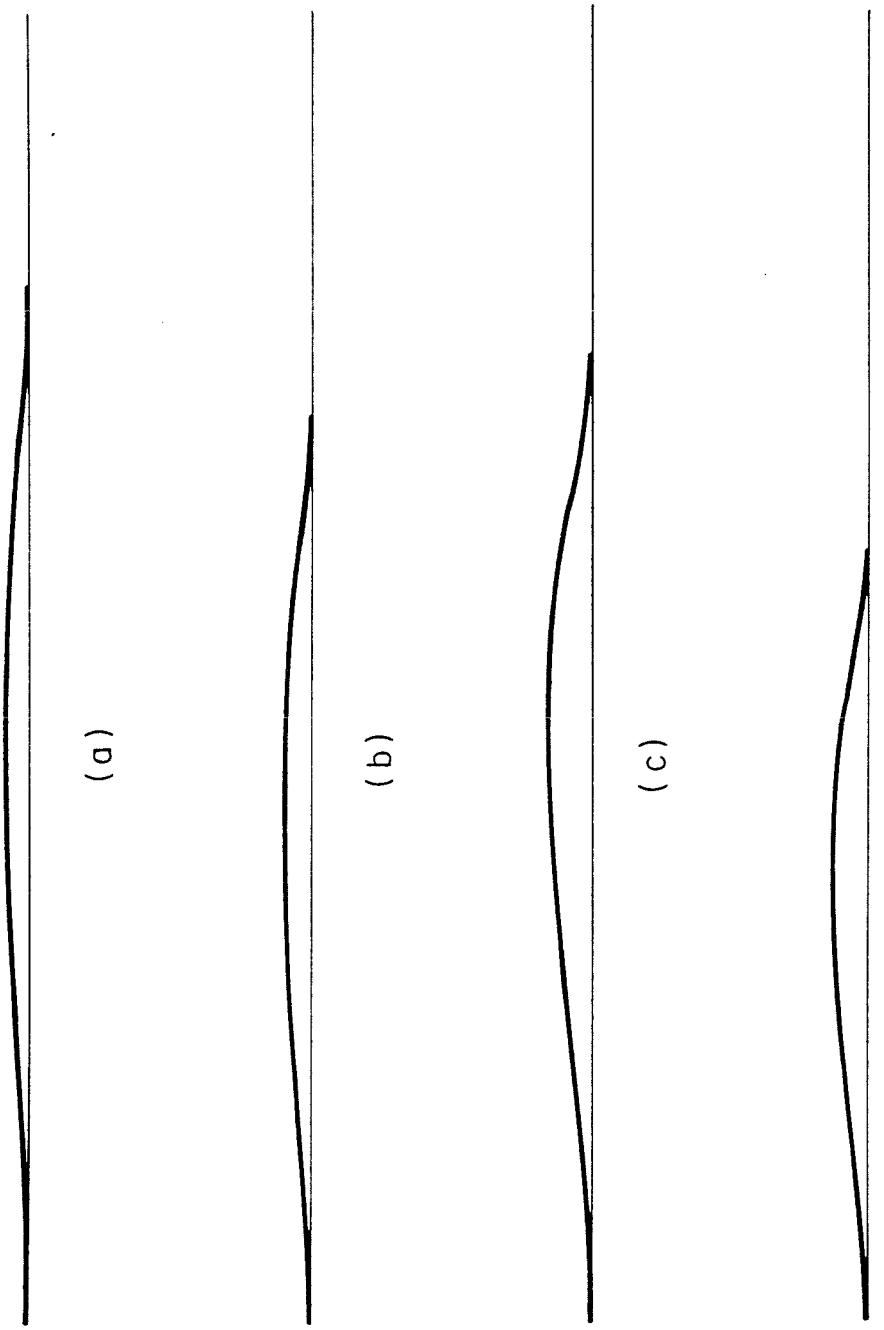

Figure 5.6

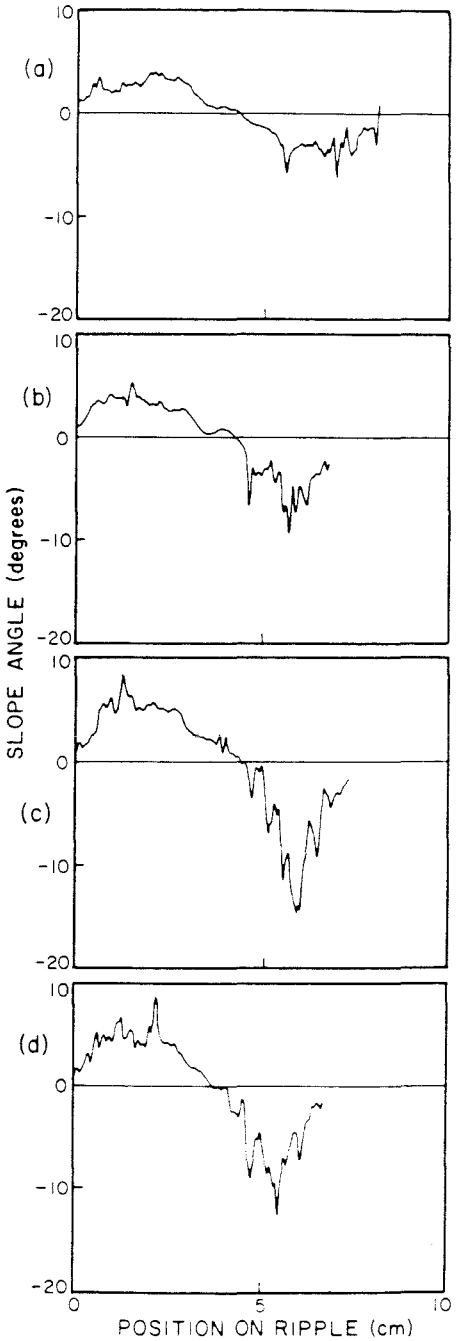
(a)
(b)
(c)
(d)
10
0
-10
-20
SLOPE ANGLE (degrees)
0
5
10
POSITION ON RIPPLE (cm)

Figure 5.7

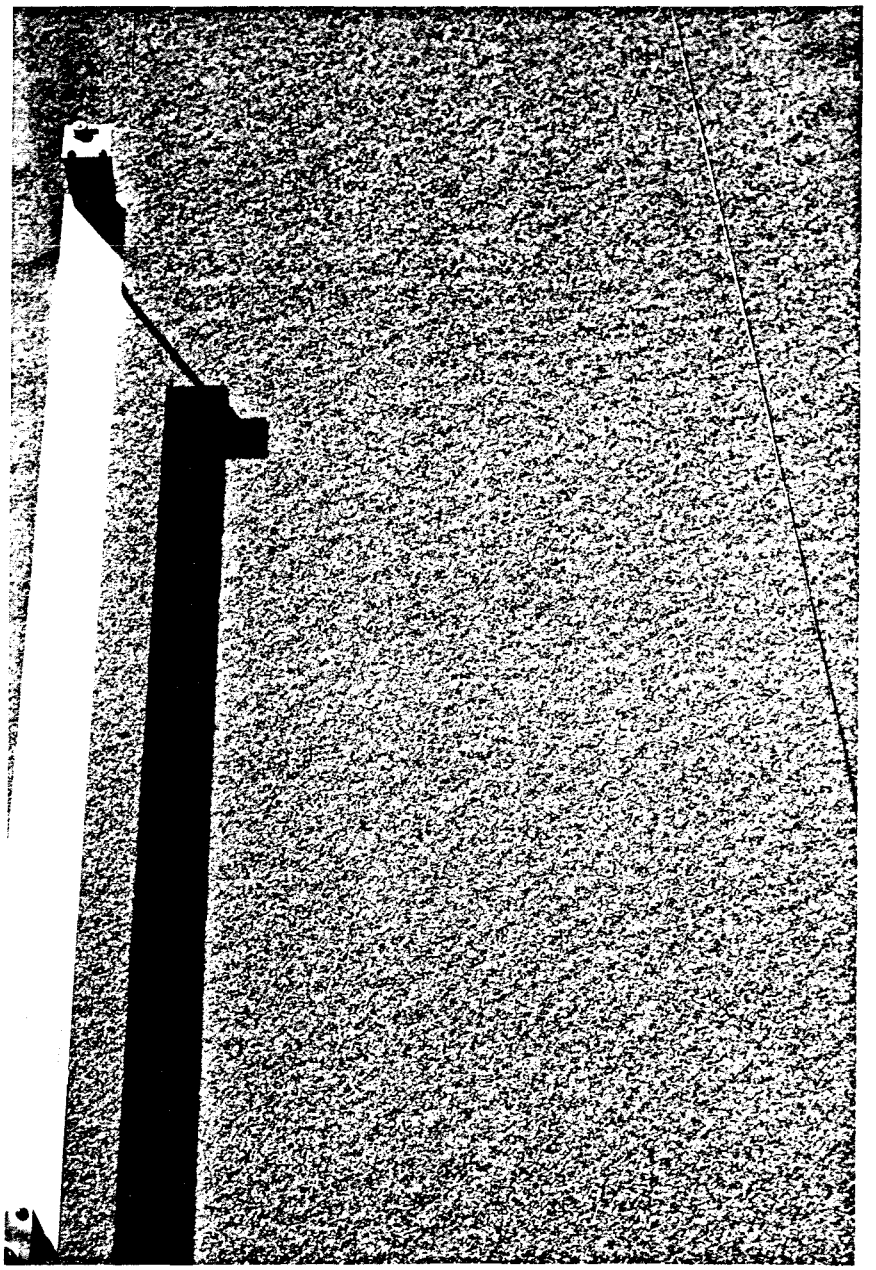

Figure 5.8

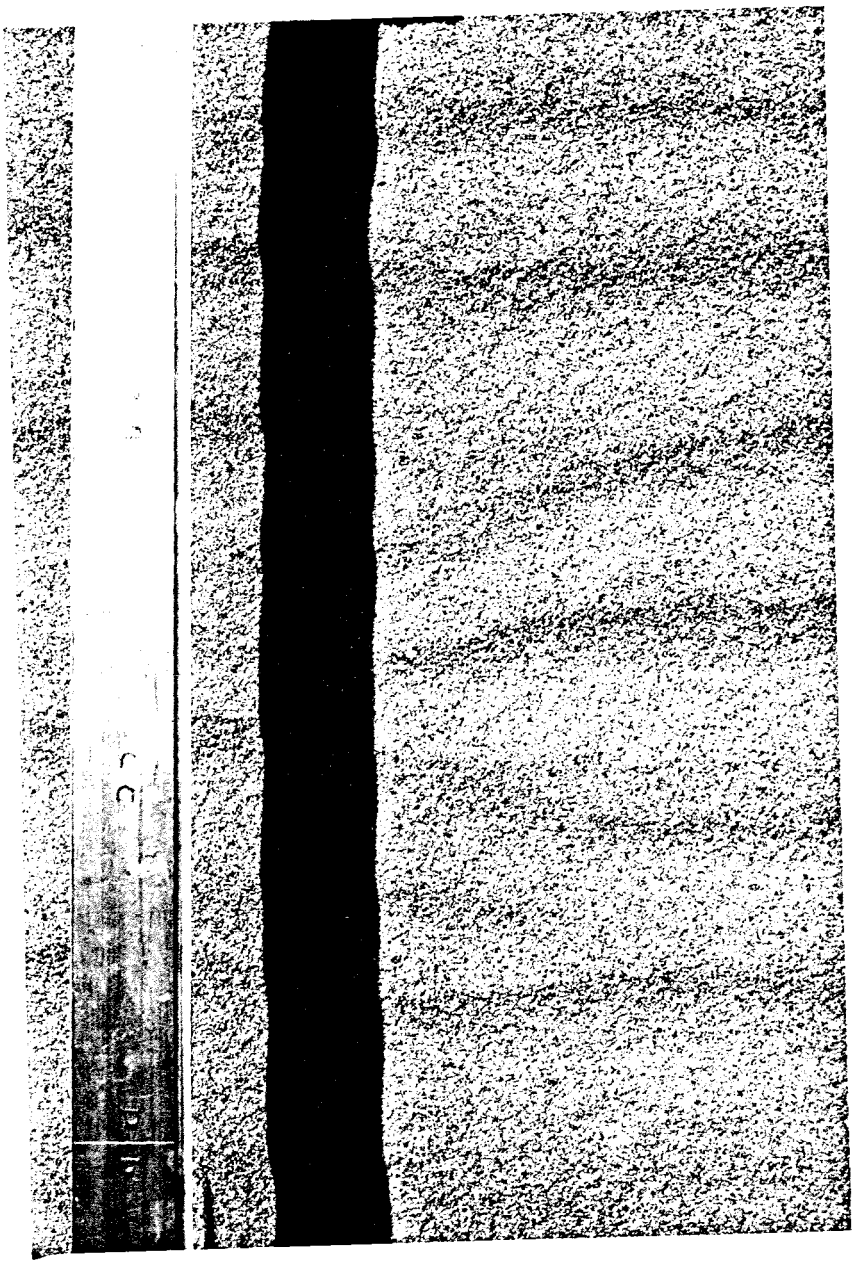

Figure 5.9

Figure 5.10

(a)

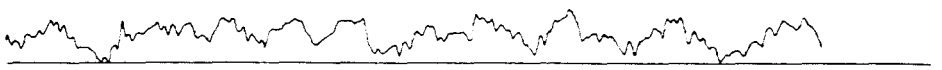

(b)

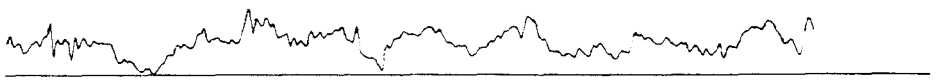

(c)

(d)

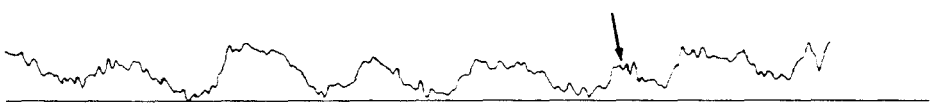

(e)

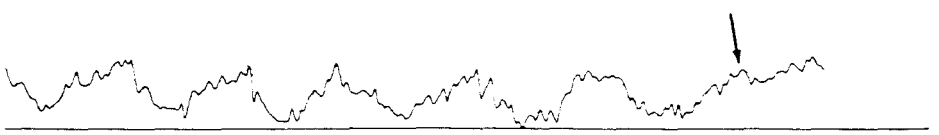

(f)

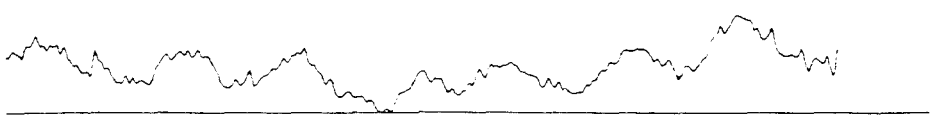

(g)

Figure 5.11

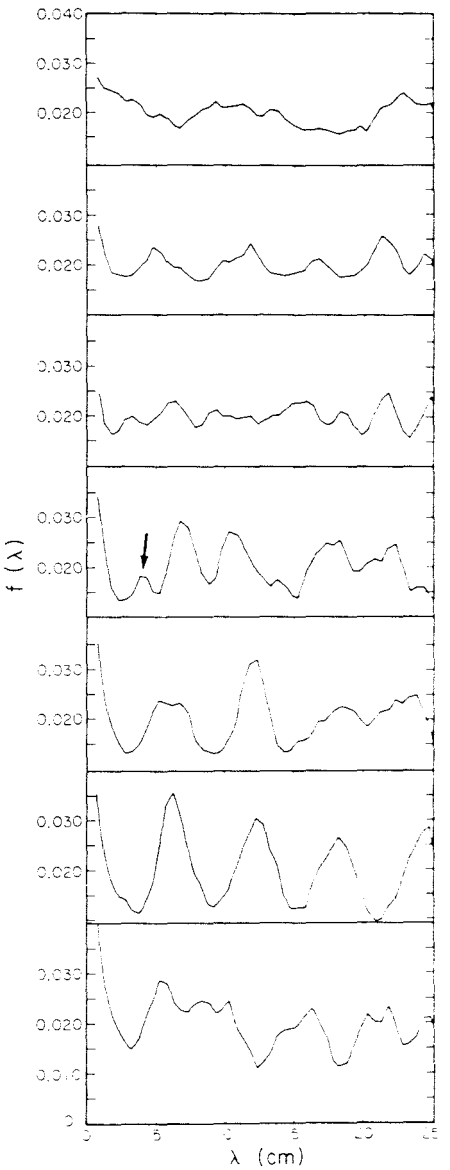
0.040
0.030
0.020
0.030
0.020
0.030
0.020
0.030
0.020
f (λ)
0.030
0.020
0.030
0.020
0.030
0.020
0.030
0.020
0.010
0
λ (cm)

Figure 5.12

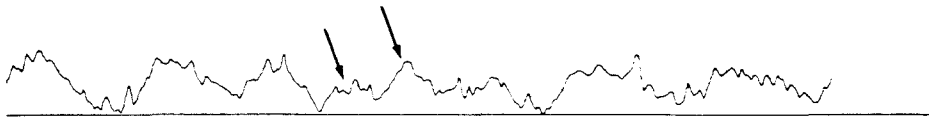

(a)

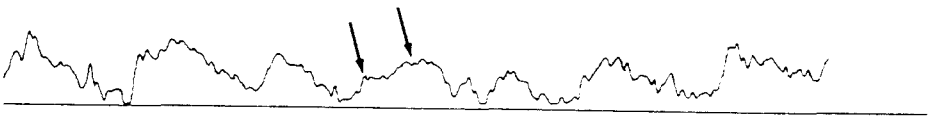

(b)

(c)

Figure 5.13

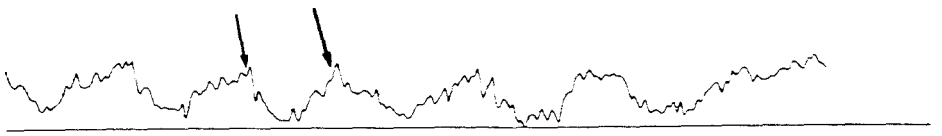

(a)

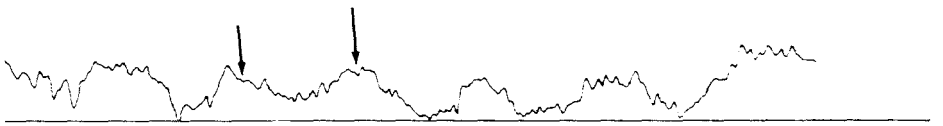

(b)

(c)

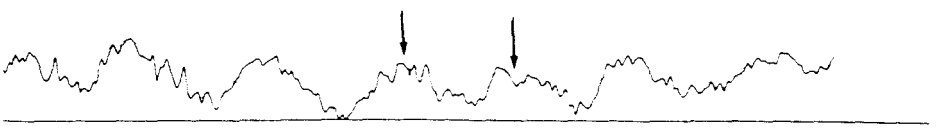

(d)

Figure 5.14

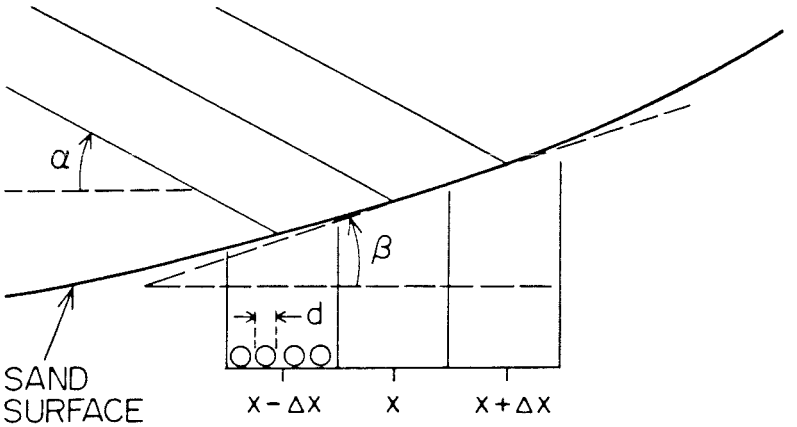

(a)

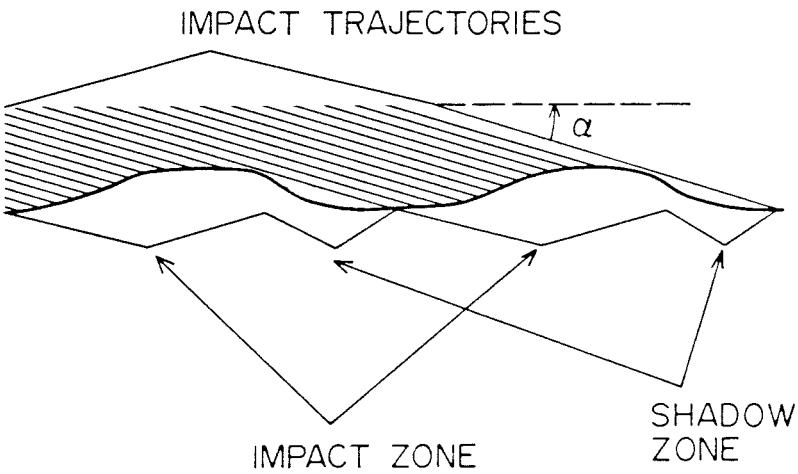

(b)

Figure 5.15

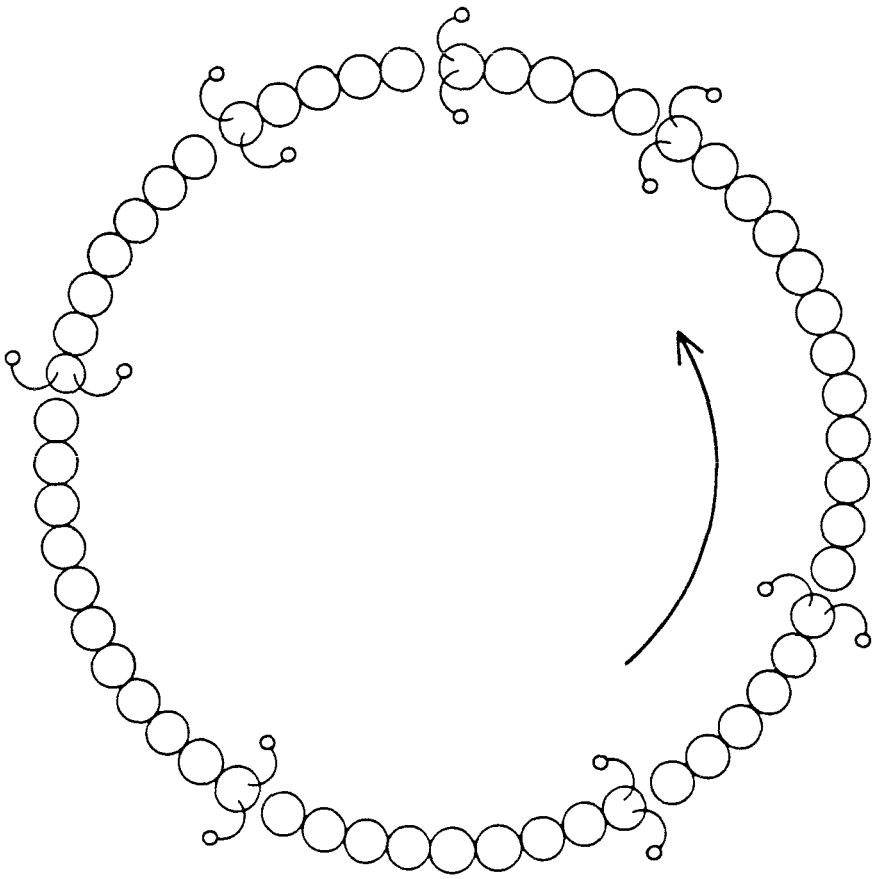

Figure 5.16

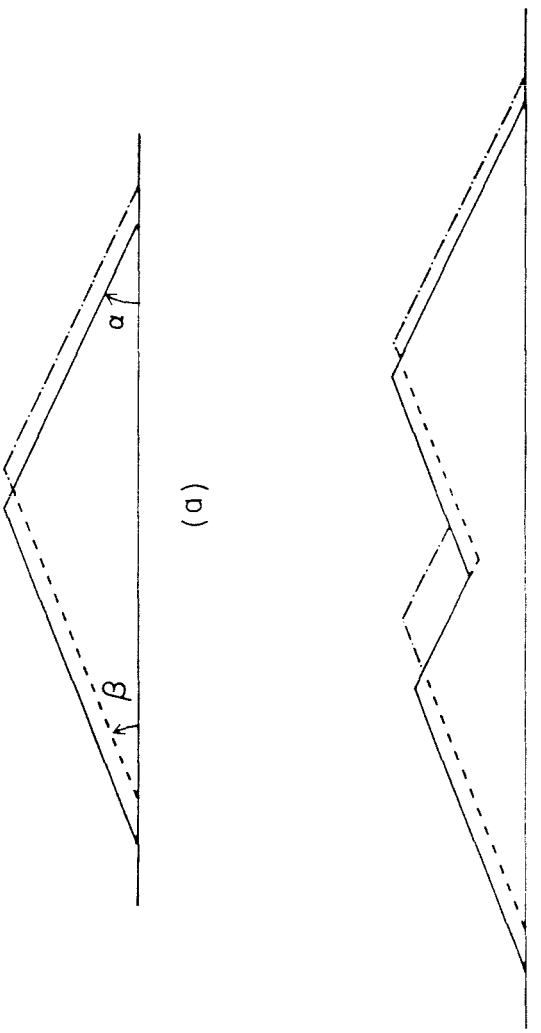

Figure 5.17

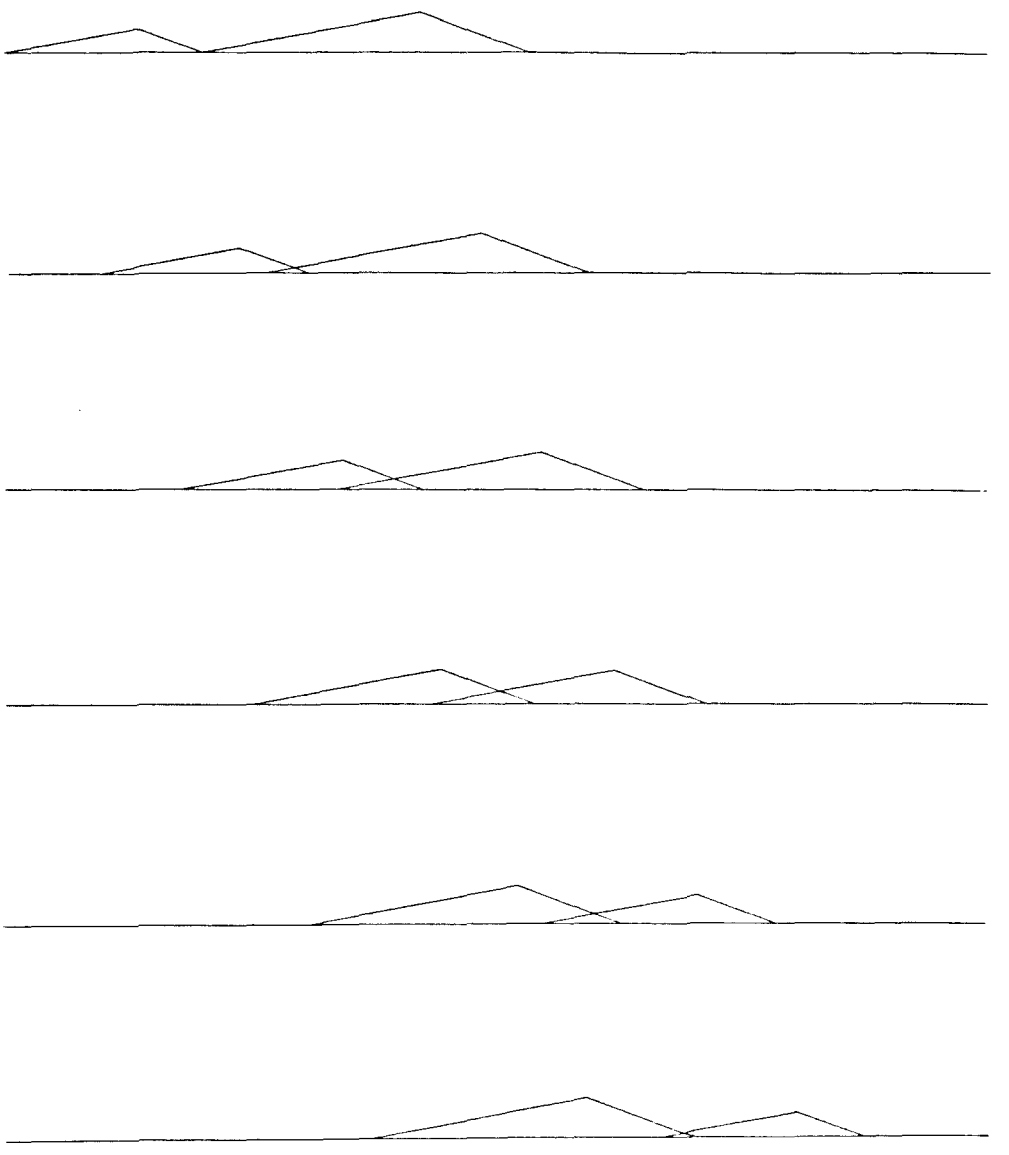

Figure 5.18

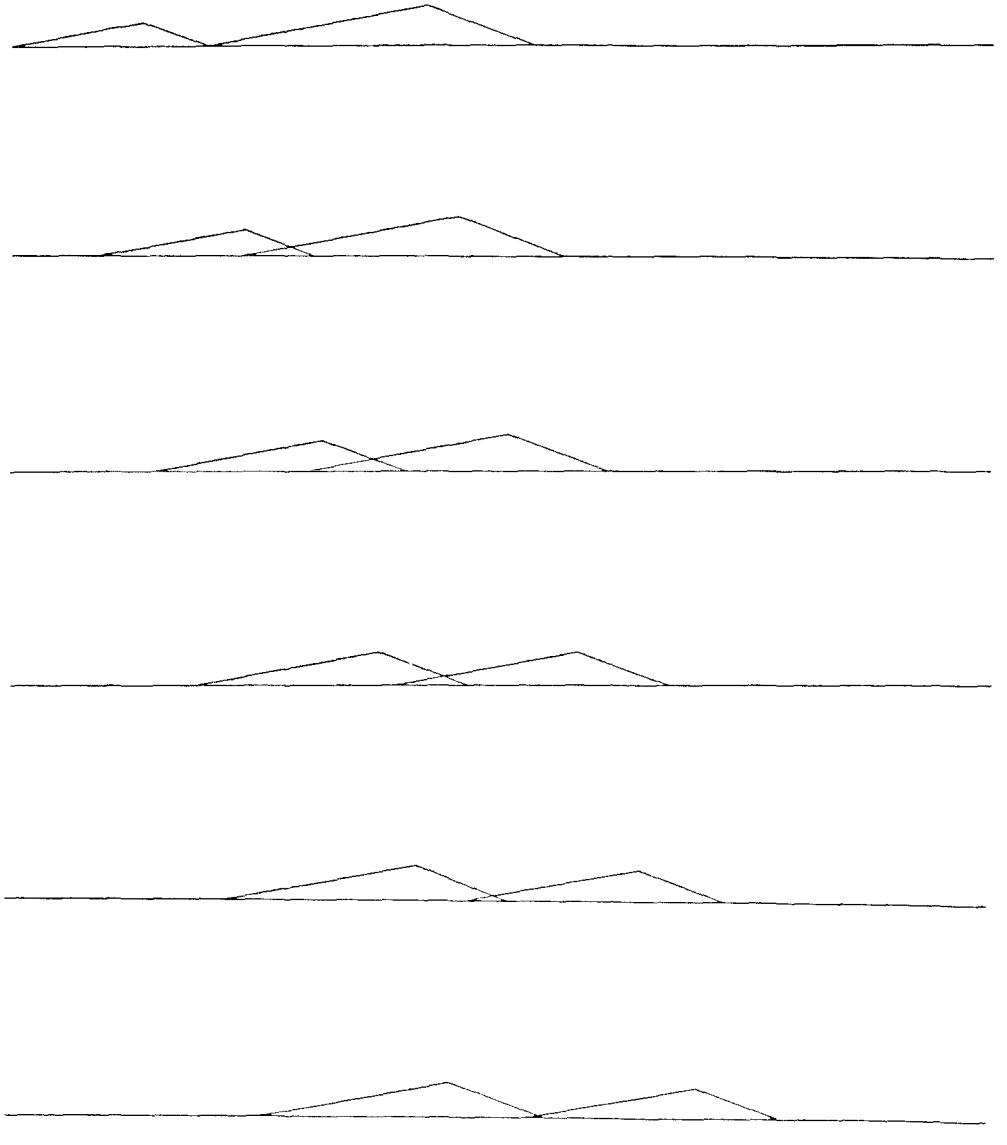

Figure 5.19

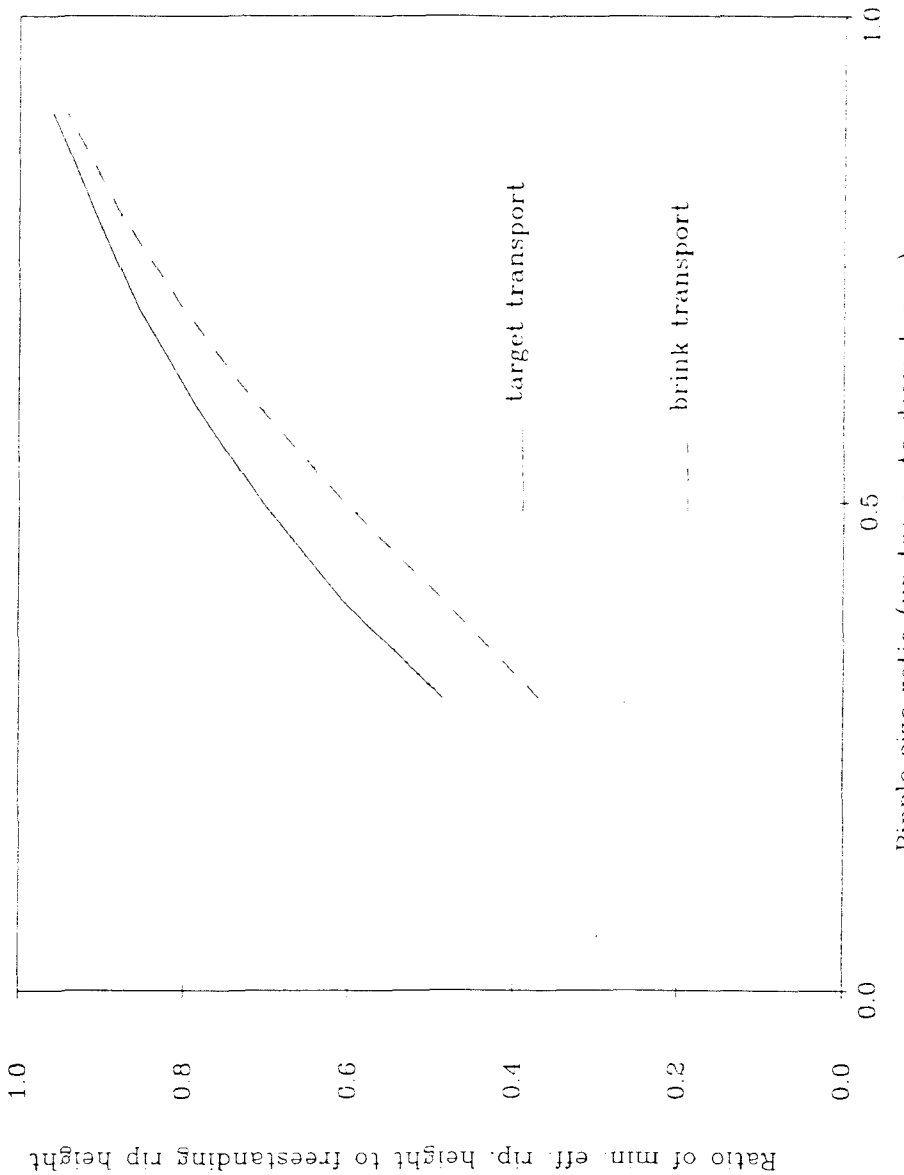
Ratio of min. eff. rip. height to freestanding rip height
1.0
0.8
0.6
0.4
0.2
0.0
0.0
0.5
1.0
Ripple size ratio (upstream to downstream)
target transport
brink transport

Figure 5.20

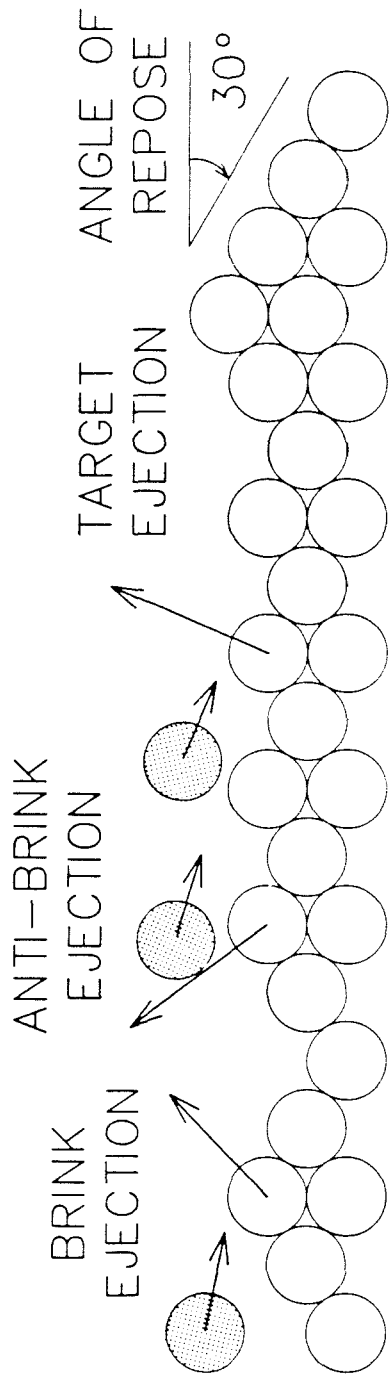
ANGLE OF REPOSE
30°
TARGET EJECTION
ANTI-BRINK EJECTION
BRINK EJECTION

Figure 5.21

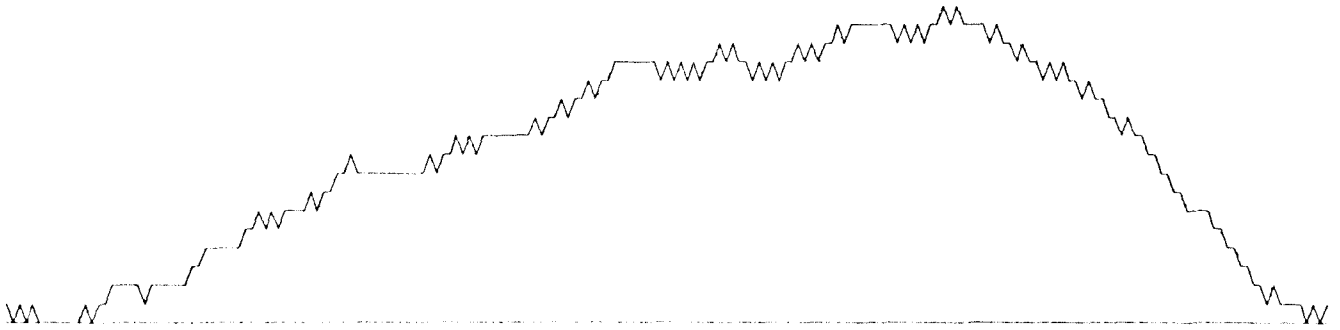

Figure 5.22

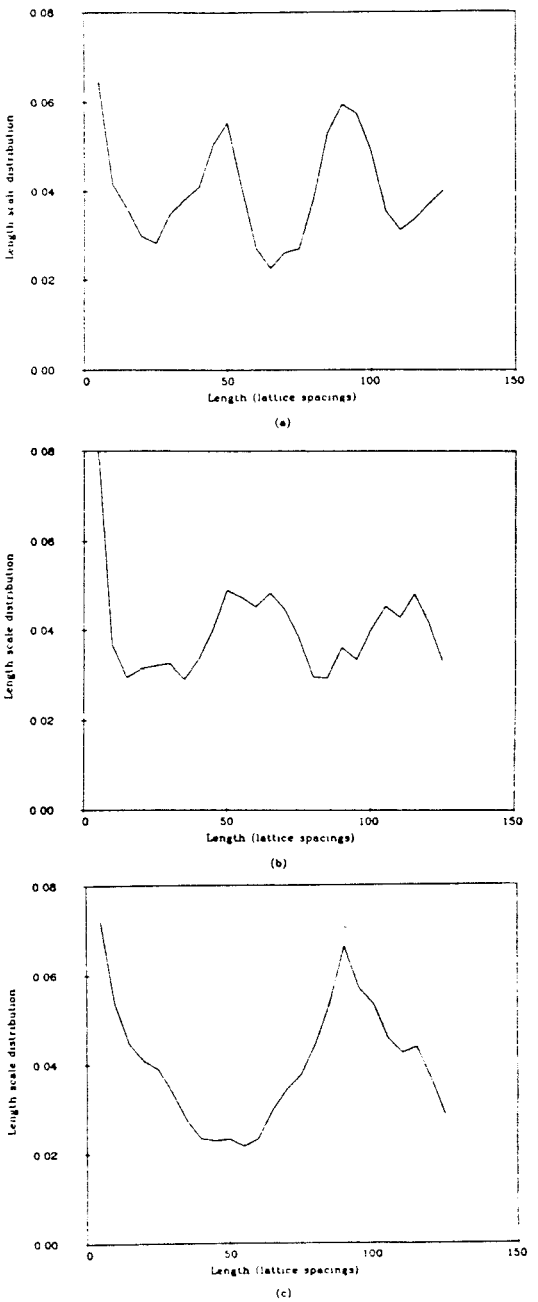
0.08
0.06
0.04
0.02
0.00
Length scale distribution
0
50
100
150
Length (lattice spacings)
(a)
0.08
0.06
0.04
0.02
0.00
Length scale distribution
0
50
100
150
Length (lattice spacings)
(b)
0.08
0.06
0.04
0.02
0.00
Length scale distribution
0
50
100
150
Length (lattice spacings)
(c)

Figure 5.23

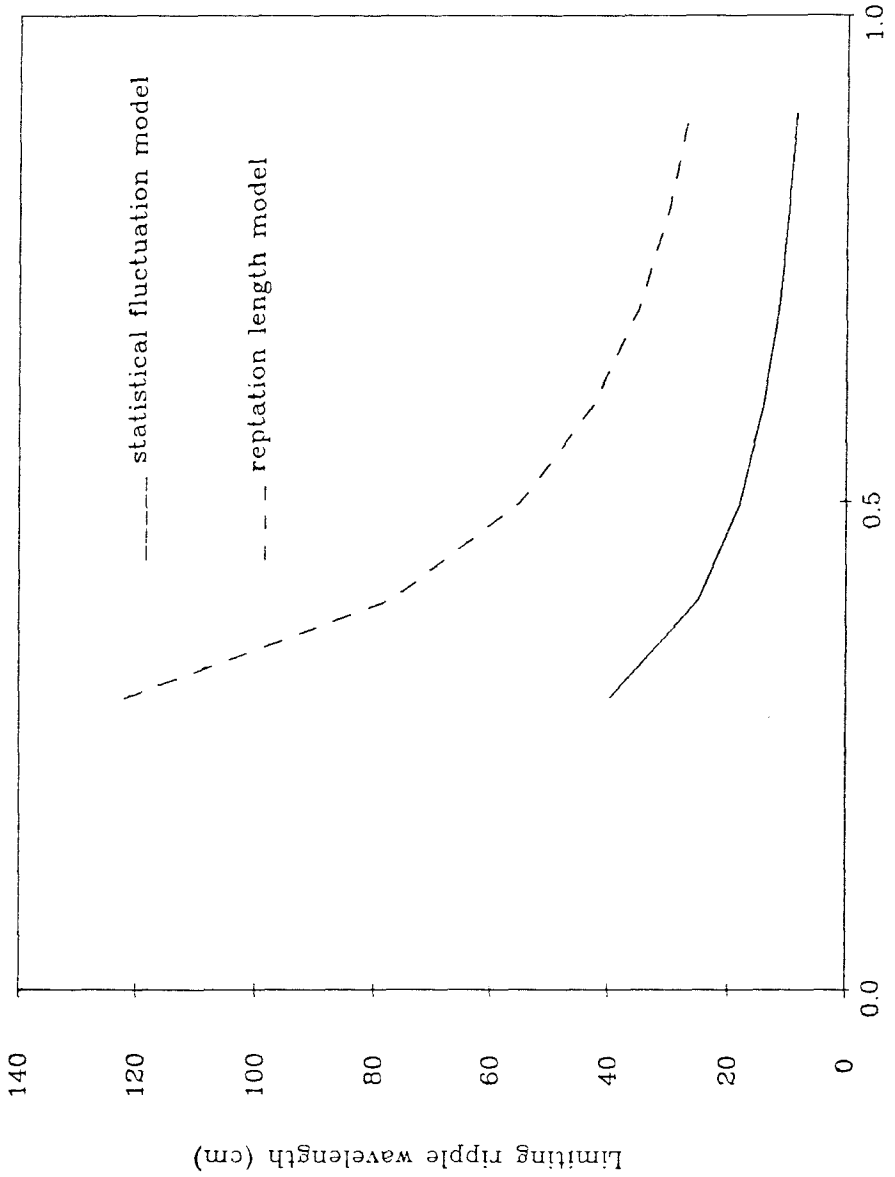
statistical fluctuation model
reptation length model
Limiting ripple wavelength (cm)
140
120
100
80
60
40
20
0
0.0
0.5
1.0
Ripple size ratio (upstream to downstream)

Figure 5.24

VI. SUMMARY AND FUTURE DIRECTIONS

"There's a dark cloud rising from the desert floor, I packed my bags and I'm heading straight into the storm."

-Bruce Springsteen

At most locales in the Mojave Desert, mountain ranges fill a fraction of the horizon. While walking toward one of these ranges, its appearance will evolve. A great distances, the mountains will seem like a formless slab of rock. With each passing mile, however, a new level of detail is revealed. First, one finds that the slab is rent with great slashes. Then, as the ragged base of the range is attained, these canyons themselves display a plethora of detail. The three-dimensionality becomes apparent: what was once a flat wall of rock is now an intricate maze of passageways.

The problem of eolian sand transport has been like that mountain range to us. Each question we answer, each small advance we make, opens up a new facet of the system, with an attendant range of questions to be answered. In this brief chapter, we summarize the work described in this document, emphasizing the assumptions and conclusions, and propose some directions for future research.

Grain Dynamics

One of the major limitations to the use of grain dynamics computer simulations is the computing power required to study a system composed of a sufficient number of particles to resemble realistic problems. We have demonstrated that it is possible to apply a new and developing technology, the concurrent processing computer, to the study of a problem in grain dynamics. The issue for granular simulations is computer time, not memory, because of the complicated nature of the particle-particle interactions. As the field evolves, and simulations of granular materials become more sophisticated, it is likely that researchers will continue to desire the most advanced computing facilities available.

Our work has employed primarily circular-grain simulations. We hope to be able to extend the simulation of grain-bed impacts to polygonal and spherical particles, using codes already in existence. Eventually, the development of a polyhedral particle simulation program is anticipated.

The interaction force between grains in our simulations to date has been taken to be a damped spring in the direction normal to the plane

of contact, and a damped spring bounded by the friction limit, opposing the relative motion, in the shear direction. The mechanisms we have identified as operating in grain-bed impacts and other problems have mainly relied on geometrical effects or the gross nature of the interparticle forces, rather than a detailed formulation of these forces. As the store of knowledge of grain dynamics accumulates, the introduction of more complicated force laws, including ideas from Hertzian contact mechanics and plasticity theory, will be appropriate.

Grain-Bed Impacts

Using the grain dynamics simulation code, we found that the incident particle rebound could be considered separately from the reaction of the bed grains. A model for the rebound was developed treating the collision between incident particle and bed as a two-body collision, with the bed grain struck by the incident grain behaving as though it possessed an effective mass greater than its true mass (by a factor of two in the simulations). A detailed model for the ejection of bed grains has not been derived; however, we have identified two basic ejection types. One is centered around the impact point, and consists of bed grains rising nearly vertically, generally with a very small fraction of

the incident energy (target ejection, or cratering). The other may extend away from the impact point. Particles resting on the edge of a depression in the surface may be preferentially ejected (brink/anti-brink ejection). A prime goal of further research will be the development of a model to describe the bed ejection process in quantitative detail. Also, simulating impacts on beds of mixed grain size with the circular grain program, and with irregular-shaped grains, will be of interest. Simulation of grain-bed impacts involving spheres will give us a good idea of the differences between two- and three-dimensions, and of whatever physics might be missing in two dimensions.

The experiment in which we shoot single grains of sand at a sand bed produced a variety of interesting results, beyond confirming the general picture observed in the simulations, BB experiments (Mitha, et al., 1986) and wind tunnel experiments with sand (Willetts and Rice, 1985a); the data from the sand gun experiment has confirmed qualitatively our theoretical model. We summarize these experimental results in terms of their variation with incident velocity and incident angle. With increasing incident velocity

(1) the rebound roughly scales,

(2) the number of ejecta increases linearly,

(3) the mean reptation length and mean ejected vertical velocity do not vary,

(4) the distribution of ejected angles shifts towards the vertical, suggesting that the "crater size" in the bed has exceeded the mean distance between roughness elements on the bed, i.e., that the brink particle ejection has "saturated."

Our data on variation with incident angle is more sketchy, but, with increasing incident angle

(1) the vertical velocity amplification sharply decreases, and

(2) the number of ejecta gently increases.

Specification of other angular dependences will require additional data.

This sand gun experiment complements the work of Willetts and Rice (1985a), in that, although we are not attempting to reproduce conditions in Nature as closely as is possible in a wind tunnel, we are well-equipped to study particular aspects of the physical mechanisms operating in the grain-bed impact process. We can, for instance, prepare the bed in a variety of ways: tightly pack it or jostle it, prior to the impact, or shake the bed during the impact, in order to create a mobile

surface. Characterization of the surface topography might be effected through a variety of techniques, including the shadow technique described for ripples in Chapter V, or other related approaches (R.S. Anderson, 1987: personal communication). In addition, it is possible to prepare the bed with a specific type of sorting by size or shape, and to choose an incident particle with particular characteristics. We hope to use the sand gun to study quantitatively the ejection of dust by saltation impacts, which may be an important mechanism operating in many dust storms (Gillette, 1981).

The combination of controlled impact experiments, wind tunnel experiments, and simulations should allow for a more complete understanding of the grain-bed impact process, and the numerical information necessary for the use in models of saltation, in which grain-bed impacts play a critical role.

Eolian Saltation Model

Eolian saltation is a process which, on one hand, seeks to balance the force of the wind on the moving sand grains, and, on the other hand, seeks to ensure that a representative sample of grains leaving the surface will lead to an identical set of outgoing grains, following acceleration by

the wind and impact with the surface. In steady-state saltation, a balance between the number of grains leaving the saltating population and the number entrained will be achieved. By replacing gravity and the aerodynamic drag with a conveyer belt situated above the sand surface, the basic dynamics of the system, the journey of the system to the steady-state, and the manner in which feedback operates in saltation were elucidated.

We have presented an extension of Ungar and Haff's model for steady-state saltation which incorporates a realistic grain-bed impact (splash) function. The key components of this model are

(1) the bed is assumed to be flat and the saltation is taken to be uniform in the downstream and transverse directions,

(2) the distribution of velocities of grains leaving the bed per incident grain is related to the impact velocity and angle by a function depending primarily on the bed characteristics: the splash function,

(3) the mean wind profile is determined by the spatially averaged drag forces exerted by the grains,

(4) the grain trajectories are a function of their initial velocity, the drag exerted on them by the wind, and gravitational forces,

(5) the system is in steady-state, i.e., the distribution of grains leaving an area on the bed will, through acceleration by the wind and impact with the bed, reproduce itself,

(6) and the steady state is computed using an iterative scheme, and the space of outgoing velocities from the bed is discretized.

The saltation model reproduces the features seen in natural saltation, including the decrease in wind velocity near the bed (below the focus) with increasing free-stream wind-shear velocity u^*, the dependence of flux on u^*, and the maximum of saltating sand grain abrasion (kinetic energy flux) appearing well above the surface. The model predicts that the fluid stress on the surface will <u>decrease</u> with increasing u^*. Also, the distribution of particle trajectories and impact velocities are expected to be broadened as u^* is increased, because grains travelling above the focus will attain higher velocities and greater ranges when the free-stream wind velocity is greater, and those grains moving primarily below the focus will feel lower wind velocities at higher u^*, and hence will impact with lower velocity and shorter range.

The argument that fluid stresses on the surface decrease with

increasing u^* may be made on physical principles, independent of the details of our saltation model. Thus, we have asserted that entrainment of grains in steady-state saltation is accomplished through grain-bed impacts. Splash functions which specify that the ability of impacting saltating grains to "reproduce" themselves decreases with increasing impact velocity in some region of phase space could lead to a positive-feedback condition and oscillating behavior of the saltating system.

A quantitative evaluation of our saltation model is lacking, because it requires one to determine the splash function for a particular sand, and then measure various properties of wind-blown sand over a surface composed of this type of sand, including, perhaps, the wind velocity and sand flux as a function of height, under controlled conditions. Because attention currently is being focussed on the grain-bed impact in saltation, and at least two groups are capable of finding the splash function for sand, it would appear that such a test will be possible in the near future.

A predictive saltation model of the type we have proposed may have many uses. Using this model, we hope to explore the dependence of

saltation on a variety of parameters, including wind-shear velocity, grain size, the grain-size sorting (which will require us to keep track of size populations of grains, as well as to understand the splash function on a mixed-grain-size surface and the vertical sorting of the bed under saltation impacts), and dust ejection by saltation impacts, which necessarily requires a knowledge of the distribution of impact velocities. The model also will be well-suited to an inquiry into the character of saltation on Mars, and possibly Venus. Finally, we expect to extend the model to include time-dependence, allowing us to evaluate the possibility of non-steady behavior of saltating systems. The inclusion of time dependence in saltation likely will be of use in studying sediment entrainment and transport in the expanding shell of an above-ground nuclear detonation.

Wind-blown Sand Ripples

To aid in bringing about a resolution of the long-standing controversy surrounding the mechanism for eolian sand ripple formation, we have sought to extend the pre-existing data base, which primarily characterizes ripples by their wavelength and ripple index (wavelength-to-height ratio), by introducing a technique for measuring

ripple cross-sectional shapes easily and accurately, through recording the terminus of the shadow cast by a straightedge oriented perpendicular to the ripple crests. For static, mature ripples, we found that the ripple shape can vary substantially over the surface of a single dune. Further measurements on mature ripples are warranted. In particular, it would be of interest to correlate mature ripple shapes with wind velocity and surface slope at various positions on a sand dune.

An extension of the ripple-shadow technique to observing the evolution of ripples under saltation impacts from an initially flat surface has confirmed the findings of some previous investigators: ripples represent an end product of a process involving growth of ripple wavelengths to a final, stable value. In our data, we identified collisions between ripples, and observed both proto-ripple mergers and the repulsion between two colliding ripples. Field experiments aimed at further quantifying the evolving surface length scale, and the shapes of the ripples during collision, are in order.

In our picture of ripple formation, we have focussed on collisions between proto-ripples, and taken ripple mergers to be the means of increasing ripple wavelengths. Reptation, the movement of grains along

the surface is taken to be driven by saltating grain-bed impacts, which, on the average, are distributed uniformly over the horizontal plane. Ripple motion is the result of this mode of grain transport. Computer simulations of ripple formation have suggested that statistical fluctuations play a role in determining the asymptotic wavelength of the ripples formed under this picture.

We envision that a flat surface undergoing saltation impacts quickly assumes a state of uneven topography. Small groupings of grains (proto-ripples) on the surface will travel faster than larger groupings of grains. This variation of size in the proto-ripples, as well as fluctuations in the saltation flux, will drive collisions between them. In the collisions, the smaller ripple crawls part of the way up the back of the larger ripple. We propose that the merger of these two ripples can be effected in two ways: (1) statistical fluctuations in the saltating flux causes the upstream ripple apex to be sheared off, and (2) the shadow zone of the upstream ripple becomes smaller in length than the mean reptation length, leading to a runaway loss of grains to the downstream ripple. Order of magnitude calculations of limiting ripple wavelengths, based on these two merger mechanisms, are compatible with existing

data.

We have identified what we believe to be the mechanisms operating in eolian ripple formation. It remains to incorporate these ideas into a detailed, coherent model. To accomplish this, it will be necessary both to produce a more quantitative description of ripple collisions, and to place the collisions within an overall mathematical framework accounting for the evolution of the surface. Further study with the computer simulations of ripple formation may aid in accomplishing these tasks.

A General Model for Eolian Sediment Transport

Because of the complexity of eolian saltation, we have adopted, in this document, the strategy of decoupling the various processes comprising the whole (e.g., grain-bed impacts, wind-grain interactions and ripple formation), and analyzing them separately. In Chapter IV, we succeeded in proposing a model of eolian saltation, which, although somewhat simplified, contained all basic elements of the process excluding surface evolution. Inclusion of ripple formation in a saltation model might be approached best through computer simulations. A first step might be to include wind and trajectory calculations in our surface

evolution simulation where the bed grains constrained to lie on a two-dimensional lattice. The splash function could be specified as a rule dictating the movement of surface grains, much the same way as it is in the present version. An additional extension would include actually calculating the dynamics of the impacts, as in our grain dynamics simulations, propagating the incident particle forward along the bed, and adjusting the wind velocity as in our steady-state saltation algorithm. Ultimately, performing this type of computation with three-dimensional or irregular grains would be desirable. However, because the minimum fetch for such a simulation would be on the order of one-thousand grain diameters, the availability of computing power for this "dream" simulation lies far in the future. We may, in the meantime, content ourselves within the voluminous array of work required to extend our present conception of wind-blown sand transport.

During the period encompassing the research described above, the author was fortunate to live as a free man in a country in which innovation is encouraged and rewarded. Indeed, freedom, adventure, and unfettered access to open land played a key role in these investigations,

and contributed significantly to the ideas we have put forth. It is unfortunate that we may be living at a time when such advantages are slipping through our grasp. As knowledge expands, the liberty to seek out new areas of inquiry and to examine old problems from unusual viewpoints must be provided; the adventure and creative stimulus so important to human motivation must be available; otherwise, the well from which we draw our inspiration will soon run dry. We fear that Bagnold's (1935) dreary vision of future events, written over fifty years ago, is on the horizon; and advancing; unopposed.

> Perhaps a long time hence, when all the earth's surface has been seen and surveyed, there may be nothing left to find. Fancifully we can picture the excavator rummaging about with his pick in the last yard of unexamined soil. Behind him we catch a glimpse of experts, microscopes and notebooks, while in front, very near now, stand the locked gates in the city's misty walls.
>
> The pick is withdrawn. The time has come at last when the experts can close their notebooks, for there is nothing else unfound. We see Zerzura crumbling rapidly into dust. Little birds rise from within and fly away. A cloud moving across the sun makes the world a dull and colourless place.

As long as our fate remains in our own hands, hope will not desert us, for even if Bagnold's prophecy holds, beyond the bounds of Earth are many a grand journey.

REFERENCES

H.H. Shen and N.L. Ackermann (1982) Constitutive Relationships for fluid-solid mixtures, *J Eng. Mech. Div. (ASCE)*, **108**, No. EM5, 748-763.

F.S. Acton(1970) **Numerical Methods that Work**, New York, Harper and Row, 541p.

G. Ahmadi and M. Shahinpoor (1983) A kinetic model for rapid flows of granular materials, *Intl. J. Non-linear Mechanics*, **19**, 177-186.

B.J. Alder and T.E. Wainwright (1959) Studies in molecular dynamics I. general method, *J. Chem. Phys.*, **31,** 459-466.

B.J. Alder and T.E. Wainwright (1960) Studies in molecular dynamics II. behavior of a small number of elastic spheres, *J. Chem. Phys.*, **33,** 1439-1451.

J.R.L. Allen (1969) On the geometry of current ripples in relation to stability of fluid flow, *Geografiska Annaler*, **51A**, 61-95.

R.S. Anderson (1986) Sediment transport by the wind: saltation, suspension, erosion and ripples, unpublished Ph.D. thesis, University of Washington, 174p.

R.S. Anderson and B. Hallet (1986) Sediment transport by wind: toward a

general model, *Geol. Soc. Am. Bull.*, **97**, 523-535.

K. Araoka and N. Maeno (1981) Dynamical behaviors of snow particles in the saltation layer, *Memoirs of the National Institute of Polar Research*, **19**, 253-263.

R.A. Bagnold (1931) Journeys in the Libyan Desert, *Geographical Journal*, **78**, 13-39.

R.A. Bagnold (1935) **Libyan Sands: Travel in a Dead World**, London, Hodder and Stroughton, 288p.

R.A. Bagnold (1941) **The Physics of Blown Sand and Desert Dunes,** London, Methuen, 265p.

H.M. Barkla and L.J. Auchterlonie (1971) The Magnus or Robins effect on rotating spheres, *J. Fluid Mech.*, **47**, 437-447.

J.D. Bjorken and S.D. Drell (1964) **Relativistic Quantum Fields**, New York, McGraw-Hill, 202-207.

F.P. Bowden and D. Tabor (1950) **The Friction and Lubrication of Solids**, London, Oxford.

D. Bozzolo and R. Panami (1982) Modello Matematico per lo studio della della caduta dei massi, Laboratorio di Fisica Terrestre-ICTS, Lugano-Trevano, dicembre, 89 p.

P.W. Bridgman (1922) **Dimensional Analysis**, New Haven, Yale University Press, 112p.

C.S. Campbell and C.E. Brennen (1985) Chute flows of granular materials: some computer simulations, *J. App. Mech.*, **52**, 172-178.

S. Chapman (1960) Misconceptions concerning the dynamics of the impact ball apparatus, *Am. J. Phys.*, **28**, 705-711.

W.S. Chepil (1945a) Dynamics of wind erosion: I. Nature of movement of soil by wind, *Soil Science*, **60**, 305-320.

W.S. Chepil (1945b) Dynamics of wind erosion: II. Initiation of soil movement, *Soil Science*, **60**, 397-410.

W.S. Chepil (1945c) Dynamics of wind erosion: III. The transport capacity of the wind, *Soil Science*, **60**, 475-480.

W.S. Chepil (1958) The use of evenly spaced hemispheres to evaluate aerodynamic forces on a soil surface, *Trans. Am. Geophysical Union*, **29**, 397-404.

W.S. Chepil and N.P. Woodruff (1963) The physics of wind erosion and its control, *Advances in Agronomy*, **15**, 211-302.

V. Cornish (1914) **Waves of Sand and Snow**, London, T. Fisher Unwin, 383p.

V. Cornish (1935) **Ocean Waves and Kindred Geophysical Phenomena**, Cambridge, England, Cambridge University Press, 164p.

J.D. Cruz, Jr. (1972) Feedback in Systems, in **Feedback Systems**, J.D. Cruz, Jr., ed., New York, McGraw-Hill, 1-18.

P.A. Cundall and O.D.L. Strack (1979) A discrete numerical model for granular assemblies, *Geotechnique*, **29**, 47-65.

R.A. Davis and H. Deresiewicz (1977) A discrete probabilistic model for a mechanical response of a granular medium, *Acta Mechanica*, **27**, 69-89.

H. Deresiewicz (1958) Mechanics of granular matter, *Advances in Applied Mechanics*, **5**, 233-306.

T.G. Drake and R.L. Shreve (1985) High speed motion pictures of steady, uniform, two-dimensional, inertial flows of granular material, *J. Rheology*, **30**, 981-993.

T.G. Drake, R.L. Shreve, W.E. Dietrich, L.B. Leopold, P.J. Whiting (1986) High-speed motion-picture observations of fine-gravel bed-load motion at low excess bed-shear stresses in a natural stream, *submitted*.

J.M. Ellwood, P.D. Evans and I.G. Wilson (1975) Small scale aeolian

bedforms, *Jour. Sedimentary Petrology*, **45**, 554-561.

R. Feynman (1965) **The Character of Physical Law**, Cambridge, Massachusetts, MIT Press, 173p.

M.J. Feigenbaum (1983) Universal behavior in nonlinear systems, *Physica*, **7D**, 16-39.

G.C. Fox (1984) Concurrent processing for scientific applications, *Proceedings of the Compcon '84 Twenty-eighth IEEE Computer Society International Conference*, February 27 - March 1, IEEE Computer Society Press.

G.C. Fox and S.W. Otto (1984) Algorithms for Concurrent Processors, *Physics Today*, May, 50-59.

G.C. Fox, G. Lyzenga, D. Rogstad and S. Otto (1985) Caltech concurrent computation program, to appear in *Proceedings of the 1985 International Computers in Engineering Conference (ASME)*, August 4-8, Boston, Massachusetts.

G.K. Gilbert (1914) The transportation of debris by running water, *U.S. Geological Survey Professional Paper* **86**, 263p.

D.A. Gillette (1981) Production of dust that may be carried great distances, *in* **Desert Dust: Origin, Characteristics, and Effect**

on Man, T.L. Pewe, ed., *Geol. Soc. Am. Special Paper*, **186**, 11-26.

E. Girden (1962) A review of psychokinesis (PK), *Pychological Bulletin*, **59**, 353-388.

W.H. Gletzen and J.C. Ludwick (1963) An automated grain-shape classifier, *Jour. Sedimentary Petrology*, **33**, 23-40.

W. Goldsmith (1960) **Impact**, London, E. Arnold, Ltd., 379p.

H. Goldstein (1950) **Classical Mechanics**, Reading, Massachusetts, Addison-Wesley, 399p.

R. Gordon, J.B. Carmichael and F.J. Isackson (1972) Saltation of plastic balls in a 'one-dimensional' flume, *Water Resources Research*, **8**, 444-459.

R. Greeley, J.D. Iversen, J.B. Pollack, N. Udorich and B. White (1974) Wind tunnel studies of Martian aeolian processes, *Proc. R. Soc. Lond.*, **341A**, 331-360.

R. Greeley, J.R. Marshall and R.N. Leach (1984) Microdunes and other aeolian bedforms on Venus: wind tunnel simulations, *Icarus*, **60**, 152-160.

P.K. Haff (1983) Grain flow as a fluid-mechanical phenomenon, *J. Fluid Mech.*, **134**, 401-430.

P.K. Haff (1985) A physical model of kinetic granular fluids, *J. Rheology*, **30**, 931-948.

P.K. Haff (1986) Computing with particles, *Caltech Basic and Applied Physics: Brown Bag Preprint* **48**, 12p.

P.K. Haff and B.T. Werner (1985) The collisional interaction of a small number of confined, inelastic grains, *Proceedings of the International Symposium-Workshop on Particulate and Multi-phase Processes and 16th Annual Meeting of the Fine Particle Society*, April 22-26, Miami Beach Florida, *in press*.

P.K. Haff and B.T. Werner (1986) Computer simulation of the mechanical sorting of grains, *Powder Technology*, **48**, 239-245.

P.K. Haff, T.A. Tombrello and J.E. Ungar (1985) Kinetic model of a compressible grain-gas: applications to particles in a box, couette flow and inclined plane flow, *unpublished manuscript*.

P.J. Holmes and F.C. Moon (1983) Strange attractors and chaos in nonlinear mechanics, *J. App. Mech.*, **50**, 1021-1032.

K.R. Housen, R.M. Schmidt, K.A. Holsapple (1983) Crater ejecta scaling laws: Fundamental forms based on dimensional analysis, *Jour. Geophysical Research*, **88**, 2485-2499.

G.W. Housner (1963) The behavior of inverted pendulum structures during earthquakes, *Bull. Seismological Society of America*, **53**, 403-417.

K. Hui, P.K. Haff, J.E. Ungar and R. Jackson (1984) Boundary conditions for high-shear grain flows, *J. Fluid Mech.*, **145**, 223-233.

J.C.R. Hunt and P. Napalis (1985) Saltating and suspended particles over flat and sloping surfaces: I. Modelling concepts, *Proceedings of the International Workshop on the Physics of Blown Sand*, O.E. Barndorff-Nielson, J.T. Moller, K. Romer Rasmussen and B.B. Willetts, eds., May 28-31, Aarhus, Denmark, University of Aarhus Press, 9-36.

J.D. Iversen, J.B. Pollack, R. Greeley and B.R. White (1976) Saltation threshold on Mars: the effect of interparticle forces, surface roughness and low atmospheric density, *Icarus*, **29**, 381-393.

S.C. Jain and J.F. Kennedy (1974) The spectral evolution of sedimentary bed forms, *J. Fluid Mech.*, **63**, 301-314.

J.T. Jenkins and S.B. Savage (1983) A theory for the rapid flow of identical, smooth, nearly elastic particles, *J. Fluid Mech.*, **130**, 187-207.

J.L. Jensen and M. Sorensen (1982) On the mathematical modeling of

aeolian saltation, in *Mechanics of Sediment Transport: Euromech 156 Conference*, Istanbul, Turkey, July 12-14, 65-72.

J.G. Kemeny and J.L. Snell (1960) Finite Markov Chains, Princeton, Van Nostrand, 210p.

J.F. Kennedy (1964) The formation of sediment ripples in closed rectangular conduits and in the desert, *Jour. Geophysical Research*, **69**, 1517-1524.

L.D. Landau and E.M. Lifshitz (1970) **Theory of Elasticity**, Oxford, Pergamon, 165p.

C.K.K. Lun and S.B. Savage (1986) A simple kinetic theory for granular flow of rough, inelastic spherical particles, *J. App. Mech.*, in press.

C.K.K. Lun, S.B. Savage, D.J. Jeffrey and N. Chepurniy (1984) Kinetic theories for granular flow: inelastic particles in couette flow and slightly inelastic particles in a general flow field, *J. Fluid Mech.*, **140**, 223-256.

K.B. Mather (1963) Why do roads corrugate?, *Scientific American*, January, 128-134.

J. Mathews and R.L. Walker (1970) **Mathematical Methods of Physics**, Menlo Park, California, Benjamin/Cummings, 302-303.

J.F. McCauley, M.J. Grolier and C.S. Breed (1977) Yardangs of Peru and other desert regions, *U.S.G.S. Interagency Report: Astrogeology 81*, 177p.

D.F. McTigue (1978) A model for stresses in shear flow of granular material, *Proceedings of the U.S.-Japan Seminar on Continuum-Mechanical and Statistical Approaches in the Mechanics of Granular Materials*, S.C. Cowin and M.Satake, eds., Tokyo, Japan, Gokujutsu Bunken Fukyukai (subsequently referred to as *Proc. US-Japan Seminar*), 162-170.

M.A. Melton (1965) Debris-covered hillslopes of the Southern Arizona desert - considerations of their stability and sediment contribution, *Jour. Geology*, **73**, 715-729.

S. Mitha, M.Q. Tran, B.T. Werner and P.K. Haff (1986) The grain-bed impact process in aeolian saltation, *Acta Mechanica*, **63**, 267-278.

H. Narita (1978) Controlling factors of drifting snow, *Memoirs of the National Institute of Polar Research*, **7**, 81-92.

S. Ogawa (1978) Multitemperature theory of granular materials, *Proc. US-Japan Seminar*, 208-217.

S. Ogawa, A. Umemura and N. Oshima (1980) On the equations of fully

fluidized granular material, *J. Appl. Math. and Phys. (ZAMP)*, **31**, 483-493.

P.R. Owen (1964) Saltation of uniform grains in air, *J. Fluid Mech.*, **20**, 225-242.

W.S.B. Patterson (1981) **The Physics of Glaciers**, Oxford, Pergamon, 380p.

J.A. Reitzes (1978) Numerical study of continuous saltation, *Journal of the Hydrology Division* (ASCE), **104**, 1305-1321.

D.A. Rumpel (1985) Successive aeolian saltation: studies of idealized collisions, *Sedimentology*, **32**, 267-280.

S.B. Savage (1979) Gravity flow of cohesionless granular materials in chutes and channels, *J. Fluid Mech.*, **92**, 53-96.

S.B. Savage and J.D. Jeffrey (1981) The shear tensor in granular flow at high shear rate, *J. Fluid Mech.*, **110**, 255-272.

J. Scarne (1980) **Scarne on Dice**, New York, Crown, 496p.

H. Schlichting (1979) **Boundary Layer Theory**, New York, McGraw-Hill, 817p.

L.M. Schwartz, D.L. Johnson and S. Feng (1984) Vibrational modes in granular materials, *Phys. Rev. Letters*, **52**, 831-834.

G.D. Scott (1960) Packing of spheres, *Nature*, **188**, 908-909.

R.F. Scott (1963) **Principles of Soil Mechanics**, Reading, Massachusetts, Addison-Wesley, 550p.

M. Seppala and K. Linde (1978) Wind tunnel studies of ripple formation, *Geografiska Annaler*, **60A**, 29-42.

M. Shahinpoor and G. Ahmadi (1983) A kinetic theory for the rapid flow of rough inelastic spherical particles and the evolution of fluctuations, *Adv. in Mechanics of the Flow of Granular Materials, Vol. II*, M. Shahinpoor, ed., Houston, Gulf, 641-667.

R.P. Sharp (1963) Wind ripples, *J. Geology*, **71**, 617-636.

R.P Sharp (1964) Wind driven sand in the Coachella Valley, California, *Geol. Soc. Am. Bull.*, **75**, p. 785-804.

R.P. Sharp (1966) Kelso Dunes, Mojave Desert, California, *Geol. Soc. Am. Bull.*, **77**, 1045-1074.

R.P Sharp (1980) Wind driven sand in the Coachella Valley, California: further data, *Geol. Soc. Am. Bull.*, **91**, 724-730.

H.T.U. Smith (1966) Wind-formed pebble ripples in Antarctica (Abstract), *Geol. Soc. Am. Special Paper*, **87**, 160.

M. Sorenson (1985) Estimation of some aeolian saltation transport

parameters from transport rate profiles, *Proceedings of the International Workshop on the Physics of Blown Sand*, O.E. Barndorff-Nielson, J.T. Moller, K. Romer Rasmussen and B.B. Willetts, eds., May 28-31, Aarhus, Denmark, University of Aarhus Press, 141-190.

R.O. Stone and H.J Summers (1972) Study of subaqueous and suberial sand ripples, *Final Report: Office of Naval Research Contract No. N00014-67-A-0269-002*, Arlington, 274p.

H. Tennekes and J.L. Lumley (1972) **A First Course in Turbulence**, Cambridge, Massachusetts, MIT Press.

T.A. Tombrello (1985) Ideas for new work: smoothing curves, *Sloan Seminar Notes*, Caltech, May 15, unpublished.

D.J. Tritton (1977) **Physical Fluid Dynamics**, Berkshire, England, Van Nostrand Reinhold, 346p.

Y. Tsuchiya (1970) Succesive saltation of a sand grain by the wind, *Proc. 12th Conf. Coastal Eng. (ASCE), Vol. 3*, 1417-1427.

Y. Tsuchiya and Y. Kawata (1972) Characteristics of saltation of sand grains by wind, *Proc. 13th Conf. Coastal Eng. (ASCE), Vol. 2*, 1617-1625.

J. Tuazon, J. Peterson, M. Priel and D. Lieberman (1985) Caltech/JPL Hypercube Concurrent Processor, to appear in *Proceedings of the 1985 International Conference on Parallel Processing*, St. Charles, Illinois, IEEE Computer Society Press.

J.E. Ungar and P.K. Haff (1986) Steady-state saltation in air, *Sedimentology*, in press.

V.M. Visscher and M. Bolsterli (1972) Random packing of equal and unequal spheres in two and three dimensions, *Nature*, **239**, 504-507.

T. von Karman (1956a) Sand ripples in the desert, **Collected Work of Theodore von Karman, Vol. 4**, London, Butterworth, 352-356.

T. von Karman (1956b) Aerodynamic considerations of the formation of sand ripples, **Collected Work of Theodore von Karman, Vol. 5**, London, Butterworth, 62-66.

J.D. Walker (1981) An experimental study of wind ripples, unpublished masters thesis, Massachusetts Institute of Technology, 145p.

O.R. Walton (1983) Particle-dynamics calculations of shear flow, *Mechanics of Granular Materials, New Models and Constitutive Relations*, J.T. Jenkins and M. Satake, eds., Elsevier, Amsterdam, 327-338.

O.R. Walton (1984) Computer simulation of particulate flow, *Energy and Technology Review (Lawrence Livermore National Laboratory)*, May, 24-36.

O.R. Walton and R.L. Braun (1985) Viscosity, granular-temperature, and stress calculations for shearing assemblies of inelastic, frictional disks, *J. Rheology*, **30**, 949-980.

J.E. Weir, Jr. (1962) Large ripple marks caused by wind near Coyote Lake (dry), California (Abstract), *Geol. Soc. Am. Special Paper* **73**, 72.

B.T. Werner (1986a) Particles in motion: the case of the loaded die, *Engineering and Science*, March, 20-24.

B.T. Werner (1986b) Feedback in wind-blown sand transport, *Basic and Applied Physics: Brown Bag Preprint* **46**, July, 46p.

B.T. Werner (1987) Particle dynamics: rolling rocks, loaded dice, blown sand and optimization, presented at the *Technical Director's Seminar*, Naval Weapons Center, China Lake, California, January 14.

B.T. Werner and P.K. Haff (1985a) Grain dynamics simulations on the Caltech Concurrent Processors, *Internal Caltech Report*, 30p.

B.T. Werner and P.K. Haff (1985b) Dynamical simulations of granular materials using concurrent processing computers, *Caltech Basic and*

Applied Physics: Brown Bag Preprint **40**, December, 30p.

B.T. Werner and P.K. Haff (1986a) A simulation study of the low-energy ejecta resulting from single impacts in eolian saltation, to appear in *Proceedings of the Conference on Advancements in Aerodynamics, Fluid Mechanics and Hydraulics (ASCE)*, June, Minneapolis.

B.T. Werner and P.K. Haff (1986b) The impact process in eolian saltation: two-dimensional studies, *Caltech Basic and Applied Physics: Brown Bag Preprint* **50**, 57p.; also, *submitted to Sedimentology*.

B.T. Werner and P.K. Haff (1987) A physical model of wind-blown sand transport, *in preparation*.

B.T. Werner, P.K. Haff, R.P. Livi and R.S. Anderson (1986) Measurement of eolian sand ripple cross-sectional shapes, *Geology*, **14**, 743-745.

B.R. White (1982) Two-phase measurements of saltating turbulent boundary layer flow, *Int. J. Multiphase Flow*; **8**, 459-473.

B.R. White and J.C. Schultz (1977) Magnus effect in saltation, *J. Fluid Mech.*, **81**, 497-512.

F. White (1974) **Viscous Fluid Flow**, New York, McGraw-Hill: referenced by Ungar and Haff (1986).

P.L. Wiberg and J.D. Smith (1985) A theoretical model for saltating grains in water, *Jour. Geophysical Research*, **90**, 7341-7354.

B.B. Willetts and M.A. Rice (1985a) Inter-saltation collisions, *Proceedings of the International Workshop on the Physics of Blown Sand*, O.E. Barndorff-Nielson, J.T. Moller, K. Romer Rasmussen and B.B. Willetts, eds., May 28-31, Aarhus, Denmark, University of Aarhus Press, 83-100.

B.B. Willetts and M.A. Rice (1985b) Wind tunnel tracer experiments using dyed sand, *Proceedings of the International Workshop on the Physics of Blown Sand*, O.E. Barndorff-Nielson, J.T. Moller, K. Romer Rasmussen and B.B. Willetts, eds., May 28-31, Aarhus, Denmark, University of Aarhus Press, 225-242.

J.C. Williams and G. Shields (1967) The segregation of granules in a vibrated bed, *Powder Technology*, **1**, 134-142.